

**Viktor Eduard
Dr. Prieb**

To the eternal grateful memory of my father
Christian Eduard Prieb

**The concept of dual-energetic martensite
(CODEM) for the shape memory phenomena**

Review of my intimate and creative life with shape memory alloys over the last 45 years (1974-2019) and saying goodbye to it.

If some of my theses and conclusions seem too daring to someone from this field, these should be viewed as a stimulus for further research and discussion.

*Meanwhile, I'm withdrawing - it's time for me now to leave this field and switch to my neglected muses
Erato and Melpomene.*

Berlin, 2020

Contents:

1 Introduction	5
2 Thermodynamics of the martensitic transformations of SMA's	15
2.1 Free energy and equilibrium temperatures	15
2.1.1 Distribution of elastic energy in the two-phase system	15
2.1.2 Symmetry relationships and differentiability of free energy	16
3 Two energetic martensite forms: monodomain and polydomain	21
3.1 Physical-phenomenological consideration	21
3.1.1 Definition of macro-, micromono- and polydomains of martensite	21
3.1.2 Martensite macromonodomain transformation and the global equilibrium	24
3.1.3 Premartensitic state	25
3.1.4 Transformation of a martensite polydomain and local equilibrium	27
3.2 Transformations of the polyvariant polydomain martensite	31
3.2.1 Phase boundaries and transformation temperatures	31
3.2.2 Coalescence of martensite polydomains	33
3.2.3 The role of habitus plain and orientation relationships	43
3.2.4 Interaction complexity during the transformation	46
4 Experimental measurement methods for SMA-investigations	49
4.1 Acoustic emission	49
4.1.1 AE measurement method	49
4.1.2 AE measurement curves and their analysis	50
4.2 Resistometry	55
4.2.1 Fundamentals of resistometry	55
4.2.2 Resistance measurements during thermo-induced transformations	57
4.2.3 Ascertaining of mechanical hysteresis using resistometry	59
4.2.4 Resistometry as an indirect method of phase analysis	63
4.3 Calorimetry	65
4.3.1 Calorimetric measurement curves from various SMA's	65
4.3.2 Determination of thermodynamic parameters and hysteresis loops	70
4.3.3 Energetic parameters of the thermal hysteresis	75
4.4 Dilatometry	79
4.4.1 Relationship between entropy and thermal expansion	80
4.4.2 Elasticity modulus and thermal expansion	82
4.4.3 Length changes in two-phase temperature range	85
4.4.4 Crystallographic analysis of the transformation dilation	92
4.5 Mechanical hysteresis	97
4.5.1 Quasiplasticity, ferro- and pseudoelasticity	97
4.5.2 Interior of the mechanical hysteresis	110
4.5.3 Affinity of ferroelastic and ferromagnetic hysteresis	114
5 Observations and evidence of martensite monodomains transformations	123
5.1 Transformation with a single phase boundary	123
5.1.1 Equilibrium and stationary conditions	123
5.1.2 Equilibrium disturbance, dynamic conditions and structures	131
5.2 Effect of stacking fault energy	139
5.2.1 Change in stacking fault energy due to aging	139
5.2.2 Increase in stacking fault energy due to electron bombardment	142
5.3 Martensite monodomainization as a stabilization mechanism	149
5.3.1 Martensite stabilization through ferroelastic deformation	149

5.3.2	Martensite stabilization by mechanical impact	154
5.4	Local stabilization effects	159
5.4.1	Return points memory in ferroelastic deformation cycles	159
5.4.2	Return points memory in thermo-induced transformation cycles	163
5.5	Relationships between phase fraction and transformation heat	167
5.5.1	Hysteresis interior, equilibrium and transformation trajectories	167
5.5.2	Transformation velocity and latent transformation heat	173
6	Conclusion	183
7	References	195
8	Appendix: Practical applications of SMA's	205
8.1	Article to the German and international patent: "Composite fabric with memory metal and its applications"	205
8.2	Article to the German and international patent: "Electrical break protection with memory insert"	213
8.3	German patent: "Composite made of elastomers and SMAs and design components thereof"	227
8.4	German utility model: "Temperature control valve with a memory membrane"	251
8.5	German utility model: „Assembled, symmetrical bending actuator with memory elements“	271
9	Nomenclature	291

1 Introduction

Martensitic transformations of shape memory alloys (*SMA*'s) have various special features [1, 2]. The *SMA*'s themselves are, therefore probably, seen as something special and even something intelligent (*smart materials*) [3]. Whenever such a peculiarity is discovered, one tries to find a plausible local explanation for it. So, the local explanations multiply without a uniform concept, and the whole thing becomes more and more complicated.

This is also due to the fact that the relationship to the research object, to the *SMA*'s and their properties as such, which I describe as "intimate", is lost or never existed by theorists and developers of various models. This is how arise unrealistic, misleading theories such as the one about ideal pseudoelasticity [76] and models [107] that promise action frequencies of *SMA* actuators about 100Hz and more. The theories and models offer a lot of mathematics with computer science and little physics through the mentioned lack of relation to *SMA*'s as the research object.

It would be grotesque to desire theorists to put together and melt an *SMA*, to grow a single crystal and cut a specimen from it, to process it and to subject it to a well-considered heat treatment, to carry out a well-thought-out experiment and to analyze extensively its results in order to establish or restore a real personal relationship with the *SMA*'s. Instead, it is sufficient to take a *SMA*-specimen in hand, place it on the lips and bend it pseudoelastically in order to feel its latent heat.

It is like blasphemy to ascribe intelligence to these metal pieces, but after such a "lip test" you can't get rid of the feeling that this thing is very sensitive. In any case, this is how my "intimate" life of a young scientist began with these "metal pieces". In doing so, more questions arose while trying to understand these sensitive things than answers that I could not

find despite my hard enquiry. Now, looking back, I think to have fathomed some of the most important answers. It was only my own later experiment results that brought me to a concept that provides a fundamental, comprehensive understanding of most of the SMA properties.

It is advisable, as the Buddha still taught, to return to the *ab initio* principles with their axiomatic simplicity on branching paths and in tricky situations. One of them would be the Le Chatelier-Braun principle (*the equilibrium law or the principle of the smallest constraint*). This reads: The chemical equilibrium evades an external constraint (*temperature, pressure change*) in such a way that the effects of the external change are reduced. Formulated even more understandably, this means that every thermodynamic system strives for its stable equilibrium, for the state with minimal energy, and only those processes take place in this system that serve this striving.

A thermodynamic system is to be understood as a unit formed from several interacting components. A conglomerate of non-interacting parts as simple spatially limited systems does not form a thermodynamic system with a common equilibrium, because there is no continuous, differentiable function describing the whole system. The total energy of such a conglomerate can be described as a simple sum of the energies of the individual parts:

$$E_{total} = \sum_{i=1}^N E_i . \quad (1.1)$$

This description concerns, for example, the austenite-martensite mixture after the explosive martensitic transformation in quenched steels. Austenite and martensite have no common coherent boundaries, so that there are no

common atomic planes. They are separated from one another by areas of plastic deformation, the energies of which E_{pl} are represented in the sum

(1.1) together with the energies of austenite E^A and martensite E^M :

$$E_{total} = E^A + E^M + E_{pl}. \quad (1.2)$$

The total energy of a complex thermodynamic system, that depends on intensive state variables such as temperature T and mechanical stress σ , should be represented not only by the sum of the energies of N individual interacted parts, but also by the sum of all interaction energies E_{ij} :

$$E_{total}(T, \sigma) = \sum_i E_i(T, \sigma) + \sum_{i \neq j} E_{ij}(T, \sigma). \quad (1.3)$$

The term "thermoelastic" was introduced by Kurdjumov after his light microscopic observations of the temperature-dependent athermal and reversible growth-shrinkage of individual martensite polydomains in an $(Cu - Al - Ni)$ -alloy in 1949 [4]. As innovative as his observations were at the time of the intensive studies of martensite in steels and iron alloys, his original additive formula for the total energy of the two-phase mixture was simple:

$$E = E^A + E^M + E_{el}^{AM}, \quad (1.4)$$

where E_{el}^{AM} is the elastic energy of the AM phase boundaries. The formula (1.4) is similar to both the formulas (1.2) and (1.3) and thus says nothing about an interaction between the two phases, let alone about its analytical form.

Kurdjumov's observations and his sparse formula (1.4) only mean, in view of the above general explanations, that the austenite and the marten-

site in this alloy – at that time it was far from being about shape memory effects (*SME's*) and shape memory alloys (*SMA's*) – are separated by areas of elastic deformation, so that the both have common atomic planes, and the *AM* phase boundaries thus can remain movable. They say nothing about the energy dissipation and the hysteresis as well as about the coherence of phase boundaries despite huge martensitic shear deformation within the elastic austenite matrix, i.e. about the accommodation mechanisms, and just as little about the global equilibrium, if one talked already about the metastable (*thermoelastic*) equilibrium of two phase system during the transformation.

Since then, the thermoelasticity model developed on the basis of Kurdjumov's discovery and the innumerable it accompanying experimental investigations have tried to answer all these questions. This succeeds sometimes more sometimes less, and sometimes some experimental results in special cases, such as, for example, the isostress-isothermal transformation with a one phase boundary [5], contradict directly this model.

The thermoelasticity model considers the athermity of the martensitic forward and reverse transitions as a result of the elastic energy storage at the *AM* phase boundaries. Such storage results in a shift in the transition temperatures, i.e. the athermal growth-shrinkage of individual martensite polydomanes observed by Kurdjumov when the temperature decreases and increases. The process is represented as a transformation trajectory $z(T)$

with a negative slope $\frac{dz(T)}{dT} < 0$, where $z = \frac{m^M}{m^A + m^M}$ is the martensite phase fraction.

A major improvement in formula (1.4) was the introduction of the quantitative relationship between the system parts, e.g. [54] and [55], through

the martensite phase fraction in the additive formula:

$$E = E^A \cdot (1 - z) + E^M \cdot z + E_{el}^{AM}, \quad (1.5)$$

which are also generally used to describe the properties of SMA's, such as e.g. the electrical resistance (§4.2.2):

$$R = R^A \cdot (1 - z) + R^M \cdot z, \quad (1.6)$$

applies in the two-phase range. Only this improvement omitted the third term in (1.4), which does not occur at all in (1.1). However, this question concerns the distribution of elastic energy between the both phases and in the entire two-phase system, which is decisive for the thermodynamic behavior of the system.

The elastic energy arises from the elastic interaction of the austenite with the martensite at the coherent AM phase boundaries. But how do the martensite polydomains interact with one another, and what energy contribution does this interaction make to the elastic energy of both the individual phases and the entire system? Whether and how do the elastic energies E_{el}^A and E_{el}^M of the both phases change during the transformation? The attempt [76] to represent the third term E_{el}^{AM} in (1.4) simply by the number of AM phase boundaries as a function of the martensite phase fraction $E_{el}^{AM} = A \cdot z(1 - z)$, analogous to the model of the coherent equilibrium for coherent precipitates [38], led *ad absurdum*, since the thermoelasticity did not occur at all and seemed to be unknown to the author despite all available experimental evidence.

Without solution of these questions, the question about the course of the equilibrium temperature trajectory $T_0(z)$ during the martensitic forward

and revers transformations cannot theoretically be answered either. One tries to find out experimentally by examining the transformation start temperatures in partial transformation cycles.

It was found all possible forms and positions of this $T_0(z)$ -trajectories at that. Tong and Wayman [6] determined as the first by measuring the electrical resistance of a *Cu*-based SMA's as a function of the temperature $R(T)$ in partial transformation cycles that the equilibrium temperature trajectory $T_0(z)$ runs parallel to the transformation trajectories $z^{AM}(T)$ and $z^{MA}(T)$. Two parallel starting temperature lines $M_s(z)$ and $A_s(z)$ were determined at that for the forward (*AM*) and reverse (*MA*) transformations in partial cycles [7]. In these resistometric studies a very unusual ratio $A_s(z=1) < M_s(z=0)$ was observed, which was even considered as a criterion for the initial classification of SMA's. The equilibrium temperatures were defined as mean values on the basis of these experimental data:

$$T_0(z=0) = \frac{M_s + A_f}{2} \quad \text{and} \quad T_0(z=1) = \frac{M_f + A_s}{2}. \quad (1.7)$$

Two similar lines, forming a latent hysteresis, were also found in all other experimental investigations of this kind, in which, however, the ratio $A_s(z=1) > M_s(z=0)$ was rather the normal case. However, these lines ran very differently both to the transformation trajectories and to each other. Directly *X*-ray recordings [8] of the hysteresis loops in partial cycles of the martensitic forward and reverse transformations of polycrystalline $Ni_{0,5}Ti_{0,5}$ -SMA showed two parallel lines perpendicular to the temperature axis.

Calorimetric examinations of the partial transformation cycles [9, 11,

12, 14, and 15] also showed two lines $M_s(z)$ and $A_s(z)$ with different inclinations to the temperature axis inclusive $\frac{dT_0(z)}{dz} = 0$ (*perpendicular to the temperature axis, even if in most cases only up to $z = 0,4 \div 0,5$*), $\frac{dT_0(z)}{dz} < 0$ or also $\frac{dT_0(z)}{dz} > 0$ in different mono- and polycrystalline SMA's for various martensitic transformations. Based on these results, the equilibrium temperature was taken as the mean:

$$T_0 = \frac{M_s + A_s}{2} \quad (1.8)$$

similar to that defined for isothermal transformations in steels.

During such calorimetric studies of partial transformation cycles, the **Return Point Memory effect** (*RPM-effect*) came to light [13, 14, and 16], which can be observed as a slowdown in the subsequent complete transformation at the reversal points marked in previous partial cycles of the reverse transformation.

The RPM-effect was also discovered in partial cycles of uniaxial ferroelastic tension-compression deformation (ε_f) through reorientation of thermo-induced martensite polydomains in the martensitic state at temperatures $T < M_f$, i.e. without the involvement of *AM* phase boundaries in (*Cu – Al*)-based SMA's [10, 13, and 14]. In addition, a line $\sigma_0(\varepsilon_f) \approx 0$ of

global indifferent ($\frac{d\sigma_0(\varepsilon_f)}{d\varepsilon_f} = 0$) equilibrium between M^{m+} and M^{m-}

martensite macromonodomains and M_m^m martensite micromonodomains as transition zones between the both martensite macromonodomains or a nucleus of a macromonodomain within the other one during the reorientation

was determined for SMA's with a narrow ferroelastic hysteresis. The ferroelastic deformation starts on this line in partial cycles, so the ferroelastic yield point (*index fy*) of both the tensile σ_{fy}^t (*index t*) and the compressive deformation σ_{fy}^c (*index c*) lie on this line.

The equilibrium line $\sigma_0(\varepsilon_f) = const$ ($\frac{d\sigma_0(\varepsilon_f)}{d\varepsilon_f} = 0$) in $(\sigma - \varepsilon_f)$ -diagrams of ferroelastic deformation is very similar to the Maxwell line $p_0(V) = const$ ($\frac{dp_0(V)}{dV} = 0$) in $(p - V)$ -diagrams of the Van der Waals isotherms in kinetic gas theory. The same behavior $\sigma_0(\varepsilon_p) = const$ ($\frac{d\sigma_0(\varepsilon_p)}{d\varepsilon_p} = 0$) is shown by the $(\sigma - \varepsilon_p)$ -diagrams of the pseudoelastic tension-compression deformation of SMA-specimens in the austenitic state at temperatures $T > A_f$ [12, 14], which is caused by the nucleation and growth of martensite micromonodomains within the austenite matrix (*to be observed under a light microscope as martensite lamellae*).

Calorimetric investigations of the pieces cut out of the tensile-compression-samples after several ferroelastic deformation cycles showed [13, 14] that the starting temperature of the martensitic reverse transformation at the first heating is much higher $A_s(\varepsilon_f) = A_s + (50 \div 100)^\circ C$ than that in the initial samples as well as in further cooling-heating cycles of the same deformed specimens. Even then, the phenomenon was interpreted as stabilization of martensite through ferroelastic deformation [13].

In other studies [17, 18] also on *NiTi*-based SMA's [19 – 21], this effect was understood as a deformation- or stress-induced stabilization of marten-

site, similar to the previously known thermal martensite stabilization in *Cu*-based SMA's [22 – 24]. The explanation for this kind of stabilization as well as for the other effects such as two-way memory effect and SMART effect [25, 26] were mostly sought in external effects such as irreversible defects and plastic deformation of the matrix [27, 28].

The thermoelasticity model therefore still remains many explanations of the phenomena observed experimentally guilty and crumbles more and more in conceptless mosaic under the weight of experimental data.

2 Thermodynamics of the martensitic transformations of SMA's

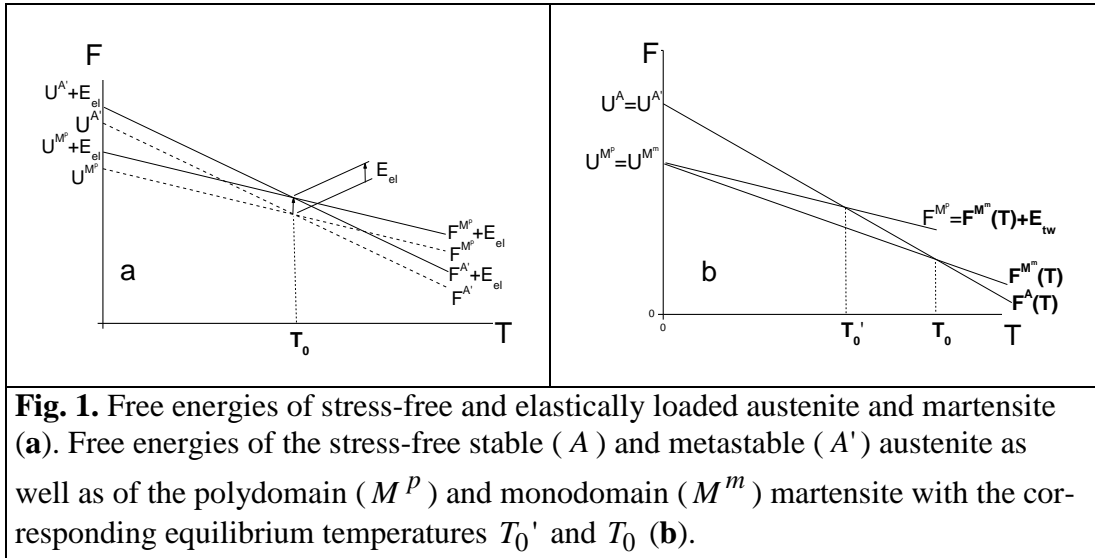
2.1 Free energy and equilibrium temperatures

2.1.1 Distribution of elastic energy in the two-phase system

The first fundamental question that needs to be clarified would be the one about the interaction. Where is the elastic energy stored, equally in the entire two-phase system or differently in individual phases, and what happens when this stored elastic energy dissipates, if its sources annihilate during the transformation?

The long-range interaction of the elastic stresses $\sigma_{el}^{AM} \neq 0$ at the coherent AM phase boundaries extends equally throughout the entire system. The elastic energy is the same everywhere with the equality $G^A = G^M = G$ valid for the elastic modulus of the both phases:

$$E_{el}^A = G^A \cdot \varepsilon_{el}^2 = E_{el}^M = G^M \cdot \varepsilon_{el}^2 = E_{el}^{AM} = G \cdot \varepsilon_{el}^2. \quad 2.1.1)$$



The arising of elastic energy only increases the energy of the entire AM two-phase system E_{el}^{AM} and thus leads to a decreasing of the transformation start temperature below the equilibrium temperature $M_s < T_0$ (**Fig.**

1 a). The increase in energy is compensated for by the difference in the free energies of the both phases (*Le Chatelier-Braun principle*): $\Delta F^{AM}(T) \equiv F^A(T) - F^M(T) = E_{el}^{AM}$. That and only that implicitly includes Kurdjumov's thermoelasticity model in (1.4). It says nothing about the equilibrium temperature T_0 in itself.

However, the elastic energy (2.1.1) does not change the equilibrium temperature T_0 (**Fig. 1 a**). The equilibrium temperature is only influenced by the relative change in the free energies of the involved phases $\Delta F_{el}^{AM}(z) \equiv F_{el}^A(z) - F_{el}^M(z) \neq 0$: this increases by the energy increasing of the austenite $\Delta E_{el}^{AM}(z) > 0$ and decreases by the energy increasing the martensite $\Delta E_{el}^{AM}(z) < 0$ (**Fig. 1 b**).

Such energetic changes take place in the system to be transformed during the martensitic forward and reverse transformations and not only in the transformation temperature range, but also permanently beyond that. The contributions E_{el}^{AM} to the elastic energy of the *AM* two-phase system during the martensitic transformation in Kurdjumov's thermoelasticity model should be defined in more detail in this regard.

2.1.2 Symmetry relationships and differentiability of free energy

Further considerations assume that the free energy (*Helmholtz potential*) of the thermodynamic system $F^{Sys} = F^X(x_i)$ is a real continuous function (**Fig. 3**) of intensive state variables $x_i \equiv \sigma, T$. The function $F^X(x_i)$ describes the entire unitary constituted complex thermodynamic system with interaction in each of its states $X \equiv A, A', A'M^p, M^p, M^m$, with indices pointing: *A* to the stable, *A'* to metastable austenite, M^m to a martensite

macromonodomain, M^P to martensite polydomains and $A'M^P$ to the two-phase ($A'+M^P$)-state. The complete free energy of the two-phase $A'M^P$ -state contains the free energies of the individual phase fraction and the energy of the complex elastic interaction $E_{el}^{A'M^P}(z)$ between the both phases (1.5).

The prerequisite for a real continuous function $F^X(x_i)$ is fulfilled if the symmetry subgroup of the low-symmetrical martensite consists exclusively of the elements of the symmetry main group of the high-symmetrical austenite, like that implies the Ginsburg-Landau theory both in its original form [29] and in its relation to the martensitic transformations [43]. This is the case in most SMA's.

In this case, the function $F^X(x_i)$ is continuous and differentiable over the whole existence area of the thermodynamic system, and all its possible changes due to changes in the intensive variables x_i can be represented by the total differential:

$$dF^X(x_i) = \sum_i \frac{\partial F^X(x_i)}{\partial x_i} dx_i. \quad (2.1.2)$$

The partial derivatives in (2.1.2) for intensive state variable $x_i \equiv T, \sigma$ result in the corresponding extensive state variables such as entropy $S = \frac{dF(T)}{dT}|_{\sigma}$ (**Fig. 1 a, b**) and martensitic deformation $\varepsilon_M = \frac{dF(\sigma)}{d\sigma}|_T$.

The system is in equilibrium at changes of the intensive state variables (*the smallest constraint*), when the function $F^X(x_i)$ shows one or more extremes at some critical points x_{0i} . This is the case when the total differ-

ential (2.1.2) at the values $x_i = x_{0i} \Big|_{x_{j \neq i}}$ corresponding to these critical points is equal to zero, as Figure 3 shows for the potential $F(\bar{e})$ at $\bar{e}_{01} = 0$ and $\bar{e}_{02} = \bar{e}_M$. The equilibrium state variables x_{0i} are determined from the equilibrium condition $dF(x_i = x_{0i} \Big|_{x_{j \neq i}}) = 0$.

An equilibrium is either unstable, if:

$$\frac{d^2 F(x_i = x_{0i})}{dx_i^2} \Big|_{x_{j \neq i}} < 0, \quad (2.1.3)$$

or stable, if:

$$\frac{d^2 F(x_i = x_{0i})}{dx_i^2} \Big|_{x_{j \neq i}} > 0, \quad (2.1.4)$$

and indifferent, if:

$$\frac{d^2 F(x_i = x_{0i})}{dx_i^2} \Big|_{x_{j \neq i}} = 0. \quad (2.1.5)$$

It is in a metastable equilibrium, if the function $F(x_i)$ has, for example, two minima at $x_i = x_{01} \Big|_{x_{j \neq i}}$ and $x_i = x_{02} \Big|_{x_{j \neq i}}$, and the free energy of the system corresponds to the energy:

$$F(x_i = x_{01} \Big|_{x_{j \neq i}}) > F(x_i = x_{02} \Big|_{x_{j \neq i}}), \quad (2.1.6)$$

while the state with energy $F(x_i = x_{02} \Big|_{x_{j \neq i}})$ would then correspond to the global equilibrium.

Most shape memory effects are described by the phase fraction of the martensite $z(T, \sigma)$ and the martensitic deformation $\varepsilon_M(T, \sigma)$ as the exten-

sive ones versus the temperature T and the mechanical stress σ as the intensive state variables. The changes in the system state are determined by the changes in these state variables in their correlation (*Le Chatelier-Braun principle*).

According to Gibbs' phase rule $f = k - p + 2$ for a one-component system $k = 1$, which also is valid for the diffusionless martensitic phase transformation without changing the phase compositions, the degree of freedom $f = 1$ is calculated in two-phase states $p = 2$. This means that only one of the both intensive variables can change independently without disturbing the equilibrium between the both phases. In other words, there is an equilibrium line $\sigma_0(T)$ separating the austenite and martensite phases on the $(\sigma - T)$ -diagram.

This equilibrium line is described by the Clausius-Clapeyron equation adopted for the stress-induced martensitic transformations:

$$\frac{d\sigma_0}{dT} = \frac{\Delta S^{A'M^m}}{\varepsilon_M}. \quad (2.1.7)$$

The variable σ is understood as an anisotropic deformation resulting from the interaction of external (*ext*) and internal (*int*) anisotropic mechanical stresses $\sigma = \sigma^{ext} + \sigma^{int}(z)$ in a SMA-body.

3 Two energetic martensite forms: monodomain and polydomain

The free energy can phenomenologically and physically describe every system state during the temperature decreasing (**Fig. 3**) with the assumptions and definitions made above. Martensite will be considered in two energetically different forms – a mono- and a polydomain form.

3.1 Physical-phenomenological consideration

3.1.1 Definition of macro-, micromono- and polydomains of martensite

The first of the two energetically relevant martensite forms would be a martensite macromonodomain M^m as a result of the homogeneous shear deformation γ_M (**Fig. 2 a**, first row, first step) of the austenite lattice as a whole without secondary invariant displacements:

$$\gamma_M = \frac{\bar{e}_M}{\bar{d}_{hkl}} = tg\beta, \quad (3.1.1)$$

where \bar{e}_M is martensitic shear vector, d_{hkl} is distance between two neighboring parallel $[hkl]$ lattice atomic planes, $[hkl]$ are Miller's indices.

The secondary invariant shear deformation, which is listed in the thermoelasticity model as the 1st accommodation mechanism and defined here as the **structural** (*crystallographic*) accommodation mechanism, leads to the formation of twins within a martensite **macromonodomain** with stacking faults as twin boundaries and thus to the reshuffle of the martensite macromonodomain into a martensite **polydomain** M^p (**Abb. 2 b**). The free energy of the martensite **polydomain** is correspondently higher than that of the martensite macromonodomain by the elastic energy of the stacking faults.

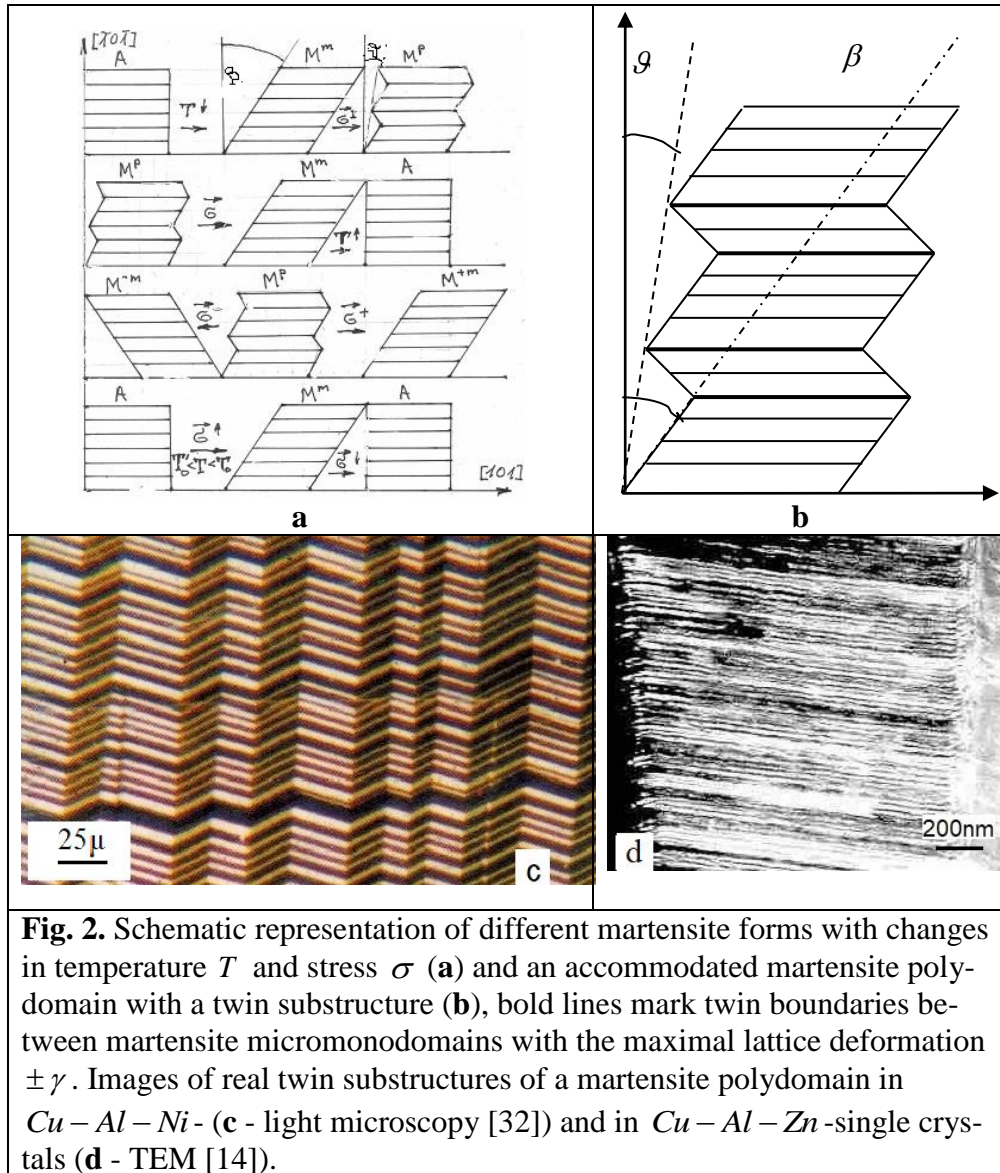
One of the both twin parts with a one stacking fault (**Fig. 2 b**) represents a martensite **micromonodomain** M_m^m as the elementary part of the martensitic phase. The direction of the martensitic shear vector \vec{e}_M (**Fig. 3**) does not change within a micromonodomain. A martensite micromonodomain is therefore the minimal carrier of the maximal martensitic deformation, the lattice shear deformation γ_M (3.1.1).

The low-symmetric martensite macromonodomain can be considered as a hypothetical martensite phase without a substructure that occurs in free space and not in an elastic environment. This martensite form, despite its hypothetical nature, plays a conclusive role in SMA's behavior, because it is in its micromonodomain form also part of a martensite polydomain. The transformation of a martensite polydomain consisting of $N^{M_m^m}$ micromonodomains into a martensite macromonodomain under mechanical external or internal stress (**Fig. 2 a**, *second level, first step*) is very real and no longer hypothetical.

This transformation into a martensite macromonodomain takes place step by step, so that each i th step leads to the reduction of the free energy of the martensite polydomain to an energy quantum $u_{i,i+1} = U_{i+1}^{M^p} - U_i^{M^p} = \gamma \cdot S_{sf}$, with generalized stacking fault energy $\gamma \left[J \cdot m^{-2} \right]$ and area of the stacking fault S_{sf} . Between the two energetic martensite forms defined above – a macromonodomain with energy U^{M^m} and a martensite polydomain with energy U^{M^p} – there is a discrete energy spectrum:

$$U^{M^P} - U^{M^m} = \sum_{i=0}^{N^{M^m}} u_{i,i+1} = N^{M^m} \cdot \gamma \cdot S_{sf}, \quad (3.1.2)$$

where $i = 0$ is valid for the martensite macromonodomain and $i = 1, \dots, N_m^m$ for all existing martensite polydomains with different stacking fault densities ν_{sf} or with different micromonodomain numbers N^{M^m} (3.1.9).



The changes in the free energy of a SMA's as a complex thermodynamic system with temperature decreasing without mechanical external stress from the existence area of stable austenite across the two-phase existence

area to the existence area of martensite down within the framework of the here developed and as a concept of dual-energetic martensite (**CODEM**) designated quantifying consideration analyzed.

3.1.2 Martensite macromonodomain transformation and the global equilibrium

During the temperature decreasing, the free energies of the austenite and the martensite macromonodomain are the same at one temperature $T = T_0$ (**Figs. 1 b and 3**):

$$F^A = U^A - T_0 \cdot S^A = U^{M^m} - T_0 \cdot S^{M^m} = F^{M^m}, \quad (3.1.3)$$

The equilibrium temperature can be determined from the equilibrium condition (3.1.3) as follows:

$$T_0 = \frac{U^A - U^{M^m}}{(S^A - S^{M^m})} = \frac{\Delta U^{AM^m}}{\Delta S^{AM^m}}. \quad (3.1.4)$$

Below the equilibrium temperature, the free energy of the low-symmetric martensite macromonodomain F^{M^m} is smaller than that of the high-symmetric austenite F^A . However, a symmetry change as a $A \rightarrow M^m$ transformation of the stable austenite into the more stable martensite macromonodomain does not take place due to the lattice shear deformation γ_M either at the equilibrium temperature T_0 or during the further temperature decreasing. An energy barrier $U_B^{AM^m} = \frac{1}{2}G \cdot \gamma_M^2$ prevents the formation of the martensite macromonodomain with the huge lattice deformation (3.1.1) within the elastic austenite matrix.

In the continuous function of free energy $F^A(\vec{e})$ (**Fig. 3**), the energy

barrier is shown as a maximum between two minima corresponding to the austenite $F^A(\vec{e} = 0)$ and to the martensite macromonodomain $F^{M^m}(\vec{e} = \vec{e}_M)$:

$$F_B(T) = \frac{1}{2} G \cdot \gamma_M^2 - (T_0 - T) \cdot \Delta S^{A'M^m}. \quad (3.1.5)$$

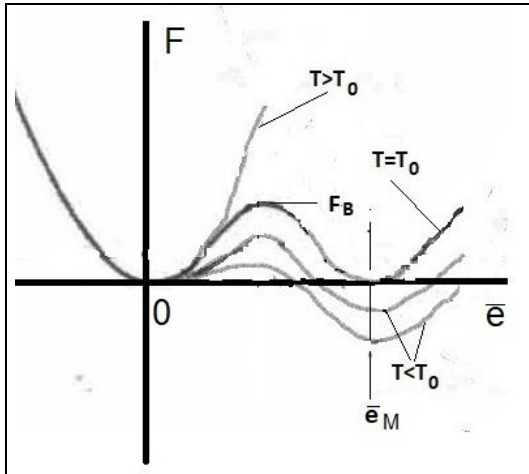


Fig. 3. Schematic representation of the free energy as a continuous function of the lattice shear vector upon temperature decreasing.

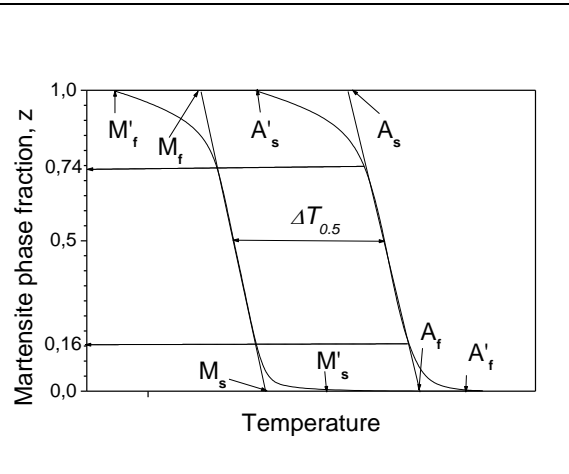


Fig. 4. A hysteresis between $z^{A'M^p}(T)$ and $z^{M^pA'}(T)$ transformation trajectories ascertained from the calorimetric data.

Thus the austenite first persists farther to exist below the equilibrium temperature (3.1.4), but in a metastable state given the positive energy difference $\Delta F^{A'M^m} = F^A(T) - F^{M^m}(T) > 0$ between the austenite and the martensite macromonodomain (2.1.6).

3.1.3 Premartensitic state

The energy difference $\Delta F^{A'M^m}(T < T_0) > 0$ increases during the temperature decreasing below the equilibrium temperature T_0 due to the increase in the second term in (3.1.5) as an entropy contribution to the free energy. The energy barrier is thereby lowered:

$$\Delta F_B(T < T_0) = (T_0 - T) \cdot \Delta S^{A'M^m} > 0. \quad (3.1.6)$$

The entropy difference $\Delta S^{A'M^m} = S^{A'} - S^{M^m} = \frac{dF^{A'}}{dT} - \frac{dF^{M^m}}{dT} > 0$ in (3.1.6) is positive (**Fig. 1 b**). This leads to a flattening of the minimum $F_{e=0\pm\delta}^{A'}(T)$ (**Fig. 3**) and accordingly to a lowering of the elasticity modulus as the temperature decreasing:

$$\frac{dG(T)}{dT} = \frac{d\left[\left(\frac{d^2 F^{A'}(\varepsilon, T)}{d\varepsilon^2}\right)_T\right]}{dT} > 0, \quad (3.1.7)$$

which was found experimentally and is known as softening of the elasticity modulus [1].

The lowering of the energetic barrier and the flattening of the $F_{e=0\pm\delta}^{A'}(T)$ -minimum can be intensified in intermetallic compounds as *NiTi*, *MnCu* well as by the electron-phonon interaction [34], in which the Fermi-surface and Brillouin-zone come into contact solely through thermal expansion. As a result of further cooling, the Fermi-surface and thus the energy of free electrons is reduced.

The equilibrium temperature T_0 reveals itself also experimentally in other effects. It is known that the deformation induced martensite is only possible up to a limit temperature $T \equiv M_d > M_s$ [35]. The stress-induced martensitic transformation of SMA's (*pseudoelasticity*) only takes place in a limited temperature interval $\Delta T_p \equiv T_s - M_s$ [36]. In this temperature interval, i.e. in the area of the softening of the elasticity modulus. In this area is valid the ratio similar to Clausius-Clapeyron-equation (2.1.7), which is derived directly from the equilibrium line $\sigma_0(T)$ resulting from the aforemen-

tioned Gibbs phase rule. On the basis of the previous statements, it can be said that there is the following correspondence between these otherwise unspecified critical temperatures $M_d \equiv T_s \equiv T_0$, which can be considered as an experimental existence evidence of the global equilibrium temperature T_0 between the stable austenite and the martensite macromonodomain.

3.1.4 Transformation of a martensite polydomain and local equilibrium

The second energetically relevant martensite form is then the actually observed thermo- induced martensite polydomain M^P (**Fig. 2 a** first level, second step; **Fig. 2 c, d**) with a substructure (*twins, stacking faults*) [31-33], which is caused by secondary invariant lattice deformation (**Fig. 2 b**), as a result of the adaptation of the martensite and austenite crystal lattices (*the structural accommodation mechanism*). The free energy F^{M^P} of such a martensite polydomain is higher than that of the martensite macromonodomain by the contribution U_{sf} (3.1.2):

$$F^{M^P} = U^{M^P} - T \cdot S^{M^P} = U^{M^m} + U_{sf} - T \cdot S^{M^P}. \quad (3.1.8)$$

The polydomain martensite form (**Fig. 2 c, d**) with movable twin boundaries is responsible for all shape memory effects. The schemes (**Fig. 2 a**) represent the structural backgrounds of the one-way memory effect (**Fig. 2 a, second level**), ferroelasticity (**Fig. 2 a, third level**) and pseudoe-lasticity (**Fig. 2 a, fourth level**). Detailed description of all these effects is given in §§4.5.1-4.5.3.

The energy contribution U_{sf} in (3.1.8) and (3.1.2) can also be deter- mined by the stacking fault density $\nu_{sf} [m^{-1}] = \frac{N_{sf}}{h^{M^P}}$ in a martensite polydo-

main (**Fig. 2 b**) with a height $h^{M^P} = N \cdot d_{hkl}$ and the shear planes number N along the normal to the stacking fault plane or to the shear planes and with the stacking faults number $N_{sf} \equiv N^{M^m}$ (**Fig. 2 b, c, d**):

$$U_{sf} = \gamma \cdot S_{sf} \cdot h^{M^P} \cdot \nu_{sf} \equiv k_{sf}^{M^P} \cdot V^{M^P}, \quad (3.1.9)$$

where $V^{M^P} [m^3] = S_{sf} \cdot h^{M^P}$ is volume and $k_{sf}^{M^P} [MPa] \equiv \gamma \cdot \nu_{sf} = \frac{U_{sf}}{V^{M^P}}$

is the specific (*per volume unit*) stacking fault energy of the considering martensite polydomain.

At a temperature $T = T_0' < T_0$, the equilibrium between the metastable austenite A' and a martensite polydomain M^P , which is also metastable compared to the stable martensite macromonodomain (**Fig. 1 b**), is reached:

$$F^{A'} = U^{A'} - T_0' \cdot S^{A'} = U^{M^m} + U_{sf} - T_0' \cdot S^{M^P} = F^{M^P}. \quad (3.1.10)$$

The equilibrium condition (3.1.10) can be rewritten as follows:

$$\Delta F^{A'M^P} = \Delta U^{A'M^m} - k_{sf}^{M^P} \cdot V^{M^P} - T_0' \cdot \Delta S^{A'M^P} = 0. \quad (3.1.11)$$

The second term in (3.1.11) corresponds to the work

$p \cdot \Delta V = k_{sf}^{M^P} \cdot \Delta V^{M^P}$ or $\sigma \cdot \varepsilon = k_{sf}^{M^P} \cdot \varepsilon$ in thermodynamic potentials, so

that the specific stacking fault energy $k_{sf}^{M^P}$ introduced in (3.1.9) can also

be identified as mechanical stress $k_{sf}^{M^P} [MPa] \equiv \sigma [MPa]$ according to its measurement unit.

The local equilibrium temperature between the metastable austenite A'

and the metastable martensite polydomain M^P results from (3.1.11):

$$T_0' = \frac{\Delta U^{A'M^m} - k_{sf}^{M^P} \cdot V^{M^P}}{\Delta S^{A'M^P}}. \quad (3.1.12)$$

The difference between (3.1.4) and (3.1.12):

$$T_0 - T_0' = \frac{\Delta U^{AM^m}}{\Delta S^{AM^m}} - \frac{\Delta U^{A'M^m} - k_{sf}^{M^P} \cdot V^{M^P}}{\Delta S^{A'M^P}} \quad (3.1.13)$$

shows the difference between the global and local equilibrium temperatures. This difference can arise not only through the contribution of the stacking fault energy, but also through the smaller entropy $S^{M^P} < S^{M^m}$ or $\Delta S^{AM^m} < \Delta S^{A'M^P}$ (**Fig. 1 b**) of the martensite polydomain.

It can be seen from the equations (3.1.4) and (3.1.12) that the global equilibrium temperature T_0 is a fundamental quantity of a SMA, which only depends on the internal energy and the factors influencing it, such as the alloy composition or valence-electron concentration e/a (*the number of valence electrons e per an atom a*) [115]. On the other hand, the local equilibrium temperature T_0' , which also determines all characteristic transformation temperatures, is additionally influenced by many other metallurgical factors (*alloying, heat treatment [37], internal stresses, etc.*) that influence the energy and density of stacking faults. These factors change the temperature difference $T_0 - T_0'$ without affecting the global equilibrium temperature T_0 .

In view of the definitions introduced above, the common term "martensite stabilization" is to be understood directly as a partial or complete transition of a metastable martensite poly domain by reducing its stacking fault

density or energy into a stable martensite monodomain with an increased equilibrium temperature T_{s0}' in the temperature range $T_0' < T_{s0}' \leq T_0$.

3.2 Transformations of the polyvariant polydomain martensite

3.2.1 Phase boundaries and transformation temperatures

Reaching the local equilibrium temperature T_0' only means that the stacking fault energy in (3.1.11) is balanced by the entropy term. However, the formation of a martensite polydomain within the elastic austenite matrix requires the surmounting of another energy barrier. The height of this barrier is determined by the elastic energy of the coherent $A'M^P$ phase boundaries between the metastable austenite and an accommodated martensite polydomain (**Fig. 2 b, c, d**), which is the real subject of Kurdjumov's thermoelasticity model.

The elastic energy of a $A'M^P$ phase boundary is directly related to the non-accommodated lattice deformation of a martensite polydomain:

$$\varepsilon_{el}^{M^P} = tg \mathcal{G} = \gamma_M \cdot (1 - k_a^I), \quad (3.2.1)$$

where $0 \leq k_a^I = \left(1 - \frac{\varepsilon_{el}^{M^P}}{\gamma_M}\right) \leq 1$ is the accommodation degree achieved by

the structural accommodation mechanism. The non-accommodated deformation causes elastic shear stresses at the coherent $A'M^P$ phase boundary:

$$\sigma_{el} = \frac{1}{2} G \cdot \gamma_M (1 - k_a^I). \quad (3.2.2)$$

These provide a contribution of elastic energy to the free energy of the two-phase system that is equally distributed in both phases A' and M^P (**Fig. 1 a**):

$$U_{el} = \frac{1}{2} G \cdot \gamma_M^2 (1 - k_a^I)^2 \quad (3.2.3)$$

The non-accommodated deformation (3.2.1) is the basis of the dilation of SMA's and can be determined experimentally (§4.4.3), although the dilation value ε_d (4.4.22) is again minimized by the morphological accommodation mechanism, so that $\varepsilon_d < \varepsilon_{el}^{M^P}$ is. The accommodation degree k_a^I in (3.2.1) is naturally linearly related to the stacking fault density ν_{sf} .

The presence of the energy barrier (3.2.3) requires a further increase in the entropy contribution due to the undercooling for the formation of a martensite polydomain, until the equilibrium

$$F^{A'M^P} = \Delta S^{A'M^P} \cdot (T_0' - M_s') = U_{el}^{M^P} \quad (3.2.4)$$

is reached at a starting temperature $T = M_s' < T_0'$ (**Fig. 4**).

The first martensite polydomains form at the martensite start temperature M_s' that can actually be measured. The energy won through further undercooling compensates for the energy contribution of coherent $A'M^P$ phase boundaries between the metastable austenite A' and the $N^{M^P}(T)$ martensite polydomains formed in the temperature range $M_s < T < M_s'$, whereby M_s is the extrapolated (**Fig. 4**) starting temperature.

The total contribution of N^{M^P} martensite polydomains, which hardly interact elastically with one another, to the free energy of the two-phase system can be calculated simply additive:

$$U_{el}^{M^P}(T) = \sum_{i=1}^{N^{A'M^P}} U_{el}^{M_i^P} = \bar{u}_{el}^{M^P} \cdot N^{M^P}. \quad (3.2.5)$$

As the cooling continues, this elastic energy is also compensated by an energetic entropy contribution:

$$F^{A'M^P} = (T_0' - M_s) \cdot \Delta S^{A'M^P} = \bar{u}_{el}^{M^P} \cdot N^{M^P}(T), \quad (3.2.6)$$

so that further $N^{M^P}(T)$ martensite polydomains can form.

How the local equilibrium temperature $T_0'(z)$ behaves during the forward transformation depends on the changes in energy within the martensitic phase, primarily due to the number of internal martensitic $M^P M^P$ domain boundaries, but also due to possible changes in the stacking fault density $\nu_{sf}^{M^P}$ in individual martensite polydomains because of the redistribution of elastic stresses during the transformation.

3.2.2 Coalescence of martensite polydomains

The elastic interaction between scattered martensite polydomain intensifies with further cooling $T < M_s$ and the increasing the martensite polydomain number $N^{M^P}(T)$. The total energy of the two-phase system can therefore no longer be calculated additively. The equation (3.2.5) must consequently get an energetic term describing this interaction.

The martensitic forward transformation generally takes place not only through the nucleation of new martensite polydomains, as in the temperature range $M_s' \div M_s$, but also through their growth. The transformation kinetics:

$$\dot{z} = \frac{dz}{dT} \cdot \dot{T} \quad (3.2.7)$$

is characterized by the slope $\frac{dz(T)}{dT}$ of the transformation trajectory $z(T)$ at

a constant scanning rate $\dot{T} = const$, at that $\frac{dz(T)}{dT} < 0$ corresponds to the

athermal kinetics represented by the thermoelasticity model.

The forward and reverse transformation trajectories $z^{A'M^P}(T)$ and $z^{M^PA'}(T)$ build a hysteresis loop (**Fig. 4**). The forward transformation trajectory ($\dot{T} < 0$) has three kinetically different sections: An acceleration section $\ddot{z}^{A'M^P} > 0$ of the autocatalytic nucleation in the temperature range $M_s' \div M_s$, a section of the rapid, almost linear increase $\dot{z}^{A'M^P} = const$, $\ddot{z}^{A'M^P} = 0$ of the martensite phase fraction through growth or nucleation and growth of scattered martensite polydomains in the temperature range $M_s \div M_f$ and a the slowing down section $\ddot{z}^{A'M^P} < 0$ of the transformation in temperature range $M_f \div M_f'$.

The reverse transformation trajectory $z^{M^PA'}(T)$ shows similar sections during heating ($\dot{T} > 0$): Acceleration $\ddot{z}^{M^PA'} > 0$ of the nucleation of austenite as splitting of each internal martensitic M^PM^P domain boundaries in two $A'M^P$ phase boundaries in the temperature range $A_s' \div A_s$, rapid almost linear ($\ddot{z}^{M^PA'} = 0$) shrinking or disappearance of martensite polydomains in the temperature range $A_s \div A_f$ and slowing down ($\ddot{z}^{M^PA'} < 0$) of the reverse transformation in the temperature range $A_f \div A_f'$.

The characteristic transformation temperatures without apostrophes are determined by extrapolating (**Fig. 4**) the linear sections of the transformation trajectories $z(T)$ to $z = 0$ (M_s, A_f) and to $z = 1$ (M_f, A_s) [9, 11, and 14], while those with apostrophes marked temperatures reflect the de-

viations of the transformation trajectories outside of the transformation temperature ranges $M_s \div M_f$ and $A_s \div A_f$ correspond to deviations on the real measurement curves [6, 7].

It is now our purpose to determine and to describe the energetic processes that are hidden behind these kinetic changes during the martensitic forward transformation. The elastic interaction between separated martensite polydomains leads to a change in the elastic energy of the two-phase system and its redistribution in single phases. Since the elastic energy is concentrated at the boundaries, the development of the number of these boundaries during the transformation is described and analyzed through the martensite phase fraction $z(T)$ instead of the separated polydomains number.

Building of complex conglomerates consisting of merged martensite polydomains or their different orientation variants as a result of the morphological accommodation mechanism effect leads to the pairwise annihilation of the $A'M_i^P$ phase boundaries with the emergence of single internal martensitic $M^P M^P$ domain boundaries. This conversion process, driven by the elastic interaction of the separated martensite polydomains, can be considered as the coalescence of martensite polydomains and qualitatively described by an empirical introduced coalescence probability factor similar to that of spinodal decomposition [30] or coherent precipitation [38]:

$$\phi_c = z \cdot (1 - z). \quad (3.2.8)$$

The difference to bubble coalescence is that an internal martensitic domain boundary remains between two coalesced martensite polydomains and makes its contribution to the free energy of the martensite phase. The energy won for the whole two-phase system:

$$\Delta U_{el}^{A'M^P} = U_{el}^{A'M^P} - U_{el}^{M^P M^P} > 0 \quad (3.2.9)$$

is mainly ensured by the fact that only one internal martensitic $M^P M^P$ domain boundary is created instead of two $A'M_i^P$ phase boundaries. The elastic energy of the two-phase system is thereby at least halved. The energy obtained (3.2.9) is dissipated as acoustic emission (§4.1) and contributes the main part to their intensity.

The morphological accommodation mechanism effects also the reduction of the elastic stresses at the $M^P M^P$ domain boundaries because of their better compatibility with one another. This reactivates the structural accommodation mechanism responsible for adapting the martensitic deformation to stress fields in the environment of the martensite polydomains and leads to a reduction in the stacking fault density within the separated martensite polydomains growing together.

The energy of these martensite polydomains is thereby reduced to a certain number of energy quanta (3.1.2), and the equilibrium temperature $T_0'(z)$ increases (**Fig. 1 b**). The internal martensitic $M^P M^P$ domain boundaries simultaneously increase the elastic energy of the martensite phase and lower the local equilibrium temperature $T_0'(z)$. The total elastic energy of the two-phase system decreases in all cases, so that the continuation of the forward transformation requires less undercooling and the slope $\frac{dz(T)}{dT}$ of the transformation trajectory $z(T)$ increases.

The number of $A'M^P$ phase boundaries during the forward transformation ($0 \leq z \leq 1$) can be described by the experimentally measurable vari-

ables $N_{M_f}^{M^P}$, the number of merged martensite polydomains at the end of the forward transformation in the martensitic state ($T = M_f$), and $z(T)$:

$$N^{A'M^P}(z) = 2N_{M_f}^{M^P} \cdot \phi_c(z). \quad (3.2.10)$$

The factor “2” in (3.2.10) only indicates that each martensite polydomain forms two $A'M^P$ phase boundaries in its lamellar or plate shape, which annihilate during the polydomain coalescence.

The development of the elastic energy of $A'M^P$ phase boundaries is accordingly determined by changing their number (3.2.10):

$$U_{el}^{A'M^P}(z) = \bar{u}_{el}^{M^P} \cdot 2N_{M_f}^{M^P} \cdot \phi_c(z) \equiv 2K_{el} \cdot z(1-z). \quad (3.2.11)$$

The number of internal $M^P M^P$ martensitic domain boundaries is naturally related to the number of $A'M^P$ phase boundaries as follows:

$$N^{M^P M^P}(z) = N_{M_f}^{M^P} \cdot [z - \phi_c(z)] = N_{M_f}^{M^P} \cdot z^2 \quad (3.2.12)$$

and determines the development of elastic energy within the martensite phase:

$$U_{el}^{M^P M^P}(z) = \bar{u}_{el}^{M^P} \cdot N_{M_f}^{M^P} \cdot z^2 \equiv K_{el} \cdot z^2(T). \quad (3.2.13)$$

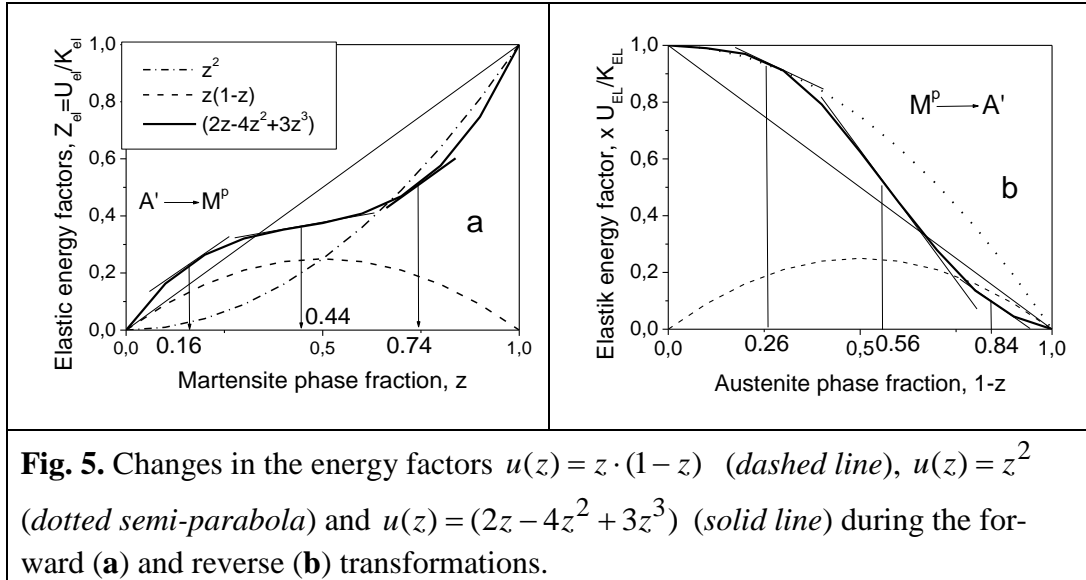
The contributions of the elastic energy of $A'M^P$ phase boundaries and internal martensitic $M^P M^P$ domain boundaries to the elastic energy U_{el} of the whole two-phase system in the area $0 \leq z \leq 1$ can then be represented in the traditional way by the phase fraction of the martensite z and the austenite $(1-z)$:

$$U_{el}(z) = U_{el}^{A'M^P} \cdot (1-z) + U_{el}^{M^P M^P} \cdot z = 2K_{el} \cdot z(1-z)^2 + K_{el} \cdot z^3. \quad (3.2.14)$$

In the normalized form:

$$\frac{U_{el}(z)}{K_{el}} = (2z - 4z^2 + 3z^3) \quad (3.2.15)$$

can the function $u(z) = (2z - 4z^2 + 3z^3)$ be easily analyzed and graphically represented including its individual terms $u(z) = z \cdot (1-z)$ and $u(z) = z^2$ (**Fig. 5 a**).



It can be seen that the elastic energy of the $A'M^P$ phase boundaries or the number of $A'M^P$ phase boundaries (function $u(z) = z \cdot (1-z)$) reaches its maximum at $z = 0.5$ and is no longer present at the end of the transformation because of the coalescence. The elastic energy or the number of internal martensitic $M^P M^P$ domain boundaries (function $u(z) = z^2$) rises meanwhile parabolically. Development of the total elastic energy from all boundaries and their interaction is represented by a sinusoidal curve with a maximum at $z \approx 0.16$ and a minimum at $z \approx 0.74$.

Such a complicated development of the elastic energy during the for-

ward transformation is mainly due to the complex interplay of two accommodation mechanisms. Accommodation itself means the adaptation of two phases with different crystal lattices to one another for the purpose of reducing the mechanical stresses on the phase boundaries and thus minimizing the free energy of the two-phase system. The structural accommodation (*accommodation degree* k_a^I) initially reduces these stresses through stacking faults incorporation [111] into the elastic range below the plastic yield point $\sigma < \sigma_y$.

The morphological accommodation (*accommodation degree* k_a^{II}) additionally reduces these elastic stresses and thus the elastic energy of the two-phase system. This also influences the accommodation degree k_a^I , so that the resulting dilatometrically (§4.4.3) determined accommodation degree $0 \leq k_a \leq 1$ cannot be represented as a simple sum of the both accommodation degrees, but as a sum, for example, of the interacting terms:

$$k_a = k_a^I + k_a^{II} + k_a^I \cdot k_a^{II}. \quad (3.2.16)$$

Since the martensitic reverse transformation in SMA's takes place in the exactly opposite sequence [6], the last-formed internal martensitic $M^P M^P$ domain boundaries split when heated above the temperature $A_s' \geq T_0'$ than the first into two $A' M^P$ phase boundaries with an increase in the elastic energy of the two-phase system, which always requires further overheating. The splitting of a $M^P M^P$ domain boundary into two $A' M^P$ phase boundaries is to be understood as the previously undefined nucleation of the austenite during the martensitic reverse transformation. With this justification, the development of the elastic energy during the reverse transformation can be presented as the line determined for the forward transformation, but mir-

rored relative to the diagonal $U_{el}(z)/K_{el} = z$ (**Fig. 5 b**).

The complete free energy of the two-phase system is now supplemented by the three-part interaction energy:

$$F^{A'+M^P}(z) = F^{A'}(1-z) + F^{M^P} \cdot z + U_{el}, \quad (3.2.17)$$

or:

$$F^{A'+M^P}(z) = F_0^{A'} - (\Delta U^{A'M^P} - T \cdot \Delta S^{A'M^P}) \cdot z + K_{el} \cdot (2z - 4z^2 + 3z^3). \quad (3.2.18)$$

After solution of the quadratic equation for the equilibrium condition:

$$\frac{dF^{A'+M^P}}{dz} = -\Delta U^{A'M^P} + T \cdot \Delta S^{A'M^P} + 2K_{el} - 8K_{el} \cdot z + 9K_{el} \cdot z^2 = 0, \quad (3.2.19)$$

can be, first the transformation trajectory $z(T)$ determined as an analytical function and, secondly the $z_{1,2}$ extremal values calculated, which are easier to determine graphically (**Fig. 5 a**): $z_1 = 0.16$ and $z_2 = 0.74$.

The second derivation:

$$\frac{d^2 F^{A'+M^P}}{dz^2} = K_{el} \cdot (18z - 8) \quad (3.2.20)$$

shows that the value $z_1 = 0.16$ corresponds to a maximum

$\frac{d^2 F^{A'M^P}}{dz^2} = -5,12 < 0$ and the value $z_2 = 0.74$ corresponds to a minimum

$\frac{d^2 F^{A'+M^P}}{dz^2} = 5.32 > 0$ of the elastic energy. The $A'M^P$ phase boundaries

and internal martensitic $M^P M^P$ domain boundaries are therefore at $z_1 \approx 0.16$ in an unstable, at $z_2 \approx 0.74$ in a stable and at $z_3 \approx 0.44$ in an in-different equilibrium.

In the thermoelasticity model, the condition of thermoelastic equilibrium

(3.2.19) means that the sum of all driving forces is zero:

$$\frac{dF^{A'+M^P}}{dz} = f_{ch} + f_{nch} + f_{dis} = 0, \quad (3.2.21)$$

where the driving forces are called f_{ch} chemical, f_{nch} non-chemical and f_{dis} dissipative [113]. By comparing equations (3.2.19) and (3.2.21), these driving forces can then be interpreted as follows:

$$f_{ch} = -\Delta F^{A'M^P}, \quad f_{nch} + f_{dis} = 2K_{el} + K_{el} \cdot (8z - 9z^2). \quad (3.2.22)$$

The non-chemical and the dissipative driving forces cannot be separated from one another in the CODEM, because these are changes in the same elastic energy that is both stored and dissipated during the transformation.

The stability condition for the thermoelastic equilibrium (3.2.20) is only fulfilled for $z > \frac{4}{9} \approx 0.44$, i.e. only for the second half of the forward transformation. The two-phase system is unstable in the $0 < z < 0.44$ area (**Fig. 5 a**).

The solutions $z_1 = 0.16$ and $z_2 = 0.74$ resulting from (3.2.19) correspond to the maximum and the minimum of the function $u(z) = (2z - 4z^2 + 3z^3)$. Between these two extremes there is a rapid increase in the martensite phase fraction with an almost linear slope of the transformation trajectory $z(T)$. The linear extrapolation to $z = 0$ and to $z = 1$ from this area of rapid growth is used to determine the characteristic transformation temperatures, which makes the meaning of these extrapolated temperatures clear.

In the area of instability $0 < z < 0.16$ ($M_s < T < M_s'$) there is an accelerated increase in the martensite phase fraction due to the nucleation of

small martensite polydomains with a large surface-to-volume ratio. In a mostly very extensive area $0.74 < z < 1$ ($M_f' < T < M_f$), where the increasing elastic energy of the martensite phase dominates the total energy of the two-phase system, the increase in the martensite phase fraction $z(T)$ is slowed down.

In which way does each of the three contributions of the elastic energy in (3.2.18) as well as their combined effect influence the local equilibrium temperature $T_0'(z)$ during the martensitic transformation cannot be calculated directly. In general, as already discussed above, the slope $\frac{dT_0'(z)}{dz}$ of the equilibrium temperature trajectory within the hysteresis loop, in contrast to the slope $\frac{dz(T)}{dT}$ of the transformation trajectory, is caused not due to a change in the energy of the two-phase system as a whole, but only due to a relative change in the energy of the martensite phase (**Fig. 1 b**).

The equilibrium temperature trajectory $T_0' = 2K_{el} / \Delta S^{A'M^P}$ becomes a vertical line, if the energy contributions $\Delta U_{el}^{M^P M^P}(z) = K_{el} \cdot z^2$ from the internal martensitic $M^P M^P$ domain boundaries and from changes in the stacking fault density due to changes of shear stress fields in the vicinity of individual martensite polydomains during their coalescence $\Delta U_{sf}^{M^P} = \gamma \cdot \Delta v_{sf} \cdot V \cdot z$, where $V \cdot z = V^{M^P}$ is the volume of a SMA sample, compensate each other: $\Delta U_{el}^{M^P}(z) = \Delta U_{sf}^{M^P}(z)$. That is the case for the growth section $0.16 < z < 0.44$.

A negative slope $\frac{dT_0'(z)}{dz} < 0$ can be attributed to the increase in the free

energy of the martensitic phase $\Delta U_{el}^{M^p M^p}(z) > \Delta U_{sf}^{M^p}(z)$ due to the intensive multiplication of the internal martensitic $M^p M^p$ domain boundaries. The case occurs at $z \geq 0.44$ where the term $U_{el}^{M^p M^p}(z) = K_{el} \cdot z^2$ (**Fig. 5 a**) dominates. A positive slope $\frac{dT_0'(z)}{dz} > 0$ sets in the case

$\Delta U_{el}^{M^p M^p}(z) < \Delta U_{sf}^{M^p}(z)$. The relationship $\frac{\Delta U_{el}^{M^p M^p}(z)}{\Delta U_{sf}^{M^p}(z)}$ is strongly

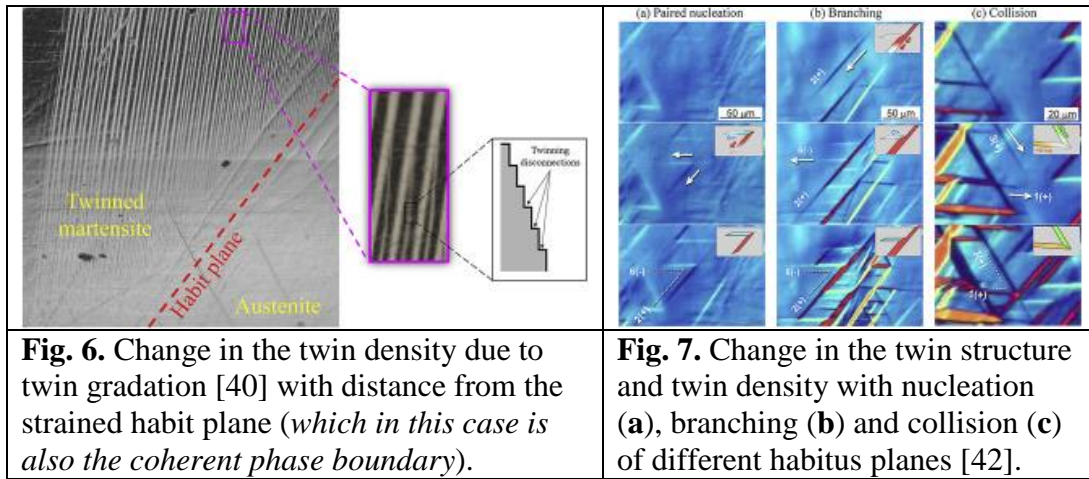
related to the hysteresis properties (*hysteresis width, slope of the transformation trajectories*), i.e. with crystallographic, morphological and thermodynamic transformation parameters.

3.2.3 The role of habitus plain and orientation relationships

The elastic energy density of single coherent $A'M^p$ phase boundaries is determined by the elastic stresses on these boundaries, which depend on the orientation relationships between the crystal lattices of the austenite and the martensite [39–42] and are mainly concentrated at the ends of wedge-shaped martensite polydomains (**Fig. 8 d**).

These stresses are reduced by the formation of twins in martensite polydomains. This structural accommodation results in a redistribution of the elastic energy between the two phases – decreasing the elastic energy of austenite, increasing the elastic energy of martensite and thereby lowering the local equilibrium temperature T_0' . The energy increase of the martensite is greater, the higher the twin density in the field of internal stresses. The transition zones between different twin densities are formed by twin gradation (**Fig. 6**), which causes an additional energy increase in the martensite phase.

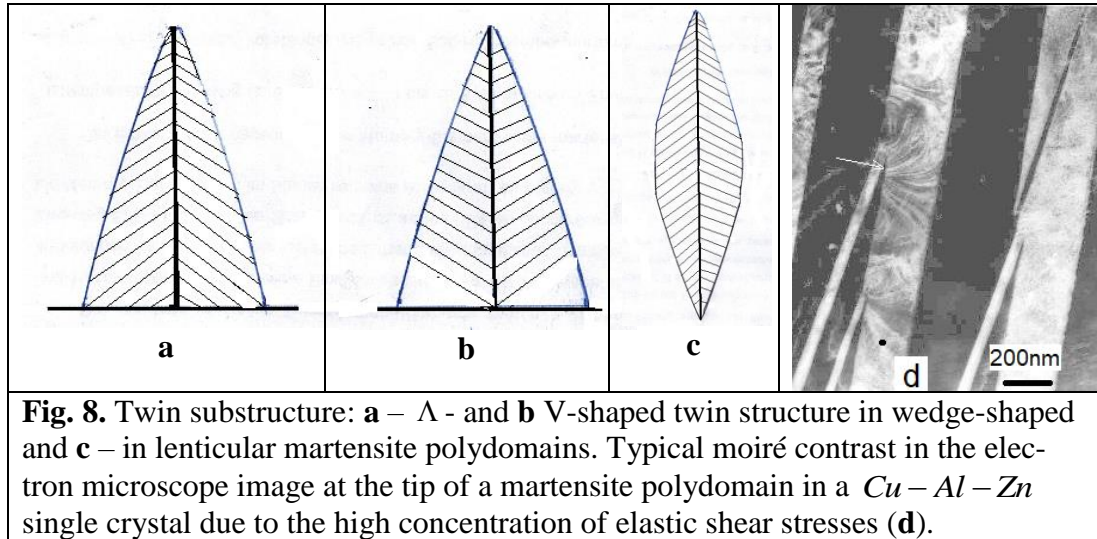
Compatibility of the connection planes during the nucleation, growth and coalescence of different martensite polydomains influences changes in the twin structure and density just as strongly (**Fig. 7 a-c**). The greater are the distortion forces and torques acting on a habitus plane, the further away Miller indices (hkl) of the habitus plane from their rational numbers. The rationality of the habitus plane indices depends on the symmetry relationships between the crystal lattices of both phases, as already discussed in §2.1.2.



For most non Fe -basic SMAs, the symmetry group consisting of the symmetry elements of the low-symmetrical martensite lattice is a subgroup of the symmetry main group consisting of the symmetry elements of the high-symmetrical austenite lattice. This is the prerequisite for the continuity of the analytical free energy function of order parameters (such as e.g. the lattice shear vector in **Figure 3**).

Consequently, the more of symmetry elements of the main symmetry group contains the symmetry subgroup of the martensite crystal lattice, the closer to rational numbers are the indices of the habitus plane [44, 45], the smaller is the stress on the habitus plane (smaller elastic energy of phase boundaries), and the narrower is the thermal hysteresis of a corresponding

martensitic transformation [46]. This stress is accordingly minimal at an invariant habitus plane. The transformations with invariant habitus planes should have the narrowest hysteresis loops.



A strained habitus plane is relieved by the formation of twins as an invariant secondary lattice shear deformation (*Figs. 6 and 7 a-c*). Consequently, the smaller the stress on the habit plane, the smaller are the twin density and the elastic energy of the martensite phase, and the higher are the transition temperatures.

In theory [47], the Λ - (*Fig. 8 a*) and V-shaped (*Fig. 8 b*) twin structures are energetically equivalent. However, the Λ -shaped always and V-shaped twin structures never are observed experimentally. It is because each of the twin shearing deformation begins at the habitus plane in order to relieve it and should end at a free interface (*phase, grain, block boundary*). Therefore, the V structure in Figure 8 b with its twin-free lower corners does not seem to make also energetically much sense. In a lenticular polydomain (*Fig. 8 c*), this question is obviously irrelevant.

3.2.4 Interaction complexity during the transformation

All of these considerations indicate that the martensitic forward and reverse transformations are accompanied by several cooperating and interacting and not necessarily the same processes. These processes influence as well the transformation trajectories $z^{A'M^P}(T)$ and $z^{M^P A'}(T)$ as the equilibrium temperature trajectories $T_0'(z)$ during the forward and reverse transformations in various ways.

This is why most of the experimentally determined hysteresis loops are asymmetric. The elastic stresses of $A'M^P$ phase boundaries lead to athermal kinetics with a negative slope $\frac{dz(T)}{dT} < 0$ of the transformation trajectories $z(T)$ without influencing the local equilibrium temperature. The elastic stresses of internal martensitic $M^P M^P$ domain boundaries, on the other hand, determine the position and form of the equilibrium temperature trajectories $\frac{dT_0'}{dz}$.

The internal martensitic $M^P M^P$ domain boundaries in the conglomerates that have grown together from different orientation variants of martensite polydomains (*always in proportion* $N^{M^P M^P} = 2N^{A'M^P}$) increase the free energy of the martensite phase and thus lower the local equilibrium temperature $\frac{dT_0'(z)}{dz} < 0$. A possible negative change in the stacking fault density $\frac{dv_{sf}(z)}{dz} < 0$ in the dynamic field of the internal stresses increases the local equilibrium temperature $T_0'(z)$ ($\frac{dT_0'(z)}{dz} > 0$), while a positive

change $\frac{dv_{sf}(z)}{dz} > 0$ leads to its negative slope $\frac{dT_0'(z)}{dz} < 0$.

Consideration of redistribution processes of elastic energy through changes in the martensite substructure implies different structural-energetic martensite states during the transformation. Expressed in a simple way, this means that the martensite at the end of the forward transformation $M_1^P \equiv M^P(z=1)$ related to its substructure (*macro symmetry*) and energy is not the martensite at the beginning of the transformation $M_0^P \equiv M^P(z=0)$.

As a result, the equilibrium conditions and thus the local equilibrium temperature between the martensite M_1^P and the metastable austenite A' in the reverse transformation are also different from those between the martensite M_0^P and the metastable austenite A' in the forward transformation. This justifies the splitting of the equilibrium temperature trajectory $T_0'(z)$ into two trajectories $T_0^{A'M_0^P}'(z) \equiv M_s(z_i)$ for the forward transformation and $T_0^{M_1^PA'}(z) \equiv A_s(z_i)$ for the reverse transformation, where i is the number of the partial cycle. The two trajectories show their own behavior relative to the martensite phase fraction and build an internal latent hysteresis. The area of the latent hysteresis corresponds to the energy difference:

$$\Delta F_{el} = \left[T_0^{M_1^PA'}(z) - T_0^{A'M_0^P}(z) \right] \cdot \Delta S^{A'M^P} = w_D^l(z) \quad (3.2.23)$$

or the energy won through the redistribution of elastic energy between the both phases and dissipated as acoustic emission.

Due to such jumble situation, it is difficult to make any theoretical statements about the shape of the hysteresis loop of a concrete martensitic transformation and about the changes in the local equilibrium temperature $T_0'(z)$ during the transformation. On the other hand, it is quite possible to determine the position (*the equilibrium and transformation temperatures*) and the width of the hysteresis loops experimentally with the help of diverse measuring methods and to control it in a well-aimed manner by adding alloying and thermomechanical treatment, which affects material constants such as the generalized stacking fault energy.

4 Experimental measurement methods for SMA-investigations

The martensitic transformations of SMA's are accompanied by changes in many properties, such as, e.g. the lattice parameters, the specific electrical resistance, the entropy, which are different in the martensite and the austenite. This enables, the changes to register and to investigate in various experimental measurement methods. In addition, the accompanying processes discussed above such as nucleation of the martensite, building and annihilation of phase boundaries, formation of domain boundaries as morphological accommodation and their splitting as nucleation of the austenite, development and redistribution of stacking faults as structural accommodation cause the dissipation or radiation of the elastic energy, which is also registered and analyzed experimentally.

4.1 Acoustic emission

4.1.1 AE measurement method

One of such measurement methods is the registration of the acoustic emissions (*AE*). *AE* measurement has been used successfully since the 1960s as a non-destructive testing method for the formation and propagation of cracks in materials [114], based on the measurements of the elastic waves accompanying these processes. It did not take long before this method was also used in investigating martensitic transformations, because the nucleation and growth of a martensite crystal are completely similar to those of a crack.

In the *AE*-method, the elastic impulses are converted into electrical impulses in a piezoelectric quartz sensor attached on the polished sample surface with a resonance frequency of 400kHz that is the opposite of an ultrasonic transducer. The electrical impulses are electronically amplified and registered dependent on the temperature. The elastic energy (3.2.9) released

and dissipated during the martensitic transformations is emitted and registered as acoustic emission when the temperature changes.

The AE-intensity $I_{AE}(T)$ is determined by the number of impulses $N_{AE}(T)$ in the scanning range $M_f' \div A_f'$ with a constant scanning rate $\dot{T} = const$ and the released, dissipated part $\frac{U_d}{U_{el}}$ of the elastic energy

$U_{el}^{A'M^P}$ stored at the $A'M^P$ phase boundaries (3.2.3):

$$I_{AE} \left[imp \cdot s^{-1} \right] \propto N_{AE}(T) \cdot \frac{U_d}{U_{el}} \cdot \frac{\dot{T}}{A_f' - M_f'}. \quad (4.1.1)$$

The AE-intensity of the experimentally determined AE measurement curves (**Fig. 9 a-c**) is in the range of $(10^3 \div 10^4) imp \cdot s^{-1}$.

4.1.2 AE measurement curves and their analysis

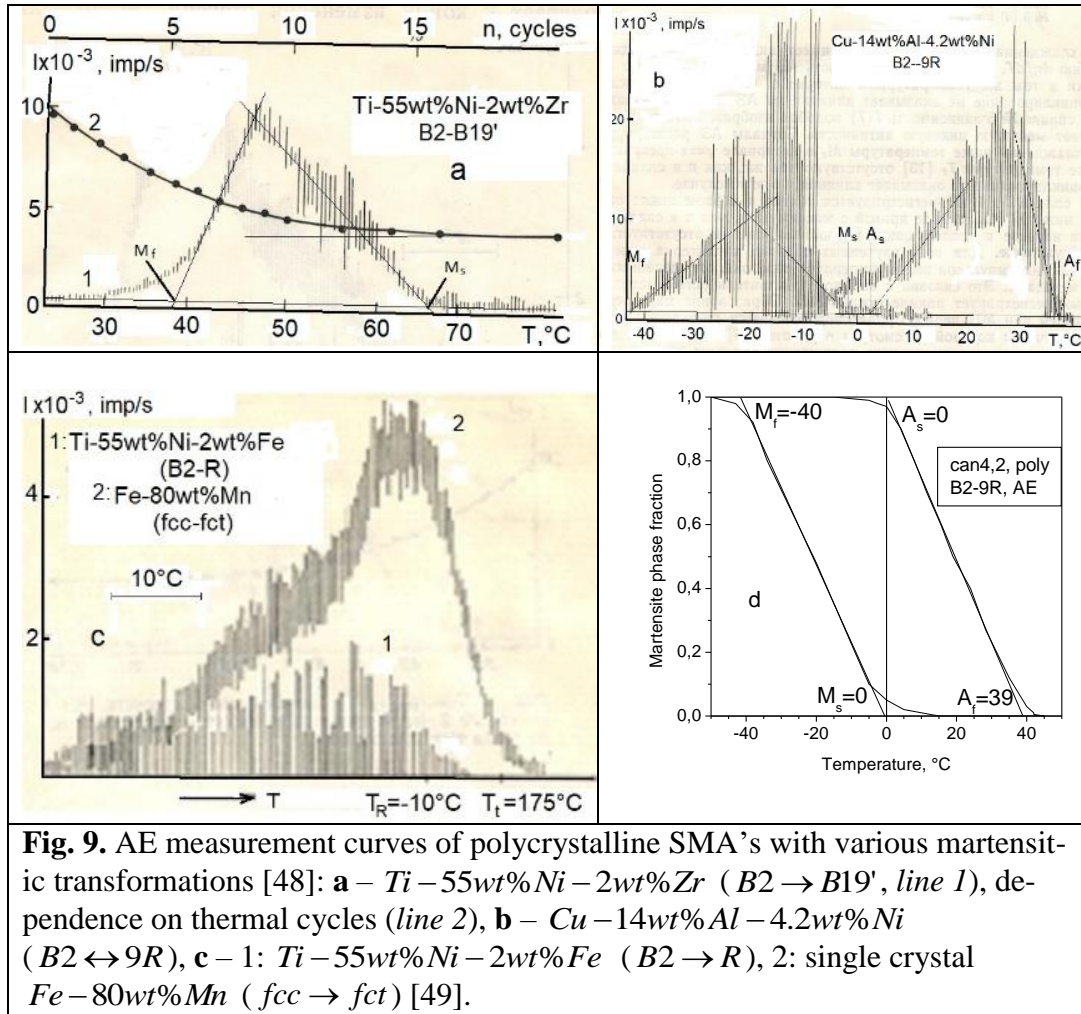
The main AE sources during the martensitic transformations of SMA's are, as discussed above, the formation of $A'M^P$ phase boundaries and $M^P M^P$ domain boundaries as well as their annihilation and splitting. The contribution of the friction of these movable boundaries at various structural defects to the AE intensity should be negligible compared to the first AE sources.

Consequently is the number N_{AE} of AE-impulses in (4.1.1) directly related to the number of $A'M^P$ phase boundaries depending on the martensite phase fraction z (3.2.10):

$$N_{AE} \approx N^{A'M^P} = 2N_{M_f}^{M^P} \cdot z(1-z). \quad (4.1.2)$$

The measurement curves $I_{AE}(T)$ show purely discrete (**Fig. 9 c1**), pre-

dominantly continuous with a maximum (*Figs. 9 a1, c2*) and mixed (*Fig. 9 b*) types in different SMA's with different martensitic transformations.



A martensite stabilization was found in *Ti* – 55wt%*Ni* – 2wt%*Zr* SMA through thermo-induced transformation cycles, as is shown by a decrease in AE-intensity in the first thermal cycles (*Fig. 9 a2*). The decrease in AE-intensity with the number of thermal cycles has an exponential character:

$$I_{AE}(i) = I_0 \cdot e^{-ki}, \quad (4.1.3)$$

where k is a coefficient to be determined experimentally.

The characteristic transformation temperatures can also be determined in the AE-method by extrapolating linear sections of the continuous AE

measurement curves around the maximum to $z = 0$ (M_s, A_f) and to $z = 1$ (M_f, A_s) (**Fig. 9 a, b**). Since the AE measurement method is very sensitive to single acoustic sources, the first AE-impulses, which are obviously associated with the building of severally martensite nuclei, are registered at temperatures $M_s' \approx M_s + (10 \div 20)^\circ\text{C}$ (**Fig. 9 a, b**). In the case of discrete AE measurement curves, these temperatures should be assumed as the transformation start temperatures.

With these key data and the coordinates of maxima:

$$z_{\max}^{A'M^P} = \frac{M_s - T_{\max}}{M_s - M_f} \quad \text{or} \quad 1 - z_{\max}^{M^P A'} = \frac{T_{\max} - A_s}{A_f - A_s}, \quad (4.1.4)$$

the hysteresis loops can be constructed from continuous AE measurement curves, even though somewhat schematically (**Fig. 9 d from Fig. 9 b**).

The differences in the character of AE measurement curves determined at the same scanning rate allow some conclusions about the morphology of the martensite phase. Since it can be assumed that most of the AE-impulses within the transformation temperature range $M_s \div M_f$ are caused by the coalescence of martensite polydomains, it can be said that the strong discrete AE-signals (**Figs. 9 b and 9 c2**) are caused by the coalescence of a few large martensite polydomains, while the continuous AE measurement curves indicate the coalescence of many small martensite polydomains.

Discrete AE-impulses can also arise from the elastic interaction of martensite polydomains with grain boundaries or sample edges, which can be regarded as a kind of the morphological accommodation mechanism. In a wedge-shaped martensite polydomain (**Fig. 8 a**), the shear stresses are concentrated at the spike of the martensite wedge and drastically strengthen this interaction, so that martensite wedges with their spikes, driven by the

mirror forces, rapidly reach the grain or sample boundaries and transform in the martensite lamellas with plane-parallel sides. The elastic energy stored at the wedge spikes is released and emitted as AE.

The discontinuity of the measurement curves $I_{AE}(T)$ is related to the number of AE-sources N_{AE} , the velocity $\dot{N}_{AE} [imp \cdot s^{-1}]$, at which they arise [109], the AE impulse duration $\tau_{imp} [s]$ and the scanning rate $\dot{T} [K \cdot s^{-1}]$. If several AE-impulses with a longer duration overlap, the measurement curve $I_{AE}(T)$ becomes continuous. In the AE measurement process, the dissipated elastic energy $\frac{dU_{el}}{dt} [J \cdot s^{-1}]$ released by individual sources is registered as separate AE-impulses.

The first discrete AE sources during martensitic transformations are the martensite nuclei that arise explosively after reaching their critical size [110]. These are recorded either as individual impulses or as continuous measurement curves (**Fig. 9 c1 or 9 a1**). The growth of martensite polydomains through the movement of partial dislocations, on the other hand, does not produce any AE impulses or at most a noise background.

The annihilation of $A'M^P$ phase boundaries due to the coalescence of martensite polydomains provides the main part of the AE-intensity. The larger the coalescing martensite polydomains, the greater the intensity of every AE-impulses, as in the case of the $B2 \rightarrow 9R$ -transformation of a $Cu - Al - Ni$ -polycrystal in the range $0.1 < z < 0.4$ (**Fig. 9 b, d**). The fractal structure of the martensite phase [112] means that the AE-intensity is determined in the case of the coalescence of smaller and smaller martensite polydomains, so that the measurement curve has a progressively continuous character.

Given this relationship between AE source size and AE-intensity, a morphological factor λ_m could be introduced:

$$\lambda_m[-] \equiv \frac{\Delta V^{M^p}}{V} = \frac{1}{V} \cdot \sum_{i=1}^{N_{M^p}^{M^p}} \left| V_i^{M^p} - \bar{V}^{M^p} \right|, \quad (4.1.5)$$

which represents the dependence $I_{AE} \propto \lambda_m$ of the AE-intensity on the martensite polydomain size or on the average relative deviation $\frac{\Delta V^{M^p}}{V}$

(V is the sample volume) of the volume $V_i^{M^p}$ of i th martensite polydomain volume from the average volume \bar{V}^{M^p} of all $N_{M^p}^{M^p}$ martensite polydomains in an analytical form. Such a morphological factor, however, did not serve a theoretical description of the martensite morphology, but rather helps the interpretation of experimental AE measurement data with regard to the morphology of sources of the elastic impulses.

The AE caused by the coalescence is always accompanied by AE pulses that correspond to the energy quanta released by reducing the stacking fault density (§3.1.1). The reduction takes place in a changing stress environment of coalescing martensite polydomains. So, every AE-impulse with great intensity cannot be directly assigned to a morphological AE-source. It can be added from several impulses from the AE-sources described above. Therefore, the morphological factor λ_m (4.1.5) only partially corresponds to its morphological-structural sense and purpose.

Since the AE-method does not set any special requirements on the AE-samples other than their sufficient mass and reliable contact with the quartz sensor, this is very well suited for the immediate quick tests of the trans-

formation temperatures during SMA-melting. This method is also, based on the research results presented in [48], at the Kiev Polytechnic University e.g. successfully used in practice to determine and to more precisely correct during manufacture the characteristic transformation temperatures of SMA's, which are very sensitive to the composition.

4.2 Resistometry

In the case of thermo-induced martensitic transformations $z = z(T)|_{\sigma}$, the characteristic temperatures and thus the parameters of the thermal hysteresis are determined by measuring one of the properties X that change due to the transformation as a function of the temperature $X = X(T)$. One of the simplest and therefore most frequently used methods is resistometry, the measurement of electrical resistance as a function of temperature or of mechanical stress.

4.2.1 Fundamentals of resistometry

When measuring the SMA-resistance, changes in the conductivity of a SMA-sample are generally registered. In addition, information about their electronic structure or changes are indirectly supplied, which can be not only caused by a phase change.

The specific electrical resistance $\rho[\Omega \cdot m]$ of phases with low symmetry is usually higher than that of phases with high symmetry $\Delta\rho^{AM} = \rho^A - \rho^M < 0$ due to the increasing electron-phonon interaction, as it shows the most measurements of martensitic transformations of SMA's. In intermetallic compounds, the Fermi surface and the Brillouin zone can intersect when the temperature decreasing because of thermal expansion alone (§3.1.3), so that the Fermi surface and thus the number of

free electrons are reduced. As a result, the electrical resistance increases even in a narrow temperature interval, where e.g. the martensitic $B2 \leftrightarrow R$ -transformation takes place. With further cooling, in the $B2 + R \leftrightarrow B19'$ transformation range, the electrical resistance decreases again.

So, all changes in the electrical resistance can serve as indicators of martensitic phase changes and be measured, while a precise measurement of absolute resistance values is of no great importance, since the specific resistance values for most SMA's have already been determined.

The so-called 4-pole measuring method for general measurements of electrical resistance is based on Ohm's law $U = I \cdot R$, where I is current and U is electrical voltage. Through measurements, the specific electrical resistance is calculated as a material constant, which is linearly dependent on the temperature with a positive temperature coefficient k_T :

$$\rho(T) = k_T \cdot T, \quad k_T = \frac{d\rho}{dT} > 0. \quad (4.2.1)$$

The measured electrical resistance is also essentially determined by the geometry of a SMA-sample with a length L and a cross-section S :

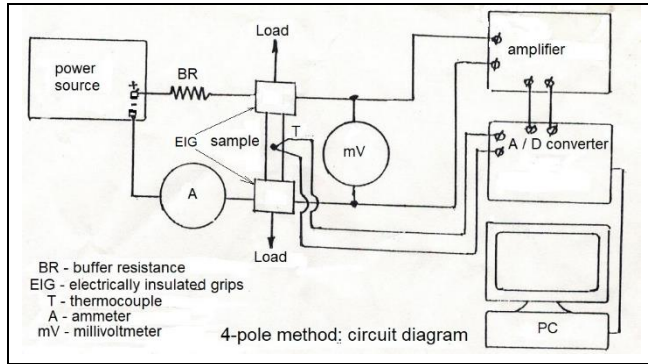
$$R(T) = \frac{L}{S} \cdot \rho(T). \quad (4.2.2)$$

The 4-pole measuring method (*see circuit diagram*) requires four conducting wires: two ones from a direct current source with a stabilized electrical current and adjustable amperage to string the test specimens, and two more to measure the voltage drop ΔU across the sample between two contact points at a distance L .

Since the measurements are often carried out in special measuring chambers under complex conditions (*temperature, mechanical stress*), only two electrical contacts or wires can be attached to the sample, mostly by

resistance spot welding, and the wires that conduct the measurement signal are branched off the first two wires outside the measuring chamber.

The measurement signal $\Delta U = I \cdot \Delta R(T)$ can be additionally amplified



by increasing the amperage I kept constant during the measurements when measuring of massive tensile-compression-specimens with a large cross-section and with high conductivity, e.g. *Cu*-based SMA's

(**Fig. 10 c**). It is advantageous that the noise remains unchanged in contrast to the electronic amplification. The specimen is though additionally heated by the Joule heat $Q = I^2 \cdot R \cdot t$, but the measurement results are not affected, if the temperature measurements by a thermocouple take place directly on the specimen with good thermal contact, because the thermo-induced martensitic transformation itself is the kind of the heat supply and removal is basically no matter.

4.2.2 Resistance measurements during thermo-induced transformations

The most of actually resistometric investigations of SMA's are limited to the determination of relative deviations of the electrical resistance from linearity in the case of temperature changes, through which the transformation temperatures (**Fig. 10 a-c**) are determined immediately. These deviations are due to different electrical properties of the metastable austenite A' and the polydomain martensite M^P :

$$\Delta R^{M^P A'} = R^{M^P} - R^{A'} = \frac{L}{S} \cdot \Delta \rho^{M^P A'} \neq 0. \quad (4.2.3)$$

The measured temperature-dependent electrical resistance of a SMA-specimen in the two-phase temperature range is represented by the martensite phase fraction $z(T)$ according to the additive standard formula (1.5), (1.6):

$$\begin{aligned} R(T, z) &= R^{A'}(T) \cdot (1 - z) + R^{M^p}(T) \cdot z = \\ &= R^{A'}(T) + \Delta R^{M^p A'}(T) \cdot z \end{aligned} \quad (4.2.4)$$

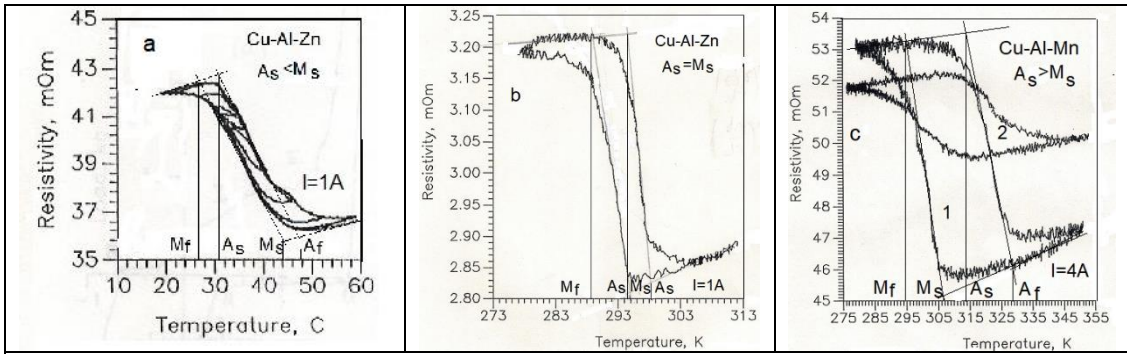


Fig. 10. Resistometric measurement curves of *Cu*-based SMA's that differ in their crystalline state, composition and geometry: *Cu* – *Al* – *Zn*-polycrystal (a) and single crystal (b) with a cross-section $S = 0.5\text{mm}^2$ and a single crystalline *Cu* – *Al* – *Mn*-tension-compression specimen with the same Length and a cross-section $S = 5\text{mm}^2$ (c) in the initial state (1) and after a few tension-compression-deformation cycles (2).

From the linear dependence of the electrical resistance on the martensite phase fraction, the trajectories $z^{A'M^p}(T)$ and $z^{M^p A'}(T)$ of the thermo-induced martensitic forward and reverse transformations, which build a hysteresis loop, can be determined by the difference $\Delta R^{M^p A'}(T)$ against the background of the normal temperature changes in the electrical resistance (4.2.1) of the two phases $R^{A'}(T)$ and $R^{M^p}(T)$:

$$z(T) = \frac{R(T) - R^{A'}(T)}{\Delta R^{M^p A'}(T)}. \quad (4.2.5)$$

In (4.2.5) the resistance values at measuring temperatures T_m in the

two-phase temperature range are to be determined by linear extrapolation of the functions $R^{M^P}(T)$ and $R^{A'}(T)$ to the measuring temperature T_m . So, the numerator in (4.2.5) is:

$$R(T_m) - R^{A'}(T_m) = R(T_m) - R^{A'}(A_f) - k_T^{A'} \cdot (A_f - T_m), \quad (4.2.6)$$

and the denominator is:

$$\Delta R^{A'M^P}(T_m) = \left[R^{M^P}(M_f) + k_T^{M^P} \cdot (T_m - M_f) \right] - R^{A'}(T_m). \quad (4.2.7)$$

The easiest way to perform these calculations is to use a ruler on the graphic representation of the determined hysteresis loop.

The hysteresis loop is so distorted by the temperature dependence of the electrical resistance of the both phases $k_T^{M^P} \neq k_T^{A'}$ that a ratio $A_s < M_s$ (**Fig. 10 a**) was measured for some SMA's, and suggested as one of the classification features for the SMA's [6, 7]. However, the relationship never happened in others, e.g. calorimetric measurement methods and remains rather a resistometric artifact.

4.2.3 *Ascertaining of mechanical hysteresis using resistometry*

The stress-induced martensitic transformations $z(\sigma)|_T$ of SMA's are caused by the action of an external mechanical stress $\sigma = \sigma^{ext}$ at a constant temperature $T_0' < T < T_0$ within the area of application of the Clausius-Clapeyron relationship (2.1.7). In this case, the electrical resistance depending on the mechanical external stress $R(\sigma)$ and the specimen deformation $R(\varepsilon)$ can be measured simultaneously in one test.

With this method, the measured resistance value is not only determined

by the specific resistance change $\Delta\rho^{M^m A'}$ (4.2.3) due to the martensitic transformation of the metastable austenite A' into one or more stress-induced martensite monodomains (4.2.4):

$$\Delta R(z) = \Delta R_0^{M^m A'} \cdot z, \quad (4.2.8)$$

where $\Delta R_0^{M^m A'} = \frac{L_0}{S} \cdot \Delta\rho^{M^m A'}$ is, but also due to the change in length as a result of the martensitic deformation $\varepsilon = \varepsilon_M \cdot z$ ($\varepsilon_M = \gamma_M \cdot \mu$, μ is Schmid's orientation factor) of the specimen $\Delta L(z) = L(z) - L_0 = L_0 \cdot \varepsilon$ due to the stress-induced martensitic transformation:

$$\Delta R(\varepsilon) = \frac{\Delta L}{S} \rho^{M^m} = R_0^{M^m} \cdot \varepsilon, \quad (4.2.9)$$

so that the total measured resistance change is the sum of physical (4.2.8) and geometric (4.2.9) factors:

$$\Delta R(\varepsilon) = \Delta R_0^{M^p A'} \cdot z + \Delta R_0^{M^m} \cdot \varepsilon. \quad (4.2.10)$$

The resistance contribution $\Delta R^{A'}(\varepsilon_{el}) \leq 0.01 \cdot R^{A'}$ from the elastic deformed residual austenite and the resistance changes due to the change in cross-section are neglected in (4.2.9) because of their insignificance. This is justified by the fact that the stress-induced martensitic transformation and the corresponding martensitic specimen deformation take place when the external mechanical stress hardly changes. The whole geometric factor is only determined by the sample length change $\Delta L = L_0 \cdot \varepsilon$, whereby L_0 is the distance between the two electrical contacts before the load. In the investigation of the mechanical hysteresis, the electrical contacts are at the

same time the from the tensile-compression-machine well-insulated sample grips.

How important the part of the geometric factor (4.2.9) is, can best be seen from the asymmetry of the hysteresis loops $R(\sigma)|_T$ recorded during the symmetrical tension-compression deformation (**Fig. 11 a**) and of the linear function $R(\varepsilon)|_T$ without hysteresis (**Fig. 11 b**). The asymmetry arises from the fact that the sign of the specimen deformation $\varepsilon = \frac{\Delta L}{L_0}$ changes when changing from tension (*index t*.) to compression (*index c*) (**Fig. 10**):

$$\begin{aligned}\lambda_R \cdot \Delta R^t(\varepsilon) &= \Delta R_0^{M^p A'} \cdot z + R_0^{M^m} \cdot \varepsilon \\ \lambda_R \cdot \Delta R^c(\varepsilon) &= \Delta R_0^{M^p A'} \cdot z - R_0^{M^m} \cdot \varepsilon\end{aligned}\quad (4.2.11)$$

The subtracting the second equation in (4.2.11) from the first one reveals the geometric factor λ_R :

$$\lambda_R = \frac{2R^{M^m} \cdot \varepsilon}{R^t(\varepsilon) - R^c(\varepsilon)}.\quad (4.2.12)$$

The symmetrization of the experimental measurement curves $R^t(\varepsilon)$ and $R^c(\varepsilon)$ can be done by calculating the purely physical values $\Delta R(\varepsilon)$ with the help of the geometric factor (4.2.12). Graphically, it is similar to rotation of the deformation axis in the direction of the tension branch $R^t(\varepsilon)$ until the angle α between this axis and the both branches $R^t(\varepsilon)$ and $R^c(\varepsilon)$ becomes the same (**Fig. 11 b**), but without correction of the measured values.

Somewhat surprising is the presence of a linear dependence of the elec-

trical resistance on the deformation during the reorientation of the thermo-induced martensite polydomains $\Delta R^{M^P \rightarrow M^+}(\varepsilon_q^t)$ (**Fig. 11 c**, line 2) and

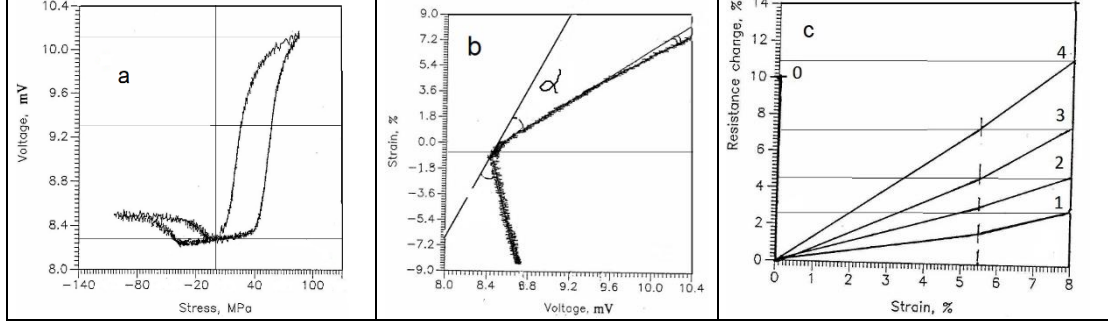


Fig. 11. Resistometric measurement curves of monocrystalline $Cu - Al - Zn$ tension-compression samples (*cross-section* $S = 5mm^2$, *initial distance between the grips as electrical contacts* $L_0 = 40mm$, *amperage* $I = 4A$): **a** – $R_T(\sigma^{ext})$, **b** – $R(\varepsilon)$ and **c** – changes in the electrical resistance during the thermo-induced transformation $\Delta R^{A' \leftrightarrow M^P}(T)$ (*vertical line at* $\varepsilon = 0$) and in different isothermal deformation processes (*only on the tension side with exclusion of the geometric factor through graphic symmetrization*):

1 – ferroelastic ($T < M_f$) deformation $\Delta R^{M^- \rightarrow M^+}(\varepsilon_f^t)$, 2 – quasiplastic ($T < M_f$) deformation of thermo-induced martensite $\Delta R^{M^P \rightarrow M^+}(\varepsilon_q^t)$, 3 – quasiplastic-pseudoelastic ($M_f < T < A_f$) deformation $\Delta R^{A'+M^P \rightarrow M^+}(\varepsilon_{qp}^t)$, 4 – pseudoelastic ($T > A_f$) deformation $\Delta R^{A' \rightarrow M^+}(\varepsilon_p^t)$.

during the reorientation $\Delta R^{M^- \rightarrow M^+}(\varepsilon_f^t)$ of a martensite macro-monodomain mixture M^\pm at $\varepsilon_f = 0$ in a tensile martensite macro-monodomain M^+ at ferroelastic tensile deformation (**Fig. 11 c**, Line 1):

$$\Delta R^{M^\pm M^+} \approx 0.24 \Delta R^{A' M^+} < \Delta R^{M^P M^+} \approx 0.42 \Delta R^{A' M^+}, \quad (4.2.13)$$

where M^P as the polyvariant polydomain martensite and M^\pm as a mixture of two mutually oriented martensite macromonodomains are two different martensite states.

Actually, it can be assumed that the electrical properties of differently

oriented martensite macromonodomains are the same, so that their reorientation into one another should not result in any change in electrical resistance. In thermo-induced polyvariant polydomain martensite M^P , one can still assume that the austenite remains between chaotically oriented martensite variants, the transformation of which into monovariant martensite, as in the case of stress-induced transformations (**Fig. 11 c**, lines 3 and 4), could cause an increase in electrical resistance. The only thing that changes sub-structurally with reorientation $R^{M^\pm} \rightarrow R^{M^+}$ is the reduction and disappearance of internal martensitic macromonodomain boundaries.

In all of the shown $R(\varepsilon)$ -lines (**Fig. 11 c**), an increase in the linearity coefficient $k_R = \frac{\Delta R(\varepsilon)}{\Delta \varepsilon}$ can be determined for deformations over and above $\varepsilon = (5 \div 6)\%$, which indicates a change in the deformation mechanism, as has already been determined in other experiments §5.2.2 [50]. Explanation of these two phenomena lies outside the CODEM presented here.

4.2.4 Resistometry as an indirect method of phase analysis

The relationships presented in equations (4.2.4) and (4.2.5) between the changes in the electrical resistance and the martensite phase fraction, which generally apply to all changes measured in the two-phase range, can be used to calculation of the martensite phase fractions. However, these are only correct, if the entire sample with mass m is transformed into martensite on cooling and into austenite on heating ($m = m^{M^P} + m^{A'}$).

If a part $z_s = \frac{m_s^{M^P}}{m^{M^P} + m^{A'} + m_s^{M^P}}$ of the martensitic phase with a mass

$m_s^{M^P}$ is switched off from the transformation, e.g. by stabilization, the

measured changes in electrical resistance are smaller to the same part. This allows to use such measurement methods for determination of the phase fraction of the stabilized martensite, i.e. as an indirect kind of quantitative phase analysis, and to calculate the phase fraction $z_s^{M^P}$ of the stabilized martensite:

$$z_s^{M^P} = 1 - \frac{\Delta R_s^{M^P A'}}{\Delta R_0^{M^P A'}}, \quad (4.2.14)$$

where $\Delta R_0^{M^P A'}$ is the change in electrical resistance measured on the initial specimen that has completely transformed into martensite (**Fig. 10 c**, loop 1), and $\Delta R_s^{M^P A'}$ is the change in electrical resistance measured after the partially martensite stabilization (**Fig. 10 c**, loop 2).

Are such measurements after every i th thermal or deformation cycle carried out, the martensite stabilization can be examined depending on the cycle number:

$$z_s^{M^P}(i) = 1 - \frac{\Delta R_s^{M^P A'}(i)}{\Delta R_0^{M^P A'}}. \quad (4.2.15)$$

The phase fraction of the stabilized martensite determined and calculated in this way reached approximately $z_s^{M^P} \approx 60\%$ the original value (**Fig. 10 c**) after a few ferroelastic deformation cycles. In the same way you can of course calculate the martensite phase fraction $z_s^{M^P}(i)$ at which the forward and reverse transformations were interrupted in partial thermal cycles (**Fig. 10 a**) and the dependence of the transformation start temperatures $A_s(z)$ or $M_s(z)$ in partial cycles on the martensite phase fraction examine

and analyze the position of the line $T_0'(z)$ within hysteresis loops (**Fig. 4**).

4.3 Calorimetry

Calorimetry offers itself as the most informative investigation method for the thermally induced forward and reverse transformation between the metastable austenite A' and the mixed orientation variants of martensite polydomains M^P . This measurement method delivers not only the characteristic transformation temperatures and thus the equilibrium temperature T_0' (1.8) like many others measurement methods including these already presented above, but also important thermodynamic characteristics such as the latent transformation heat $\Delta Q^{A'M^P}$ and thus the transformation entropy $\Delta S^{A'M^P} = \Delta Q^{A'M^P} / T_0'$, for the calculation of which the determination of the local equilibrium temperature T_0' is necessary and important. From the measured and calculated data, both hysteresis loops with characteristic transformation temperatures (**Fig. 4**) are determined and other quantitative energetic transformation parameters such as the dissipated energy.

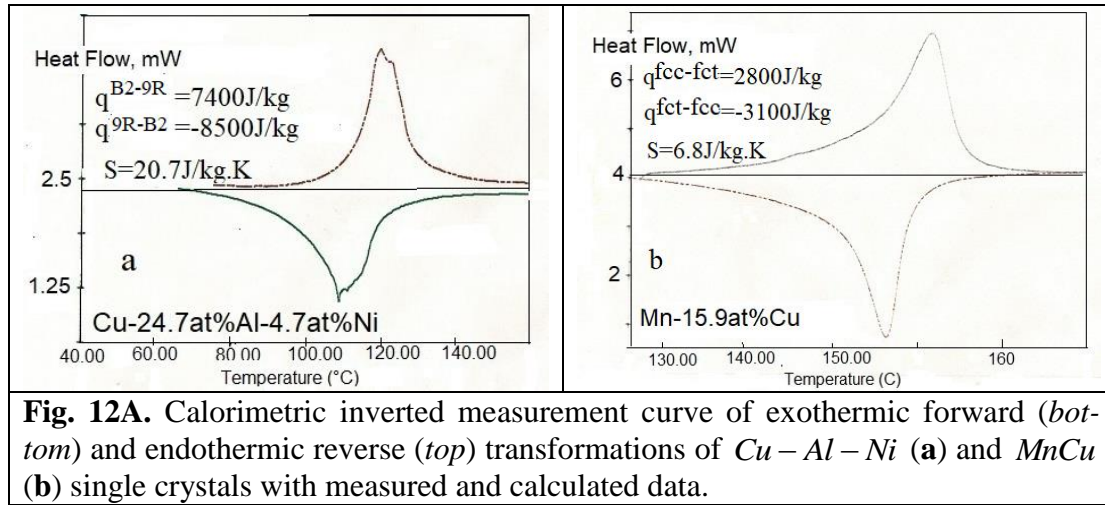
4.3.1 Calorimetric measurement curves from various SMA's

Calorimetric measurement curves from the most known SMA have been determined and are presented here. The SMA are precision alloys in which the difference in composition of 0.1at% can lead to a shift in the characteristic transformation temperatures up to 10°C. The $Cu - Al - X$ single crystals with $X \equiv Zn, Mn, Ni$ were selected as representatives of Cu -based SMA's with the $B2 \leftrightarrow 9R$ martensitic transformations.

In addition, intermetallic $MnCu$ single crystals with a specific martensitic transformation of the face-centered cubic crystal lattice into the face-centered tetragonal crystal lattice $fcc \leftrightarrow fct$ with the lattice deformation

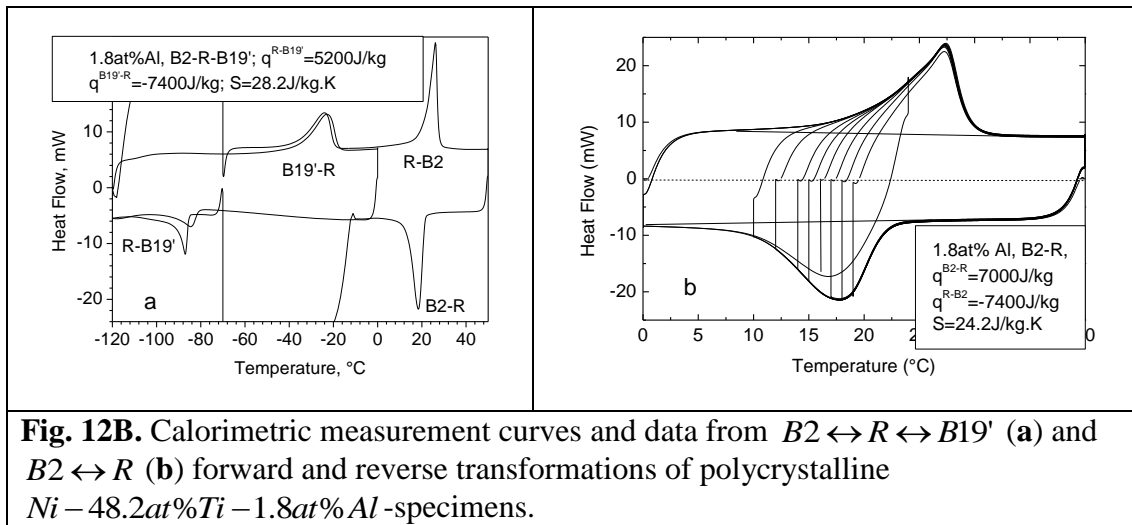
$\gamma_M = (1 - \frac{c}{a}) \approx 0.02 > 0$ (c, a are lattice parameters) were investigated. The martensitic transformation $fcc \leftrightarrow fct$ at the temperature T_t in $MnCu$ SMA's is coupled with the paramagnet-antiferromagnetic transition [49] at the Neel temperature $T_N \approx T_t$ and has a very narrow hysteresis. The kinds of heat treatment of Cu -based SMA's were determined considering their phase diagrams [50] (*more details in §4.5.1*).

Calorimetric measurement curves (**Fig. 12 A-F**) show the heat flow $h[W]$ as a function of the temperature $T[^\circ C]$. The presentation of the measurement curves is reversed, because the heat flow is measured, that is generated in a differential scanning calorimeter (*DSC-7 "PERKIN ELMER" PC series*) to compensate the heat flow created by the transformation.



The latent transformation heat is responsible for the temperature difference between the object- and reference-cameras, which is compensated by the device. The minimum recorded during cooling (**Fig. 12A a, b**) therefore corresponds to the heat emission during the forward transformation (*exothermic effect*), i.e. the positive transformation heat. The maximum recorded during the heating corresponds to the heat absorption during the reverse transformation (*endothermic effect*), i.e. the negative transformation heat.

The intermetallic compounds on the $NiTi$ -basis with two and more alloy components represents another of the most investigated and used SMA-groups, which, with the exception of a $Ni_{0.5}Ti_{0.5}$ -single crystal, have been calorimetrically investigated in their polycrystalline state. The measurement specimens of this SMA's were subjected to the standard heat treatment known for them [51]: 0.5h homogenize annealing at $850^{\circ}C$ and quenching in cold water.



The crystal lattices of the austenite and the martensite were determined using transmission electron microscopy (TEM) and X -ray diffraction, the orientation and block structure of single crystals using the Laue method, and the compositions using scanning electron microscopy (SEM).

The $NiTi$ -based SMA's run through a series of martensitic transformations with different crystallographic and thermodynamic characteristics. The well-known martensitic transformation $B2 \leftrightarrow B19'$ takes place in the equiatomic polycrystalline two-component base $Ni_{0.5}Ti_{0.5}$ alloy. $B19'$ -martensite is an ordered phase with an orthorhombic monoclinically distorted crystal lattice. Actually, it is an orthorhombic lattice structure like $B19$ ($a \neq b \neq c$, $\alpha = \beta = 90^{\circ}$, $\gamma \neq 90^{\circ}$).

The distortion arises from the fact that another martensitic transformation of the $B2$ -austenite into the rhombohedral R -martensite runs parallel to the $B2 \leftrightarrow B19'$ -transformation, i.e. according to the scheme $B2 \leftrightarrow \frac{R}{B19'}$. An increase in the Ni -content or the addition of some third components, such as Fe and Al in small amounts, instead of Ti , decreases the $R \leftrightarrow B19'$ transformation temperatures and consequently separates the both transformations. That allows to investigate the both transformations separately (**Fig. 12B a, b**).

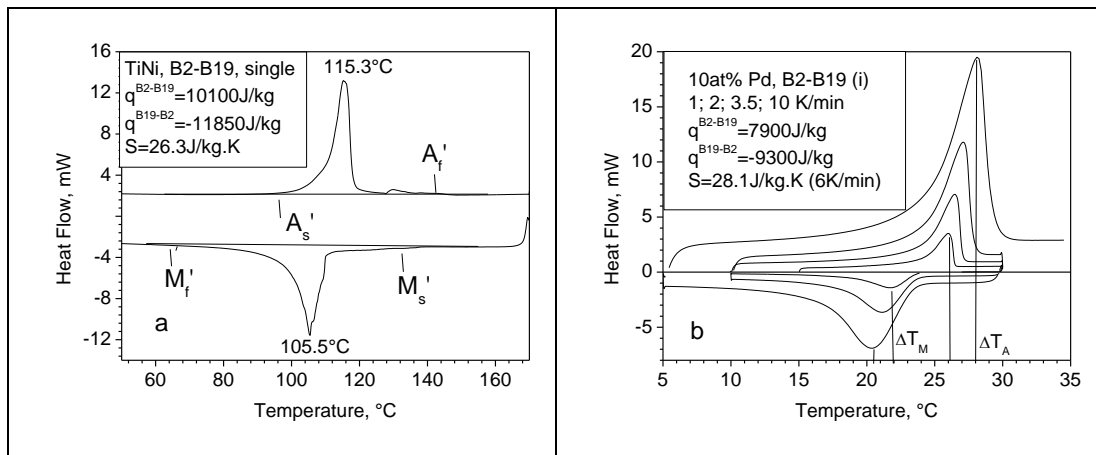
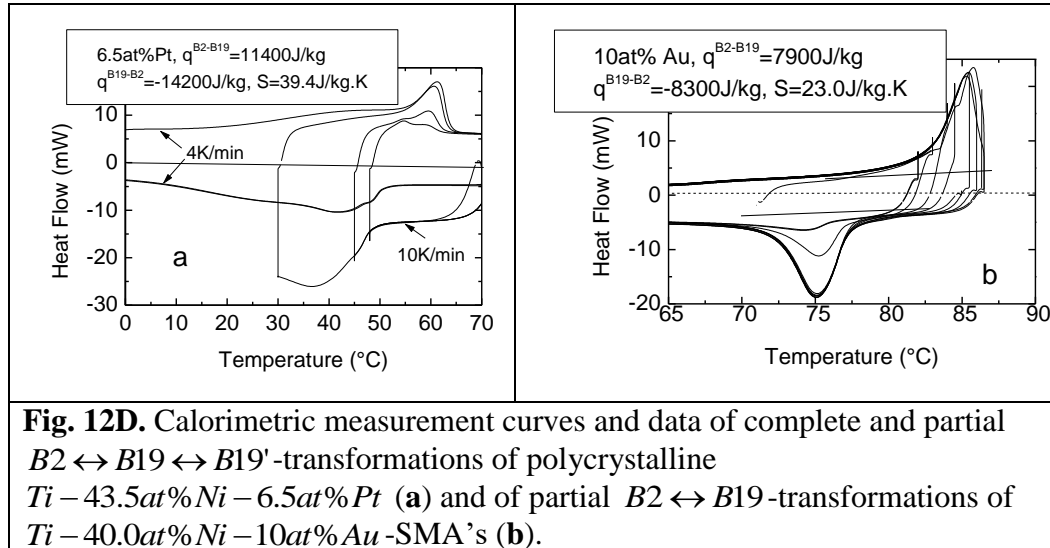


Fig. 12C. Calorimetric measurement curves and data from $B2 \leftrightarrow B19$ - transformations of a $Ni - 49.9at\%Ti$ -single crystal (**a**) and a $Ti - 40.0at\%Ni - 10at\%Pd$ - polycrystal at different scanning rates (**b**).

The same $Ni_{0.5}Ti_{0.5}$ SMA in a single crystalline state shows a transformation into martensite with an orthorhombic crystal lattice at significantly higher temperatures (**Fig. 12C a**). Alloying the elements Cu, Au, Pt, Pd instead of Ni first causes a lowering of the $B2 \leftrightarrow B19'$ transformation temperatures in the concentration range $< 5at\%$. A further increase in their concentration leads to the formation of the purely $B19$ orthorhombic martensite at higher temperatures. At the concentrations about $10at\%$, the $B2 \leftrightarrow B19$ transformations take place with an invariant plane.

The transformation temperature interval depends essentially [51] on the

scanning rate (**Fig. 12C b**), so that the information on the calorimetrically measured transformation temperatures for SMA-certification without data about their dependence on the scanning rate are pointless and misleading.

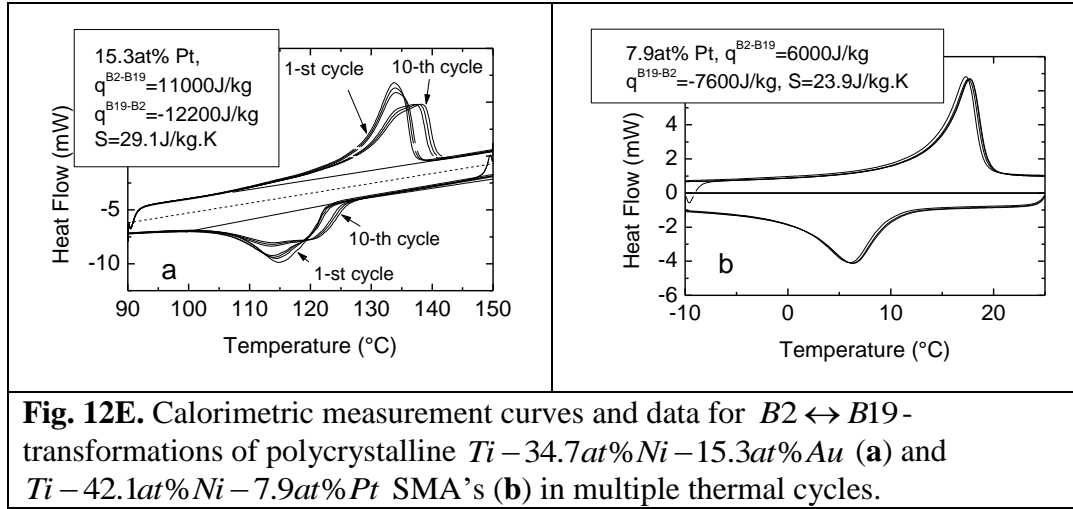


Even with other transformation sequences, the temperature ranges of several transformation overlap and thus unresolved calorimetric peaks occur. However, it is possible to resolve these peaks in partial cycles (**Fig. 12D a**).

Several complete transformation cycles cause a lowering temperatures of the $B2 \leftrightarrow B19'$ transformations due to phase hardening [52, 53], which is said to be related to the formation of dislocations [27, 28]. The calorimetric investigations show (**Fig. 12E b**) that the transformation temperatures of one part of the martensite increase due to the thermal cycles, while those of the other part remain constant.

It leads to the formation of doublets instead of single peaks in calorimetric curves and proves that the martensite stabilization takes place through thermal cycles. This fact has already been established in the AE-investigations (4.1.3) (**Fig. 9 a**), where only 40% the AE initial intensity remains after (10 ÷ 15) thermal cycles, which proves the switch off of al-

most 60% the phase fraction of the $B19'$ -martensite from the $B2 \leftrightarrow B19'$ -transformations due to the martensite stabilization by thermal cycles.



The thermal cycles hardly affect (**Fig. 12E b**) the $B2 \leftrightarrow B19'$ -transformations with an invariant plane, i.e. with maximal adaptation of the crystal lattices of $B2$ -austenite and $B19'$ -martensite to each other, with minimal stresses at the coherent $A'M^P$ phase boundaries and therefore minimal density of twin boundaries or stacking faults inside the martensite polydomains.

4.3.2 Determination of thermodynamic parameters and hysteresis loops

The latent transformation heat is calculated by integrating the calorimetric measurement curve over the transformation temperature interval:

$$Q^{A'M^P} = \int_{M'_s}^{M'_f} h(T) dT = q^{A'M^P}(T) \cdot m \quad \text{and} \quad (4.3.1)$$

$$Q^{M^P A'} = \int_{A'_s}^{A'_f} h(T) dT = q^{M^P A'}(T) \cdot m$$

where $q(T) = \frac{Q}{m} \left[\frac{J}{kg} \right]$ is the specific (*per mass unit*) transformation heat.

The deviations of the calorimetric measurement curve from the straight baseline (**Fig. 12C a**) correspond to the transformation temperatures drawn with apostrophes (**Fig. 4**) and are in use as the integration limits. The thermal hysteresis loops are reproduced with the help of the "Partial Area" program integrated in the DSC, which automatically calculates the transformation completeness at any given temperature T :

$$z^{A'M^P}(T) = \frac{M_s}{M_f} \frac{\int_{M_s}^T h(T) dT'}{\int_{M_s}^{M_f} h(T) dT'} = \frac{q^{A'M^P}(T)}{q^{A'M^P}} \quad \text{and} \quad (4.3.2)$$

$$z^{M^P A'}(T) = \frac{A_s}{A_f} \frac{\int_{A_s}^T h(T) dT'}{\int_{A_s}^{A_f} h(T) dT'} = \frac{q^{M^P A'}(T)}{q^{M^P A'}}$$

At that, it is strongly assumed that the transformation heat is proportional to the martensite phase fraction [54, 55].

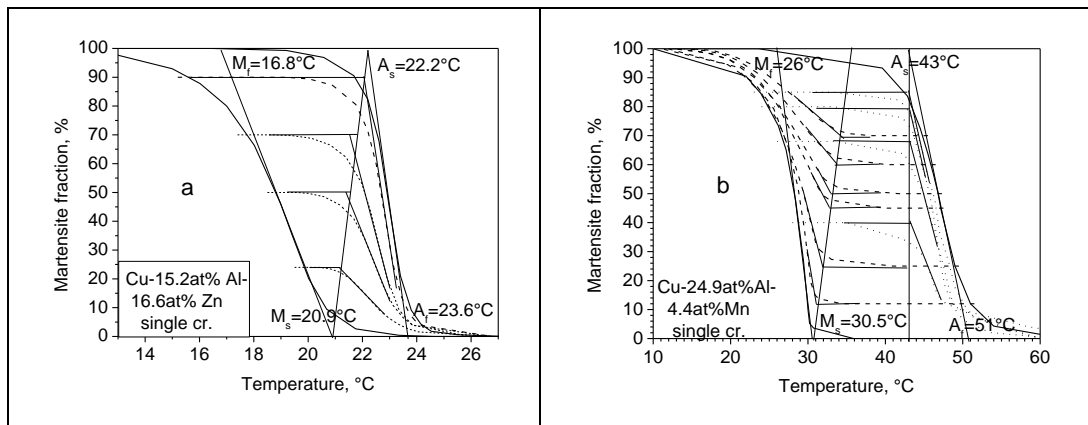


Fig. 13. Hysteresis loops in complete and partial cycles of the thermo-induced $B2 \leftrightarrow 9R$ -transformations of $Cu - Al - 16.6at\% Zn$ (a) and $Cu - Al - 10.7at\% Mn$ single crystals (b).

The complete and partial loops of the thermal hysteresis were repro-

duced in this way for some of the investigated ($Cu-Al$)-based SMA's (**Figs. 13 a, b**).

The transformation temperatures (**Fig. 4**) in both complete and partial transformation cycles are determined by extrapolating linear sections of the transformation trajectories to the z limit values (§3.2.2).

For the $fcc \leftrightarrow fct$ transformation of the $Mn-15.9at\%Cu$ single crystals (**Fig. 14 a**), the extrapolation method applies, if at all, only to the determination of M_s and A_f transformation temperatures, since the transformation trajectories hardly have any linear sections. The equilibrium temperature trajectory determined in partial transformation cycles corresponds rather to a Brillouin function (**Fig. 14 b**).

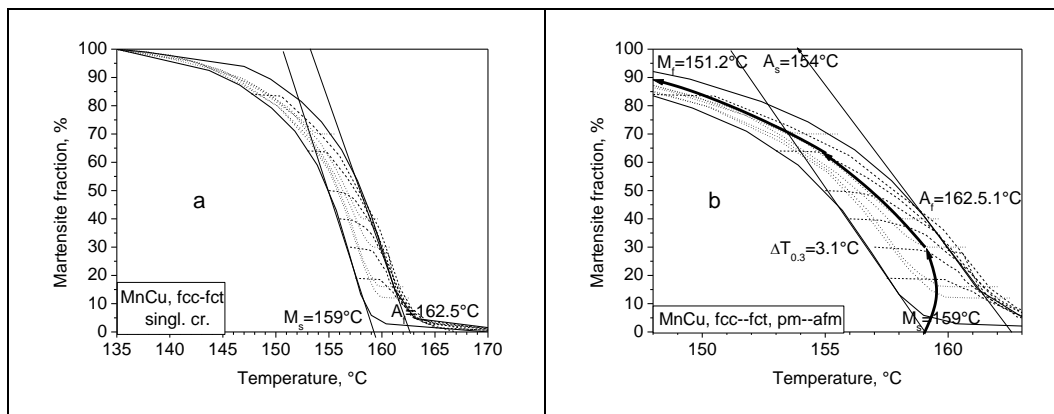


Fig. 14. Hysteresis loops in complete and partial cycles of the thermo-induced $fcc \leftrightarrow fct$ -transformations of the $Mn-15.9at\%Cu$ single crystals (**a**) with the equilibrium temperature trajectory $T_0'(z)$ in the form of a Brillouin function (**b**, bold line).

The hysteresis loops of the thermo-induced martensitic transformations of $Ti_{0.5}Ni_{0.5}$ poly- and single crystals were determined and analyzed in the same way (**Figs. 15 a, b**). The essential differences found between the calorimetrically determined transformation parameters were so surprising that the composition accordance of the both had to be checked and confirmed

by the SEM-analysis. The change in transformation from $B2 \leftrightarrow \frac{R}{B19'}$ in $Ni_{0.5}Ti_{0.5}$ -polycrystals to $B2 \leftrightarrow B19$ in $Ni_{0.5}Ti_{0.5}$ single crystals has been established for the first time by calorimetric investigations [9, 11].

In the case of partial transformation cycles (*p.c.c.* denotes interruption of the forward transformation at z_i and heating over $T = const > A_f$, *p.c.h.* denotes interruption of the reverse transformation at $(1 - z_i)$ and cooling under $T = const < M_f$) of the $Ni_{0.5}Ti_{0.5}$ -polycrystals, a doublet appears in the calorimetric measurement curves of $B19' \rightarrow B2$ and $R \rightarrow B2$ reverse transformations already at $z_i < 0.8$. That also causes the dents in the reverse transformation trajectories in partial hysteresis loops (**Fig. 15a**).

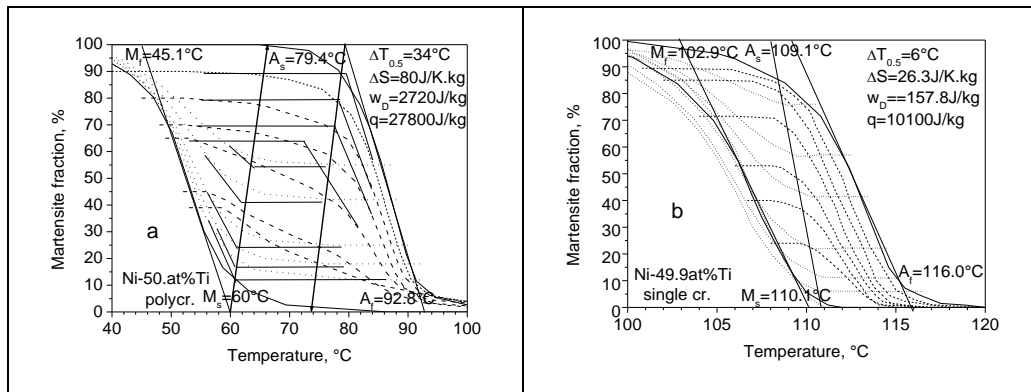


Fig. 15. Hysteresis loops in complete and partial cycles of the thermo-induced $B2 \leftrightarrow \frac{R}{B19'}$ -transformations of $Ni - 50.0at\%Ti$ -polycrystals (a) and of $B2 \leftrightarrow B19$ -transformations of a $Ni - 49.9at\%Ti$ single crystal (b) with the corresponding thermodynamic data.

The transformation temperatures determined from the hysteresis loops are used to determine the equilibrium temperatures $T_o'(z = 0)$ [11, 14] or equilibrium temperature trajectories:

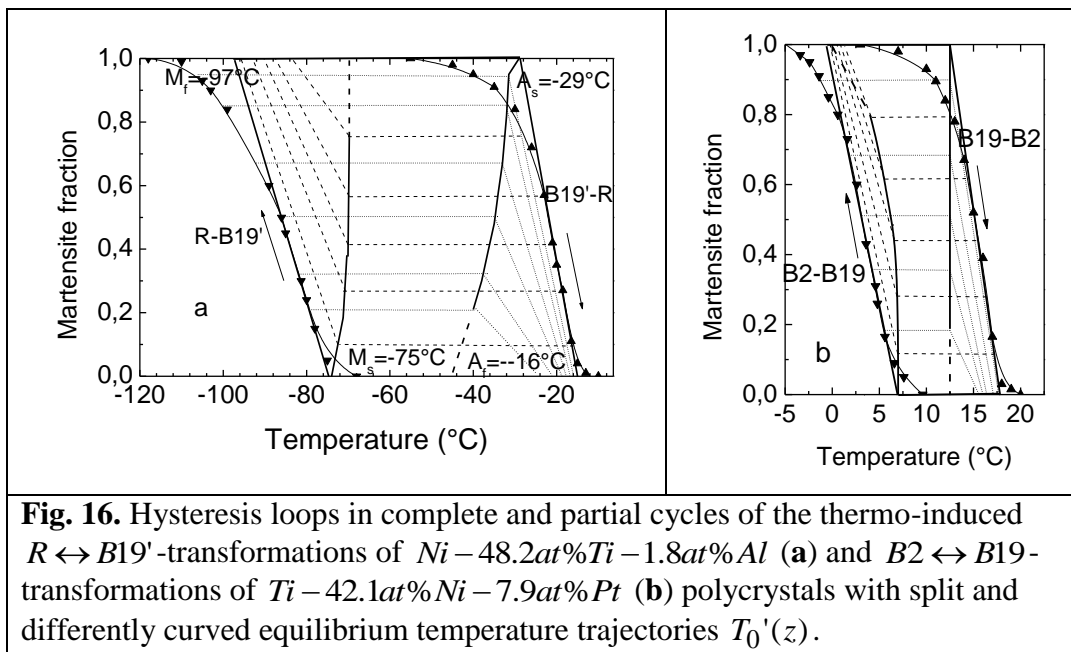
$$T_o'(z) = \frac{M_s(z) + A_s(z)}{2}. \quad (4.3.3)$$

The equilibrium temperature trajectories can deviate far away from straight

lines and show very different courses (**Figs. 16 a, b**).

With the determined equilibrium temperatures $T_0'(z=0)$, the transformation entropies can finally be calculated as the average value between the forwards and reverse transformation entropies [11, 14]:

$$S \equiv \Delta s \left[\frac{J}{kg \cdot K} \right] \approx \frac{q^{A'M^P} + |q^{M^P A'}|}{2T_0'} \quad (4.3.4)$$



With the help of the transformation entropy determined in (4.3.4), all important parameters of the thermal hysteresis can be calculated in their energetic form, such as for example the energy of the phase boundaries treated in §3.2.1 as the energy barrier (3.2.4), (3.2.6) for the formation of first martensite polydomains:

$$U_{M_s}^{A'M^P} = (T_0' - M_s) \cdot \Delta s = 423 J / kg \quad (4.3.5)$$

for the $R \rightarrow B19'$ -transformation (**Figs. 12B a and 16 a**) or the specific elastic energy of the phase boundaries introduced in §3.2.2 (3.2.13) (3.2.19):

$$K_{el} = \frac{T_0' \cdot \Delta S^{A'M^P}}{2} = q^{A'M^P} / 2 = 3500 J / kg \quad (4.3.6)$$

for the case $\frac{dT_0(z)}{dz} = 0$ for $B2 \rightarrow R$ with latent transformation heat

$$q^{A'M^P} = 7000 J / kg \text{ (Fig. 43 b).}$$

The equilibrium temperature used for the calculations is defined in (4.3.3). Other parameters can now also be introduced and calculated in their energetic form.

4.3.3 Energetic parameters of the thermal hysteresis

It makes sense to describe the negative trajectory slope $\frac{dz}{dT} < 0$ of the thermo-induced transformations as a positive energetic thermoelasticity coefficient for the forward and reverse transformations [11, 14] for the purpose of the direct and uniform comparability of thermal and mechanical hysteresis properties with each another:

$$\begin{aligned} k_T^{A'M^P} &= \frac{1}{2} (M_s - M_f) \cdot \Delta s \\ k_T^{M^P A'} &= \frac{1}{2} (A_f - A_s) \cdot \Delta s \end{aligned} \quad \text{and} \quad (4.3.7)$$

The equations (4.3.7) basically describe the elastic energies dissipated during the transformations. It applies to a symmetrical hysteresis loop

$$k^{A'M^P} = k^{M^P A'}.$$

The main characteristic of the thermal hysteresis loop is its area in $\Delta s - T$ -coordinates, which in general represents the energy w_D^T dissipated in a closed transformation cycle:

$$w_D^T \left[\frac{J}{kg} \right] = \Delta s \cdot \Delta T_{0.5}. \quad (4.3.8)$$

In order to recognize the dissipation mechanisms, one should investigate the hysteresis interior in partial transformation cycles in more detail. Such investigations show [11, 14, 15] that within the main hysteresis loops mostly the one in §3.2.2, Eq. (3.2.19) calculated splitting of the equilibrium temperature trajectory $T_0'(z)$ in two starting temperature lines $M_s(z_i)$ for the forward transformation and A_s for the reverse transformation takes place (**Figs. 13 b; 15 a; 16 a, b and 43 b**).

An idealized hysteresis loop can be represented by two linearly extrapolated transformation trajectories and the internal latent hysteresis by two linearly extrapolated lines $M_s(0)$ and $A_s(0)$. The total area of such an idealized hysteresis loop is then calculated in simplified form as the sum of two right triangle areas and of a square area as the dissipated energy depending on the martensite phase fraction in partial transformation cycles:

$$w_D^T = k_T^{A'M^P} + k_T^{M^P A'} + k_T^l, \quad (4.3.9)$$

where $k_T^{A'M^P}$, $k_T^{M^P A'}$ are the energetic thermoelastic coefficients of the forward and reverse transformations introduced above and $k_T^l = [A_s(0) - M_s(0)] \cdot \Delta s$ the energy dissipated within the latent hysteresis, if available.

The dependence of the dissipated energy on the martensite phase fraction is determined by the values of these coefficients in partial transformations cycles:

$$k_T^{A'M^P}(z) = \frac{1}{2} \cdot [M_s(0) - M_f(z_i)] \cdot z \cdot \Delta s \cdot z = k_T^{A'M^P A'} \cdot z^2 \quad (4.3.10)$$

$$k_T^{M^P A'}(z) = \frac{1}{2} \cdot [A_f(z_i) - A_s(0)] \cdot z \cdot \Delta s \cdot z = k_T^{M^P A'} \cdot z^2, \quad (4.3.11)$$

$$k_T^l(z) = [A_s(0) - M_s(0)] \cdot \Delta s \cdot z = k_T^l \cdot z. \quad (4.3.12)$$

The full dissipated energy as a function of z consists in a simplified form (*symmetrical hysteresis loop* $k_T^{A'M^P} = k_T^{M^P A'} \equiv k_T$) of a parabolic term and a linear term:

$$w_D^T(z) = k_T \cdot z^2 + k_T^l \cdot z. \quad (4.3.13)$$

At transformations with a narrow hysteresis, i.e. with small elastic energy of the coherent $A'M^P$ phase boundaries and a small stacking fault density in martensite polydomains as at the transformations with an invariant plane, only one equilibrium temperature trajectory is observed (**Figs. 13 a and 15 b**), at which the starting temperatures of both the forward and reverse transformations are in partial cycles $T_0'(z) = M_s(z) = A_s(z)$. Two equilibrium temperature trajectories, which build an internal latent hysteresis loop, exhibit different shapes from two parallel straight lines (**Figs. 15 a and 43 b**) to curves with different curvatures (**Fig. 16 a, b**) and different inclinations (**Figs. 13 a, b and 15 b**) to the temperature axis.

The slopes of the internal lines $\frac{dM_s(z)}{dz}$ and $\frac{dA_s(z)}{dz}$, as show the theoretical treatment in §3.2.2 and the calorimetric experiments with partial transformation cycles, can be positive (**Figs. 13 a, b and 15 a**), negative (**Fig. 15 b**) or close to zero (**Figs. 16 b, 15 b, 43 b**), which indicates various dissipation mechanisms associated with the elastic energy redistribution between the both phases during the transformation.

The calorimetric results for the investigated SMA's can be summarized

as follows:

1. The $(Cu - Al)$ -based SMA's have similar values of the latent transformation heat and the transformation entropy, but very different values of the thermoelasticity coefficient and the dissipated energy. These parameters for the $fcc \leftrightarrow fct$ -transformation of $MnCu$ -SMA's differ fundamentally in that. They have much lower values of thermodynamic parameters than those for the $(Cu - Al)$ -based SMA's.
2. The thermodynamic parameters in $NiTi$ -based SMA's build a wide value spectrum from values similar to those in $(Cu - Al)$ -based SMA's such as parameter of $B2 \leftrightarrow B19$ -transformations of $NiTi$ single crystals, of $B2 \leftrightarrow B19$ -transformations with invariant planes, of $B2 \leftrightarrow R$ -transformations up to very large latent heat values of the $B2 \leftrightarrow 19'$ -transformations.

The first group has a narrower hysteresis and less dissipated energy than the second group. The $R \leftrightarrow B19'$ -transformations have small latent transformation heat and transformation entropy, as in the first group, but the broadest hysteresis and the dissipated energy as those for the $B2 \leftrightarrow B19'$ -transformations.

The latent transformation heat $q^{A'M^p} = U^{A'} - U^{M^p} = \Delta U^{A'M^m} + U_{sf}$ arises from the difference in the internal energies of the transforming phases (**Fig. 1 a, b**), which consist of phonon, electron and stacking fault energies U_{sf} . So, it can be concluded from the measured values that the $B19'$ -martensite has the smallest internal energy in comparison to the $B19$ -martensite with invariant plane and in single-crystalline $NiTi$ -SMA's as well as to the R -martensite. The energetic relationships among the involved martensite phases can be represented in the following sequence:

$$U^{B2} > U^{R(B2)} \geq U^{B19(i)} > U^{B19} > U^{B19'(R)} > U^{B19'(B2)}, \quad (4.3.14)$$

The transformation entropy $\Delta S^{A'M^P} = \left(\frac{dF^{A'}}{dT} - \frac{dF^{M^P}}{dT} \right)$ is to be understood as the slope difference. This means that the greater the transformation entropy $\Delta S^{A'M^P}$, the smaller the slope $\frac{dF^{M^P}}{dT} = S^{M^P}$. Interaction of the transformation enthalpy and transformation entropy $\Delta S^{A'M^P}$ determines the position of the equilibrium temperature and thus, taking into account the dissipated energy, the characteristic transformation temperatures.

Differences in the specific latent transformation heats $q^{A'M^P}$ and the transformation entropies $\Delta s^{A'M^P}$ indicate the greatest symmetry vicinity of the crystal lattices of the both phases, i.e. the greatest overlap between their symmetry groups. This means a maximal adjustment of the crystal lattice at the phase boundaries and, accordingly, a minimum stacking fault density in martensite polydomains due to the minimal degree of accommodation, and as a consequence minimal hysteresis and higher equilibrium temperatures (*Figs. 1 a, b*) or the characteristic transformation temperatures. This is proven by the results for the near to 2-nd order ($fcc \leftrightarrow fct$)-transformation, the ($B2 \leftrightarrow B19$)-transformation with invariant planes and in *NiTi* single crystals.

4.4 Dilatometry

At first appearance, dilatometry does not suit for the investigation of SMA's, since the crystallographic changes at the martensitic transformations do not lead to any volume change ($V^A \approx V^M$) or to any change in

the thermal volume expansion coefficient ($\alpha_V^A \approx \alpha_V^M$). Unless a SMA-sample is pre-deformed and textured or monodomained [56-58], i.e. was mechanically pre-stressed [57] or trained for the two-way memory effect prior to the measurements.

However, in a dilatometer it is not volume changes, but length changes from the temperature $\Delta L(T)$ or dilation $\varepsilon_d = \frac{\Delta L(T)}{L_0}$ that are measured and the coefficients of linear thermal expansion are calculated:

$$\alpha = \frac{1}{L_0} \cdot \frac{d\Delta L(T)}{dT} \equiv \frac{d\varepsilon_d(T)}{dT}. \quad (4.4.1)$$

Dilatometry offers unique possibilities to measure and to analyze specific characteristics of SMA's especially in its single-crystalline form such as the accommodation degree and the elasticity module softening [58].

4.4.1 Relationship between entropy and thermal expansion

Coefficient of thermal expansion is related to other fundamental properties and characteristics of a solid. Measurements of the thermal expansion coefficient can therefore provide additional information about these characteristics.

Since the mixed derivatives of the thermodynamic potential $F(T, p)$:

$$\left(\frac{\partial^2 F}{\partial T \partial p} \right) = - \left(\frac{\partial S}{\partial p} \right)_T \quad \text{and} \quad \left(\frac{\partial^2 F}{\partial p \partial T} \right) = \left(\frac{\partial V}{\partial T} \right)_p = V \cdot \alpha_V \quad (4.4.2)$$

are identical, there is an important relationship between the thermal expansion coefficient α_V and the pressure dependence of the entropy:

$$\left(\frac{\partial S}{\partial p} \right)_T = -V \cdot \alpha_V. \quad (4.4.3)$$

In the case of anisotropic solids, which mainly include crystals with low symmetry, linear characteristics of the thermal expansion should be introduced that are valid in different axial directions of the crystal lattice. The volume change with a temperature or stress change is represented by a dimensionless expansion:

$$\varepsilon(T, \sigma) \equiv \ln\left(\frac{\varepsilon}{\varepsilon_0}\right) = \ln\left(\frac{L}{L_0}\right), \quad (4.4.4)$$

where L is crystal length in one direction.

If a crystal is not loaded by a hydrostatic pressure but by a uniaxial mechanical stress σ_i in any direction j ($j \neq i$), the reaction of the crystal to this effect is described by a compressibility coefficient κ_{ij} in its tensor form:

$$\kappa_{ij} = \left(\frac{\partial \varepsilon_i}{\partial \sigma_j} \right)_{T, \sigma'}. \quad (4.4.5)$$

For small tensions (*in the elastic range*) the following applies:

$$\vec{\varepsilon} = \kappa \cdot \vec{\sigma} \quad \text{or} \quad \vec{\sigma} = \kappa^{-1} \cdot \vec{\varepsilon} \equiv c \cdot \vec{\varepsilon}, \quad (4.4.6)$$

where $c \equiv \kappa^{-1}$ is the elasticity tensor (*both are second order tensors*). In this consideration, equation (4.4.3) is used in connection with the coefficients of linear thermal expansion:

$$\alpha_i = \frac{1}{L_i} \cdot \left(\frac{\partial L_i}{\partial T} \right)_{\sigma} \quad (4.4.7)$$

as the stress dependency of the entropy rewritten:

$$\alpha_i = \frac{1}{\varepsilon} \cdot \left(\frac{\partial S}{\partial \sigma_i} \right)_{T, \sigma'}, \quad (4.4.8)$$

where σ' are all other except σ_i possible tensor components denote the mechanical stress in different directions.

4.4.2 Elasticity modulus and thermal expansion

In the theoretical treatise [58] the relationship between the linear thermal expansion coefficient and the temperature coefficient of the elasticity modulus $\frac{dG}{dT}$ was clarified. The elastic properties of a solid reflect the interaction of atoms that build the crystal lattice of this body. The interaction is represented by a model potential in the form that corresponds most closely to experimentally measured values or that best describes them and their behavior. One of the most widely used forms of model potential is:

$$U(r) = \frac{a}{r^m} - \frac{b}{r^n}, \quad m > n; \quad a, b > 0, \quad (4.4.9)$$

known by $m = 12$, $n = 6$ as the Lenard-Jones potential.

From the equilibrium condition at $r = r_0$, where the potential (4.4.9) has a minimum:

$$U'(r_0) = -\frac{am}{r_0^{m-1}} + \frac{bn}{r_0^{n-1}} = 0, \quad (4.4.10)$$

we get the value for $r_0 = \left(\frac{am}{nb} \right)^{\frac{1}{m-n}}$, so that the equilibrium values of the

potential and all its derivatives at $r = r_0$ can be calculated as follows:

$$U(r_0) = \frac{a(1 - \frac{m}{n})}{r_0^m} < 0, \quad (4.4.11)$$

$$\begin{aligned}
U^{(k)}(r_0) &= \frac{(-1)^k}{r_0^k} \cdot \frac{mn}{n-m} \left[\prod_{i=0}^{k-1} (m+i) - \prod_{i=0}^{k-1} (n+i) \right] U(r_0) = \\
&= (-1)^k \cdot K(k) \cdot \frac{U(r_0)}{r_0^k}
\end{aligned}
\tag{4.4.12}$$

where $K(k)$ is a constant combination of numbers for each derivative.

The model potential and its derivatives can now be represented in the vicinity of r_0 by the equilibrium value $U(r_0)$ with the help of the Taylor series:

$$\begin{aligned}
U(r) &= U(r_0) + \frac{1}{2}U''(r_0) \cdot (r-r_0)^2 + \frac{1}{6}U'''(r_0) \cdot (r-r_0)^3 + \dots \\
U'(r) &= U''(r_0) \cdot (r-r_0) + U'''(r_0) \cdot (r-r_0)^2 + \dots \approx U''(r_0) \cdot (r-r_0) \\
U''(r) &= U''(r_0) + U'''(r_0) \cdot (r-r_0) + 2U^{(4)}(r_0) \cdot (r-r_0)^2 + \dots \approx U''(r_0) + U'''(r_0) \cdot (r-r_0)
\end{aligned}
\tag{4.4.13}$$

The potential rushes into the infinity with the approach of atoms in the area $r < r_0$ where the interatomic repulsive forces predominate. In the area $r > r_0$, the forces of attraction between atoms predominate, which rapidly weaken as the distance between the atoms increases, so that the potential at $r \gg r_0$ approaches zero.

The same potential describes the elastic deformation of a solid in the vicinity of r_0 , where its shape is still close to parabolic-symmetrical one, while its asymmetry (*anharmonicity*) is the cause of thermal expansion. This allows elastic characteristics to be related to those of thermal expansion.

The elasticity modulus G can be determined from Hooke's law $\sigma = G \cdot \varepsilon$, $G = \frac{\sigma}{\varepsilon}$ and the form of the potential $U(r)$ (4.4.9), if the deformation is represented through the interatomic distances before r_0 and after r the load due to the external stress σ as the force

$F = -gradU(r) = -U'(r)$ acting on an attack surface $A = r_0^2$:

$$\varepsilon = \frac{r - r_0}{r_0}, \quad \sigma = \frac{F}{A} = \frac{-U'(r)}{r_0^2}, \quad G = \frac{1}{r - r_0} \cdot \frac{-U'(r)}{r_0}. \quad (4.4.14)$$

From (4.4.14), taking equation (4.4.13) into account, one gets the proportionality of the equilibrium elastic modulus G_0 at absolute zero $T = 0K$ (*without heat oscillations* $r = r_0 = const$) and the elastic modulus G at a temperature T to the second derivative of the potential:

$$G_0 \equiv G(r_0) = \frac{-U''(r_0)}{r_0} \text{ and } G \equiv G(r) = \frac{-U''(r)}{r}. \quad (4.4.15)$$

Now the change in the elasticity modulus with the temperature rise from zero to the temperature T and thus its relationship with the linear thermal expansion can be calculated using the second derivative of the model potential (4.4.9) and taking into account (4.4.13) as follows:

$$\frac{G - G_0}{G_0} = \frac{U'''(r_0)}{U''(r_0)}(r - r_0) = -\frac{K(k=3)}{K(k=2)} \cdot \frac{(r - r_0)}{r_0} = -k_1 \cdot \alpha \cdot T, \quad (4.4.16)$$

where $k_1 = \frac{K(k=3)}{K(k=2)}$ is.

Differentiation of equation (4.4.16) over temperature reveals the relationship between the temperature coefficient $\frac{dG}{dT}$ of the elasticity module and the coefficient of linear thermal expansion α :

$$\alpha = -\frac{k_1^{-1}}{G_0} \cdot \frac{dG}{dT}. \quad (4.4.17)$$

The coefficient of linear thermal expansion is therefore one of the fundamental characteristics of a solid. Its behavior allows certain conclusions about the other internal parameters such as entropy or elasticity modulus at

changes in the intensive state variables (*temperature, stress*). On the other hand, analysis of other known transformation characteristics allows to make certain predictions about linear thermal expansion.

So, if the temperature dependence of the elasticity modulus in the pre-martensitic temperature range shows an abnormal behavior that is directly related to changes in the atomic interaction potential $U(r)$, such as its softening $\frac{dG}{dT} \geq 0$, it can be recognized by the sign $\alpha \leq 0$ of the coefficient of thermal expansion in dilation measurements.

Since the theoretical analysis above does not refer in any way to SMA's, its conclusions apply to all metallic alloys whose elasticity behavior can be described by the Lenard-Jonson potential (4.4.9). So, the following general statement is valid from (4.4.17): If an alloy exhibits the invar behavior $\alpha = 0$ in a temperature range, the elinvar behavior $\frac{dG}{dT} = 0$ can also be expected in the same temperature range.

4.4.3 Length changes in two-phase temperature range

The aim of the dilatometric investigations of SMA's is not actually to determine the thermal expansion coefficients of the pure austenite and martensite phases per se, and if so, then only in the vicinity of transformation temperatures in view of the relationships with other parameters considered above. The main focus is on the dilation behavior of SMA's in the temperature ranges of the martensitic forward and reverse transformations.

Various SMA-specimens (**Table 1**) were investigated dilatometrically for this purpose. The martensitic transformations of these SMA's have already been described in §4.3.1. All dilatometric specimens had parallel polished endings. All single crystals were grown according to the

Bridgman method and only the $Cu - 24.7at\%Al - 4.7at\%Ni$ single crystals according to the Chochralsky method.

Table 1. Composition (at%), crystalline state, transformation kind, specimen longitudinal axis orientation and the initial length of the investigated specimens

no.	crystalline state	transformation kind	Cu	Al	Zn	Mn	Ni	Ti	$[hkl]_A$	L_0 , mm
1	single	$B2 \leftrightarrow 9R$	68.0	15.0	16.0	---	---	---	100	9,6
2	single *	$B2 \leftrightarrow 9R$	68.6	20.7	---	10.7	---	---	110	9,5
3	single	$B2 \leftrightarrow 9R$	70.7	24.9	---	---	4.4	---	110	9,6
4	single**(rod)	$B2 \leftrightarrow 9R$	70.6	24.7	---	---	4.7	---	110	14,3
5	single	$fzk \leftrightarrow fzt$	15.9	---	---	84.1	---	---	100	9,6
6	Poly	$B2 \leftrightarrow B19'$	---	---	---	---	49.8	50.2	---	9,6
7	Poly	$B2 \leftrightarrow \frac{B19'}{R}$	---	---	---	---	50.5	49.5	---	13,0

* Single crystal with a developed block structure

** Czochralski method

The specimen length changes were measured in the temperature range $(-100 \div +300)^\circ C$ at different cooling and heating rates (*scanning rate*) kept constant during each measurement in a "NETZSCH"-dilatometer using the low-temperature measuring element. A horizontal tube furnace pushed over it with a jacket that could be cooled by the liquid nitrogen made it possible to change the temperature of the entire measuring cell with the specimen holder. The thermocouple was placed directly on the surface of the test sample, with good thermal contact being ensured by a thermal paste. The thermal expansion coefficients was calculated from the measurement data using the "Thermal Analysis"-software integrated in the dilatometer.

All experimentally measured and calculated values are summarized in Table 2 for all investigated SMA's. The columns in Table 2 contain absolute elongations $\Delta L = L - L_0$ in μm as well as relative elongations of specimens (*dilation*) $\varepsilon_d = \frac{\Delta L}{L_0} \cdot 100\%$ and coefficients of linear thermal expansion

$$\varepsilon_d = \frac{\Delta L}{L_0} \cdot 100\% \quad \text{and coefficients of linear thermal expansion}$$

sion in pure austenite ($\alpha^{A'}$) and martensite phases (α^{M^P}) as well as in two-phase temperature ranges during the forward ($\alpha^{A'M^P}$) and reverse ($\alpha^{M^PA'}$) transformations.

Table 2. Length change (μm), dilation (%) and coefficients of the linear thermal expansion in austenitic, martensitic and two-phase states

no.	ΔL	ε_d	$\alpha^{A'} \cdot 10^6$	$\alpha^{A'M^P} \cdot 10^6$	$\alpha^{M^P} \cdot 10^6$	$\alpha^{M^PA'} \cdot 10^6$	A_H	k_a
1:	+3,7 -1,7	+0,04 -0,03	18,0	-170 +130	7,0	-240 +100	0,7 1,3	0,994 0,996
2	-120,0	-1,26	24,0	1490	24,0	2950	0,5	0,750
3	+60,0	+0,63	18,0	-380	0,0	-380	1,0	0,840
4	+22,0	+0,15	5,0	-1180	13,0	-1050	1,1	0,960
5	-48,0	-0,50	45,0	510	40,0	430	1,2	0,750
6	-15,0	-0,16	8,0	210	8,0	190	1,1	0,970
7:								
B19'	+2,4	+0,02	25,0	-22	12,0	-30	0,7	0,997
R	+4,0	+0,03		--	10,0	-210	--	0,990

The values in the two-phase temperature ranges reflect the kinetic characteristics of the transformation rather than the thermal expansion of two-phase mixtures. One speaks here of transformation or deformation velocity, because:

$$\frac{\alpha^{A'M^P}}{\alpha^{M^PA'}} = \frac{d\varepsilon^{A'M^P}}{\dot{T} \cdot dt} / \frac{d\varepsilon^{M^PA'}}{\dot{T} \cdot dt} = \frac{\dot{\varepsilon}^{A'M^P}}{\dot{\varepsilon}^{M^PA'}}, \quad (4.4.18)$$

where \dot{T} is constant scanning rate pre-programmed for each measurement and

$$\dot{\varepsilon}^{A'M^P / M^PA'} = \frac{1}{L_0} \cdot \frac{d\Delta L^{A'M^P / M^PA'}}{dt} \quad (4.4.19)$$

is the length change velocity during the transformation.

Different values $\alpha^{A'M^P}$ and $\alpha^{M^PA'}$ also indicate asymmetry of the

hysteresis loops. So, a quantitative dimensionless degree of the hysteresis loop asymmetry can be introduced:

$$A_H = \frac{\alpha^{A'M^P}}{\alpha^{M^P A'}} . \quad (4.4.20)$$

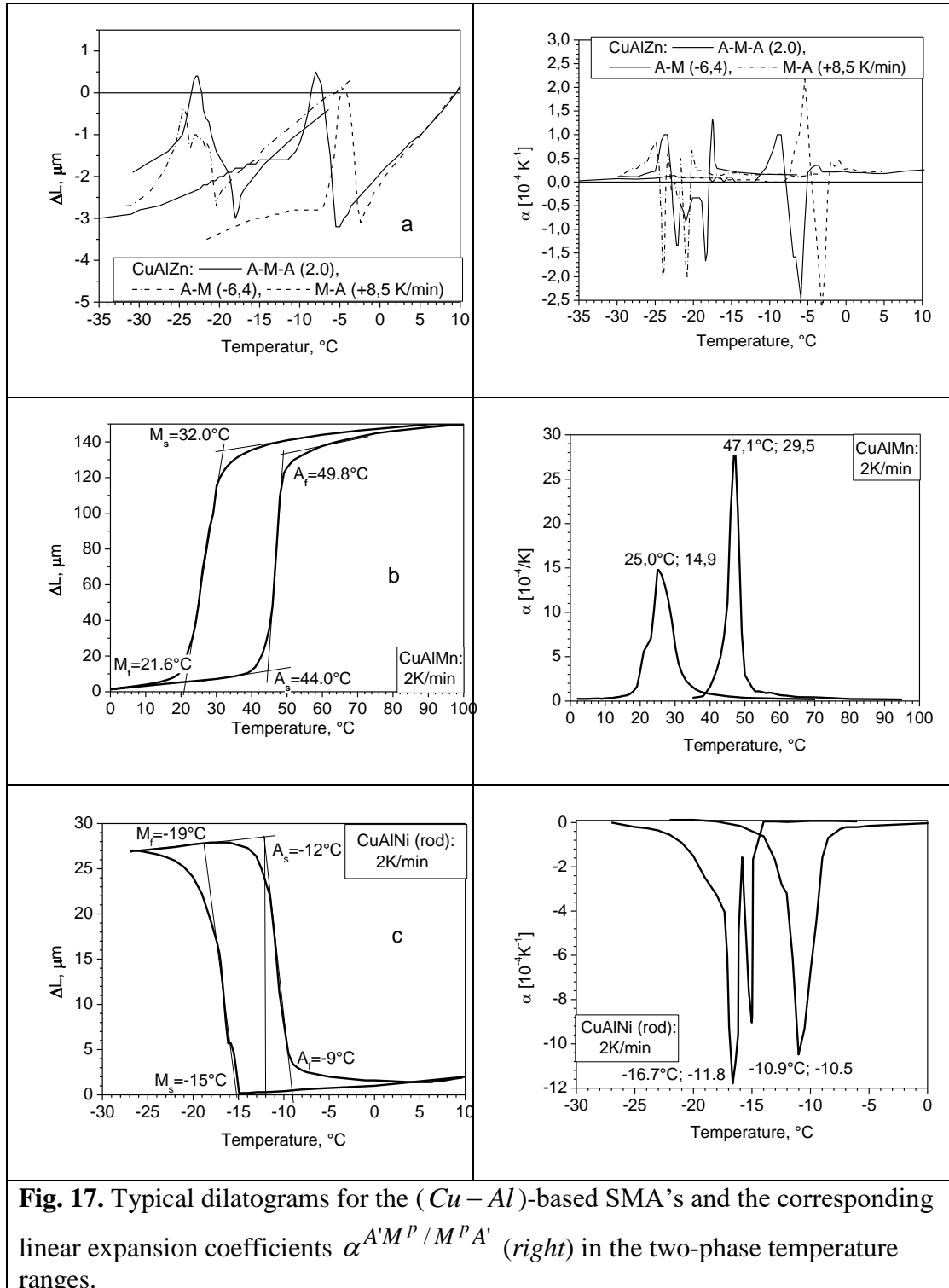
The hysteresis loop is ideally symmetrical at $A_H = 1$. The degree of asymmetry calculated in this way are also introduced in Table 2 and show that only the hysteresis loop of specimen 3 is symmetrical. Most of the other hysteresis loops are asymmetrical, with both cases $A_H < 1$ (*specimens 1, 2, 7*), i.e. the forward transformation is slower than the reverse transformation, and $A_H > 1$ (*specimens 4, 5, 6*) with reverse behavior.

The measured and calculated parameters such as the length change and the coefficient of linear thermal expansion differ not only in terms of their values, as can be seen from Table 2 and the graphs (*Figs. 17 and 18*), but also in terms of their signs.

The sign shows whether a shortening ($-\Delta L, +\alpha$) or lengthening ($+\Delta L, -\alpha$) of a specimen takes place during the transformation. In the two-phase temperature ranges of the martensitic forward and reverse transformations, the same additive two-phase rule as in (1.5) applies to the expansion coefficient:

$$\alpha^{A'M^P / M^P A'} = (1 - z) \cdot \alpha^{A'} + z \cdot \alpha^{M^P} . \quad (4.4.21)$$

This means that if the expansion coefficients of the austenite and the martensite are the same ($\alpha^{A'} \approx \alpha^{M^P}$, $\alpha^{A'M^P / M^P A'} = \alpha^{A'}$), no deviations of the dilation measurement curve from its linear trace ($\Delta L = \alpha \cdot L_0 \cdot T$) are recorded in the temperature ranges of the martensitic transformations.



The deviations in the form of a transformation hysteresis loop (**Fig. 17 and 18**) are only registered in the dilatometer if a non-accommodated martensitic deformation (3.2.1) is present as a resulting spontaneous specimen deformation (*dilation*) in the direction of its longitudinal axis during the

transformations:

$$\varepsilon_d = \varepsilon_{el}^{M^p} = \frac{\Delta L}{L_0} = \mu \cdot \gamma_M (1 - k_a) \cdot z \quad (4.4.22)$$

where γ_M is the primary martensitic lattice deformation (**Fig. 2 b**), k_a is the accommodation degree and $\mu = \cos\xi \cdot \cos\zeta$ is the Schmid's orientation factor.

The accommodation degree k_a can be determined experimentally from dilation measurements as follows:

$$k_a = \left(1 - \frac{|\varepsilon_d|}{\varepsilon_{\max}^M}\right), \quad (4.4.23)$$

where ε_{\max}^M is the maximal martensitic deformation determined experimentally, e.g. from the $(\sigma - \varepsilon)$ -diagrams of the pseudoelastic deformation (**Fig. 20 c**).

The accommodation degree (4.4.23) calculated by the dilation ε_d is a result of the both structural (*crystallographic*) and morphological accommodations, the individual contributions of which cannot be distinguished dilatometrically. Nevertheless, their effects can be analyzed in view of the dilation magnitude and the sign of the thermal expansion coefficient. The number of secondary invariant displacements of atomic planes in a martensite polydomain (**Fig. 2 b**), which leads to the formation of internal twins (**Fig. 2 c, d**), is a priori dependent on the mechanical shear stress $\tau = \sigma \cdot \mu$ acting on the martensite macromonodomain in the shear plane.

The stress σ is the mechanical external stress acting along the longitudinal specimen axis or the internal stress acting on a martensite polydomain from its surroundings along the longitudinal specimen axis.

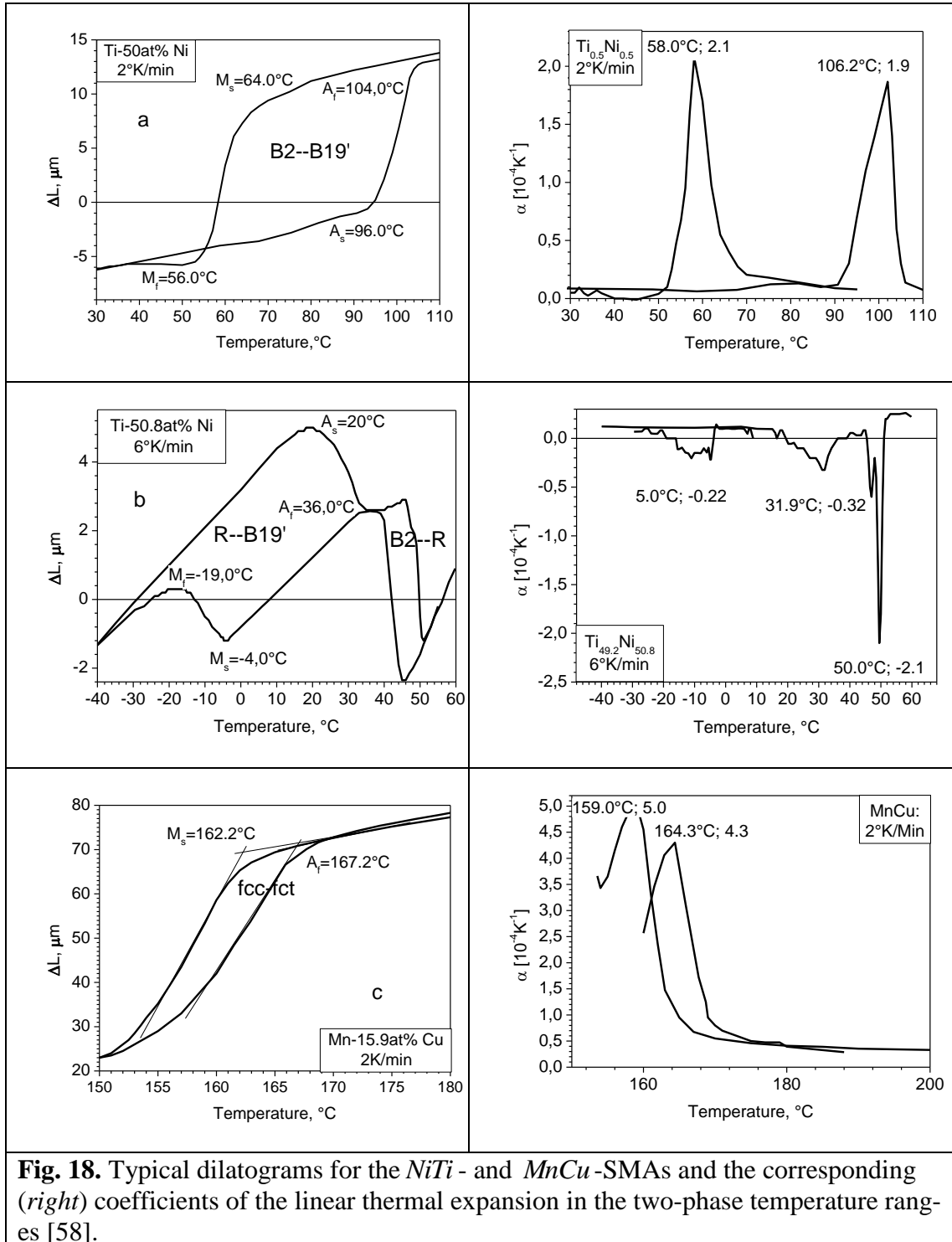


Fig. 18. Typical dilatograms for the *NiTi*- and *MnCu*-SMAs and the corresponding (*right*) coefficients of the linear thermal expansion in the two-phase temperature ranges [58].

The angle between the longitudinal axis of a single crystalline specimen and the normal to the shear plane is designated in Schmid's orientation factor (4.4.22) as ξ and the angle between the longitudinal specimen axis and

the shear direction as ζ . The shear stress $\tau = \frac{1}{2}\sigma = \tau_{\max}$ is maximal at

$$\xi = \zeta = \frac{\pi}{4}.$$

The behavior of the coefficient of linear thermal expansion in two-phase $A'M^P/M^PA'$ temperature ranges is dominated by the parameters of the martensite phase involved in (4.4.22) and not determined by the conventional coefficients of the linear thermal expansion of the austenite and the martensite (4.4.21):

$$\alpha^{A'M^P/M^PA'} = \mu \cdot \gamma_M (1 - k_a) \cdot \frac{dz}{dT} - \mu \cdot \gamma_M \cdot z \cdot \frac{dk_a}{dT}, \quad (4.4.24)$$

which enables the understanding and analysis of the dilatation effects experimentally measured in these ranges.

4.4.4 Crystallographic analysis of the transformation dilation

If the stacking fault or twin density, which determine the accommodation degree in (4.4.23), remains constant $\frac{dk_a}{dT} = \frac{dk_a}{dz} \cdot \frac{dz}{dT} = 0$ during the transformation $0 < z < 1$ the sign of the thermal expansion coefficient is determined by the first term in (4.4.24). Here are $\frac{dz}{dT} < 0$, $(1 - k_a) > 0$ always, then:

1. The case $\alpha^{A'M^P/M^PA'} > 0$ (**Fig. 17b**, *Cu-Al-Mn*, $B2 \leftrightarrow 9R$, $\langle 110 \rangle$) only occurs if $\mu < 0$ or $\cos \xi < 0$ ($270^\circ > \xi > 90^\circ$) and $\cos \zeta > 0$ ($90^\circ > \zeta > 270^\circ$) or vice versa;
2. The case $\alpha^{A'M^P/M^PA'} < 0$ (**Fig. 17c**, *Cu-Al-Ni*, $B2 \leftrightarrow 9R$, $\langle 110 \rangle$) only occurs if $\mu > 0$ or $\cos \xi > 0$ ($270^\circ < \xi < 90^\circ$) and $\cos \zeta < 0$ ($90^\circ < \zeta < 270^\circ$) or vice versa.

3. If the expansion coefficient $\alpha^{A'M^P/M^P A'}$ changes its sign during the transformation (**Fig. 17a**, $Cu - Al - Zn$, $B2 \leftrightarrow 9R$, $\langle 100 \rangle$), this means that either the both terms in (4.4.24) are involved, and the twin density changes during the transformation ($\frac{dk_a}{dz} \neq 0$) or that it switches on another transformation then $B2 \leftrightarrow 9R$ by the increasing internal stresses in the austenite matrix.

The first two cases occur with the same probability if there are no orientating internal or external stresses.

It is obvious that the purely physical entropy and elasticity effects discussed above remain according to their value in background of the length changes caused by transformation and accommodation related length changes of the additive thermal expansion coefficient in the two-phase temperature range and only become effective when the accommodation is close to perfect ($k_a \approx 1$).

It follows from equation (4.4.24) that the case $\alpha^{A'M^P/M^P A'} = 0$ occurs when $k_a = 1$ or $\mu = 0$ ($\zeta = \frac{\pi}{2}$), i.e. all martensite polydomains are oriented perpendicular to the longitudinal specimen axis and $\frac{dk_a}{dT} = 0$. The condition $k_a = 1$ means that the number of positive and negative twin variants (*martensite micromonodomains*) and their thickness (**Fig. 2 b**) are the same, and the condition $\frac{dk_a}{dT} = 0$ means that the stacking fault density ν_{sf} within martensite polydomains and thus the accommodation degree k_a remain constant during the transformation.

The contribution of the coefficients of the true linear thermal expansion of SMA's in the two-phase temperature range $\lambda^{A'M^P/M^P A'}$ (4.4.24) can-

not be neglected in dilation measurements if it is also in the elastic deformation range ($\varepsilon_d < \varepsilon_y \approx 1,5\%$). Its value is $500 \cdot 10^{-6} K^{-1}$ even at $\varepsilon_M = 0,5\%$ or $\frac{\Delta L}{L_0} = 0,005$ in the temperature range of the martensitic transformation about $10^\circ C$, while the conventional expansion coefficient is, e.g. for *Cu*, only $17 \cdot 10^{-6} K^{-1}$.

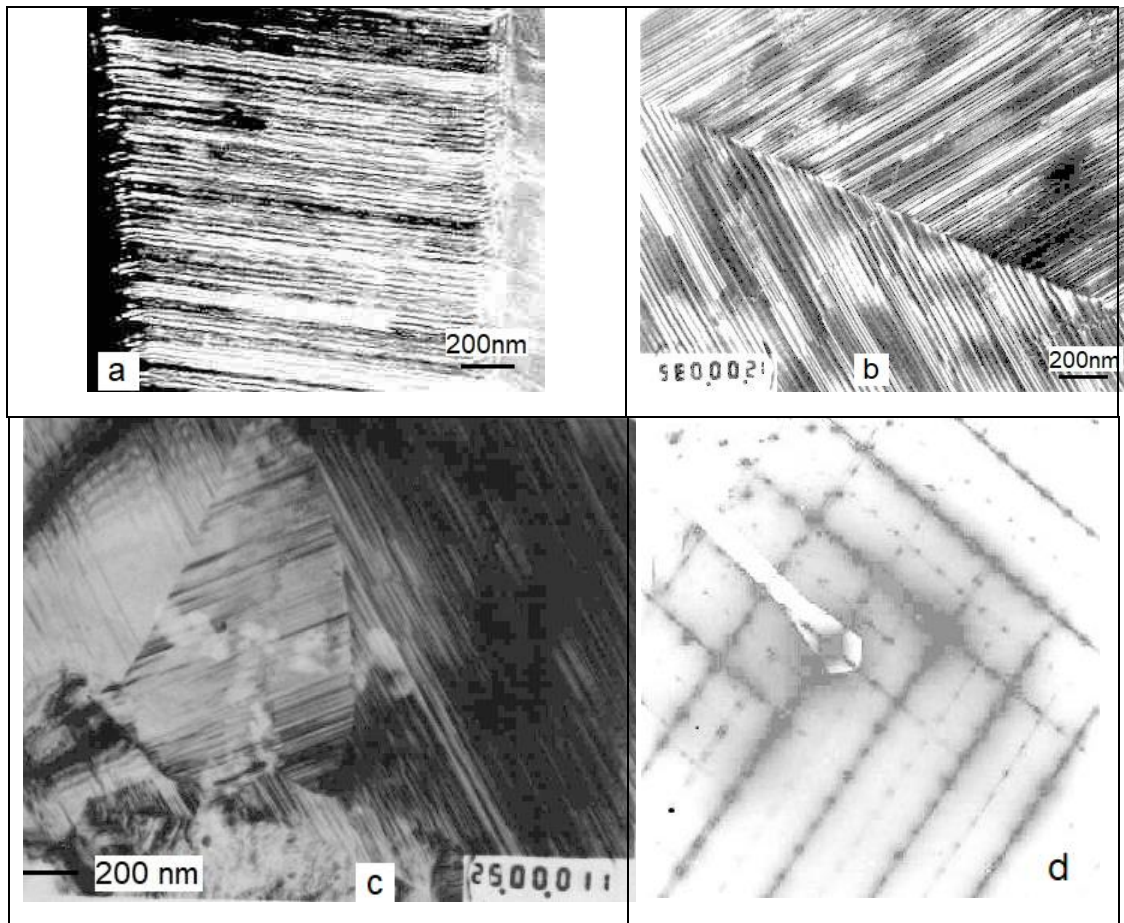


Fig. 19: **a** – a single martensite polydomain with internal twins, **b** – a martensite plate fused together from two martensite polydomains, **c** – a complex fused together from several martensite polydomains [9, 14]. Electron diffraction from the twinning ratio of two grown together martensite polydomains (b), foil surface $(110)_{9R}$ (d).

The contributions to dilation considered above are based primarily on the formation of twins in martensite polydomains (*Fig. 19 a*) as a result of the structural accommodation. The second, morphological accommodation occurs through the elastic interaction and the coalescence of different-

ly oriented martensite polydomains (*Figs. 19 b, c, d*).

Through coalescence, each single martensite polydomain is relieved of the internal stresses that arise at the phase boundaries, as two $A'M^P$ phase boundaries are transformed (*annihilated*) into a one internal martensitic $M^P M^P$ boundary with smaller elastic stresses (3.2.9), thereby making it possible to reduce the twin density within single martensite polydomains.

Table 3 summarizes all the contributions to the dilation in the direction of the $\langle 110 \rangle_{B2}$ axis as projections of the shear deformations in all possible shear systems on this axis, which form the 12 different orientation variants of martensite polydomains.

It can be understood from Table 3 how occurs negative or positive deformation of a single crystalline specimen in the direction $\langle 110 \rangle_{B2}$, and how takes place complete or partial accommodation of the martensitic lattice deformation γ_M within the entire specimen volume due to the elastic interaction and the coalescence of differently oriented martensite polydomains. Figure **19 b** shows, e.g., a martensite plate consisting of two merged martensite poly domains.

The shear systems $(101)\langle 101 \rangle$ and $(\bar{1}01)\langle \bar{1}01 \rangle$ in both martensite polydomains are perpendicular to each other, so that their shear deformations $+0.5\gamma_M$ and $-0.5\gamma_M$ compensate each other at the common $M^P M^P$ boundary as the habitus plane of the resulting martensite plate.

All of the transformation specifics discussed above, including the heat effects and accommodation processes, determine the transformation kinet-

ics, which do not necessarily have to be athermal and in that sense thermoelastic. The velocity of the martensitic transformations of SMA's therefore much lower than the sound velocity of the classic explosive martensitic transformation in steels when they are quenched.

Table 3. Contributions to dilation in the direction of the $\langle 110 \rangle$ -axis of displacements in 12 possible shear systems

Shear plane	(110)	(110)	($\bar{1}\bar{1}0$)	($1\bar{1}0$)	(011)	(011)
Shear direction	$\langle 110 \rangle$	$\langle \bar{1}\bar{1}0 \rangle$	$\langle \bar{1}10 \rangle$	$\langle 1\bar{1}0 \rangle$	$\langle 011 \rangle$	$\langle \bar{1}0\bar{1} \rangle$
Deformation in direction $\langle 110 \rangle$	$+\gamma_M$	$-\gamma_M$	0	0	$+0.5\gamma_M$	$-0.5\gamma_M$

Table 3. Continuation

Shear plane	($\bar{1}01$)	($\bar{1}01$)	(011)	(011)	($0\bar{1}1$)	($0\bar{1}1$)
Shear direction	$\langle \bar{1}01 \rangle$	$\langle \bar{1}0\bar{1} \rangle$	$\langle 011 \rangle$	$\langle 0\bar{1}\bar{1} \rangle$	$\langle 0\bar{1}1 \rangle$	$\langle 01\bar{1} \rangle$
Deformation in direction $\langle 110 \rangle$	$+0.5\gamma_M$	$-0.5\gamma_M$	$+0.5\gamma_M$	$-0.5\gamma_M$	$+0.5\gamma_M$	$-0.5\gamma_M$

The accommodation processes relax the A^1M^P phase boundaries below the yield point of the true plastic deformation and thereby preserve their coherence and mobility. This is the basis of the unique memory effects in SMA's.

4.5 Mechanical hysteresis

4.5.1 Quasiplasticity, ferro- and pseudoelasticity

The investigation of the ferroelastic hysteresis on single crystals is extremely informative for understanding of SMA-behavior. In this case, nucleation, latent transformation heat and the effects of crystalline and phase boundaries are excluded. The behavior of a SMA-specimen in the completely martensitic state under a uniaxial cyclic tension-compression load is, in contrast to "quasiplasticity" and for the reasons explained below, described with a special term "ferroelasticity".

Uniaxial tensile loads σ_t on a SMA-specimen at a constant test temperature in the martensitic temperature range $T < M_f = const$ leads to macroscopic deformation ε_q after reaching a critical quasiplastic yield (*index* qy) point $\sigma_{qy}^{M^P}$ (**Fig. 20 a**). This deformation is irreversible at the test temperature, i.e. it retains after the load removing and the elastic deformation reversing, similar to the true plastic deformation. This behavior is therefore called "quasiplasticity", and the deformation itself is called "quasiplastic".

The SMA-specimen remains in this quasiplastically deformed state because martensite as a deformation carrier is stable at temperatures below the equilibrium temperatures $T < T_0' < T_0$ both in its monodomain and in its polydomain state (**Figs. 1 a, b**). When heated above the temperature range $(A_s \div A_f) > T_0'$, the martensitic reverse transformation of the $(M^{m+} + M^P)$ -martensite takes place, which is partially monodomained by uniaxial tensile stress, into metastable austenite $(M^{m+} + M^P) \rightarrow A'$. The quasiplastic martensitic deformation is returned by disappearance of

the deformation carrier. This is known as the one-way memory effect [1-3].

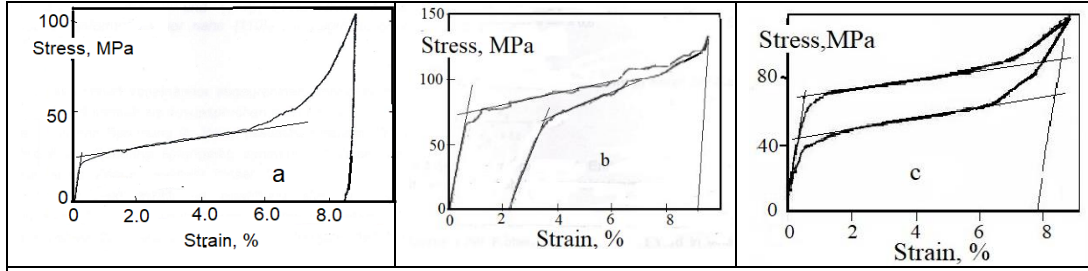


Fig. 20. Quasiplastic deformation of a $Cu - 13.4at\%Al - 4.0at\%Ni - \langle 100 \rangle$ single crystal in a martensitic state $T < M_f < T_0'$ (a), mixed deformation of the same single crystal in the two-phase temperature range $M_f < T < A_f$ (b), and pseudo-elastic deformation of a $Cu - 15.2at\%Al - 16.6at\%Zn - \langle 100 \rangle$ single crystal in an austenitic state $T > A_f > T_0'$ (c).

The one-way memory effect can be better illustrated using the scheme in Figure 2 a (*the second level*). If a martensite polydomain as the end product of the stress-free thermo-induced martensitic transformation is loaded by sufficient external stress $\sigma_{qy}^{M^p} < \sigma_t < \sigma_{qy}^{M^{m+}}$, the quasi-plastic deformation of the polydomain martensite take place. The designations are used in that stress region: $\sigma_{qy}^{M^p}$ for the yield point of the quasiplastic deformation shown in Figure 20 a as the intersection of the extrapolated elasticity and flow lines, and $\sigma_y^{M^m}$ for the yield point of the true plastic deformation of the martensite monodomainized by the tensile stress σ_t .

The quasiplastic martensitic deformation occurs by the movement of partial dislocations that leads to the reorientation of twin variants in each martensite polydomain. This deformation can therefore be defined by a re-orientation factor $0 \leq r_{tw} = (1 - v_{tw}) \leq 1$:

$$\varepsilon_q(\sigma) \equiv \varepsilon_M = r_{tw}(\sigma) \cdot \mu \cdot \gamma_M. \quad (4.5.1)$$

The definition is based on the similarity with the accommodation degree in

(4.4.23), which determines the dilation.

The one-way memory effect that originally led to the term “*shape memory*” is one of the most well-known and the most spectacular in the whole spectrum of memory effects: A heavily deformed metal specimen recovers its initially shape when it is insignificantly heated. This effect is most investigated experimentally and applied practically (*Appendix I*) [59-62].

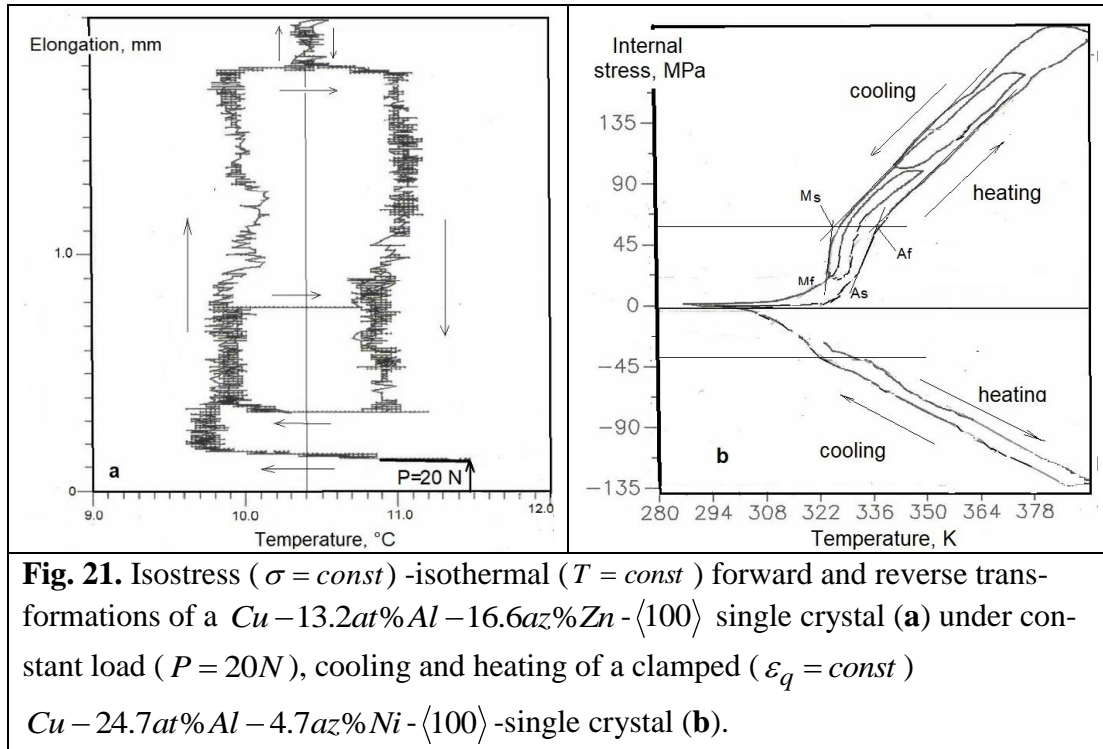
The problem with the application of the shape memory effect (SME) is due to its uniqueness, i.e. the addition of “one-way”. In the subsequent cooling-heating cycles, there are no more shape changes. In order to enforce such shape change into recurrent action cycles, its low-temperature shape must be restored by renewed quasiplastic deformation of the martensite. For this purpose, the memory element is coupled with a bias element, the counterforce of which ensures this martensite deformation during cooling [63-65].

The same effect is achieved when a constant load $P[N]$ (*weight*) is attached to a memory element (*Fig. 21 a*). The memory element then changes its shape reversibly at the cyclical temperature changes: It takes its low-temperature shape during the cooling below the local equilibrium temperature $T < T_0'$ by the transformation of the metastable austenite into the martensite monodomained under the constant tensile load (*Fig. 2 a, first level, first step*), and it takes its original high-temperature shape during the heating above the local equilibrium temperature $T > T_0'$ by reverse martensitic transformation with increasing the restoring force (*Figs. 21 b*).

The recovering the original high-temperature shape happens against the external load P , so that a mechanical work is done:

$$a(T) = \frac{A(T)}{m} = \frac{P \cdot \Delta L(T)}{m} = \frac{1}{\rho} \sigma \cdot \varepsilon_q(T), \quad (4.5.2)$$

where $a \left[\frac{J}{kg} \right]$ is specific (per mass unit) work, $S \left[m^2 \right]$, $L_0 \left[m \right]$, $V_0 \left[m^3 \right]$, $\rho \left[kg \cdot m^{-3} \right]$ and $\Delta L \left[m \right]$ are cross-section, initial length, initial volume, density and reversible length change of the memory element.



The one-way memory effect can therefore be defined thermodynamically as a temperature-dependent recovery of the quasiplastic deformation of a SMA-specimen, which was generated at the temperature $T < (M_s \div M_f) < T_0'$ by an external stress or by a constant load, if it is heated above a temperature $T > (A_s \div A_f) > T_0'$ without external stress or under a constant load ($\sigma \geq 0 = const$):

$$\varepsilon_q(\sigma > \sigma_{qy}) \Big|_{T < T_0'} = \varepsilon_r(T > T_0') \Big|_{\sigma}, \quad (4.5.3)$$

where ε_r is the reversible martensitic deformation, which value may be different from quasiplastic deformation value, if a part of that remains irreversible for whatever reason.

Another variant of the shape memory effects cannot be illustrated in such structural schemes (**Fig. 2 a**), namely the force memory effect, which is also responsible for the quasiplastic deformation recovery against an external force as above. If a quasiplastically deformed SMA-specimen is held in its low-temperature shape during heating over the temperature range $T > (A_s \div A_f) > T_0'$, internal stresses $\sigma = \sigma^{\text{int}}(T)|_{\varepsilon_r}$ arise in it (**Fig. 21 b**), which initially exceed the plastic yield point $\sigma_y^{M^{m+}}$ and then also the breaking point of the martensite $\sigma_B^{M^{m+}}$ at the breaking temperature T_B , and lead to self-destruction of the specimen (**Appendix 2**).

The slope of the internal stress dependence on the temperature in the temperature range ($A_f < T < T_B$) corresponds on the other hand to the

Clausius-Clapeyron ratio (2.1.7) $\frac{d\sigma(T)}{dT} \approx 2.4 \frac{\text{MPa}}{\text{K}}$ (**Fig. 21 b**). The trans-

formation entropy calculated from it $\Delta S^{9R \rightarrow B2} = \frac{1}{\rho} \cdot \frac{d\sigma}{dT} \cdot \varepsilon_q \approx 24 \frac{\text{J}}{\text{kg} \cdot \text{K}}$ at

values: $\rho \approx 8 \cdot 10^3 \text{ kg/m}^3$, $\varepsilon_q \approx 0.08$ for $\text{Cu} - 24.7\text{at}\% \text{Al} - 4.7\text{at}\% \text{Ni}$ -

$\langle 100 \rangle$ single crystals agrees well with that from the calorimetric measurements (4.3.4). The force memory effect is used in electrical break protection devices with a memory insert, applicable, e.g. for electrical networks against overloads and short circuits [66 - 69] (**Appendix 2**).

Reversible cyclic deformation of a memory element can also take place without bias elements and without external stress (*constant load*), if an ani-

sotropic field of internal stresses $\|\tau_{ij}\|$ is induced in the memory element by a few cycles of thermo-induced transformation under constant load or by other training methods. The source of such orienting internal stresses are separate martensite macromonodomains with increased reverse transformation temperatures that have arisen during training, which are thereby switched off from the thermo-induced transformation cycles.

This ability of SMA's to deform spontaneously both during heating and cooling is called two-way memory effect [1-3] and, thermodynamically, just like the one-way memory effect described above without external load $\sigma^{ext} = 0$, is defined as a special case:

$$\varepsilon = \varepsilon_q(T, \|\tau_{ij}\|) \Big|_{\sigma^{ext}=0} \quad (4.5.4)$$

where the stress tensor $\|\tau_{ij}\|$ is to be regarded as an internal parameter that describes the internal stresses field caused by training before. The martensitic deformation generated by the two-way memory effect is, however, much smaller than that of the one-way memory effect and is only of 1% up to 2%. In addition, no mechanical work (4.5.2) can be done in this process.

The better overview of all SME's in their representation as thermodynamic functions offers the following formally illustrated scheme similar to the triangle learning scheme for Ohm's law $\frac{U}{I \cdot R}$:

$$\varepsilon \rightarrow \sigma \rightarrow T. \quad (4.5.5)$$

If you cover a symbol in the scheme (4.5.5) as a constant held variable, two remaining symbols form an SME-function (*left*) from the argument (*right*).

If you cover ε , you get internal stress $\sigma = \sigma^{\text{int}}(T)|_{\varepsilon_r}$ as a function of the temperature with the quasiplastic detent deformation kept constant, i.e. the memory force effect. If you cover σ , you get recoverable quasiplastic deformation $\varepsilon_r(T)|_{\sigma}$ as a function of the temperature at zero or constant external stress or load, i.e. the one-way (4.5.3) or two-way memory effect (4.5.4). If you cover T , you get quasiplastic, ferroelastic or pseudoelastic deformation $\varepsilon_{q,f,p}(\sigma)|_{T < T_0, T > T_0}$ as a function of the external stress at constant temperature, i.e. quasiplastic, ferroelastic or pseudoelastic memory effect.

The existence of the substructure consisting of the martensite micromonodomains (*Figs. 2 a-d*) with easily movable martensite micromonodomain boundaries (*stacking faults*) is the basis of all kind of shape memory effects and is one of the criteria of thermoelasticity. The properties of internal martensitic boundaries determine (§3.2.2) fundamentally the characteristics of the mechanical hysteresis of SMA's.

These characteristics are complicated in most experiments by the influence of other factors such as the presence of $A'M^P$ phase boundaries (3.2.14). That is why there is such a lot of shapes and sizes of experimentally determined hysteresis loops that are complicated for the analysis. Despite the obvious advantages of investigating the ferroelastic hysteresis, there are hardly any experimental results in this area. It is evidently due to the difficulties in carrying out such experiments, which require the use of one and the same specimen for the tensile and compressive loads in ferroelastic deformation cycles.

In order to carry out the uniaxial tension-compression loading of a flat

SMA-specimen, this specimen is inserted into a rabbet milled in the copper thermal camera that is adapted to the width, height and length of the working part of the specimen and is held back by a copper cover attached to the top. A gap in the cover cut along the specimen enables light microscopic observations (**Fig. 22 d**) during the deformation cycles and placement of a thermocouple on the specimen surface. The thermal camera is connected to a thermostat by rubber hoses and thus enables a constant test temperature to be set. This device, which prevents lateral movements of the specimen during the compression load, as well as the relatively small mechanical stresses required for the ferroelastic deformation, enable clean tension-compression deformation even without massive standard specimens required for such tests.

Uniaxial tension-compression loading of the austenite, which is metastable in the temperature range $T_0' < T < T_0$, obliges it to transform into a martensite macromonodomain $A' \rightarrow M^m$ and thus to the macroscopic pseudoelastic martensitic deformation $\varepsilon_p(\sigma) = \varepsilon_M \cdot z(\sigma)|_T$ (**Fig. 22 a**). When the load is removed, the martensite macromonodomain transforms back into the metastable austenite $M^m \rightarrow A'$ (**Fig. 2 a, fourth level**). The macroscopic martensitic deformation is recovered by the disappearance of the martensite as a deformation carrier, so that two hysteresis loops are created – one on the tensile and one on the compression side. This behavior is known as pseudoelasticity, or sometimes, because of the amount of deformation, superelasticity.

The pseudoelastic hysteresis loops are thus formed by two pseudoelastic flow lines and two elasticity lines (**Fig. 22 a**). The slope of the flow lines or the entire hysteresis loop is described by an energetic pseudoelasticity coef-

efficient like the energetic thermoelasticity coefficient (4.3.7) introduced in §4.3.3:

$$k_p \left[\frac{J}{kg} \right] = \frac{1}{\rho} \frac{d\sigma}{d\varepsilon_p}, \quad (4.5.6)$$

where ρ and ε_p are density and pseudoelastic deformation.

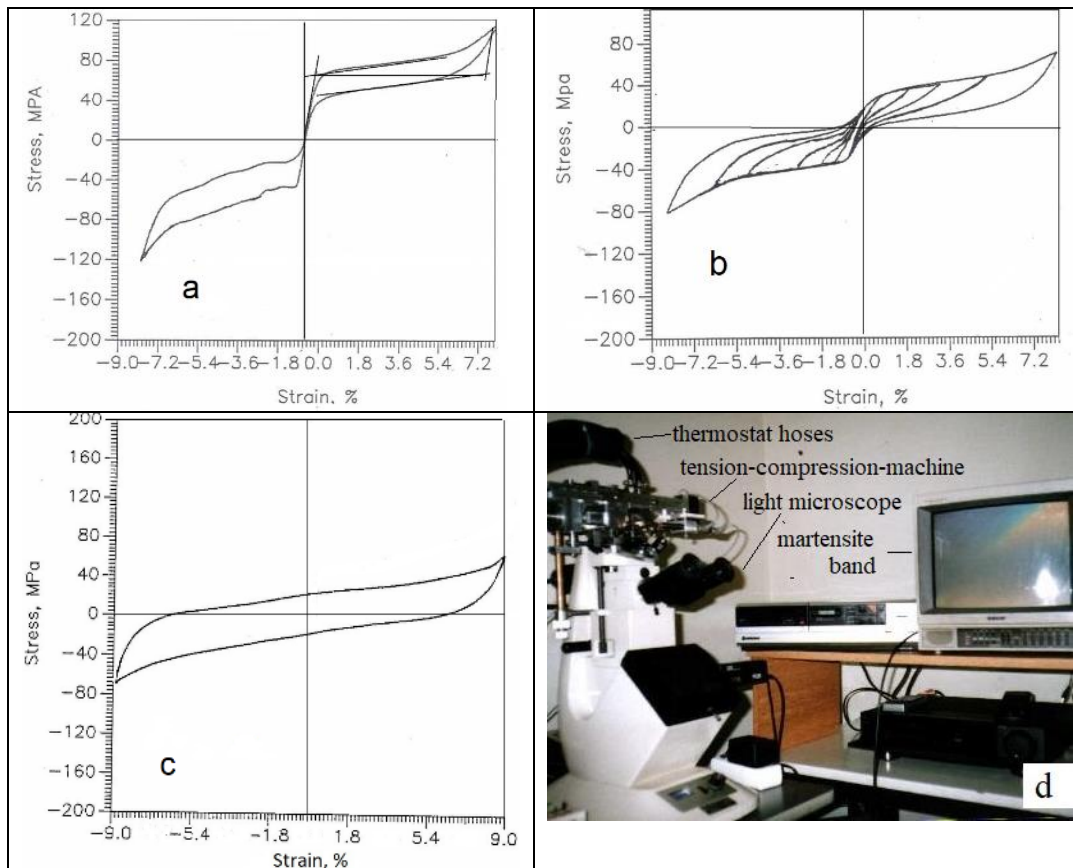


Fig. 22. Pseudoelastic tension-compression deformation by the stress-induced $A' \rightarrow M^{m+}$ (tension side) and $A' \rightarrow M^{m-}$ (compression side) transformations in the premartensitic temperature range $T_0' < A_f < T < T_0$ (a), complete and partial cycles of the mixed pseudo- and ferroelastic deformation by the same transformations of the austenite part $(1-z)$ and by the $M^{m+} \leftrightarrow M^{m-}$ -reorientation of the martensite part z of the initial sample in the two-phase transition range $M_f < T < A_f$ (b), the ferroelastic deformation cycles in the martensitic state $T < M_f < T_0'$ (c) of a $Cu-15.2at\%Al-16.6at\%Zn-\langle 100 \rangle$ single crystal. The tension-compression device on the light microscope (d).

The intersection points of the extrapolated elasticity and flow lines mark

the pseudoelastic yield points during loading $\sigma_{py}^{A'M^{m\pm}}$ and unloading $\sigma_{py}^{M^{m\pm}A'}$. The equilibrium stress σ_{p0} is defined as the mean value between the two yield points:

$$\sigma_{p0}(T) = \frac{\sigma_{py}^{A'M^{m\pm}}(T) + \sigma_{py}^{M^{m\pm}A'}(T)}{2}. \quad (4.5.7)$$

If the test temperature, which is kept constant during each tension-compression cycle, is changed from test to test, the yield points $\sigma_{py}^{A'M^{m\pm}}(T)$ and $\sigma_{py}^{M^{m\pm}A'}(T)$ change also according to the Clausius-Clapeyron ratio (2.1.7). The experimentally determined temperature dependence of the equilibrium stress $\sigma_{p0}(T)$ is used for other than calorimetric determination and calculation of the transformation entropy $\Delta S^{A'M^{m\pm}}$:

$$\Delta S^{A'M^{m\pm}} = \frac{\varepsilon_p^+}{\rho} \cdot \frac{d\sigma_{p0}^\pm(T)}{dT}. \quad (4.5.8)$$

In eq. (4.5.8) the determination of the transformation entropy is only given by the temperature dependence of the tensile stress (+), because the tensile and compressive hysteresis loops are not always symmetrical due to differences in the shear systems.

When the test temperature decreases, the two hysteresis loops slide along the elastic branch towards each other, their shape and area remaining in the process unchanged. During the transition from pseudoelasticity ($T > A_f > T_0'$) to ferroelasticity ($T < M_f < T_0'$), when the test temperature reaches the two-phase temperature range ($M_f < T < A_f$), where the initial

specimen consists only partly ($0 < z < 1$) of martensite, a neck-shaped hysteresis narrowing develops between two pseudoelastic hysteresis loops instead of one elasticity line (**Fig. 22 b**).

The slope of the pseudoelastic lines is determined as an effective elasticity modulus $\frac{d\sigma}{d\varepsilon} = G_{eff}^{A'+M^p}$ of the two-phase mixture by the phase fraction z of the martensite in the SMA initial specimen:

$$G_{eff}^{A'+M^p}(T)[MPa] = G^{A'}[1 - z(T)] + \rho \cdot k_f \cdot z(T), \quad (4.5.9)$$

where:

$$k_f \left[\frac{J}{kg} \right] = \frac{1}{\rho} \frac{d\sigma}{d\varepsilon_f} \quad (4.5.10)$$

is the slope of the ferroelastic hysteresis loop, which to be understood as an energetic ferroelasticity coefficient corresponding to the thermoelasticity k_T (4.3.7) and pseudoelasticity k_p coefficients (4.5.6), and ε_f is the ferroelastic deformation.

Equation (4.5.9) adequately describes the experimentally observed change in the effective elasticity modulus in the transformation temperature range as a function of the martensite phase fraction $0 \leq z \leq 1$ in the initial specimen. This means that the martensitic deformation ε_M (4.5.1) of the specimen in the two-phase state (**Abb. 20 b**) as well as within the transition sections of the $(\sigma - \varepsilon)$ -diagram (**Fig. 22 b**) takes place due to the reorientation of the existing martensite and the pseudoelastic deformation of the retained austenite $\varepsilon_M = \varepsilon_{q,f} \cdot z + \varepsilon_p \cdot (1 - z)$.

When the reorientation of the existing martensite is completed, i.e. after

resource of the quasiplastic or ferroelastic deformation $\varepsilon_M = \varepsilon_{q,f} \cdot z$ has been exhausted, the pseudoelastic deformation begins by transformation of the retained austenite phase fraction $(1-z)$ under external stress into a tensile M^+ or compression M^- martensite macromonodomain, the value $\varepsilon_M = \varepsilon_p \cdot (1-z)$ of which is also determined by the martensite phase fraction.

Decreasing the amplitude of the pseudoelastic deformation $\Delta\varepsilon_p$ in partial deformation cycles (**Fig. 22 b**) leads to a decrease in the width $\Delta\sigma_p$ of pseudoelastic hysteresis loop, while the slope $\frac{d\sigma}{d\varepsilon} = G_{eff}^{A'+M^p}$ of the linear sections increases with the transition from tensile to compression and vice versa. As a result, if the deformation amplitude is sufficiently small, two pseudoelastic hysteresis loops are again observed, which are separated by a purely elastic section:

$$\lim_{\Delta\varepsilon_p \rightarrow 0} G_{eff}^{A'+M^p} = G^{A'} = G^{M^\pm}. \quad (4.5.11)$$

This means that the martensitic phase is completely monodomainized, and the SMA-specimen is only deformed by the elastic deformation of the two-phase mixture.

In the temperature range $T < M_f < T_0'$, in which the initial specimen is in a purely martensitic state, the two pseudoelastic hysteresis loops permute into a single ferroelastic hysteresis loop (**Fig. 22 c**). The stress and deformation amplitudes $\Delta\sigma_f$ and $\Delta\varepsilon_f$ of the ferroelastic hysteresis loop are equal to the width of the pseudoelastic hysteresis loop and the entire pseudoelastic tension-compression deformation, and do not change with

further temperature decrease [14].

At the first tensile loading (**Fig. 39 a**) the quasiplastic yield point $\sigma_{qy}^{M^P}$ ($i=1$) and the entire quasiplastic flow line is almost twice as high as the flow line in the subsequent cycles of the ferroelastic deformation:

$$\sigma_{qy}^{M^P} (i=1) \approx 2 \cdot \sigma_f^{M^{m+}} \quad (\varepsilon_f = 0, i > 1). \quad (4.5.12)$$

This is due to the partial reorientation $M^P \rightarrow M^{m+} + M^{m\pm}$ of the martensite polydomains, which are favorably oriented relative to the strain axis, from the complex mixture of twelve orientation variants (**Table 3**) of the thermo-induced polydomain martensite.

Only the subsequent compression loading leads to a complete reorientation $M^{m\pm} + M^{m+} \rightarrow M^{m-}$ of this mixture to a compression martensite macromonodomain. In the event of further tension-compression-load cycles, only the reorientation of the tension and compression martensite macromonodomains takes place with one another (**Fig. 2 a, third level**). The corresponding tension and compression flow lines as well as two elasticity lines build a complete ferroelastic hysteresis loop $\varepsilon_f(\sigma)|_T$ (**Fig. 22 c**). The difference in deformation mechanisms also makes the essential difference between quasiplastic and ferroelastic deformation.

However, light microscopic observations show that the martensitic $A' \rightarrow M^{m+}$ -transformation under an external stress is morphologically very similar to the martensite reorientation $M^{m-} \leftrightarrow M^{m+}$. The both processes take place only through the continuous nucleation of narrow lamellae without their growth similar to those in Figure 27 b. In both cases, these lamel-

lae are single tensile (M^{m+}) or compression (M^{m-}) martensite micromonodomains that arise under the external stress, defined in §3.1.1. The martensite micromonodomains become to a tensile (M^{m+}) or compression (M^{m-}) martensite macromonodomain at the end of the pseudo- or ferroelastic deformation. The difference between the both processes consists in the energy of the $A'M_m^{m+,m-}$ phase boundaries and the internal martensitic $M^{m\mp}M_m^{m\pm}$ domain boundaries.

The presented experimental results on the transition from pseudoelastic to ferroelastic hysteresis disprove the following predictions of theories and models of SMA's [70, 71]:

1. Temperature dependence of the pseudoelastic hysteresis area.
2. Area doubling of the ferroelastic hysteresis compared to the common area of the pseudoelastic tension and compression hysteresis loops.
3. Transition from pseudoelastic to ferroelastic hysteresis by moving the two pseudo-elastic hysteresis loops together along the elasticity line without the additional dissipative transition area.

4.5.2 Interior of the mechanical hysteresis

The interior of the ferroelastic hysteresis is revealed in partial cycles similar to the thermal hysteresis. The area of a hysteresis loop consisting of two triangles between two flow lines and the abscissa $\sigma = 0$ (**Figs. 23 a, b**) is determined by the energy dissipation $w_D^f(\varepsilon_f)$ in a complete cycle of ferroelastic deformation:

$$w_D^f(\varepsilon_f) = k_f \cdot \varepsilon_f^2. \quad (4.5.13)$$

The tensile and compression ferroelastic yield points $\sigma_{fy}^{M^{m-}}$ and $\sigma_{fy}^{M^{m+}}$ determined as the intersection of the extrapolated tensile and compression flow lines with extrapolated elasticity lines lie on the abscissa, i.e. on the zero stress axis, in both complete and partial deformation cycles (**Fig. 23 a, b**):

$$\sigma_0^f = \frac{\sigma_{fy}^{M^{m-}} + \sigma_{fy}^{M^{m+}}}{2} = 0. \quad (4.5.14)$$

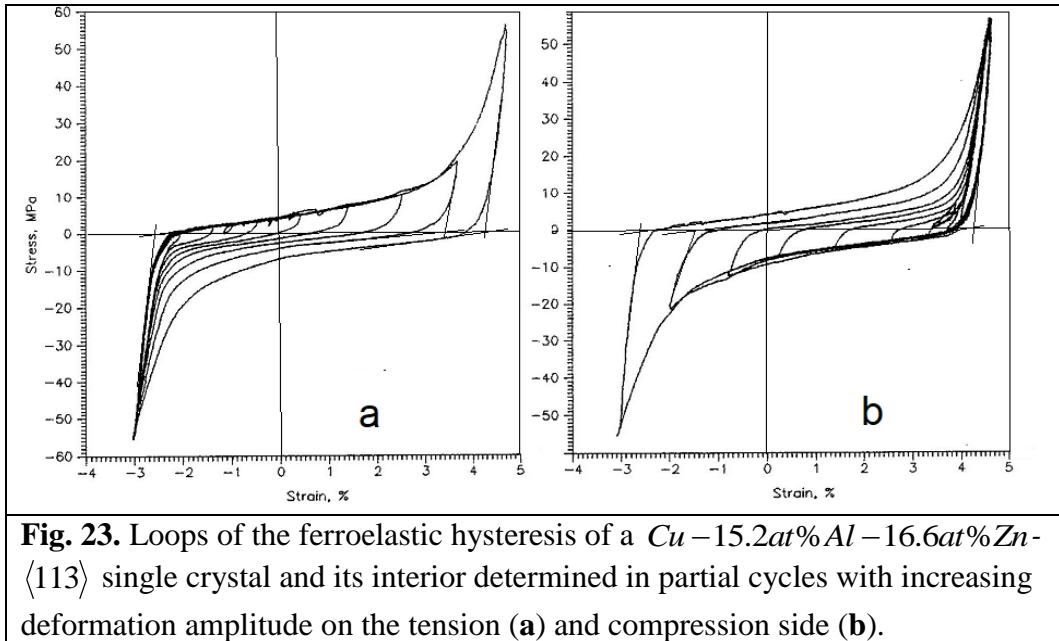


Fig. 23. Loops of the ferroelastic hysteresis of a $Cu - 15.2at\%Al - 16.6at\%Zn - \langle 113 \rangle$ single crystal and its interior determined in partial cycles with increasing deformation amplitude on the tension (**a**) and compression side (**b**).

This also applies to the pseudoelastic hysteresis loops (**Fig. 22 a**), which is a horizontal-right line of the equilibrium stress $\sigma_{p0} = const \neq 0$ or

$$\frac{d\sigma_{p0}}{d\varepsilon_p} = 0 \quad (4.5.7).$$

The energy dissipated in completed cycles of pseudoelastic deformation is also calculated as the area of two triangles:

$$w_D^p(\varepsilon_p) = k_p \cdot \varepsilon_p^2. \quad (4.5.15)$$

These experimental results fundamentally disprove the theoretical speculations [72-77], in which could be calculated a negative slope $\frac{d\sigma_{p0,f0}}{d\varepsilon_{p,f}} < 0$ of the equilibrium lines and a positive slope of the equilibrium lines $\frac{dT_0'}{dz} > 0$ within the thermal hysteresis loop with simultaneous zero values of the thermo- $k_T = 0$, pseudo- $k_p = 0$ and ferroelasticity $k_f = 0$ coefficients. The slopes $\frac{dT_0'}{dz} > 0$ and $\frac{d\sigma_{p0,f0}}{d\varepsilon_{p,f}} < 0$ should also determine the width of the thermo-, pseudo- and ferroelastic hysteresis loops. The thermoelastic component observed in all experiments, i.e. $\frac{dz}{dT} < 0$, $\frac{d\sigma_{p,f}}{d\varepsilon_{p,f}} > 0$ or $k_{T,p,f} \neq 0$ is completely ignored in these theories.

It follows from equations (4.5.13) and (4.5.15) that the pseudoelastic (**Figs. 20 c; 26 HTI**) or ferroelastic (**Fig. 23 a, b**) hysteresis loops are narrower, the smaller the pseudo- or ferroelastic coefficients. This also means that pseudoelastic, oversized wide hysteresis loop with $k_p = 0$ published in [73] is unrealistic. This was constructed by Chinese doctoral student from the hysteresis loop of the same $Cu - 15.2at\% Al - 16.6at\% Zn - \langle 100 \rangle$ single crystal (**Fig. 26 HTI**) by means of a temperature manipulation, which was, however, calculated physically with the help of the Clausius-Clapeyron equation, in order to experimentally prove the unrealistic theory of his german professor, and thereby grant your own doctoral thesis.

The relationship between the stress and the ferroelastic deformation is generally determined by the width of the latent hysteresis loop:

$$\Delta\sigma_l = \sigma_{fy}^{M^{m-}} - \sigma_{fy}^{M^{m+}}, \quad (4.5.16)$$

and the ferroelasticity coefficient k_f is determined as the slope of the two flow lines:

$$\sigma(\varepsilon_f) = \frac{1}{2}\Delta\sigma_l + k_f \cdot \varepsilon_f. \quad (4.5.17)$$

The dissipated energy as the area of the entire hysteresis loop is calculated by integrating the function (4.5.17):

$$w_D^f(\varepsilon_f) = 2 \int_0^{\varepsilon_f} \sigma(\varepsilon_f) \cdot d\varepsilon_f = \Delta\sigma_l \cdot \varepsilon_f + k_f \cdot \varepsilon_f^2 \quad (4.5.18)$$

and supplemented by an additional linear term compared to (4.5.13) and (4.5.15).

The empirical equation (4.5.18) is formally similar to that in theoretical models [84]:

$$d\sigma = d\left(\frac{dF}{d\varepsilon}\right) \pm h d\varepsilon, \quad (4.5.19)$$

where F is the free energy of a deformed solid described by an internal ε and an external σ parameters; h is the dissipation parameters for a general description of a system with friction or with hysteresis.

The first term in (4.5.19) actually corresponds to the stress values, at which equilibrium between austenite and martensite is reached in the isothermal pseudoelastic deformation. The second term describes the deviation of this stress from the equilibrium values due to the hysteretic energy losses. Comparison of the two equations (4.5.19) and (4.5.18) gives:

$$h(\varepsilon_f) = k_f \cdot \varepsilon_f. \quad (4.5.20)$$

This experimentally determined parabolic dependence of the dissipated energy on an internal parameter thus represents a general law for the description of hysteresis and is characteristic, for example, of ferromagnetic hysteresis [80].

4.5.3 Affinity of ferroelastic and ferromagnetic hysteresis

The term "ferroelastic" comes from the affinity of reorientation processes in the polydomain martensitic phase in SMA's and in the polydomain ferromagnetic phase in ferromagnetics in an external uniaxial force field (*the mechanical external stress or the magnetic field*). Even a purely visual comparison of the ferroelastic and ferromagnetic hysteretic behavior (**Figs. 24 a, b or 24 b and 40 a**) justifies the assumption about their affinity and their common mechanisms.

In order to better illustrate this affinity, the ferroelastic hysteresis loops in these figures are shown in a ferromagnetic axis arrangement that is unusual for mechanical hysteresis: deformation $\vec{\varepsilon}_f$ as the ordinate like magnetic induction \vec{B} and stress $\vec{\sigma}$ as the abscissa like magnetic field strength \vec{H} . So, you can see that the two hysteresis loops, which at first appearance come from physically very different areas, are affine down to their last interior detail.

But the two phenomena are not that different either, because the two hysteresis are due to the energy dissipation caused by the movement of domain boundaries during their reorientation: In SMA's this is the reorientation of martensite micromonodomains and in ferromagnetics from Weiss areas (*microdomains*). Because of this, the theoretical models [78, 80] and terms developed for some time in the field of ferromagnetism can also be used for the description and understanding of ferroelastic hysteresis, such

as these, e.g., which are adopted in [81].

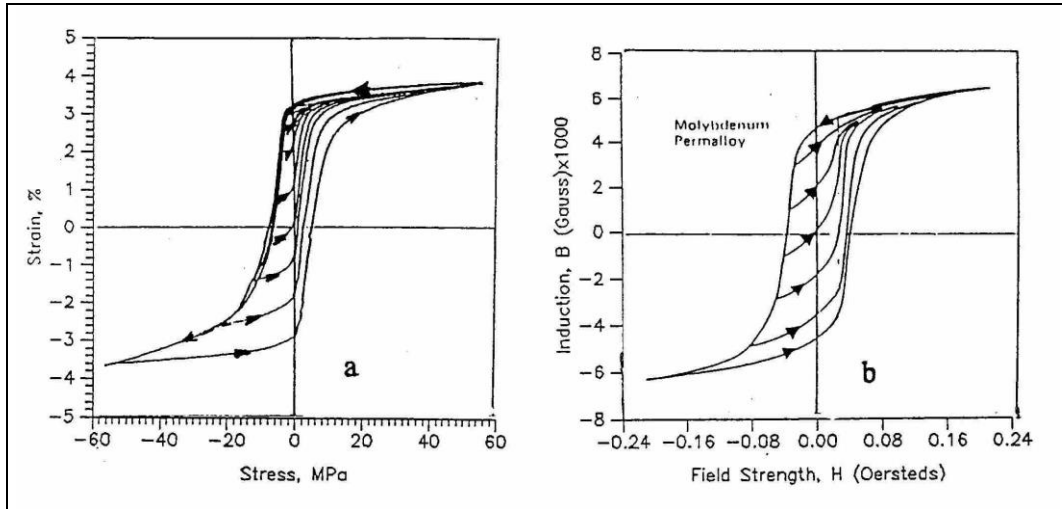


Fig. 24. Affinity of the ferroelastic hysteresis of a $\text{Cu}-15.2\text{at}\% \text{Al}-16.6\text{at}\% \text{Zn}-\langle 113 \rangle$ single crystal (a) and the ferromagnetic hysteresis of a molybdenum permalloy ferromagnetics [78, 79] (b).

A ferromagnetic hysteresis loop (**Fig. 24 b**) shows the relationship between the magnetic induction \vec{B} and the magnetic field strength \vec{H} , similar to the ferroelastic hysteresis loop (**Fig. 24 a**) the relationship between the ferroelastic deformation $\vec{\varepsilon}_f$ and the external mechanical stress $\vec{\sigma}$:

$$\vec{B} = \mu \cdot \vec{H} \propto \vec{\varepsilon}_f = \kappa \cdot \vec{\sigma}, \quad (4.5.21)$$

where μ is the magnetic permeability and $\kappa = G^{-1}$ is the mechanical compressibility (4.4.5). The residual magnetization B_R (also called remanence) and the coercive force or coercive field strength H_c are the most important characteristics of ferromagnetic hysteresis [78].

In the case of ferroelastic hysteresis, the ferroelastic deformation that the specimen has after the external field has been switched off, i.e. remains in the specimen after the external stress is set to zero, corresponds to the residual magnetization. The ferroelastic residual deformation (*ferroelastic remanence*) can be represented as a half of the deformation amplitude $\Delta\varepsilon_f$

of the ferroelastic hysteresis when assuming the symmetry of the tensile and compression deformation:

$$\varepsilon_f^+ = |\varepsilon_f^-| = \frac{\Delta\varepsilon_f}{2} . \quad (4.5.22)$$

The pseudoelastic hysteresis loops are not always symmetrical relative to the stress coordinate axis (**Fig. 22 a**). In the case of the stress-induced martensitic transformation, lamellae are observed in the light microscope, which build to the single crystal specimen longitudinal axis $\langle 100 \rangle_{B2}$ the angle 45° at the tension stress and 30° at the compression one. This discrepancy naturally changes the relationship between the normal and tangential stresses acting in the shear plane (4.5.24) in the cases of tension and compression.

The ferroelastic hysteresis loops of single crystals with a favorable orientation $\langle 100 \rangle_{B2}$ nevertheless show symmetry relative to the tensile and compressive effects (**Figs. 22 c; 23 a, b; 24 a, c**). Because of this, the internal stresses within a ferroelastically deformed (“magnetized”) SMA specimen can be estimated. These stresses must be compensated by the external stress of the opposite sign so that the ferroelastic residual deformation is recovered. The stress value is then measured as half the stress amplitude $\Delta\sigma_f$ of the ferroelastic hysteresis loop:

$$\sigma_f^+ = |\sigma_f^-| = \frac{\Delta\sigma_f}{2} . \quad (4.5.23)$$

This stress value corresponds to the sense of the coercive field strength in ferromagnetic materials. The coercive field strength is known as a characteristic of the magnetic hardness of ferromagnetic materials.

The coercive field strength of ferromagnetic materials and the hysteresis, which corresponds to the frictional energy losses during magnetization, are due to the pinning of magnetic domain boundaries by structural defects [80]. The resulting friction leads to the residual magnetization because it prevents the return of the magnetic domains to their initial state after the external field has been switched off. The initial state also corresponds to the indifferent equilibrium of magnetic monodomain mixture, as demonstrated by the position, parallel to the magnetization coordinate axis, of intersections of the internal "elasticity lines" with the "flow lines" of the magnetization curves in partial cycles (*Fig. 24 b*).

The mechanical coercive field strength reflects the quantity of the dissipative, hysteretic losses due to the friction during the ferroelastic deformation and is described by the ferroelastic coefficient (4.5.10). It is caused by the blocking of the micromonodomain or twin boundaries by structural defects [80, 87, and 88], i.e. by increasing the stacking fault energy.

The absence of temperature dependence found for the shape and size of the ferroelastic hysteresis loop is also known for ferromagnetic hysteresis. Another common feature of the two hysteresis behaviors is the natural orientation dependency of their hysteresis for the vector fields (*field strength, stress*). The dependence of the resulting martensitic deformation on the orientation of the longitudinal specimen axis is due to the nature of the martensitic shear deformation and has been proven several times experimentally.

Such orientation dependency was investigated and found on the polycrystalline *Ti–50.5at%Ni* specimens textured by rolling [85]. The test specimens were cut out of a rolled strip with the texture $(112)[\bar{1}10]$, determined by *X*-ray method, in such a way that their longitudinal specimen

axes build different angles to the rolling direction. In thermal cycles under constant load, these specimens showed the quasiplastic hysteresis loops with different widths, with different transformation temperatures and with different maximal quasiplastic deformations (**Fig. 25 a**).

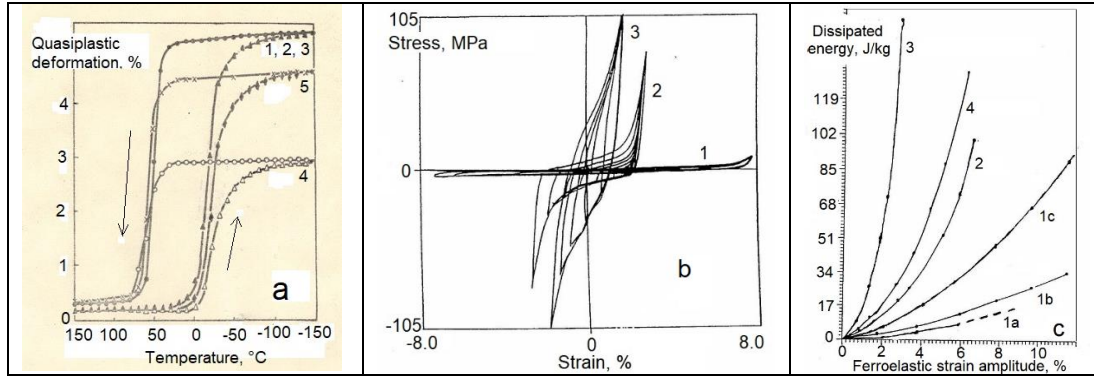


Fig. 25. a - influence of the rolling texture $(112)[\bar{1}10]$ of rolled polycrystalline $Ti - 50.5at\%Ni$ - specimens with different orientations of the longitudinal axis relative to the rolling direction 0° (1); 22.5° (2); 45.0° (3); 67.5° (4); 90.0° (5) and their quasiplastic deformation under constant load [85]; **b** - Influence of the orientation of $Cu - 15.2at\%Al - 16.6at\%Zn$ single crystals with orientations of the longitudinal axis $\langle 100 \rangle$ (1), $\langle 113 \rangle$ (2), $\langle 111 \rangle$ (3) on their ferroelastic deformation as well as on the ferroelasticity coefficient and thus (4.5.13) on the dissipated energy (**c**, *the same numbering*) including the values (4) calculated from the pseudoelastic hysteresis of the single crystals with the same composition and orientation in work [73] as well as those of $Cu - 15.2at\%Al - 16.6at\%Zn - \langle 100 \rangle$ single crystals after different aging times: fresh quenched from $850^\circ C$ into cold water (1a), after storage at room temperature for $24h$ (1b) and for one month (1c) [10, 12, and 14].

The orientation dependency of the shape and the size of the ferroelastic hysteresis loops can naturally be seen most clearly in single crystals. This was investigated on $Cu - 15.2at\%Al - 16.6at\%Zn$ single crystals with longitudinal axes orientations $\langle 100 \rangle_{B2}$, $\langle 113 \rangle_{B2}$ and $\langle 111 \rangle_{B2}$ (**Fig. 25 b**).

If the orientation deviates from the cubic axis $\langle 100 \rangle_{B2}$ to the axis $\langle 111 \rangle_{B2}$ via the orientation $\langle 113 \rangle_{B2}$, the ferroelasticity coefficient increases drastically, while the martensitic deformation decreases. The square of the ferroelastic hysteresis loop also increases, despite the substantial reduc-

tion in its deformation amplitude. Based on ferromagnetic materials, the axis $\langle 100 \rangle_{B2}$ can related to the ferromagnetics be considered as the axis of the lightest ferroelastic deformation, along which maximal deformation is achieved with minimal dissipative energy loss (*minimal work*).

The pseudoelastic hysteresis shows the same orientation dependency: The equilibrium stress and pseudoelasticity coefficient increase when the longitudinal axis deviates from the orientation of the lightest deformation $\langle 100 \rangle_{B2}$ whereas the deformation amplitude decreases. If the experimental σ_0 - and ε_p -values are used in the calculation of the transformation entropy in (4.5.8), the result is the constant entropy value as a scalar, which neither depends on the single crystal orientation nor on polycrystal anisotropy [82], and is approximately equal to the calorimetrically determined entropy value.

The dissipated energy (*Fig. 25 c*), which is a parabolic function of the deformation amplitude (4.5.13), (4.5.18), is essentially determined by the ferro- or pseudoelasticity coefficient. The increase in the ferroelastic coefficient when deviating from the crystallographic direction $\langle 100 \rangle_{B2}$ is related to the increase in the frictional force in the shear plane $(100)_{B2}$ due to the increase in the normal stress component.

This component acts on the shear plane and generates a bending moment on the habit plane of a martensite polydomain (§3.2.3), which is an invariant plane. The distortion of the invariant plane leads to the expansion of the mechanical hysteresis loop [86]. The normal σ_N and tangent τ components of the maximal shear stress τ_{\max} that act in the planes at an angle 45° to the longitudinal specimen axis depend on the angle α be-

tween the habitus plane observed in the light microscope and the longitudinal specimen axis:

$$\begin{aligned}\sigma_N &= \tau_{\max} \cdot \sin(\alpha - 45^\circ) \\ \tau &= \tau_{\max} \cdot \cos(\alpha - 45^\circ)\end{aligned}\quad (4.5.24)$$

The analysis of this dependences shows that for single crystals with orientation $\langle 100 \rangle_{B2}$ ($\alpha = 45^\circ$) the normal component is zero and the tangent component is maximal. When it comes to orientation $\langle 111 \rangle_{B2}$, the both are

the same: $\sigma_N = \tau = \frac{\sqrt{2}}{2} \cdot \tau_{\max}$.

The determined orientation dependence also supports the common character of the hysteretic behavior of ferromagnetics and SMA's. The orientation dependence of the non-elastic properties of SMA's naturally follows from the crystallographic reversibility of the martensitic transformation as a cooperative atomic displacement in certain shear systems, as well as from the mechanism of the non-elastic deformation. The mechanism consists in the monodomainization of the martensitic polyvariant polydomain phase through the growth of martensite variants favorably oriented relative to the external stress at the expense of the unfavorably oriented variants. Such reorientation also takes place through the shear movement of partial dislocation in certain shear systems. These are responsible for the formation of twins, of which consists a martensite polydomain (*Fig. 2 b*).

One of the two twin parts has been defined here as a martensite micromonodomain, i.e. as an elementary area of the martensitic phase, within the framework of which the martensitic shear direction does not change, and which is regarded as a carrier of the maximal martensitic deformation – the lattice shear deformation γ_M . Such a definition of the martensite mi-

cromonodomain corresponds to the definition of the magnetic monodomain (*Weiss domains in the Ising model of ferromagnetism* [89]), within which the direction of all magnetic moments on atoms remains constant. Such a monodomain is accordingly the minimal microcarrier of its own internal magnetization or of its own martensitic deformation.

5 Observations and evidence of martensite monodomains transformations

In this chapter, observations of the transformations from martensite micromonodomains to martensite macromonodomains and their transformation into austenite are presented and discussed in a wide variety of experiments.

5.1 Transformation with a single phase boundary

5.1.1 Equilibrium and stationary conditions

The hysteretic behavior of $Cu - Al - Zn$ -SMAs depends essentially on its heat treatment, which is firstly related to the $B2 \rightarrow DO_3$ -transformation between two austenite phases [50] and secondly to the composition, which is far away from both the $B2$ and DO_3 stoichiometries. That causes a lot of excess, non-equilibrium vacancies in the Cu -based SMA's.

The usual heat treatments [14] contain, as a first common step, annealing at $850^\circ C$ for $0.5h$, which homogenizes the $B2$ ordered austenite. The following heat treatment variants are then possible:

HTI: (*standard heat treatment*) $B2 \rightarrow DO_3$ transformation suppressive quenching in oil at $150^\circ C$, the equilibrium distribution of excess vacancies promoting aging at $150^\circ C$ during $0.5h$ and quenching in water at the room temperature;

HTII: Both the $B2 \rightarrow DO_3$ transformation and the equilibrium distribution of excess vacancies promoting cooling with the furnace to the room temperature;

HTIII: Both the $B2 \rightarrow DO_3$ transformation and the equilibrium distribution of excess vacancies suppressive quenching into cold water.

The three methods of heat treatment fundamentally influence the behavior of single crystals (**Fig. 26** HTI, HTII, and HTIII).

The first heat treatment (HTI) causes a very narrow loop of the pseudoe-

lastic hysteresis with the pseudoelastic coefficient $k_p \rightarrow 0$ (**Fig. 26 HTI**). The stress-induced martensite in $Cu-15.2at\%Al-16.6at\%Zn-\langle 100 \rangle$ single crystals shows in the light microscope the lamellae that are parallel to each other and build an angle of 45° to the longitudinal specimen axis. These lamellae were interpreted above (§4.5.2) as a martensite micromonodomain oriented in one and the same direction.

The pseudoelastic deformation increases by increasing the lamellae density without their noticeable growth (*heterogeneous transformation*) until they grow together into several and finally into a single martensite macromonodomain. This morphology is a model of the interaction and coalescence of the $A'M^{m+}$ phase boundaries and their transformation into the internal martensitic $M^{m+}M^{m+}$ monodomain boundaries, similar to those considered above in §3.2.2 for the thermos-induced transformation.

The second heat treatment (**HTII**) increases the critical stress of the stress-induced martensitic transformation (**Fig. 26 HTII**). Overcoming the yield point $\sigma_{py}^{A'M^P}$ and increasing martensitic deformation are accompanied by a stress drop. The sudden stress drop is caused by the formation of a martensite band (*homogeneous transformation*) against the background of the fine martensite lamellas.

The light microscopic observations during temperature changes under constant load or during the tension-compression deformation under constant temperature (**Fig. 22 d**) showed that the narrow lamellae are still formed in the elastic range, do not lead to any macroscopic deformation, and, therefore, they are interpreted as martensite micromonodomains oriented in opposite directions or as twin areas consisting of several marten-

site micromonodomains within the metastable austenite in the premartensitic state.

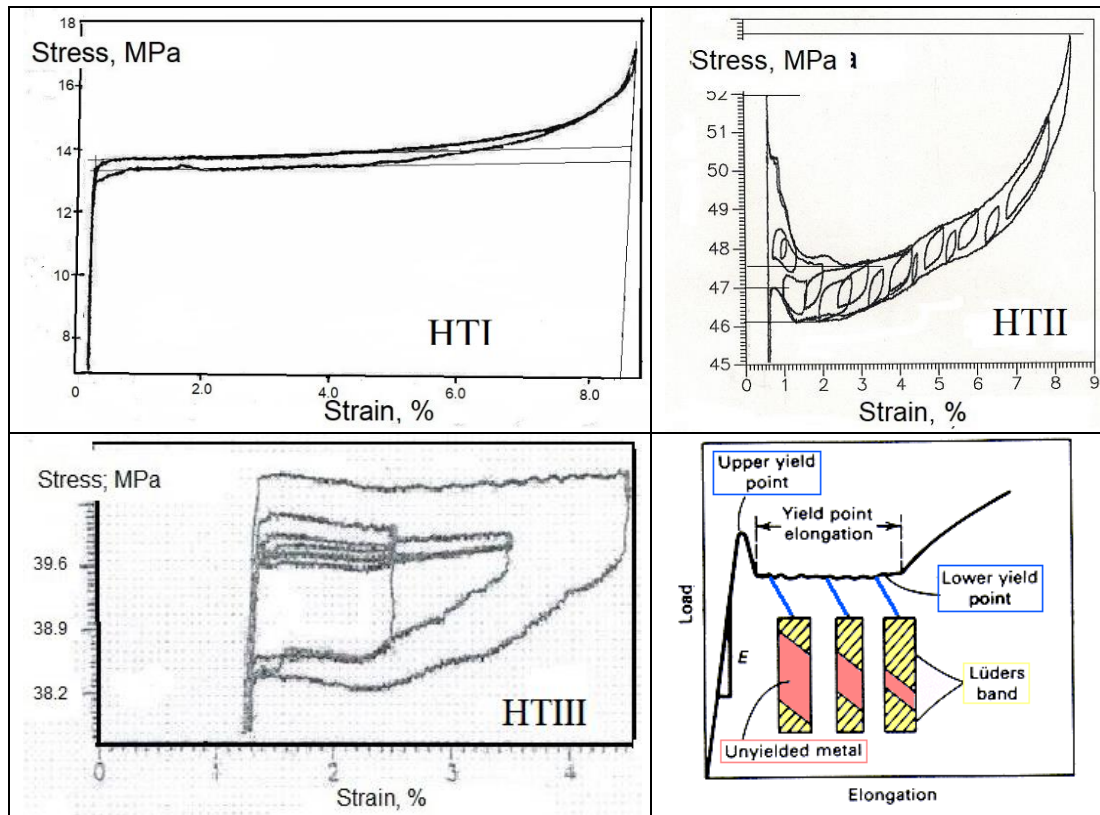


Fig. 26. Pseudoelastic hysteresis loops of $Cu - 15.2at\%Al - 16.6at\%Zn - \langle 100 \rangle$ single crystals after various heat treatments listed above. Schematic representation of the stress-strain diagram in the case of plastic deformation due to the formation and spread of Lüders bands [91].

The fresh quenched specimens (*HTIII*) show very unstable loops of the pseudoelastic hysteresis (**Fig. 26 HTIII**). If the specimen loading is stopped during deformation, and the specimen is held under these conditions (*constant deformation, constant temperature*), the stress on the specimen decreases depending on the holding time and the preload, so that the reverse transformation takes place during the subsequent unloading at lower stresses.

Such stress relaxation is due to the diffusion of non-equilibrium vacancies in the gradient of mechanical stresses in the crystal lattice. The time-dependent relaxation processes are described by the kinetic Arrhenius

equation:

$$\sigma(t) = \sigma_0 \cdot e^{-\frac{E_A}{R \cdot T}}, \quad (5.1.1)$$

where σ_0 is the initial stress, R is the universal gas constant, $E_A [J \cdot kg^{-1}]$ is the activation energy of the process responsible for the relaxation. This energy can be determined as the negative slope of the Arrhenius graph $\ln \sigma = f(T^{-1})$ if the tests (**Fig. 26 HTIII**) are carried out at different temperatures and the stress decreasing over the same time is determined every time. Such expansion of the hysteresis is known as martensite stabilization in these alloys [90] and is explained by the redistribution of the excess quenching non-equilibrium vacancies.

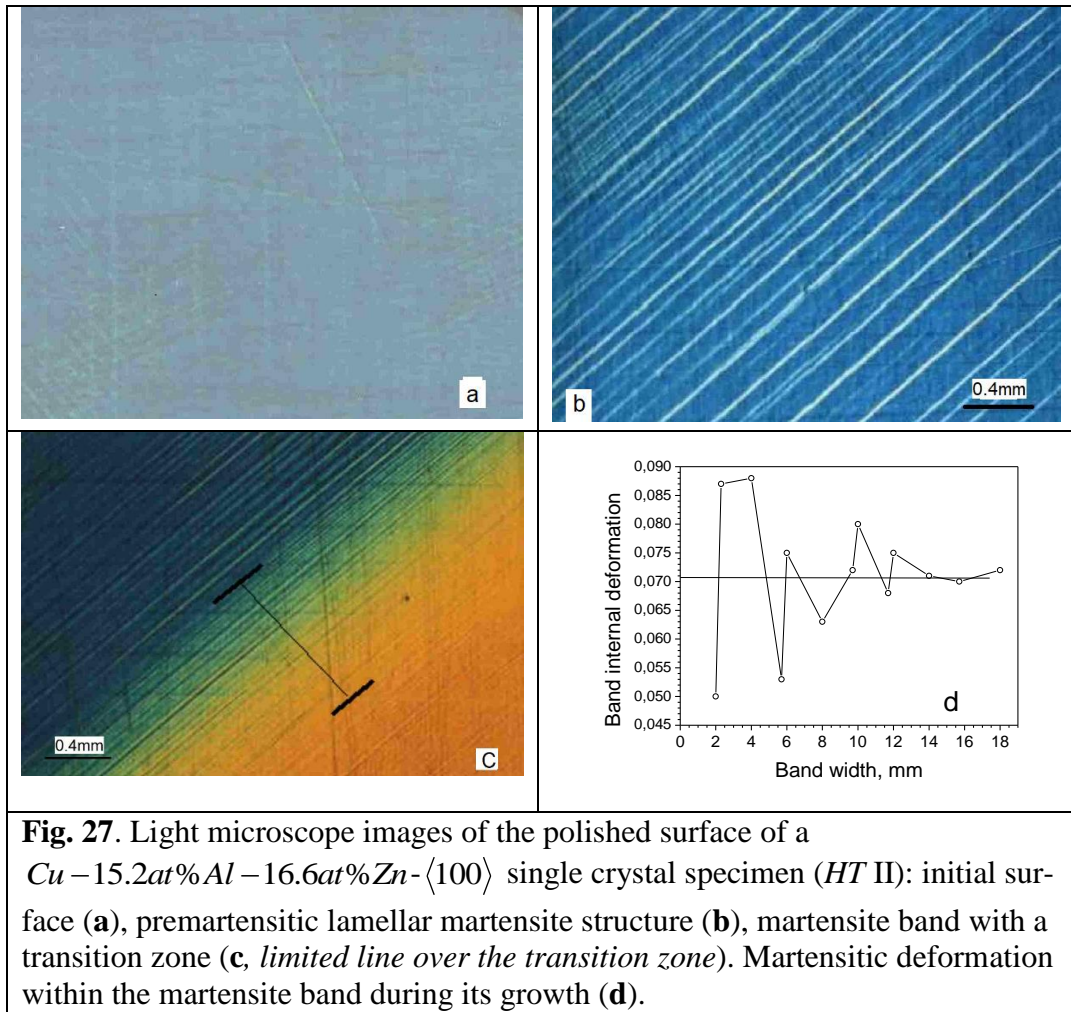
Formation of martensite lamellae and a martensite band was observed directly (**Fig. 22 d**) in the light microscope both during pseudoelastic deformation at a constant temperature (*isothermal condition*) $\varepsilon_M(\sigma)|_T$ (**Fig. 26 HTII**) and during cooling under constant load (*isostress condition*) $\varepsilon_M(T)|_\sigma$ the same single crystal specimens after the same heat treatment HTII (**Figs. 27 a-c**) [5].

In this process, narrow martensite lamellae initially appeared on the polished specimen surface (**Fig. 27 a**) at a temperature $T > T_0'$ during the slow, step by step cooling (**Fig. 27 b**). Their density:

$$\delta^l = \frac{n_l \cdot \bar{b}_l}{L}, \quad (5.1.2)$$

where n_l is the lamellae number, \bar{b}_l is the average lamellae width, and L is the specimen length, increased continuously with further cooling without causing any macroscopic specimen deformation (**Fig. 28 a**). When the la-

mellae width and the distance between the lamellae became the same on average, i.e. $z_{cr}^l \approx 1/2$ a martensite band with a critical width $B_{cr}^M \approx 2mm$ (**Fig. 27 c**) was built at a position with the said maximal critical lamellae density.



The critical phase fraction of martensite lamellae $z_{cr}^l \approx 1/2$ corresponds exactly to the critical z_0 -value, at which the maximal coalescence probability (3.2.8) is reached, and the system becomes unstable:

$$\frac{d\phi_c(z)}{dz} = 1 - 2z = 0, \quad z_0 = \frac{1}{2} \quad \text{and} \quad \frac{d^2\phi_c(z)}{dz^2} = -2 < 0.$$

After the band formation, a single boundary of the martensite band

moved away over the lamellae field with a velocity of:

$$\dot{B}_M = \frac{1}{\varepsilon_M} \cdot \frac{d(\Delta L)}{dt} \approx (1 \div 2) \cdot 10^{-4} \text{ m} \cdot \text{s}^{-1}. \quad (5.1.3)$$

The martensitic deformation ε_M within the martensite band was calculated as the ratio of the machine-measured sample elongation ΔL to the band width B_M measured in the light microscope at the same time:

$$\varepsilon_M = \frac{\Delta L}{B_M}. \quad (5.1.4)$$

The internal deformation changes sharply (**Fig. 27 d**) between 0.050 and 0.088 at the beginning of the band growth, where the ratio between the width b_{tr} of the transition zone with $0 < \varepsilon_M < 0.08$ and the band width B_M is still comparably large $\frac{b_{tr}}{B_M} > 0.1$, and at the end ($\frac{b_{tr}}{B_M} \ll 0.1$) fluctuates around the value of $\varepsilon_M \approx 0.07$. This internal deformation also corresponds to the total deformation of the specimen at the end of the martensitic transformation, if $B_M = L$ and $\frac{b_{tr}}{B_M} = 0$. These data suggest that the martensite band is a martensite macromonodomain.

The single martensite band boundary moves spontaneously while the outside temperature remains constant. The specimen temperature was lowered step by step (*each* 1°C), kept constant for one minute until a stationary state was reached, and then lowered further (**Fig. 28 a**), until the spontaneous temperature elongation in one of the next steps caused by the martensite band formation begins as a spontaneous isostress-isothermal ($P = 20\text{N} = \text{const}$, $T = 12.1^\circ\text{C} = \text{const}$) martensitic deformation of the specimen with a starting temperature that is then kept constant (**Fig. 28 a**)

and increases to its maximal value (*Fig. 28 b*).

The temperature $A_s = 13.9^\circ\text{C}$ was sensed in the same way during step by step heating and also kept constant after the onset of the martensitic deformation recovery. On the way between M_s - and A_s - temperatures, the indifferent equilibrium was reached at an equilibrium temperature T_0' , in which the martensite band boundary creeps back and forth or stops at the constant temperature $T = T_0' \approx 12.7^\circ\text{C}$, so that the martensitic deformation increases and decreases (*Fig. 28 b*).

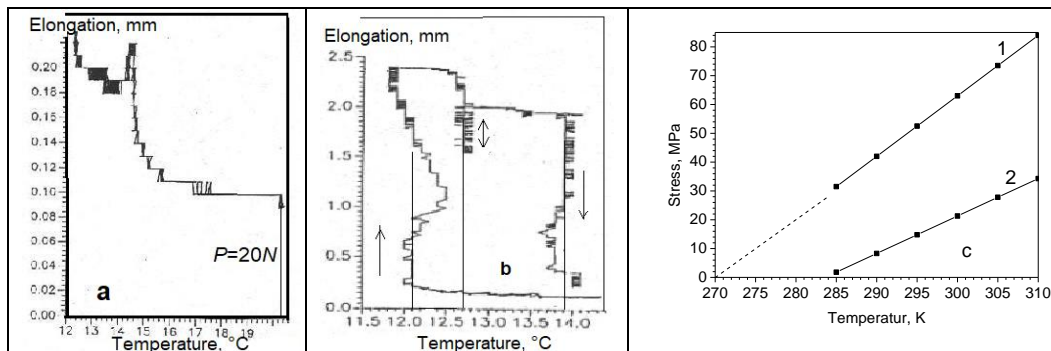


Fig. 28. Elongation-temperature diagrams ($\Delta L - T$) of a $\text{Cu} - 15.2\text{at}\% \text{Al} - 16.6\text{at}\% \text{Zn} - \langle 100 \rangle$ single crystal (*HT II*) in the premartensitic temperature range of the lamellae formation during step by step cooling (**a**), isostress-isothermal deformation (*up to an elongation of approx. 1.8mm*) due to the growth-shrinkage of the martensite macromonodomain (**b**), temperature dependency of the critical stresses (**c**) of the martensite band formation (1) and the martensite lamellae appearance (2) during cooling under various constant loads.

At the critical martensite lamellae density $\delta_{cr}^l = 1/2$, the neighboring mutually oriented α -martensite micromonodomains or martensite twins upset. They build under constant load the martensite band as a martensite macromonodomain, the growth of which occurs through the upsetting of the remaining micromonodomains like the domino effect at approximately the same velocity as at isothermal loading. The upsetting of martensite micromonodomains is registered as the sharply change in the martensitic deformation within the martensite band.

Linear dependencies of the yield points $\sigma_{py}^{M^l}(T)$ for the martensite lamellae appearance (**Fig. 28 c, line 2**) and $\sigma_{py}^{M^B}(T)$ for martensite band formation (**Fig. 28 c, line 1**) on the temperature were determined at various constant loads. The extrapolation of the both lines to $\sigma = 0$ gives the equilibrium temperatures $T_0^{A'M^l} = 284K$ between the metastable austenite and the martensite lamellae (*micromonodomains*) and $T_0^{M^lM^B} = 270K$ between the martensite lamellae and the martensite band (*macro-monodomain*).

The $(A' \rightarrow A'+M^l)$ -transformation entropy calculated from the Clausius-Clapeyron equation (2.1.7) $\Delta s^{A' \rightarrow A'+M^l} = 14.0J/kg \cdot K$ is smaller than the entropy $\Delta s^{A'+M^l \rightarrow M^B} = 22.4J/kg \cdot K$ of the $A'+M^l \rightarrow M^B$ -transformation, i.e. $S^{M^l} > S^{M^B}$. Calculation of the latent transformation heat from these data gives values $\Delta q^{A' \rightarrow A'+M^l} = 3976.0J/kg$ and $\Delta q^{A'+M^l \rightarrow M^B} = 6048.0J/kg$. The entropy and heat values of the $A'+M^l \rightarrow M^B$ -transformation agree with those for the $B2 \rightarrow 9R$ -transformation which were determined calorimetrically on the same $Cu - 15.2at\% Al - 16.6at\% Zn$ single crystals after the HTI heat treatment.

The critical phase fraction $z_{cr}^l = 1/2$ of the martensite lamellae also results from the analysis of the unstable equilibrium (3.2.11) of martensite polydomains with the elastic interaction energy $U_{el}(z) = K_{el} \cdot z(1-z)$:

$$\frac{dU_{el}}{dz} = K_{el}(1 - 2z_{cr}^l) = 0, \quad z_{cr}^l = 1/2, \quad \frac{d^2U_{el}}{dz^2} < 0. \quad (5.1.5)$$

So, the analysis shows that the elastic stored energy of martensite lamellae reaches its maximum at a critical density $\delta_{cr}^l = \frac{n_l \cdot b^l}{L} = \frac{m^{M^l}}{m} = z_{cr}^l = \frac{1}{2}$ and thus the unstable equilibrium.

5.1.2 Equilibrium disturbance, dynamic conditions and structures

The building of a homogeneous martensite band in this unstable state minimizes the number of $A^l M^l$ phase boundaries and thus the elastic energy of the two-phase system, without increasing the energy of the martensite through the formation of internal martensitic $M^l M^l$ domain boundaries. This leads to a positive slope $\frac{dz}{dT} > 0$ of the transformation trajectory due to increasing the equilibrium temperature $T_0'(z)$.

As a result, the stored elastic energy is dissipated as the acoustic emission and heat, with the subtraction of the energy used to upsetting the remaining martensite micromonodomains and to transform the remaining austenite (**Figs. 28 b and 29 a, b**).

The exothermic and endothermic temperature changes measured by a thermocouple placed directly on the surface in the middle of the specimen are approx. $(0.4 \div 0.2)K$ for isothermal ($\dot{T} = 0$, **Fig. 28 b**) and approx. $2K$ for adiabatic ($\dot{T} = 1K/s$, **Figs. 29 a, b**) band growth and shrinkage. The released Joule heat is $q_J = c_p \cdot \Delta T \approx 115J/kg$ for isothermal and approx. $230J/kg$ for adiabatic conditions and is thus much smaller than the latent transformation heat calculated above, which is completely dissipated into

the environment under these stationary transformation conditions ($\dot{T} = 0, \dot{\sigma} = 0$).

The energy 115J/kg corresponds rather to the height (**Fig. 3**) of the energy barrier F_B (3.1.5), which has to overcome the martensite band boundary that grows by upsetting single martensite micromonodomains. This energy is released after crossing the barrier. The energy barrier is so low $F_B \rightarrow 0$ that the martensite boundary is in an almost indifferent equilibrium on the flat bottom of the potential function $F(\bar{e})$ (**Fig. 3**) in the range $0 < \bar{e} < 1$. The martensite boundary moves during the slow heating process at the same temperature 10.4°C (**Fig. 21 a**), 12.7°C (**Fig. 28 b**) and 11.9°C (**Fig. 29 b**) forwards (*lengthening*) or back (*shortening*).

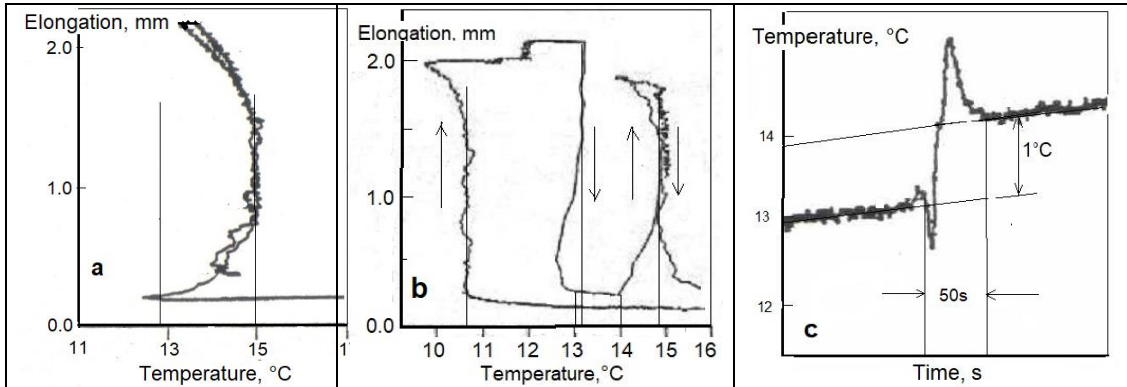


Fig. 29. Change in length $\Delta L(t, T)$ of a $\text{Cu} - 15.2\text{at}\% \text{Al} - 16.6\text{at}\% \text{Zn} - \langle 100 \rangle$ single crystal (*HTII*) due to adiabatic growth-shrinkage of the martensite band (**a**), indifferent equilibrium at the temperature $T \approx 12^\circ\text{C}$ and disturbance of the indifferent equilibrium through an elastic impulse (**b**), temperature jumps $\Delta T(t)$ in the dynamic range at the equilibrium disturbance (**c**).

If the indifferent equilibrium ($\frac{d^2 F}{de^2} \approx 0$) is disturbed by an elastic impulse, e.g. by a light click on the *Cu*-thermostat, on which the sample is lying, the martensite boundary goes completely crazy: It flies forward and reverse at multiple velocity of $(0.8 \div 1.1) \cdot 10^{-3} \text{m} \cdot \text{s}^{-1}$ through the entire

length of the sample with gaudy acoustic signals at the turning points (**Fig. 29 b, right**) and at first appearance ignores all physical laws. The $(\Delta L - T = -)$ -diagram shows a negative hysteresis ($A_s < M_f$), so that a temperature jump appears on the $(T - t)$ -diagram (**Fig. 29 c**), which can only be explained by a heat capacity jump and, according to the Ehrenfest classification, would only be expected for the 2-nd order phase transformations. Such behavior of the single-phase boundary is similar to the formation and movement of a soliton theoretically described by Falk [43].

It can at that transformation be the talk neither about a specific local equilibrium temperature T_0' nor about a hysteresis in the usual sense, let alone about any approaches of the thermoelasticity model. Even under the same stationary conditions, the martensite band is formed at different temperatures in the range of $(10 \div 14)^\circ\text{C}$. The width of the hysteresis also changes without recognizable laws in the range from $(1 \div 2)^\circ\text{C}$ to 0°C under dynamic conditions (**Fig. 29a**) or even in the negative range (**Fig. 29b**).

The “lawless” behavior of the martensite macromonodomain, which is neither controlled by temperature ($\varepsilon_M \neq f(T)$) nor by external stress ($\varepsilon_M \neq f(\sigma)$), is possibly to explain by the uncertainty of the Clausius-

Clapeyron ratio (2.1.7) at $\frac{\Delta s^{AM^m} \rightarrow 0}{\Delta \varepsilon_M \rightarrow 0}$ for the almost 2-nd order transi-

tions (**Fig. 28c**), to which $A' \leftrightarrow M^m$ austenite-martensite macromonodomain transformation may belong. On the other hand, the behavior of the martensite macromonodomain is not so lawless at all if it is considered relative to the behavior of the excited interaction potential as their reference system.

The band kinetics of the homogeneous martensitic transformations after the heat treatment HTII can be associated with the heterogeneous $B2 + DO_3$ austenite mixture in the high temperature range, as the TEM-investigations show (*Figs. 30 a, c, d*). The dark-field images in reflections from both austenite phases show a homogeneous distribution of the both phases through the specimen volume (*Figs. 30 c, d*), which results from slow cooling through the temperature range of the DO_3 -ordering [50]. The partial rearrangement of the $B2$ -phase into the DO_3 -phase (*Fig. 30 a*) is energetically favorable, since it minimizes the concentration of excess non-equilibrium vacancies of the Cu -based SMA's with the composition between two stoichiometries.

Calorimetric data show in these samples approximately halved values of the $B2 \leftrightarrow 9R$ transformation entropy compared to the $Cu - Al - Zn$ -specimens treated according to the HTI and HTIII methods. The entropy difference can be explained by the transformation of only the $B2$ -phase into the $9R$ -martensite, the phase fraction of which $Z^{B2} = \frac{m^{B2}}{m^{B2} + m^{DO_3}}$, similar to (4.2.15), should be around of 60%, while all calorimetric parameters are calculated by dividing the measured values by the specimen mass $M = m^{B2} + m^{DO_3}$.

This means that, for example, the measured transformation entropy depends not only on the martensite phase fraction $z^{9R} = \frac{m^{9R}}{m^{B2}}$, but also on the austenite phase fraction Z^{B2} :

$$\Delta s(z, Z) = \frac{\left(q^{A'M^m} + \left| q^{M^m A'} \right| \right) \cdot z^{9R} \cdot Z^{B2}}{2T_0} \quad (5.1.6)$$

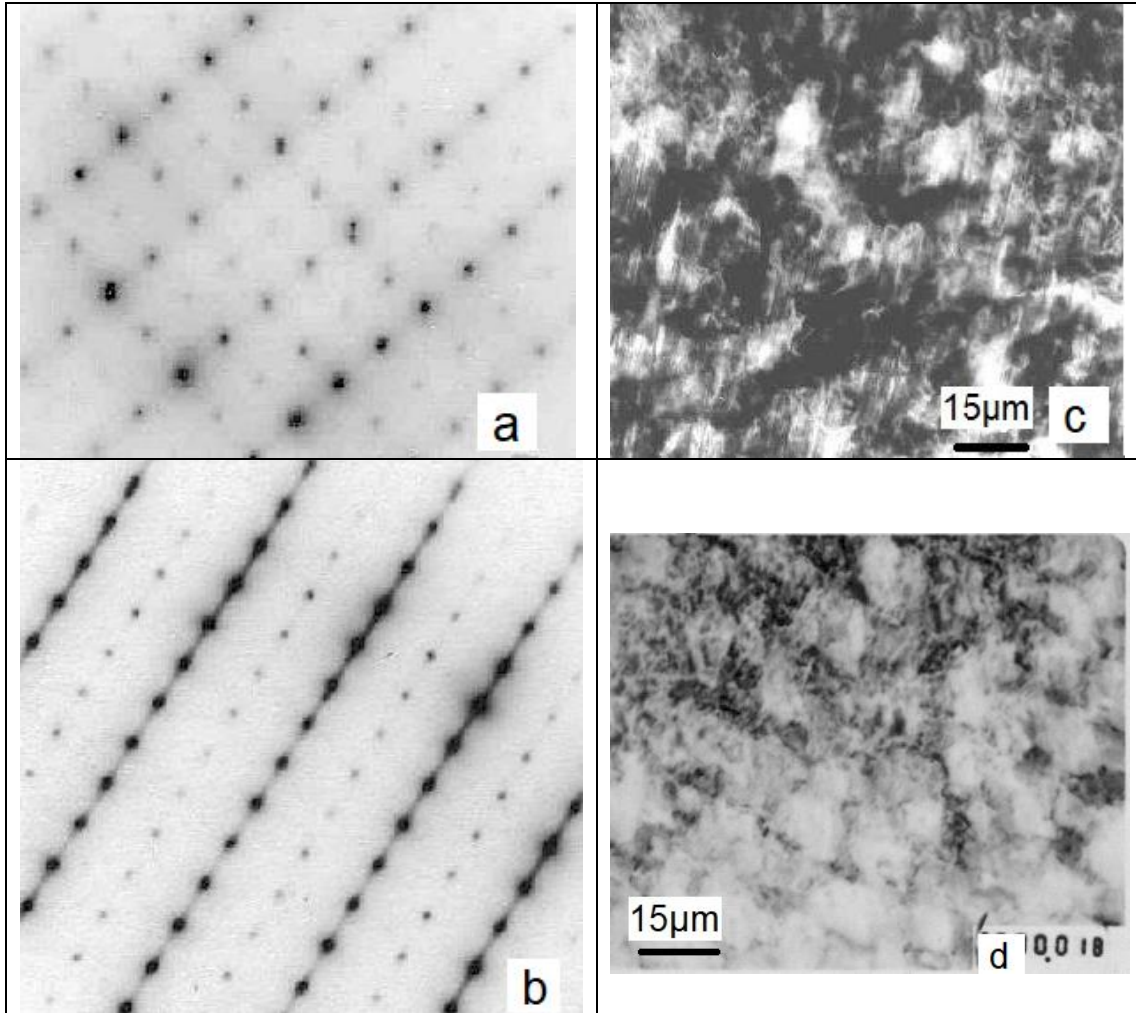


Fig. 30. Electron diffraction from the $B2 + DO_3$ austenite mixture of $Cu - 15.2at\%Al - 16.6at\%Zn$ single crystals ($HTII$), foil surface $(100)_{B2}$ (a) and from $9R$ -martensite, foil surface $(110)_{9R}$ in tetragonal axes (b); Dark field images in reflections $(100)_{B2}$ (c) and $\left(\frac{1}{2} \frac{1}{2} 0\right)_{DO_3}$ (d).

If the transformation entropy $\Delta s^{A'M^p}$ for the 100% sample corresponds to the complete $B2 \rightarrow 9R$ martensitic transformation, a transformation incompleteness parameter k_c can be introduced similar to (4.2.14):

$$k_c = \left(1 - \frac{\Delta s}{\Delta s^{A'M^P}} \right). \quad (5.1.7)$$

This parameter is equal to the phase fraction of the unconverted DO_3 -austenite. This rule can be applied not only to the composite structure of the $B2 + DO_3$ austenite, but also generally to a transformation, which for whatever reason is incomplete.

The stress drop in the stress-strain diagram (**Fig. 26 HTIII**) is due to the fact that the velocity $3 \cdot 10^{-4} s^{-1}$ calculated from the $\Delta L(t)$ -diagrams (**Fig. 46 a, b**) also measured depends on the deformation caused by the explosive formation of the martensite band and its expansion, the constant deformation velocity $2 \cdot 10^{-5} s^{-1}$ of the tension-compression-machine exceeds more than an order of magnitude and can first no longer be controlled by the external stress.

So, different kinds of transformation kinetics of the same $Cu - 15.2at\%Al - 16.6at\%Zn - \langle 100 \rangle$ single crystals are determined by the starting austenite structure depending on the heat treatment. The equilibrium structure of this alloy with a usual composition between two stoichiometries is a mixture of two stoichiometric austenite phases.

Crystallographically identical martensitic transformations of homogeneous and heterogeneous austenite have different kinetics: Nucleation of several martensite micromonodomains and increase of the phase fraction of martensite by increasing its density during the deformation (*pure nucleation kinetics*) or formation of a single martensite macromonodomain and its propagation through movement of a phase boundary surface (*pure growth kinetics*). The heterogeneous stress-induced martensitic transformation is

energetically more favorable for the homogeneous austenite and the homogeneous for the heterogeneous austenite.

The multiple martensite micromonodomain kinetics is similar to the heterogeneous plastic deformation due to multiple sliding of dislocations, while the single martensite macromonodomain kinetics is very similar to the homogeneous plastic deformation due to the formation and expansion of single or several Lüders bands (**Fig. 26**), and it has the same energetic reason.

These single crystals show development of specific dynamic shear structures in the premartensitic state ($M_s < 20^\circ\text{C} < T_0$) of the metastable $B2$ -austenite phase (**Figs. 31 a, b**), which can be registered through distortion (*diffusion scattering*) of the austenitic main reflections $(110)_{B2}$ and the appearance of diffuse satellite reflections in the vicinity of $\vec{q} = \left(\frac{1}{3}, \frac{1}{3}, 0\right)$ (**Fig. 31 c**) before $9R$ -martensite is arised at $T < M_s$ (**Fig. 30 b**).

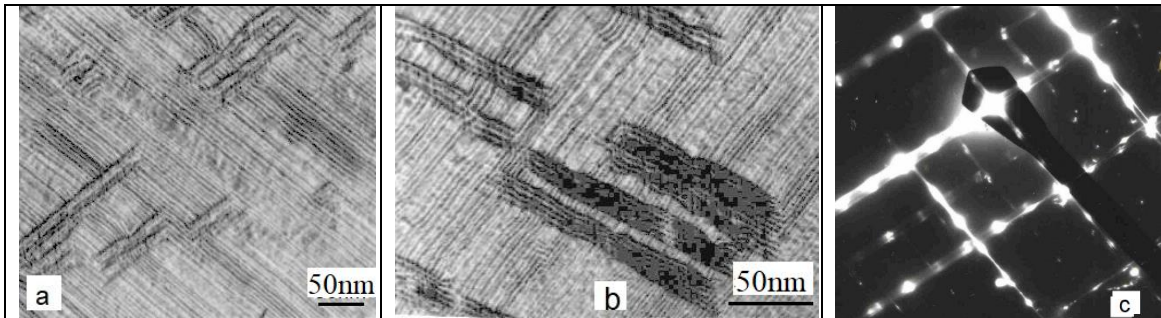


Fig. 31. Dynamic shear structures in premartensitic temperature range $T_0 > T > T'_0$ of the metastable $B2$ -austenite of a $\text{Cu} - 15.2\text{at}\% \text{Al} - 16.6\text{at}\% \text{Zn} - \langle 100 \rangle$ single crystal (HTII) (**a, b**); Electron diffraction from the same area with diffuse $1/3\langle 110 \rangle$ extra reflections, foil surface $(111)_{B2}$ (**c**).

These results show that neither the martensite lamellas nor the martensite band correspond directly to the martensite macromonodomain defined in §3.1.1. The martensite lamellae represent single martensite mi-

cromonodomains oriented in the opposite direction or their groups (*twins*) that have grown together with zero overall deformation as dynamic unstable martensite nuclei in the premartensitic temperature range, which build $A'M_m^m$ phase boundaries with the metastable austenite. The transformation temperature of martensite micromonodomains depends on the mechanical stress according to Clausius-Clapeyron equation, while the equilibrium temperature T_0 between the stable austenite A and the martensite macro-monodomain M^m is a material constant, which marks the upper validity limit of the Clausius-Clapeyron equation.

The martensite band is an area of the martensitic phase that is only partially monodomained (§5.4.1) due to external stress. The temperature of its local equilibrium with the metastable austenite $T_0'(\sigma)$ is also determined by the Clausius-Clapeyron equation in relation to the external stress. Nevertheless, the two types of martensite can be viewed as parts of the quantized energy spectrum (3.1.2) in accordance with CODEM.

5.2 Effect of stacking fault energy

5.2.1 Change in stacking fault energy due to aging

The ferroelastic deformation of a SMA-specimen in its martensitic state in the temperature range $T < M_f < T_0'$ is only caused by the movement of twin boundaries, i.e. partial dislocations in the martensite phase. That ultimately leads to its monodomainization by reorientation of micromonodomains, which are negatively oriented relatively the external stress axis. The ferroelastic hysteresis is thus determined by the mobility of these twin boundaries or by the stacking fault energy. This in turn depends strongly on the concentration of point defects (*vacancies, self-interstitial atoms, foreign atoms, etc.*). The hysteretic behavior of the ferroelastic deformation of SMA's is, as already shown in §4.5.3, completely similar to that of the magnetization of ferromagnetic materials [10, 12, and 14], in which the hysteresis is caused by the energy dissipation during the reorienting movement of magnetic domain boundaries because their friction on points defects (*pinning*).

The *Cu*-based SMA's with an ordered *B2* austenite structure contain many excess, non-equilibrium vacancies because of their composition is far away from *B2*-stoichiometry. It was assumed [92, 93] that the martensite stabilization in these SMA's is related to the high mobility of the non-equilibrium vacancies created by quenching at HTIII, even at the room temperature, as the pseudoelastic behavior of *Cu – Al – Zn* single crystals after heat treatment HTIII also reveals (**Fig. 26 c**). It can be assumed that aging after the quenching leads to a more stable equilibrium distribution of the non-equilibrium vacancies.

The ferroelastic behavior of *Cu – Al – Zn* single crystals was investigated in the fresh quenched state (HTIII) and after aging during 24h and

one month at the room temperature (**Figs. 32 a-c**). A unique behavior of the fresh quenched specimens was discovered, which rather corresponds to the behavior of a viscous liquid and not a solid (**Fig. 32 a**). The maximal amplitude of the ferroelastic deformation is not only achieved with minimal tension-compression external stresses (**Fig. 25 b**, *hysteresis loop 1*) and accordingly with almost zero ferroelasticity coefficients or with almost zero energy dissipation (**Fig. 25 c**, *line 1a*) on the single crystalline specimens with orientation of the longitudinal axis $\langle 100 \rangle$ of the lightest ferroelastic deformation, but also with orientation $\langle 113 \rangle$ (**Fig. 32 a**).

In practice it looks like that the specimens with the orientation of the longitudinal axis $\langle 100 \rangle$ clamped in a simple device can be at room temperature with bare hands slightly deformed ferroelastically up to an amplitude of 15%. You can visually observe the movement of monodomain boundaries on the polished surface and clearly hear loud specific crunching, i.e. perceive intense AE signals without any technical effort. The behavior serves as an absolutely clear demonstration of reorientation processes in martensite during its ferroelastic tension-compression deformation.

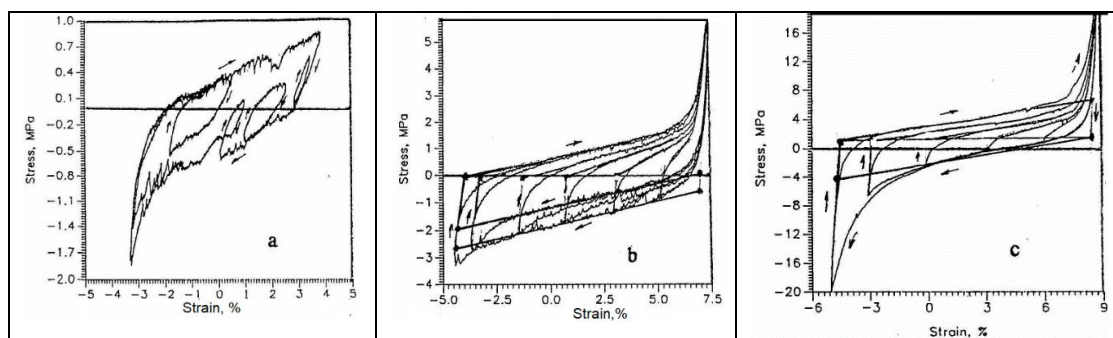


Fig. 32. Ferroelastic hysteresis loops of the $Cu - 15.2at\%Al - 16.6at\%Zn - \langle 113 \rangle$ single crystals after quenching from $850^{\circ}C$ in cold water (*HTIII*): **a** – fresh quenched, **b** – after $24h$ and **c** – after one month aging at the room temperature.

However, the service is not long-lasting: The martensite strengths noticeably already after a few deformation cycles. The same happens after

aging at the room temperature (**Figs. 32 b, c**). The hysteresis width only increases by increasing the ferroelasticity coefficient k_f , without the development of latent hysteresis. This leads to an increase in the dissipated energy (**Fig. 25 c, lines 1a, 1b, 1c**), which depends parabolically on the ferroelastic deformation ε_f in completed partial deformation cycles in the absence of the latent hysteresis $\Delta\sigma_l = 0$ (4.5.18).

Since there are no phase boundaries in the ferroelastic deformation process, and the reorientation of martensite micromonodomains comes about exclusively through the movement of twin boundaries (*micromonodomains boundaries*), such behavior can obviously only be achieved through changes in the stacking faults energy due to the migration of excess vacancies into this. The vacancies diffuse with the aging time, accelerated by the stress gradients $\vec{F} = -grad_x\sigma$ in the vicinity of stacking faults, to the twin boundaries, settle there and thereby reduce their mobility and thereby increase the stacking faults energy. The time-dependent stabilization process can also be described by the Arrhenius equation (5.1.1), and its activation energy can be determined experimentally.

In view of the concept of two energetically different martensite states – with and without substructure – represented here both the stabilization and degradation of the martensite and the great sensitivity of the local equilibrium temperature T_0' to all possible influences can easily be explained. Any change in the density of internal defects in martensite, as well as any change in the stacking fault energy, e.g. by adding vacancies, by alloying with different alloying elements not only changes the local equilibrium temperature T_0' , but also the hysteresis width of the $A' \leftrightarrow M^P$ martensitic transformations. From this point of view, one can perhaps better understand

the very complex effects of the thermo-mechanical treatments on the characteristic transformation temperatures and on the hysteresis parameters.

5.2.2 Increase in stacking fault energy due to electron bombardment

In order to investigate the effect of stacking faults on the transformation temperatures and hysteresis in more detail, the surface of polycrystalline $Ti-50.5at\%Ni$ -specimen was bombarded at the room temperature in a completely martensitic state by strong electron impulses with amperage density $j_{el} = 10^7 A/m^2$, acceleration voltage $U_e = 5 \cdot 10^4 V$ or electron energy $E_0 = 250 keV$, impulse duration $t_{imp} = 50 \cdot 10^{-9} s$ (**Fig. 33 a**) and diameter $D = 10^{-2} m$ of the round attack surface [94].

The structural changes in the bombarded surface zone were examined by X-ray analysis. The hysteresis loops $z(T)$ were recorded directly by changes in the intensity of the $(110)_{B2}$ austenite main reflex of the $NiTi$ -specimen with temperature changes in a temperature chamber placed on the goniometer of the diffractometer:

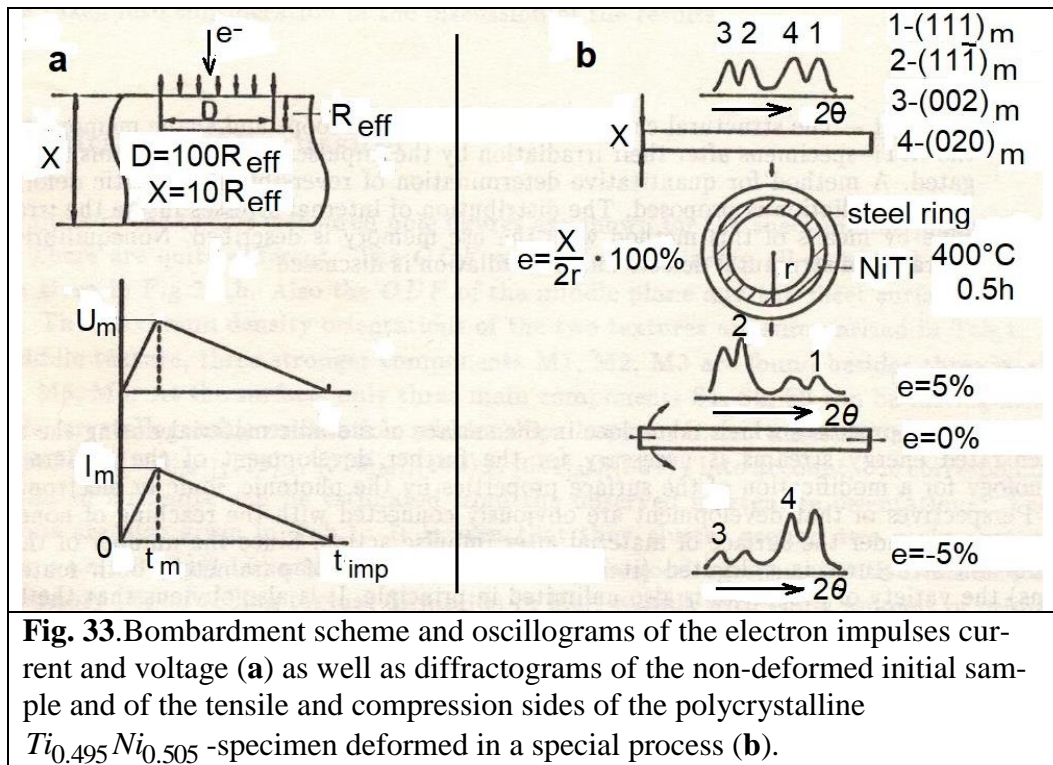
$$z(T) = 1 - \frac{I_{(110)_{B2}}(T)}{I_{(110)_{B2}}(T \geq A_f)}. \quad (5.2.1)$$

The electron bombardment of $NiTi$ -specimens in a completely martensitic state leads to the expansion of the transformation hysteresis loop to lower temperatures compared to those of the initial specimen (**Figs. 34 a, b**). This expansion takes place by lowering the transformation temperatures M_f and A_s so that up to 30% austenite appears at the room temperature after electron bombardment, while the temperatures M_s and A_f remain practically unchanged (**Fig. 34 a, hysteresis loop 2**).

The presence of the austenite phase at the room temperature after the electron bombardment also indicates that the temperature of the bombarded surface zone rose above a temperature $A_s < T < A_f$, i.e. $40^\circ\text{C} < T < 90^\circ\text{C}$ (**Fig. 34 a**, hysteresis loop 1) during the electron impulse duration, and that a partial reverse $B19' \rightarrow B2$ -transformation took place. This temperature also results in the calculation of the Joule heat using the parameters of the electron impulse:

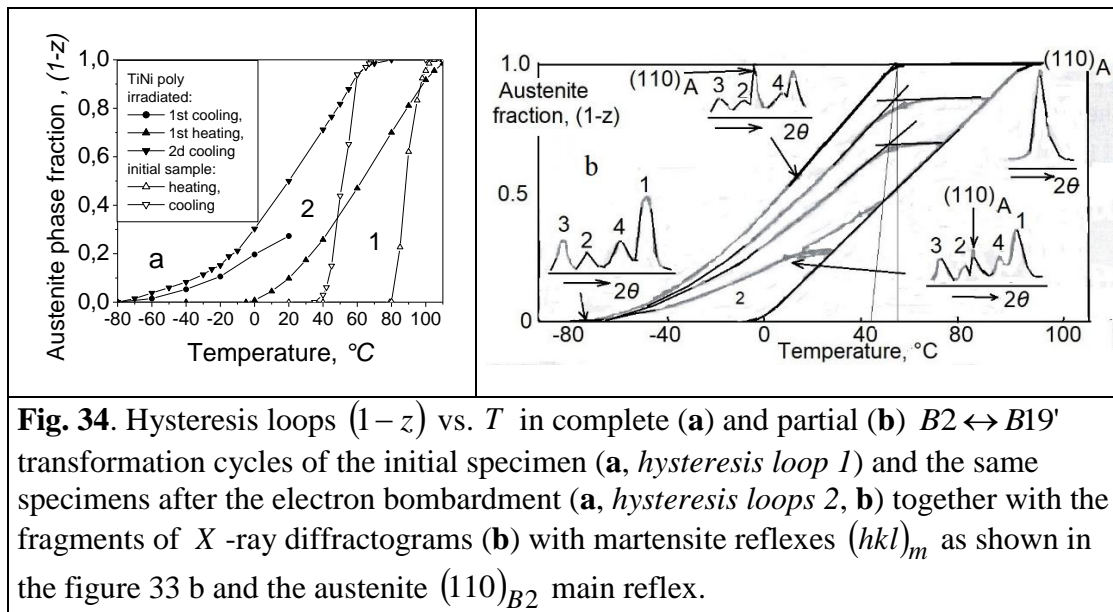
$$T_{\max} = \frac{j_{el} \cdot U_{el} \cdot t_{imp}}{(\rho \cdot c_p)_{NiTi} \cdot R_{eff}} + 20^\circ\text{C} \approx 80^\circ\text{C}, \quad (5.2.2)$$

where ρ and c_p are the density and the heat capacity of the *NiTi*-SMA's, R_{eff} is the effective penetration depth.



The expansion of the hysteresis loop is, as partial transformation cycles show (**Fig. 34 b**), due to the lowering of the equilibrium temperature, which is sensitive to the stacking fault energy. The stacking fault energy of

the martensite phase can, as it was demonstrated in the previous section, be significantly increased by introducing defects into the bombarded surface area. However, it is not entirely clear, which defects are supposed to be involved in the bombardment by light electrons with an impulse duration in the nanosecond range. The bombardment electrons could only stimulate the electron system and hardly the phonon system in the bombardment zone in order to remove the heavy atoms from their positions in the crystal lattice.



The bombarded surface shows traces similar to the material evaporation, which could cause the formation of radiation defects (*vacancies*) and compressive stress in the top layer. The temperature increase calculated in (5.2.2) during the electron bombardment can only be a matter of sublimation by reaching the critical sublimation pressure on the surface of the bombarded SMA-specimen.

On the diffractograms from the bombarded specimen surface, a redistribution of intensity between martensite reflexes with a factor

$$K_{12} \equiv \frac{I_{(111)_m}}{I_{(11\bar{1})_m}} \gg 1 \text{ (Fig. 34 b) can be clearly seen.}$$

The electron bombardment therefore significantly influenced the structure of the specimen through strong electron-electron interactions. In order to investigate this effect in the entire penetration depth R_{eff} of the impact zone, material layers of $(5 \div 10)\mu m$ were step by step etched away, and the diffractograms were recorded at each step (**Fig. 35 a**).

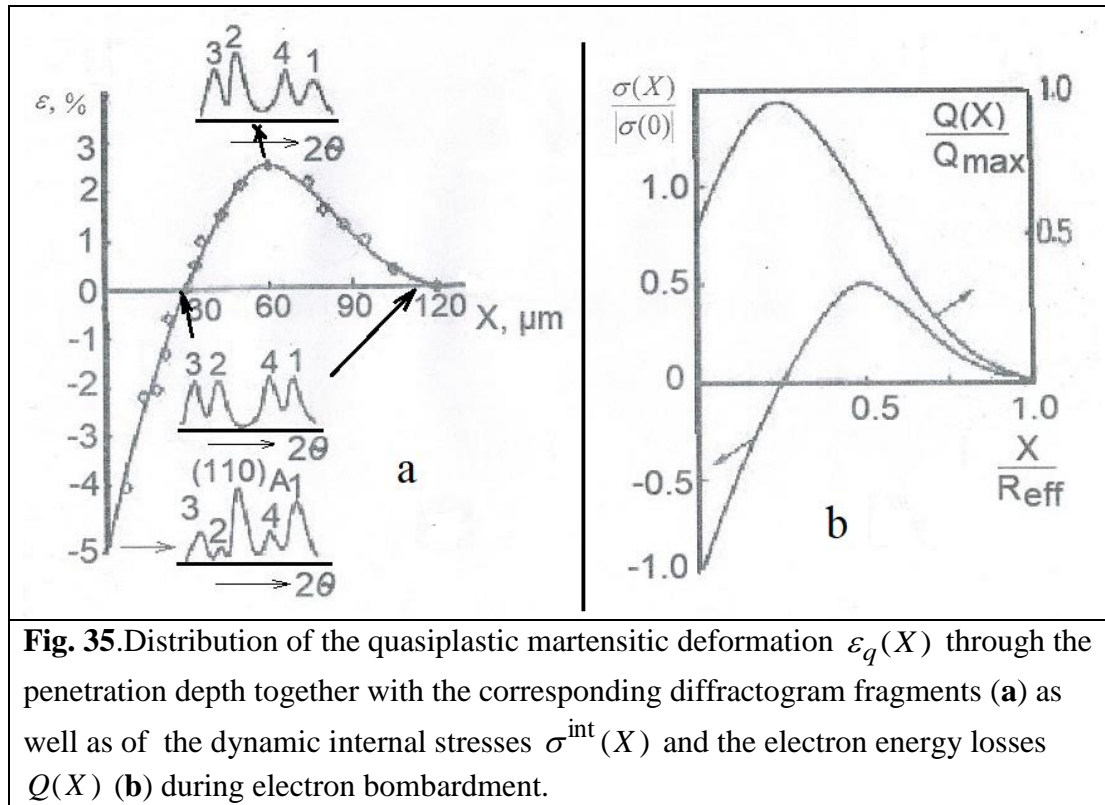


Fig. 35. Distribution of the quasiplastic martensitic deformation $\varepsilon_q(X)$ through the penetration depth together with the corresponding diffractogram fragments (a) as well as of the dynamic internal stresses $\sigma^{int}(X)$ and the electron energy losses $Q(X)$ (b) during electron bombardment.

The effective penetration depth of the electrons with energy E_0 when bombarding metals with density ρ is theoretically:

$$R_{eff} \cong E_0^2 / \rho \cdot b \cong 130 \mu m , \quad (5.2.3)$$

where b is an empirical parameter related to the atomic number of the metal. The electrons lose all their energy E_0 along this route, which creates a shock wave that acts in this zone. The experimentally measured length [94, 95] of this shock wave is approx. $120 \mu m$ (**Fig. 35 a**) and agrees well with the calculated penetration depth of electrons (5.2.3).

The intensity of the X -ray diffraction reflexes is determined by the plane frequency factor under the same other conditions. The plane frequency factor is the number of atomic planes with the same 2θ -Bragg angle. If the orientations of these atomic planes are distributed equally, the reflex intensities are also statistically distributed equally. An intensity redistribution between the martensite reflexes naturally occurs in the case of martensitic deformation through monodomainization or texturing of the martensite polydomains under the action of external or internal mechanical stresses. The quantitative relationship between the martensite deformation due to mechanical stress and the intensity redistribution had been investigated and defined experimentally (**Fig. 33 b**).

Since the X -ray diffraction recordings require the flat specimens, the same polycrystalline $NiTi$ -specimens in a martensitic state were deformed into steel rings with different radii and aged $0.5h$ at $400^\circ C$ in order to relax the stresses (§4.5.1, **Fig. 21 b**) caused by the force memory effect during the recovery attempt by plastic deformation, and to fix the ring shape as the low temperature shape. When straightening to a flat shape, the specimen is deformed quasiplastically, namely stretched on the inside (*tensile deformation*) and compressed on the outside (*compression deformation*). The deformation value is determined by the radius r of the steel rings and the thickness X of the SMA-specimen $\varepsilon_q = \frac{X}{2r} \cdot 100\%$ (**Fig. 34 b**).

The intensities of reflexes $(111)_{B19'}$ and $(020)_{B19'}$ measured on the specimens deformed in this way are significantly greater on the compression side than those of reflexes $(11\bar{1})_{B19'}$ and $(002)_{B19'}$, while the ratio is inverse on the tensile side. As already explained, the reflex intensity $I_{(hkl)}$ is determined by the plane frequency factor, i.e. by the number $N_{(hkl)}$ of

atomic planes involved in X -ray diffraction with the Brag angle 2θ :

$$I_{(hkl)} \propto N_{(hkl)}. \quad (5.2.4)$$

The reorientation (*monodomainization, texturing*) of martensite polydomains (**Fig. 2 b**) takes place through an increase in the number of martensite polydomains or positively oriented atomic planes $N_{(hkl)}^+$ that are favorably oriented relative to the external stress axis and their signs, the displacement of which results in a positive deformation contribution in the direction of the stress axis at the expense of negatively oriented atomic planes $N_{(hkl)}^-$, similar to how it was treated in §3.1.1 and §4.4.4.

The total deformation can then be calculated using the ratio between these numbers or reflex intensities:

$$\varepsilon_q(\sigma) = \gamma_M \cdot \frac{1 - N_{(hkl)}^- / N_{(hkl)}^+}{1 + N_{(hkl)}^- / N_{(hkl)}^+} = \gamma_M \cdot \frac{1 - K_{ij}}{1 + K_{ij}} \cdot \delta_{ij}, \quad (5.2.5)$$

where $K_{ij} < 1$ is always, and δ_{12} is a conversion symbol

$$\delta_{ij} = \begin{cases} 1, & \text{wenn } K_{ij} = K_{12} < 1 \\ -1, & \text{wenn } K_{ij} = K_{21} < 1 \end{cases} \text{ similar to the Kronecker Delta. The ratio}$$

(5.2.5) agrees well with experimentally measured deformation values (**Fig. 33 b**), but only up to deformation $\varepsilon_q(\sigma) \leq 5\%$. The discrepancies in the case of larger deformations $\varepsilon_q(\sigma) > 5\%$ apparently arise from a change in the deformation mechanism from pure reorientation of the martensite phase to another in the case of higher stresses, which has also been approved in resistometric studies of the ferroelastic deformation (§4.2.3, **Fig. 11 c**).

With the help of this method, the profile of dynamic compression-tensile

dynamic stresses acting during the irradiation was investigated on the basis of the remaining quasiplastic martensitic deformation (**Fig. 35 a**). However, the intensity ratios in bombarded specimens differ from those in mechanically deformed samples: The intensity of the $(002)_{B19'}$ - and $(020)_{B19'}$ -reflexes remains unchanged and constant, while the intensity of the $(111)_{B19'}$ - and $(11\bar{1})_{B19'}$ -reflexes is distributed in the same way as with mechanical deformation and corresponds to equation (5.2.5). This is explained by the symmetry effect: The electron beam acts isotropically in two-dimensional atomic planes directed perpendicular to the beam (*axial symmetry or axial texture*), while the mechanical stress acts uniaxial.

The dynamic stress distribution is like that of shock wave through the depth of the bombarded zone. Compressive stresses act on the surface, which change to tensile stress at the depth $X \approx 30\mu m$. This creates a non-deformed zone, which is responsible for the original values of the transformation temperatures M_s and A_f . The profile of dynamic stresses (**Fig. 35 b**, *left ordinate axis*) is a structural image of dynamic processes that take effect in the bombarded zone in the nanosecond range and that would be impossible to record in real time.

This profile (**Fig. 35 b**, *right ordinate axis*) is a direct derivation of the distribution function of the electron energy losses through the penetration depth [94, 95]:

$$\sigma(X) = -grad_X [U(X)], \quad (5.2.6)$$

where $U(X) \equiv P \cdot Q(X)$ is the interaction energy between impulse electrons and the electron-phonon system of the solid and P is a coupling parameter. The latter allows a quantitative relationship between the dynamic stress and the electron impulse parameters to be restored, if it can be de-

terminated experimentally. So, this property of SMA's can also be called and used as a memory for the effects of impulses with a duration of up to nano-seconds.

The X -ray diffraction takes place in a surface layer with a depth of $(20 \div 30) \mu m$. The intensity losses in X -ray recorded from these depths are $(75 \div 95)\%$. In this zone, quasiplastic martensitic compression deformation has been proven experimentally (**Fig. 35 a**). The dynamic compression causes intense sublimation on the surface, which results in the formation of radiation defects in the surface layer. The absorption of the radiation defects through the stacking faults leads to an increase in the free energy of the martensite. This lowers the local equilibrium temperature T_0' (**Fig. 1 b**) and thus the transformation temperatures M_f and A_s (**Figs. 34 a, b**).

Such extended hysteresis loops are sometimes useful for practical applications and are otherwise brought about by creating artificial structure gradients in complex structured SMA-specimens [96-98].

5.3 Martensite monodomainization as a stabilization mechanism

5.3.1 Martensite stabilization through ferroelastic deformation

With the thermo-induced martensitic transformation, up to twelve different orientation variants of martensite polydomains arise through shear in 24 energetically equivalent shear systems (§4.4.4, **Table 3**). The formation of a martensite monodomain is only possible with the transformation in an anisotropic stress field, e.g. under uniaxial external stress or by reorientation of the thermo-induced martensite. Complete monodomainization, however, is only achieved through complete cycles of ferroelastic tension-compression deformation of a SMA-specimen in the martensitic state ($T < M_f < T_0'$).

Investigation of the temperature dependence of the mechanical hysteresis in the transition from pure pseudoelastic tension-compression hysteresis in the austenitic state ($T > A_f > T_0'$) via the mixed hysteresis in the two-phase temperature range $M_f < T < A_s$ to pure ferroelastic hysteresis in the martensitic state (**Figs. 22 a-c**) with a step by step temperature decrease showed not only none temperature dependence of the mechanical hysteresis, but also a very surprising effect.

After the measurement run of the mechanical hysteresis with a temperature decrease from $T > A_f > T_0'$ to $T < M_f < T_0'$, the return run of these measurements with a temperature increase from $T < M_f < T_0'$ to $T > A_f > T_0'$, i.e. back to the pseudoelastic hysteresis, was no longer possible, or the transition from ferroelasticity to pseudoelasticity was not achieved. The specimen remained in its martensitic state in a temperature range well above the finish temperature A_f of the thermo-induced reverse transformation of the initial specimen. In order to investigate this behavior, small pieces for calorimetry were cut out of the monodomained samples with a completely structureless, smooth surface and examined [13, 14].

The calorimetric results showed that the martensitic reverse transformation of a martensite macromonodomain created by ferroelastic deformation cycles into stable austenite $M^m \rightarrow A$ takes place during the first heating at elevated temperatures $A_f^{M^m \rightarrow A} = A_f^{M^p \rightarrow A'} + (50 \div 100)^\circ\text{C}$ (**Figs. 36 a-c**). This reverse transformation temperature is the higher, the broader the initial thermal hysteresis loop (*Cu – Al – Mn and Cu – Al – Ni- single crystals compared to Cu – Al – Zn single crystals*) and the larger the amplitude of the ferroelastic deformation $\Delta\varepsilon_f$.

These tests show that the martensite macromonodomains produced by cyclic ferroelastic deformation participate in the ferroelastic deformation, but are no longer transform into the metastable austenite A' when the temperature rises above the initial temperature range $M_f \div A_f$.

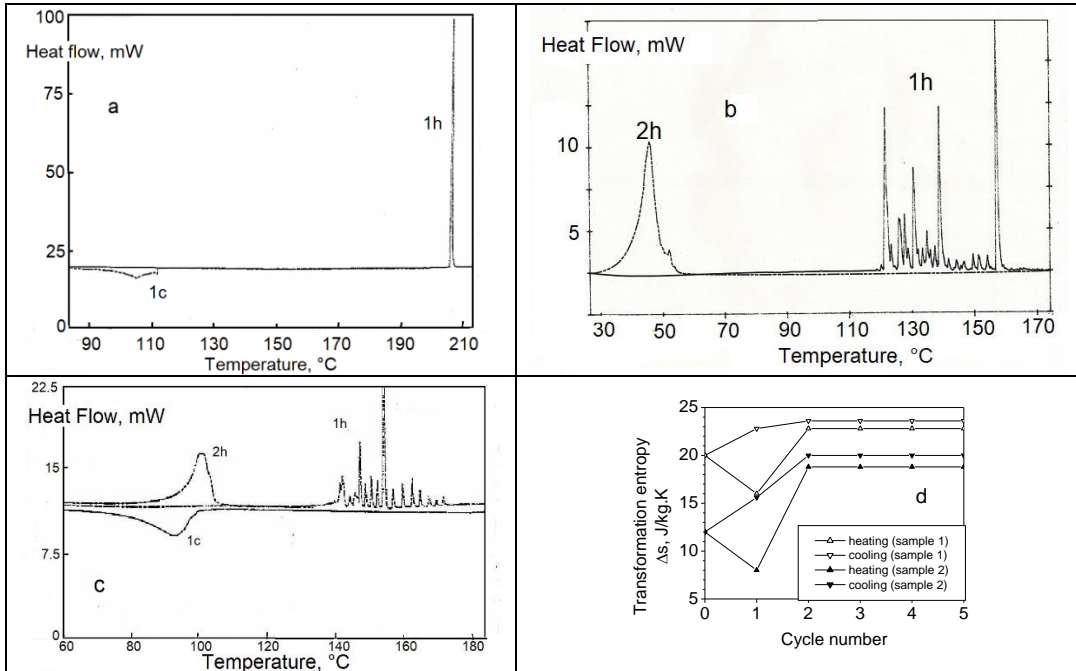


Fig. 36. Calorimetric measurement curves [13, 14]: Temperatures of the martensitic reverse transformations $M^m \rightarrow A$ during the first heating (1h), of $A' \rightarrow M^p$ transformation during the first cooling (1c) and of $M^p \rightarrow A'$ -transformation during the second heating (2h) of the $Cu - 24.0at\%Al - 4.7at\%Ni - \langle 110 \rangle$ single crystals after the ferroelastic deformation cycles with amplitudes $\Delta\varepsilon_f^M = 8\%$ (a) and $\Delta\varepsilon_f^M = 4\%$ (c) as well as the $Cu - 20.7at\%Al - 10.7at\%Mn - \langle 110 \rangle$ single crystals with a strongly developed block structure after the ferroelastic deformation cycles with an amplitude $\Delta\varepsilon_f^M = 8\%$ (b). Transformation entropy (d) of the $Cu - 15.2at\%Al - 16.6at\%Zn - \langle 110 \rangle$ single crystals, HTI (sample 1) and HTII (sample 2) in the initial state ($n = 0$) immediately after their stabilization by ferroelastic deformation ($n = 1$, 1h and 1c) and in further thermal cycles ($n \geq 2$).

The reverse transformation takes place at elevated temperatures and shows explosive $M^m \rightarrow A$ -transformation kinetics in a narrow temperature interval $A_s^{M^m A} \div A_f^{M^m A}$ or occurs in several discrete steps with sharp sep-

arate maxima. The number of such discrete maxima (**Figs. 36 b, c**) is obviously intended to be the number of substructureless macromonodomains of different sizes.

The latent transformation heat $\Delta q^{M^m \rightarrow A}$ measured during the first heating is the same as that $\Delta q^{M^p \rightarrow A'}$ in the initial specimen. This contradicts the data measured on monodomained polycrystalline *NiTi*-specimens [19, 20], which report not only an increase in the reverse transformation temperatures up to 40°C , but also an increase in the latent transformation heat up to a contribution of 10J/kg .

The increase in the latent transformation heat would mean a reduction in the internal energy of the monodomained martensite compared to the energy $U^{M^m} = F^{M^m}(T=0) < U^{M^p} = F^{M^p}(T=0)$ of the martensite polydomains and would also lead to an increase in the reverse transformation temperature with the same entropy values during the first heating $\Delta s^{M^m A} = \Delta q^{M^m A} / T_0 = \Delta s^{M^p A'} = \Delta q^{M^p A'} / T_0'$ (**Fig. 1 b**).

The entropy difference $\Delta s^{M^m A}$ between a martensite macromonodomain and the stable austenite is accordingly smaller than that $\Delta s^{M^p A'}$ between the martensite polydomains and the metastable austenite. In these calculations, the equilibrium temperatures were placed in the middle of the transformation temperature range for the sake of uniformity, even with discrete shapes of the measurement curves $T_0 = \left(A_s^{M^m A} + A_f^{M^m A} \right) / 2$ and $T_0' = \left(A_s^{M^p A'} + A_f^{M^p A'} \right) / 2$ (**Figs. 36 b, c**). Discrete reverse transfor-

mation indicates that the monodomained martensite consists of several large macromonomains with different degrees of monodomainization and, accordingly, with different reverse transformation temperatures.

Smaller transformation entropy means that the difference in slope of the straight lines $F^{M^p}(T)$ and $F^{A'}(T)$ has become smaller than that of the straight lines $F^{M^m}(T)$ and $F^A(T)$ (**Fig. 1 b**), either because the entropy $S = S_{config} + S_{vib}$ of the martensite monodomain is greater than that of the martensite polydomain $S^{M^m} > S^{M^p}$ due to greater configuration entropy $S_{config}^{M^m} > S_{config}^{M^p}$, or because the entropy of the metastable austenite is greater than that of stable austenite $S^{A'} > S^A$ due to greater vibration entropy $S_{vib}^{A'} > S_{vib}^A$.

Such a stabilization effect was also registered by resistance measurements $\Delta R(T)$ (**Fig. 10 c, hysteresis loop 2**). The phase fraction of the stabilized martensite $z_s^{M^p}$ (*subscript s*) can be calculated from the difference in resistance $\Delta R_s^{M^p A'}$ between the electrical resistance of the initial specimen and that of the ferroelastically deformed specimen with part of the stabilized martensite (4.2.14).

The martensite monodomains stabilized from the thermo-induced transformation by reorientation and thus eliminated from the transformation cycles generate internal stress fields in the austenite, which have an important orienting effect on the nucleation and growth of reversible thermo-induced martensite polydomains for the two-way shape memory effect (§4.5.1).

All these martensite stabilization effects, also incorrectly called hystere-

sis expansion effects [99-101], were explained in most research works as the result of the blocking of phase or domain boundaries by various irreversible defects such as dislocations, vacancies, inclusion atoms or their combinations, i.e. as the result of an external influence on the movable internal martensitic boundaries and not regarded as the specific and fundamental difference in properties between a martensite macromonodomain and a martensite polydomain, as it was first claimed in [13, 14].

5.3.2 Martensite stabilization by mechanical impact

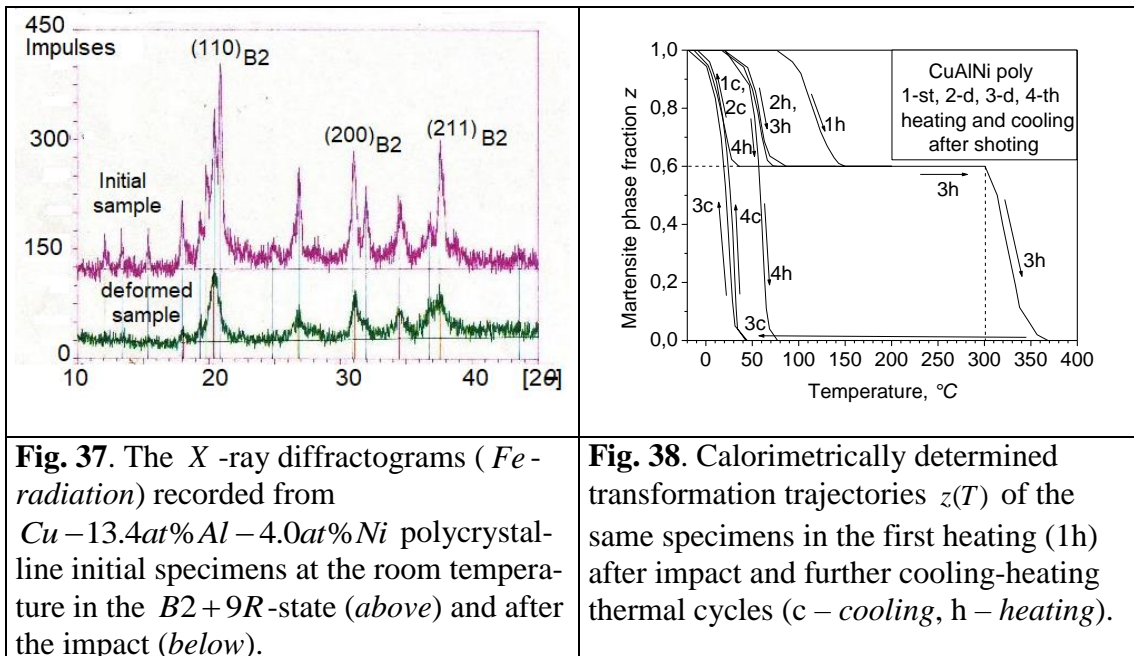
In order to clarify the role of irreversible defects such as dislocations in the martensite stabilization, a rolled and standard heat-treated (*HTI*) polycrystalline $Cu - 13.4at\% Al - 4.0at\% Ni$ -specimen was treated in its two-phase state at the room temperature by mechanical impact, i.e. shot through by a projectile with a weight of approx. $10^{-2} kg$ and a velocity of $200 m/s$.

The *X*-ray diffractograms of the specimens cut out at the edge of the penetration hole (*Fig. 37*) show an intensity redistribution of the *9R* martensite phase reflexes and a reduction in their number as well as in the intensity of *B2* austenite reflexes. This points to the deformation of the martensite due to reorientation of thermo-induced martensite polydomains or a strong texturing of the martensite phase (*Fig. 33 b*) [85, 94, and 95] as well as the pseudoelastic deformation of the specimen due to the transformation of the remaining austenite into the monodomainized martensite $A' \rightarrow M^m$. The increase in the ratio of the width to the height of reflexes is evidence of intensive plastic deformation of martensite under the action of mechanical impact.

The effect of these factors on martensite stabilization is shown by the transformation trajectories calculated from calorimetric data in subsequent

heating-cooling thermal cycles (**Fig. 38**). The martensitic reverse transformation does not take place during the first heating in the temperature range $A_s \div A_f$ of the initial reverse $M^P \rightarrow A'$ -transformation (approx. $(40 \div 70)^\circ\text{C}$) of the initial specimen, but at much higher temperatures in the range of approx. $(90 \div 140)^\circ\text{C}$ (**Fig. 38, line 1h**).

The measured latent transformation heat $\Delta q^{M^m A}$ is only approx. 40% of the same as the initial latent heat $\Delta q^{M^P A'}$ of the reverse transformation. This means that the rest of the martensite phase of 60% (4.3.2) still remained irreversible. In the subsequent cooling-heating cycles, the forward and reverse transformations of the martensite polydomains restored by the first heating take place again in the normal ($M_s \div M_f$) and ($A_s \div A_f$) temperature ranges for the initial specimen (**Fig. 38, lines 1c, 2h, 2c, 3h**).



When the specimen was in the calorimeter further heated to over 300°C during the third heating (3h), the remaining part of 60% the stabilized martensite transforms in a temperature range of $(300 \div 360)^\circ\text{C}$ into the austen-

ite. During the subsequent cooling and heating, the complete forward and reverse transformations of the specimen take place again in a temperature range normal for the initial specimen (**Fig. 38**, lines 3c, 4h). The temperature shift between transformations trajectories (**Fig. 38**, lines 3c, 4c) can be simple explained by the different scanning rates during the 3rd ($\dot{T} = 10K/min$) and 4th ($\dot{T} = 5K/min$) cooling [51]. The measurement results are independent of the distance to the penetration hole, which proves that the shock wave acted with the same intensity through the entire sample volume.

These results show that the martensite phase was stabilized by the mechanical shock effect by two mechanisms. The first is the same as that for the above-discussed increase in the reverse transformation temperature up to $100^\circ C$ ($A_f^{M^m A} = A_f^{M^p A'} + 100^\circ C$) after the ferroelastic deformation cycles (**Figs. 36 a-c**): monodomainization and texturing of the initial differently oriented thermo-induced martensite polydomains through reorientation during the mechanical shock impact. This is supported by the quantitative increase in the initial reverse transformation temperatures in the same range of $(50 \div 100)^\circ C$ (**Fig. 38**, line 1h).

The difference to single crystalline ferroelastically deformed specimen is that the reverse transformation of the martensite monodomains created by the shock effect in polycrystalline specimens does not take place explosively in a narrow temperature range $A_s \div A_f$, but in a temperature range $A'_s \div A'_f$, which is even $50^\circ C$ greater than that in the initial specimens. This is obviously due to a much more complicated than uniaxial mechanical action on the martensite polydomains of a polycrystalline specimen and, accordingly, on a much larger number of energetically different, e.g. due to

the reorientation degree, martensite monodomains.

A similar picture was also observed in $Cu - Al - Mn$ single crystals with a strongly developed block structure, in which the reverse transformation after the ferroelastic deformation cycles at elevated temperatures consists of several single explosive reverse transformations in an extended temperature range (**Fig. 36 b**). The ferroelastic deformation with smaller amplitudes evidently produces a mixture of martensite variants with different monodomainization degrees, which leads to the similar reverse transformation kinetics of the $Cu - Al - Ni$ single crystals (**Fig. 36 c compared with Fig. 36 a**).

The second stabilization mechanism can also be explored through the experimentally determined increase in temperature of the reverse transformation for 60% of the remaining stabilized martensite. It is well known from materials science that the relaxation or recovery of the plastically deformed and by metastable dislocation structure hardened metals occur by the thermally activated movement of dislocations. This movement begins when the activation energy in Arrhenius equation (5.1.1), which is characteristic for each metal, is reached when heated above a critical tempering temperature $T_a \approx 0,4 \cdot T_m$, where T_m is the melting temperature.

The tempering temperature is $T_a \approx 543K$ for copper, i.e. approx. $270^\circ C$ for shock-treated Cu -based SMA's specimens. The reverse transformation of the remaining stabilized martensite, experimentally determined by heating directly in the calorimeter, also takes place in the temperature range from $(300 \div 360)^\circ C$ (**Fig. 38, line 3h**) with 60% of the measured latent transformation heat of the initial specimens. So, the second mechanism of martensite stabilization is its hardening through the true plastic deformation or through intensive multiplication of dislocations within the previously

monodomained martensite, which makes it irreversible up to the tempering temperature T_a .

It can be concluded from this that the deformation of a SMA-specimen during the impact runs through the entire stress-strain diagram known for SMA's with an elastic area, a quasi-plastic flow by reorientation and partial monodomainization of martensite polydomains or a pseudoelastic flow by the stress-induced transformation of the existing austenite into the partially monodomained martensite, the second elastic area and a true plastic flow, hardening of the martensite by multiplying and moving dislocations, up to the breaking point.

The martensite is stabilized by the two flow mechanisms and eliminated from the martensitic $M^P \leftrightarrow A'$ -transformation, which is reversible at normal transformation temperatures around the local equilibrium temperature T_0' , until it is heated, initially through the temperature $A_f^{M^m A} > A_f^{M^P A'} > T_0'$ and finally through the temperature $T > T_a$.

The two stabilization mechanisms, monodomainization (*index "m"*) and plastic deformation by multiplying dislocations (*index "d"*), can be clearly differentiated experimentally through the temperature differences

$$\Delta T_m = A_f^{M^m A} - T_0' \approx 60^\circ C \text{ and } \Delta T_d = T_a - T_0' \approx 300^\circ C.$$

The knowledge obtained here about martensite stabilization through monodomainization without plastic deformation plays a decisive role for practical applications of SMA's as actuators that can be stressed cyclically, such as e.g. [59-65]. The degradation of the shape memory properties with the number of action cycles, which can be attributed to martensite stabilization, is the fundamental problem for such applications.

Now the problem can be solved in that the device with the SMA-actuators by a short heating, e.g. is treated by an electrical current impulse or in a drying oven up to a maximal temperature $T_{\max} = A_f + 100^\circ\text{C}$. Such a short low-temperature heat treatment completely restores the shape memory properties with the least amount of effort, without damaging the non-SMA components of the device.

5.4 Local stabilization effects

5.4.1 Return points memory in ferroelastic deformation cycles

The thermo-induced martensite polydomains represent all twelve orientation variants, which make different determined by the Schmid's orientation factor $\mu = \cos\phi \cdot \cos\varphi$ (§4.4.3, **Table 3**) contributions to the martensitic total deformation of a SMA-specimen by a uniaxial load in the martensitic state and are loaded differently.

At the first tensile load $\sigma_f^+ > 0$ of the polydomain martensite, the martensitic yield point σ_{qy}^p as the beginning of the quasiplastic martensitic deformation due to reorientation $M^p \rightarrow M^{m+}$ is about twice as high (**Fig. 39 a**) as the tensile stress σ_f^+ at $\varepsilon_f = 0$ in further complete cycles of the ferroelastic martensitic deformation, in which a martensite macromonodomain M^{m+} created during tensile deformation is converted (*reoriented*) into another martensite macromonodomain M^{m-} created during compression deformation.

If the specimen is relieved again to the zero-stress $\sigma = 0$ after the first tensile load, the martensitic deformation is retained (*quasiplasticity*). This deformation reverses only when it is heated above the initial A_f -

temperature (*shape memory effect*). A shift in the temperature A_f in such a typical shape memory method was not observed, or possibly not special investigated. This means that the reorientation of the martensite polydomains takes place during the first tensile load without reducing the number of internally martensitic $M^P M^P$ polydomain boundaries.

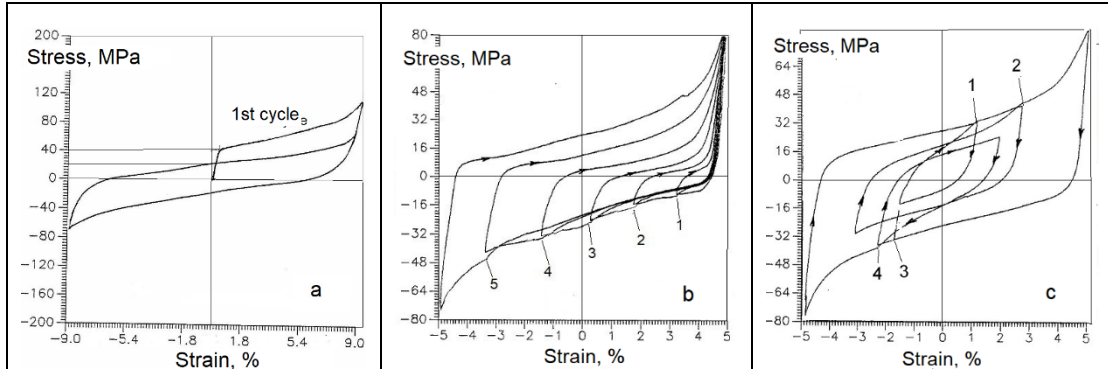


Fig. 39. a: The first tensile load of a $Cu - 15.2at\%Al - 16.6at\%Zn - \langle 100 \rangle$ single crystal (*HTI*) [14] and complete ferroelastic hysteresis; **b, c:** Memory of internal trajectories for the return points of a $Cu - 24.9at\%Al - 4.4at\%Mn - \langle 110 \rangle$ single crystal in different partial cycles of ferroelastic deformation [13].

Only the monodomainization with the annihilation of internal martensitic $M^P M^P$ polydomain boundaries and twin boundaries (*stacking faults*) through complete cycles of the ferroelastic tension-compression deformation creates a single or several martensite macromonodomains, which transform into the stable austenite at considerably higher temperatures $T \rightarrow T_0 > T_0'$.

Both the internally martensitic $M^P M^P$ polydomain boundaries and twin boundaries or stacking faults annihilate by the fusion of partial dislocations to full dislocations under external stress. These then slide, driven by mirror forces, to the edges of the single crystal or to grain boundaries in polycrystals. After several cycles of ferroelastic deformation, especially on samples with large ferroelastic hysteresis, cracks and even breakouts of

small parts appear on the specimen edges.

Similar behavior was observed in the first cycle of compression deformation $\sigma_f^- < 0$ on $Cu - 15.2at\%Al - 16.6at\%Zn - \langle 100 \rangle$ single crystals with a narrow hysteresis (**Fig. 32 b**) and on $Cu - 24.9at\%Al - 4.4at\%Mn - \langle 110 \rangle$ single crystals with a much wider hysteresis (**Fig. 39 b**). A $Cu - 20.7at\%Al - 10.7at\%Mn - \langle 110 \rangle$ single crystal (**Fig. 40 a**), however, does not have this effect. It is evidently due to the fact that the single crystal had already been subjected to a tensile pre-deformation caused by internal stresses, which is indicated by the asymmetry of the ferroelastic hysteresis loop relative to the zero-stress axis.

The presence of differently oriented martensite polydomains that have not been reoriented by tensile deformation or non-annihilated internal martensitic boundaries leads to an increase in the martensitic compression yield point σ_{fy}^- during the first compression load. The increase no longer occurs in further deformation cycles. This appears in partial cycles as a memory of internal deformation trajectories for the return points, designated here as the RPM-effect (**R**eturn **P**oint **M**emory).

If the compression load is interrupted at one point (**Fig. 39 b, 1-5**) and reduced in a partial cycle, the yield point for the subsequent compressive load is compressive stress smaller than that in the first run, but comes to the same higher stress value at the return point again. In partial cycles of ferroelastic compression deformation, two flow lines are formed: one for the first run and one for the second and subsequent runs with lower stresses.

On the tension side ($\sigma_f^+ > 0$), this RPM-effect cannot be observed, or only during the first tension load. Firstly, this proves that the thermo-

induced martensite is completely reoriented after the first tensile load and the subsequent complete compression deformation to a martensite macro-monodomain M^{m-} , so that the ferroelastic deformation in the further runs only takes place through the reorientation $M^{m-} \leftrightarrow M^{m+}$. Secondly, that the compression deformation in partial cycles only begins with the reorientation $M^{m+} \rightarrow M^{m-}$ of the M^{m+} -monodomain created through the tensile stress in previous partial cycles during the first run before the return point and continues with the reorientation $M^P \rightarrow M^{m-}$ of the remaining polydomain martensite only after the return point.

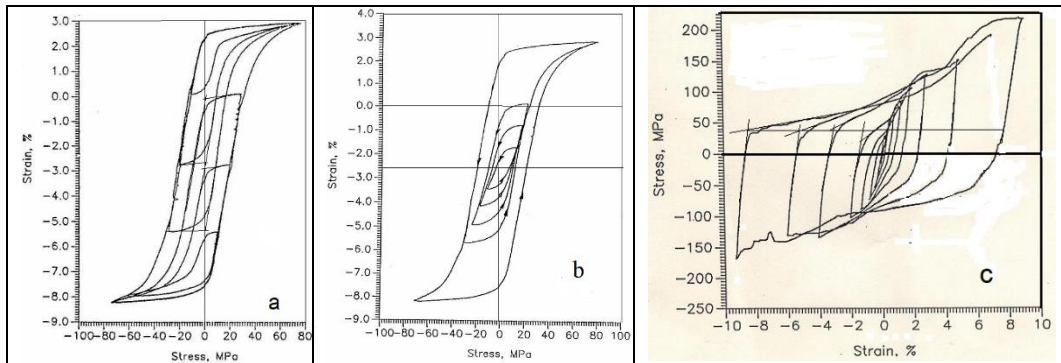


Fig. 40. Partial cycles of ferroelastic deformation of the $Cu-20.7at\%Al-10.7at\%Mn-\langle 110 \rangle$ single crystal from the tension and compression sides (a), hysteresis degradation with spirally reduction of the ferroelastic deformation amplitude of the same single crystal in partial cycles (b – both in the ferromagnetic axis representation) and of a $Cu-13.4at\%Al-4.0at\%Ni-\langle 100 \rangle$ single crystal (c).

The RPM effect ensures that even the internal trajectories of the ferroelastic deformation never intersect in a partial cycle. This again disproves the “experimental” results presented in [73]. The partial hysteresis loops always close at their return points at which they started (**Fig. 39 c**, points 1, 2, 4). If the stress does not change its sign in partial deformation cycles, i.e. $\sigma_f^+ > 0$ remain on the tension side or $\sigma_f^- < 0$ on the compression side, the deformation remains elastic (**Fig. 39 c**, line 3) with the elasticity modulus

G^M of the martensite.

If the internal hysteresis loops are driven in a spiral shape in partial cycles with ever smaller deformation amplitudes $\Delta\varepsilon_f(i) > \Delta\varepsilon_f(i+1)$ (**Figs. 40 b, c**), the ferroelastic hysteresis also degrades to an elastic line due to increasing ferroelasticity coefficients $k_f(i+1) > k_f(i)$:

$$\lim_{\Delta\varepsilon_f \rightarrow 0} k_f = \frac{1}{\rho} \cdot G^M . \quad (5.4.1)$$

5.4.2 Return points memory in thermo-induced transformation cycles

The RPM-effect is also observed during the thermo-induced martensitic transformations [13, 14]. Partial cycles of the thermo-induced transformation according to the scheme: Heating in the temperature interval of the reverse transformation up to a temperature that decreases each time (**Fig. 41 a**):

$$T_i = A_f - i \cdot \Delta T > T_{i+1}, \quad (5.4.2)$$

where $i = 1, 2, \dots, N$ is the cycle number, and subsequent cooling to the same temperature $T < M_f$ in each cycle, lead to a specific change in the kinetics of the final complete reverse transformation.

The calorimetric measurement curve (**Fig. 41 c**) of the complete reverse transformations recorded after this procedure (5.4.2) shows the fragmentation of the previously single endothermic maximum into a series of N -maxima. This RPM-effect, also called TAME (**T**hermal **A**rrest **M**emory **E**ffect) [25] or SMART-effect (**S**tep-wise **M**artensite to **A**ustenite **R**everse **T**ransformation) [26, 27], consists in the reverse transformations being slowed down at each of the return points, so that the calorimetric measurement curve forms a minimum at every return temperature. The integrated

transformation heat of these multiple maxima is the same as the initial transformation heat represented by a single maximum. This means that the same martensitic transformation takes place here, but with different "step-wise" kinetics.

The thermo-induced martensitic transformations of SMA's take place with temperature changes as the appearance-disappearance of martensite polydomains in complete or partial cycles in a strict sequence: The polydomains that were last formed during the forward transformation disappear first during the reverse transformation and vice versa, even if they are included in the self-accommodated martensite conglomerates due to their coalescence. Disappearance of a martensite polydomain as part of a morphologically accommodated group is associated with the emergence of several $A'M^P$ phase boundaries and with a radical redistribution of elastic stresses and energy in the vicinity of this group.

The RPM-effect shows that the martensite polydomains, which disappeared last in partial cycles during heating and arise during cooling in the same place in a self-accommodated group have a higher reverse temperature than those in the initial thermo-induced martensite polydomains. According to the concept of martensite stabilization through monodomainization presented here, this means that this martensite polydomain, which had to be classified in a changed stress field of a self-accommodated group of remaining martensite polydomains, has a smaller stacking fault density than the initial one, i.e. is partly monodomainized by the internal stress field. The RPM-effect is based on the preservation of the morphological martensite structure that has arisen during the heating up to the return temperature as a "memory carrier" during the training process described above (5.4.2). If this morphological carrier disappears during training, there is no

RPM-effect.

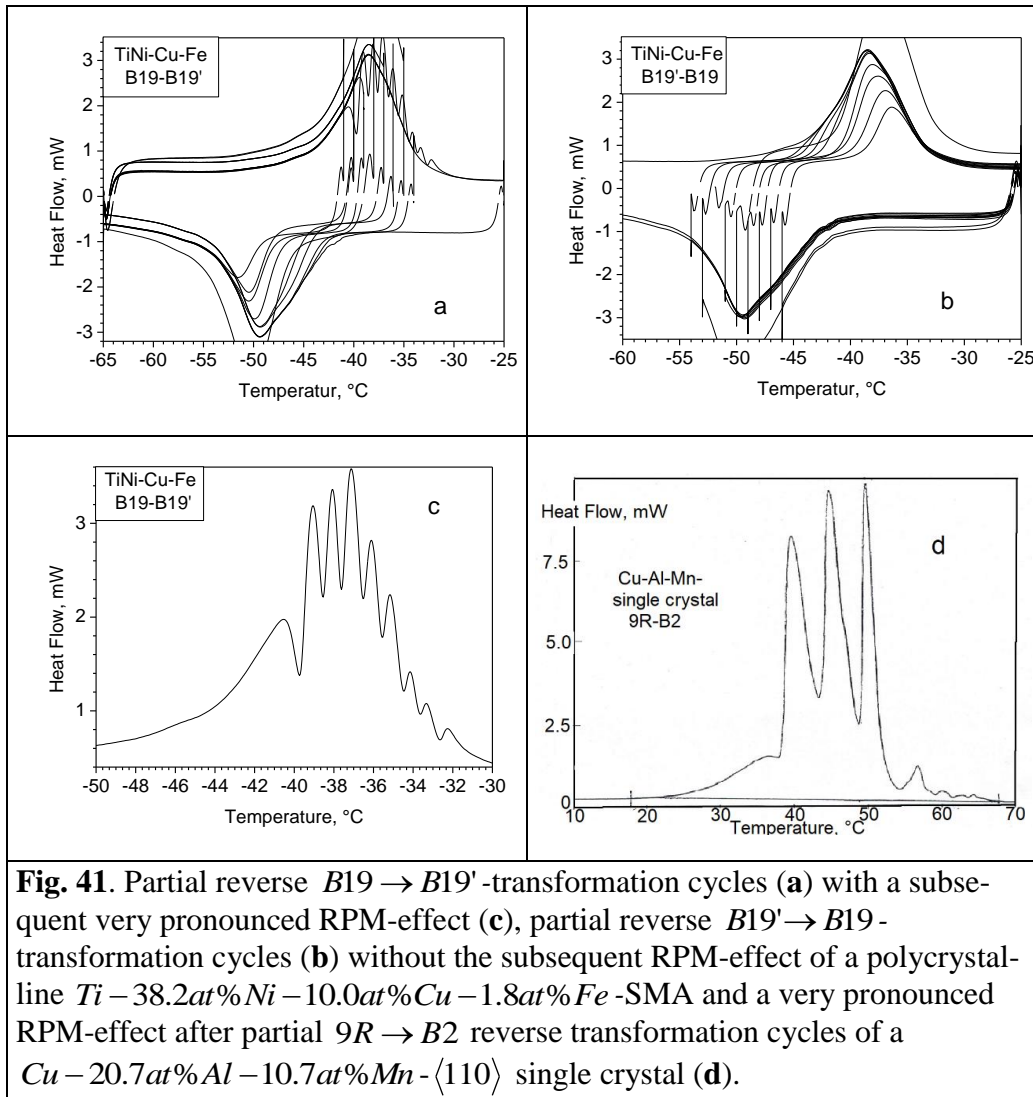


Fig. 41. Partial reverse $B19 \rightarrow B19'$ -transformation cycles (a) with a subsequent very pronounced RPM-effect (c), partial reverse $B19' \rightarrow B19$ -transformation cycles (b) without the subsequent RPM-effect of a polycrystalline $Ti - 38.2at\%Ni - 10.0at\%Cu - 1.8at\%Fe$ -SMA and a very pronounced RPM-effect after partial $9R \rightarrow B2$ reverse transformation cycles of a $Cu - 20.7at\%Al - 10.7at\%Mn - \langle 110 \rangle$ single crystal (d).

This is, e.g., the case when the transformation is interrupted according to the similar scheme: Cooling into the temperature interval of the forward transformation up to a temperature that rises $T_i = M_f + i \cdot \Delta T < T_{i+1}$ or falls $T_i = M_s - i \cdot \Delta T > T_{i+1}$ each time and the subsequent heating to the same temperature $T > A_f$ each time (Fig. 42 b), at that remains no trace of the martensite as memory carrier, and thus no RPM- or SAMFT-effect (Step-wise Austenite to Martensite Forward Transformation) can consequently take place.

For the same reasons, the RPM-effect is only observed in the reverse transformation as a single minimum on the calorimetric measurement curve at the last return point, if the partial cycles are carried out according to the reverse scheme: Heating up to a temperature that increases each time $T_i = A_s + i \cdot \Delta T < T_{i+1}$ and subsequent cooling to a temperature $T < M_f$.

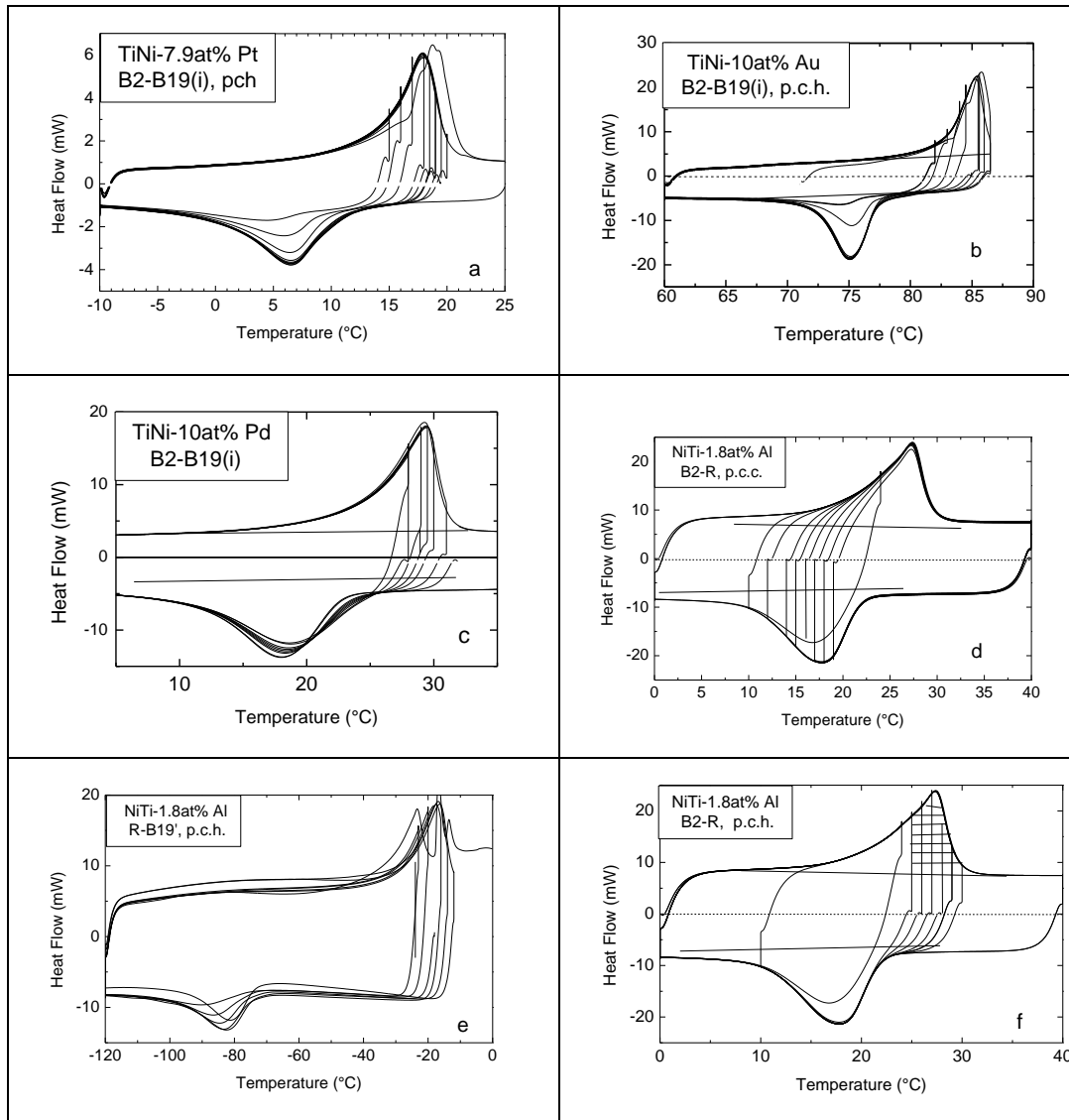


Fig. 42. Partial cycles of the reverse $B19 \rightarrow B2$ -transformation with invariant plane of a $Ti - 42.1at\%Ni - 7.9at\%Pt$ -SMA (a) and $B19 \rightarrow B2$, $Ti - 40.0at\%Ni - 10at\%Au$ (b) with a weak pronounced RPM-effect, $B19(i) \rightarrow B2$ with invariant plane, $Ti - 40.0at\%Ni - 10at\%Pd$ (c); $B2 \rightarrow R$ (d) and $R \rightarrow B2$ (f) without any RPM-effect; $B19' \rightarrow R$ (e) with a strong pronounced RPM-effect, a polycrystalline $Ti - 48.2at\%Ni - 1.8at\%Al$ -SMA.

The RPM-effect apparently has to do neither with martensite stabiliza-

tion through dislocations [26, 27], as it proves the studies of the impact, where the role of dislocations in martensite stabilization (**Fig. 38**) is clearly shown, nor with grain boundaries [25], how it proves the presence of a strongly pronounced RPM-effect in *Cu – Al – Mn* single crystal (**Fig. 41 d**) and its absolute absence in polycrystalline *NiTi* SMA's (**Figs. 42 c, f**).

However, it has to do with the elastic energy of internal $M^P M^P$ -martensitic as well as twin boundaries, i.e. with their number, stacking fault density, stacking fault energy, habitus of martensite polydomains, orientation relationships between the austenite and various orientation variants of the martensite polydomains, i.e. with the hysteresis size of the corresponding martensitic transformations, as has already been determined for ferroelastic hysteresis (**Figs. 39 b, c**) [13, 14].

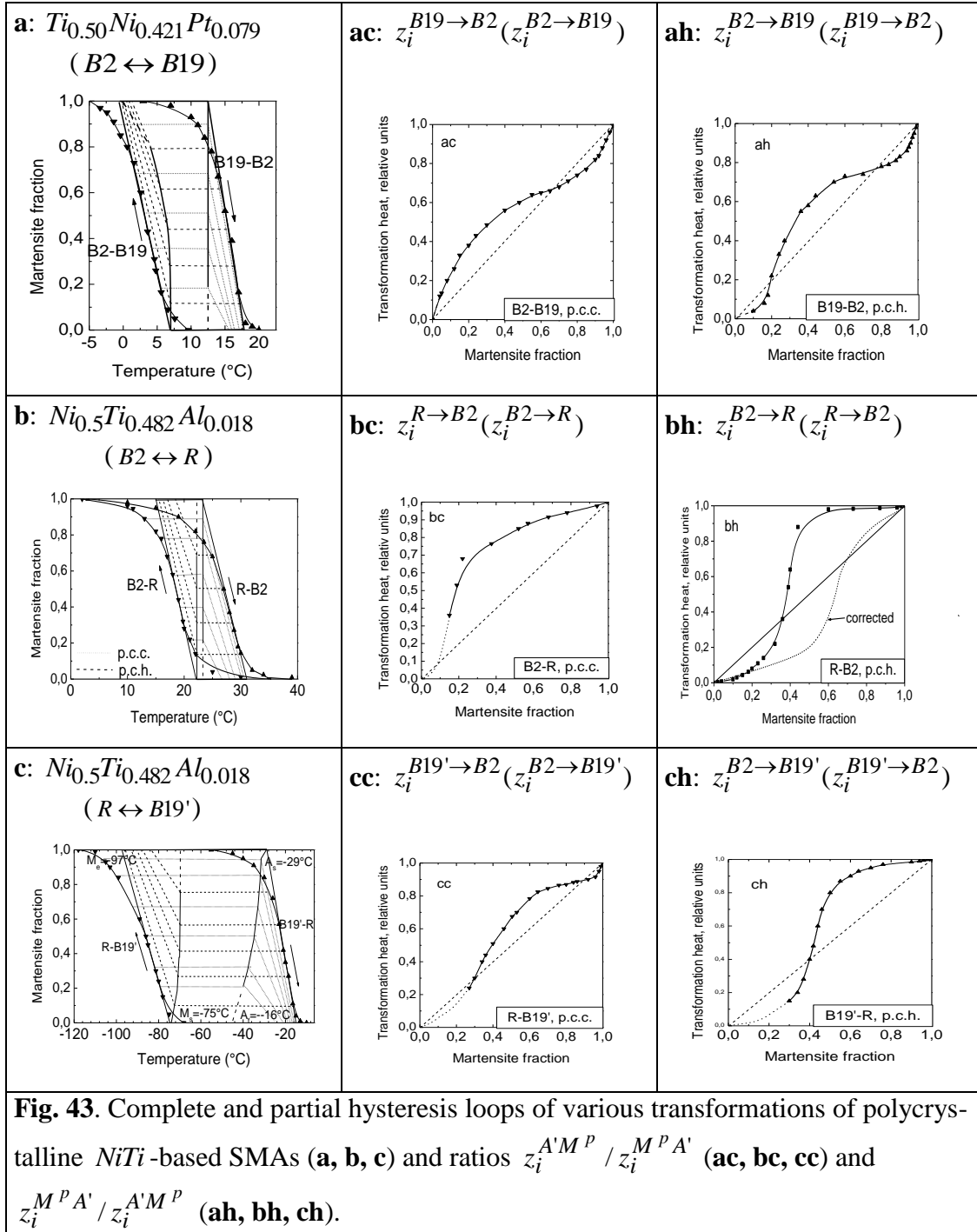
5.5 Relationships between phase fraction and transformation heat

5.5.1 Hysteresis interior, equilibrium and transformation trajectories

The RPM-effect in thermo-induced transformation cycles was discovered by investigating the hysteresis interior by means of partial forward and reverse transformation cycles in calorimeter [11, 14, and 15]. The hysteresis loops are determined from the calorimetric measurement curves $h(T)$ (4.3.2). First, complete forward transformation cycles were recorded and the corresponding values of the latent transformation heat for the complete forward ($q_c^{A^P M^P}$) and reverse transformations ($q_c^{M^P A^P}$) as well as complete $z_c(T)$ and partial $z_i(T)$ hysteresis loops were determined (**Figs. 13, 16 and 43 a, b, c**) [11, 15].

The reverse transformations was stopped in partial cycles at the temperatures T_i , which were gradually lowered according to scheme (5.4.2), and the complete forward transformation of the austenite phase fraction

$[1 - z(T_i)]$, formed during the partial revers transformations, into the martensite was carried out by cooling down to the temperature $T < M_f$.



Likewise, the forward transformations was stopped at different temperatures T_i according to a similar scheme $T_i = M_f + i \cdot \Delta T$, and the complete

transformation of the martensite phase fraction $z_i = z(T_i)$, formed during the partial forward transformation, into the austenite was carried out by heating up to always the same temperature $T > A_f$.

The forward and reverse transformation start temperatures determined from these internal transformation trajectories by the extrapolation method represent two lines $M_s(z)$ and $A_s(z)$ for all transformation of all investigated SMA's (*Figs. 43 a, b, c*).

The course of these $M_s(z)$ - and $A_s(z)$ -lines reflects the redistribution of the elastic energy between the both phases and the corresponding shift in the equilibrium temperature $T_0'(z)$ during the forward and reverse transformations, as discussed in the theoretical treatment in §3.2.2. The two lines also form an internal loop, which can be interpreted as latent hysteresis. The design and the course of these lines are so different that it is hardly possible to determine common principles.

The trajectories $M_s(z)$ in the transformations with a narrow and symmetrical hysteresis loops are straight lines parallel and close to the trajectories $A_s(z)$ and in some cases perpendicular $\frac{dM_s(z)}{dz} = 0$ to the temperature

axis (*Fig. 43 b*). The case $\frac{dM_s(z)}{dz} = 0$ is observed for almost all transformations in the range $0 < z < 0.4$ that corresponds to the instability

$$\frac{d^2 F^{A'+M^P}}{dz^2} < 0 \text{ range of the two-phase mixture analyzed in (4.2.20).}$$

In this area, the formation of ever new $A'M^P$ phase boundaries dominates through their annihilation and the emergence of the internal marten-

sitic $M^P M^P$ polydomain boundaries. After that at $z > 0.5$, in some transformations but also in the whole range $0 < z < 1$ or in the theoretically calculated range $0.16 < z < 0.74$, the slope can either be negative $\frac{dM_s(z)}{dz} < 0$ (**Figs. 15 b. 43 a**) or positive $\frac{dM_s(z)}{dz} > 0$, especially for the transformations with large hysteresis (**Figs. 15 a, 43 c**).

As already analyzed above, a negative slope $\frac{dM_s(z)}{dz} < 0$ or decrease $\frac{dT_0'(z)}{dz} < 0$ in the equilibrium temperature during the transformation is caused by increase in the free energy of the martensite phase due to the formation of internal martensitic micromonodomain boundaries (*stacking faults, the structural accommodation mechanism*) and $M^P M^P$ polydomain boundaries (*the morphological accommodation mechanism*). An increase $\frac{dT_0'(z)}{dz} > 0$ in the equilibrium temperature deals with a decrease in the stacking fault density in the martensite polydomains (*partial monodomainization*), which arise in the field of the remaining elastic shear stresses from the accommodated martensite polydomains and their conglomerates.

The presence of such stresses is responsible for the experimentally determined (**Fig. 17**) and above presented dilation effects (4.4.22) in SMA's. The more complex, curved lines point to a parallel effect of the both mechanisms considered above: Energy increase in the martensite phase due to internal martensitic boundaries and partial monodomainization of some martensite polydomains due to internal shear stresses.

The relationships $z_i^{A'M^P}(T_i) = q^{A'M^P}(T_i) / q_C^{A'M^P}$ ($M_f < T_i < M_s$) be-

tween the latent transformation heat and the martensite phase fraction determined experimentally, at which the forward transformation during cooling in i th partial cycle was interrupted, and the phase fraction of the martensite $z_i^{M^P A'}$ transforms back into the austenite during the subsequent heating show (**Fig. 43 ac, bc, cc**) significant deviations from the proportionality $z_i^{A' M^P} / z_i^{M^P A'} = 1$ of the latent transformation heat and the phase fraction of the transformed martensite, postulated in the thermoelasticity model (4.3.2). The same takes place under the opposite conditions, if the reverse transformation in i th partial cycle was interrupted and the resulting austenite completely transforms back into the martensite on cooling (**Fig. 43 ah, bh, ch**).

The latent transformation heat in the exothermic forward transformation is always smaller than that in the endothermic reverse transformation because of the entropy production (*the second law of thermodynamics*). Since the phase fractions are calculated using the ratio to their own latent transformation heat, this difference is excluded in graphic representations. For this reason, the functions $z_i^{M^P A'}(z_i^{A' M^P})$ (**Fig. 43 ac, bc, cc**) and $z_i^{A' M^P}(z_i^{M^P A'})$ (**Fig. 43 ah, bh, ch**) should each represent a diagonal, assuming the above mentioned proportionality.

However, calorimetry only deals with the latent transformation heat, while the elastic energies (3.2.19), (3.2.27) are not recorded. If the curve, e.g. in Figure 43 ch is added to that in Figure 5 a, where the latter should be multiplied by suitable absolute values K_{el} beforehand, the resulting line can already come close to the diagonal.

But the absolutely inadmissible behavior, which corresponds to the inju-

ry of the second law of thermodynamics (**Fig. 42 f and 43 bh**) [15], obviously requires a completely other correction. The behavior completely contradicts the main concern of the thermoelasticity model, namely that the martensitic transformation of SMA's strictly follows the temperature change (*athermal kinetics*), as observed by Kurdjumov [4].

It can be seen (**Fig. 42 f**) that the gradual lowering of the turning temperature T_i in partial reverse transformation cycles (*p.c.h.*), i.e. the gradual reduction of the endothermic latent transformation heat $q_i^{M^P A'} = z_i^{M^P A'} \cdot q_c^{M^P A'} > q_{i+1}^{M^P A'}$, does not change the calorimetric measurement curve and thus does not reduce the exothermic latent transformation heat $q_i^{A' M^P} = z_i^{A' M^P} \cdot q_c^{A' M^P} = q_{i+1}^{A' M^P}$ in the subsequent forward transformation (**Fig. 43 bh**). The behavior was also observed in papers [25, 102], accepted as such and interpreted as the absence of internal shear stresses, since there is no shift in temperature $M_s(z)$ in partial cycles (**Fig. 42 f**).

Only at a temperature $T_i = A_i$ that corresponds to the austenite phase fraction of $(1-z) \approx 0.6$ (*approx. 40% reverse transformed martensite*) occurs the first reduction in the exothermic latent transformation heat. This means two things: Firstly, the latent transformation heat emitted during exothermic forward transformations soon exceeds the heat absorbed during partial endothermic reverse transformation, i.e. the energy production, which is own for "perpetuum mobile" and forbidden by the 2-nd law of thermodynamics, takes place in a system that is not completely closed. Or secondly, the reverse transformation has already been completed ($z_i = 0$) at the turning temperature $T_i = A_i \equiv A_f$, and the area recorded in complete

transformation cycles in the calorimeter only shows the aftereffect ("heat tail") that is recorded by the measuring device after the heat source has been switched off (**Fig. 42 f**, *checkered area*).

5.5.2 Transformation velocity and latent transformation heat

The 2-nd law of thermodynamics is saved at the expense of the main concern of the thermoelasticity model, according to which the change in the martensite phase fraction is controlled directly by the temperature change, if the line $z_i^{A'M^P}$ ($z_i^{M^PA'}$) is converted with this assumption $z_i^{M^PA'} = 0$ instead of $z_i^{M^PA'} = 0.4$. The new corrected line is then closer to the diagonal (**Fig. 43 bh**, *dashed line*). All transformations with a small hysteresis (*narrow hysteresis loop*) such as the $B2 \leftrightarrow B19$ -transformations with an invariant plain in $Ti_{0.5}Ni_{0.4}Pd_{0.1}$ have such a "criminal" anomaly.

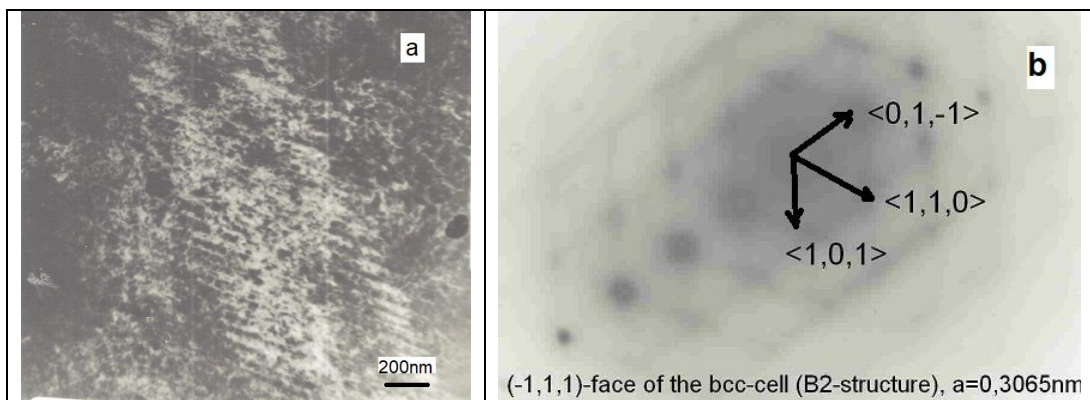


Fig. 44. TEM-image of the twin boundaries traces (*stacking faults*) of a martensite polydomain after their disappearance directly in the electron microscope due to the energy effect of the electron beam (**a**) and electron diffraction pattern of the $B2$ -austenite (*foil surface* $(\bar{1}11)_{B2}$) from the same point (**b**). $Ti_{0.5}Ni_{0.4}Pd_{0.1}$ -polycrystal, $B2 \leftrightarrow B19$ -transformation with invariant plane, temperature interval of the reverse transformation $A_s \div A_f = (24 \div 30)^\circ C$, hysteresis width $8^\circ C$.

In TEM-investigations of polycrystalline $Ti_{0.5}Ni_{0.4}Pd_{0.1}$ -SMA's, it was possible to observe how a martensite polydomain that was present at the room temperature imploded or collapsed approximately in 1s as soon as the

electron beam was directed on it, in doing so, it leaves an "imprint" of its twin substructure (**Fig. 44 a**). The imprint shows the stacking faults inherited from the austenite, because the electron diffraction pattern shows no trace of the martensite reflexes and clearly consists only of the reflexes of the high-temperature *B2*-phase (**Fig. 44 b**).

These results support the above thesis that the martensitic reverse transformation as a reverse of the martensitic lattice deformation is not only decoupled from the temperature change and its own heat front, but also from the regression of its twin substructure in SMA's with a low hysteresis and can be a lot faster than that observed by Kurdjumov on individual martensite crystals using a light microscope.

The heating from 20°C to the temperature $T = A_f = 30^{\circ}\text{C}$ lasts in calorimeter at the constant scanning rate of $\dot{T} = 4\text{K}/\text{min}$ (approx. $\dot{T} = 0.07\text{K}/\text{s}$) whole 150s . The apparent heating rate observed in the electron microscope at the time of martensite disappearance of 1s is approximately $10\text{K}/\text{s}$ or $600\text{K}/\text{min}$. An increase in the scanning rate leads to an expansion of the hysteresis loops determined from calorimetric data (**Fig. 45 a**) or the temperature range $M_f \div A_f$ of a complete transformation cycle (**Fig. 45 b**) [51]. This in turn limits the action frequency of a SMA-actuators (**Fig. 45 c**) to a few hundredths Hz . This frequency is below the value of 1Hz , which is claimed in other studies [103].

The action frequency of an SMA-actuator $f_a = t_a^{-1}[\text{Hz}]$ is calculated from the total time t_a required for a complete transformation cycle [63, 64]:

$$f_a = \left\{ 2 \cdot \frac{[A_f(0) - M_f(0)] + (k_{A_f} - k_{M_f}) \cdot \dot{T}}{\dot{T}} \right\}^{-1}. \quad (5.5.1)$$

To carry out a complete transformation cycle (*action cycle*), an SMA-actuator must be cooled once and heated once through the entire temperature interval of the transformation $\Delta T(\dot{T}) = A_f(\dot{T}) - M_f(\dot{T})$, taking into account its expansion (**Fig. 45 b**):

$$\begin{aligned} M_f(\dot{T}) &= M_f(0) + k_{M_f} \cdot \dot{T} \\ A_f(\dot{T}) &= A_f(0) + k_{A_f} \cdot \dot{T} \end{aligned}, \quad (5.5.2)$$

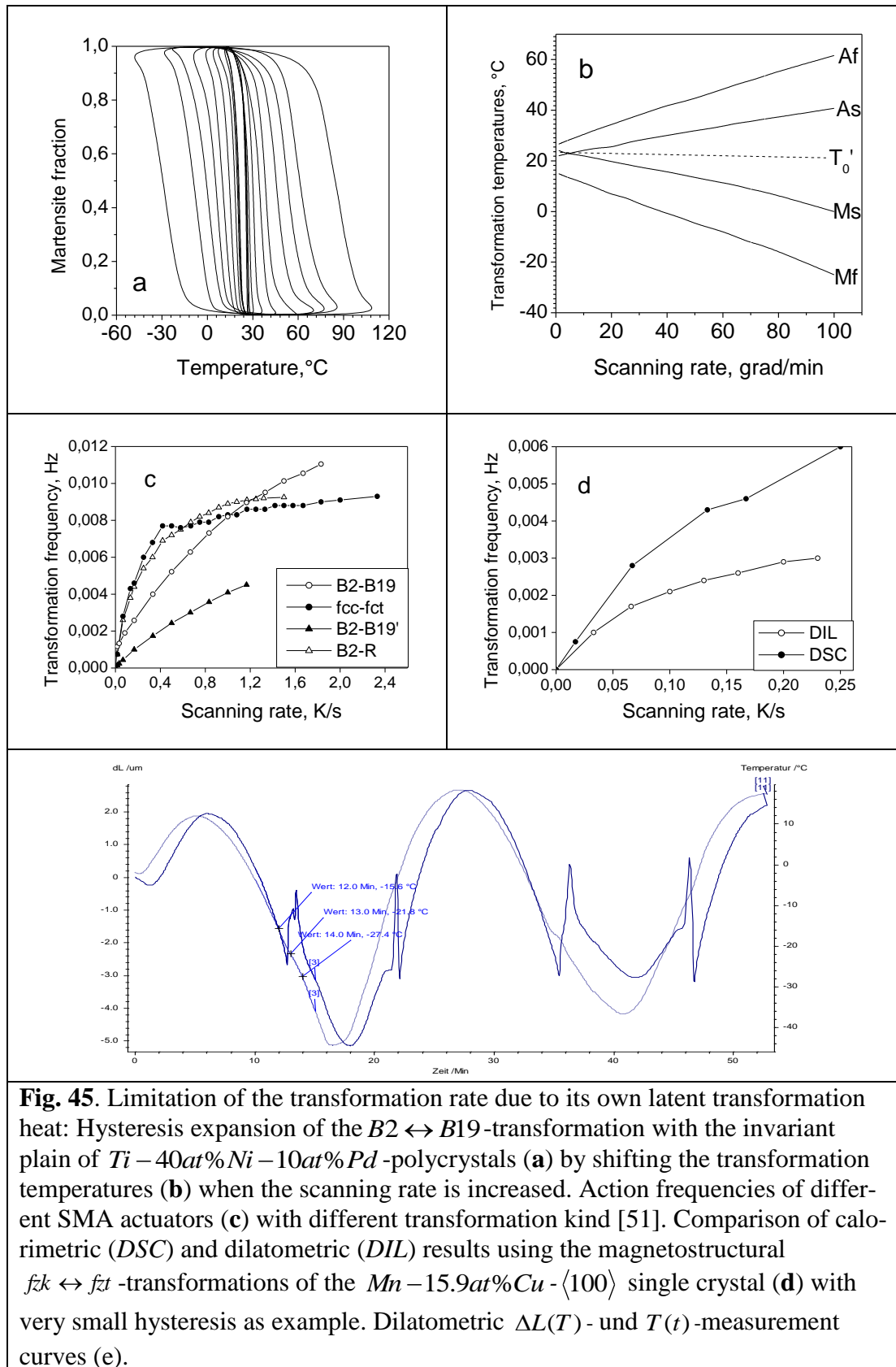
where $k_{A_f} = \frac{dA_f(\dot{T})}{d\dot{T}} = -k_{M_f} = \frac{dM_f(\dot{T})}{d\dot{T}}$ are the coefficients of the hysteresis expansion to be determined experimentally, $M_f(0)$ and $A_f(0)$ are the values extrapolated to $\dot{T}(0)$ (**Fig. 45 b**).

The heat balance in a complete transformation cycle of a SMA-actuator is described by two terms: One term for its convective cooling in the air through a heat radiation surface A_a , convection coefficients λ from a temperature $T = A_f(\dot{T})$ to a temperature $T = M_f(\dot{T})$:

$$\frac{\lambda \cdot A_a \cdot (M_f(\dot{T}) - A_f(\dot{T}))}{m_a} = c_p \cdot (T - A_f(\dot{T})) + \Delta q^{A'M^P} \cdot z(T) \quad (5.5.3)$$

and the second term for its adiabatic heating by means of an electric current with amperage I from a temperature $T = M_f(\dot{T})$ to a temperature $T = A_f(\dot{T})$:

$$\frac{I^2 \cdot R_a \cdot t}{m_a} = c_p (A_f(\dot{T}) - M_f(\dot{T})) + \Delta q^{M^P A'} \cdot z(T), \quad (5.5.4)$$



where c_p is the specific heat capacity, m_a and R_a are the mass and elec-

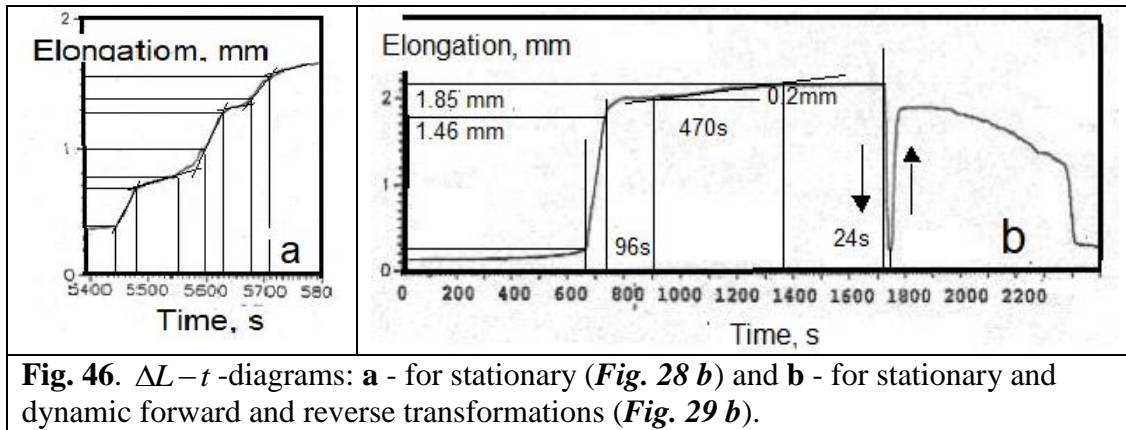
trical resistance of the SMA-actuator. The second terms in the both equations are the specific latent transformation heats $\Delta q^{A'M^P} = T_0' \cdot \Delta s^{A'M^P}(z)$ of the exothermic forward transformation and $\Delta q^{M^PA'} = T_0' \cdot \Delta s^{M^PA'}(z)$ of the endothermic reverse transformation, where T_0' is the local equilibrium temperature of the $A' \leftrightarrow M^P$ -transformations, $\Delta s^{A'M^P}$ and $\Delta s^{M^PA'}$ are the specific (*per mass unit*) transformation entropies, z is the martensite phase fraction. The latent transformation heats are of the same magnitude order as the Joule heat in the first terms of these equations.

This means that both cooling and heating require twice the amount of energy and last much longer than cooling and heating a metal body with the same parameters, but without a phase change. The latent transformation heat is also responsible for the extension of the transformation temperature intervals $M_f(\dot{T}) - A_f(\dot{T})$ and $(A_f(\dot{T}) - M_f(\dot{T}))$ in the first terms of equations (4.5.3) and (4.5.4), which causes a further energy expenditure and a further slowing down of the heat transfer in a complete cycle of the martensitic transformation. The physical limitation of the increase in the operating frequency of an SMA-actuator (4.5.3) despite the increase in the heating and cooling rate (**Fig. 45 c**) is due to the both factors.

The example with the transformation caused by the movement of a single phase boundary can show which real velocity have the martensitic transformations. The velocities are determined from the $\Delta L - t$ -diagrams (**Fig. 46 a, b**) (4.1.3), which correspond to the isostress-isothermal deformation diagrams (**Figs. 28 b, 29 b**):

$$v_M \equiv \dot{B}_M = \frac{d(\Delta L)}{\varepsilon_M dt} \approx (1 \div 2) \cdot 10^{-4} m \cdot s^{-1}, \quad (5.5.5)$$

where $\varepsilon_M \approx 0.07$ is deformation within the martensite band (**Fig. 27 d**). These velocities vary (**Fig. 46 b**) from $v_c \approx 6 \cdot 10^{-6} m/s$ when creeping (0.2mm) in indifferent equilibrium, $v_s \approx 2 \cdot 10^{-4} m/s$ under stationary conditions (1.46mm) and $v_{ad} \approx 1.1 \cdot 10^{-3} m/s$ under dynamic (*adiabatic*) conditions (1.85mm).



Even at the relatively high velocity $v_{ad} \approx 1.1 \cdot 10^{-3} m/s$, at which a complete transformation-deformation-cycle takes place in time of $t_c \approx 50s$ (**Figs. 29 c, 46 b**), the action frequency does not exceed the value of $f_a \approx 0.02 Hz$, what only confirmed the limit values of $(0.010 \div 0.012) Hz$, determined above (**Fig. 45 c**). It can be seen (**Fig. 46 a**) how the martensite boundary is repeatedly slowed down during its stationary movement after the “fast” sections ($v_s \approx 1.2 \cdot 10^{-4} m/s$), obviously through local defects or through its own heat in the range $0.7 mm < \Delta L < 1 mm$ (**Fig. 28 b**).

The question as to whether the discrepancy between the transformation finish temperature in the heat measurements and the real (*crystallographic*) transformation end in calorimetry occurs as a method-related fault was checked by the dilation measurements [49] (**Fig. 45 d**). It has been found that the action frequency determined dilatometrically, i.e. by measurements

of real crystallographically caused changes in length, is even lower than determined calorimetrically.

However, there are still doubts about possible methodological artifacts. From the dilation measurement curves (*Fig. 45 e*) it can be seen that the change in length (*the reaction*) always takes place with a time delay compared to the change in sign of the sampling rate (*from cooling to heating*), the time lag being in the range of minutes.

In the function $T(t)$ is T the temperature measured on the surface of the dilatometric sample, which is much more massive compared to the calorimetric one, while $\Delta L(t)$ -function represents the volume response of the entire massive sample ($2.0 \times 2.5 \times 10 \text{ mm}^3$) to the temperature change within this volume. This time delay is caused by the additional time required to achieve temperature equilibrium between the sample surface and the center of the solid sample by means of the heat conduction.

Unfortunately, such a time delay cannot be methodically investigated in the calorimeter for much smaller samples (*disks with a diameter of 4.0 mm and a thickness of 1.0 mm*) with direct contact with the heat transfer floor of the measuring chamber. In any case, the same problem also exists for SMA actuators under real working conditions, which one tries to solve by means of actuator miniaturization.

These results, together with those for the isostress-isotherm martensitic transformation with a single phase boundary, disprove the thermoelastic character of the martensitic transformations of SMA's, at least for transformation with a smaller hysteresis as those for $B2 \leftrightarrow 9R$ in $\text{Cu} - \text{Al} - \text{Zn}$ single crystals, $B2 \leftrightarrow B19$ with an invariant plain in NiTiX -polycrystals and in NiTi single crystals or $\text{fcc} \leftrightarrow \text{fct}$ in MnCu single crystals.

Intensive investigations aimed at solving the inertia problem of SMA's like [104-108] focus mainly on increasing the action frequency of SMA-actuators by means of their miniaturization [105], the use of alternative, more effective cooling methods, e.g. with the help of thermoelectric Peltier elements [106] and the development of new SMA's, in which the transformation cannot be controlled by the temperature or stress changes, but by changes in the electrical or magnetic field [107]. In this way, frequencies up to $10Hz$ are reported [104].

Action frequencies of up to $100Hz$ have theoretically been predicted by the miniaturization of SMA-actuators (*SMA foils with a thickness of up to $1 \div 2\mu m$*) and conventional cooling methods with the assumption [108] that the hysteresis width remains constant with an increase in the scanning rate. The transformation kinetics or a possible physical limitation of the transformation velocity is hardly taken into account in any of these studies and models.

Assuming the case that the crystallographic reverse transformation from its own heat front is separated as discussed above (**Fig. 44**) at $0.6\Delta q^{M^P A'}$, so that the action frequency is increased by such a shortening up to $100Hz$, the heat $Q = m_a \cdot 0.4\Delta q^{M^P A'} \cdot 100Hz$ accumulates in the SMA actuator.

The heat leads to $\Delta T = \frac{Q}{m_a \cdot c_p} \approx 4000 \frac{^\circ C}{s}$ temperature increase at

$\Delta q^{M^P A'} = 10^4 J/kg$ (**Fig. 15**) and $c_p^{Cu} = 10^2 J/kg \cdot grad$, i.e. a temperature increase already after a one action period far above the melting temperature of each SMA-actuator.

The experimental results presented above show that there is such an in-

ternal limitation on the transformation rate. An increase in the external scan rate does not lead to a proportional increase in the internal transformation velocity, but to an expansion of the temperature interval of the forward and reverse transformations proportional to the scanning rate. The entire process is limited by the slower process participant, namely by the growth and shrinkage of the martensite polydomains, the inertia of which is caused by its own transformation heat.

6 Conclusion

The quantifying concept of the dual-energetic martensite (*CODEM*) presented here is based on the fact, which has been proven in numerous and varied experiments, that the martensitic transformations and the associated phenomena in SMA#s are due to two energetically different martensite forms.

The first form is a martensite macromonodomain M^m , which can be represented as a whole as a result of the homogeneous martensitic lattice shear deformation γ_M of the austenite lattice. The second form is a completely accommodated ($\varepsilon_M = \gamma_M(1 - k_a^I) = 0$) martensite polydomain M^P , which arises from secondary invariant shifts within a macromonodomain (*structural accommodation mechanism*) and consists of isosceles twins each containing a stacking fault. The free energy of such a martensite polydomain is higher than that of the martensite macromonodomain of the same size/mass by the sum of all its stacking fault energies.

A twin part of the martensite polydomain substructure, as an area with the maximal martensitic shear deformation γ_M ; in which the shear vector \vec{e}_M does not change its direction, is defined as a martensite micromonodomain M_m^m and is regarded as an elementary part of the martensite phase with a stacking fault. The energy range between the energy of a martensite macromonodomain and that of a martensite polydomain can be

quantified into an energy spectrum $\sum_{i=0}^{N^{M_m^m}} u_{i,i+1}$ by defining the martensite

micromonodomain with an energy quantum $u_{i,i+1}$, where $i=0$ applies to

the martensite macromonodomain and $i = 1, \dots, N_m^m$ to all existing martensite polydomains with different numbers of micromonodomains N^{M^m} or with different monodomainization degrees.

A martensite polydomain has a lower macro symmetry with the same micro symmetry of the unit cell, smaller entropy and a free energy higher than that of a martensite monodomain by a contribution $U_{sf}^{M^P}(z, T)$ from stacking fault energy.

The global equilibrium temperature T_0 is determined by the equality of the free energies of the stable austenite A and a martensite macromonodomain M^m . It is significantly higher than the local equilibrium temperature T_0' , which is determined by the equality of the free energies of the metastable austenite A' and a martensite polydomain M^P . The global equilibrium temperature T_0 represents a fundamental material quantity, while the local equilibrium temperature T_0' is very variable and is influenced by several, primarily metallurgically factors.

The martensitic $A \rightarrow M^m$ -transformation in the vicinity of the global equilibrium temperature T_0 is prevented by the large elastic energy barrier U_B , but the austenite A' that still exists and has a higher free energy becomes metastable in the temperature range $T_0 \div T_0'$. This range is distinguished by well-known premartensitic phenomena such as the softening of the elasticity modulus, the formation of fluctuating intermediate shear structures, pseudoelasticity along the equilibrium line $\sigma_0(T)$ defined by the Clausius-Clapeyron equation.

The difference $\Delta T = T_0 - T_0'$ between the both equilibrium temperatures

is determined by the generalized stacking fault energy γ as a material constant and the average stacking fault density $\bar{\nu}_{sf}$ of the martensite polydomains, which is strongly dependent on internal stresses. These arise below the local equilibrium temperature $M_s' < T_0'$ due to the nucleation when the energy barrier $U_B = \Delta T \cdot \Delta S^{M^m M^p}$ is reduced by the entropy contribution. The internal stresses also depend on the rationality of the Miller indices (hkl) of the habit planes of the martensite polydomains and the Schmid's orientation factor $\mu = \cos\phi \cdot \cos\varphi$ of the martensitic shear system $(hkl)[uvw]$ relative to the external stress axis or the single crystal longitudinal axis $[hkl]_A$.

The main sources of the elastic stresses and thus the excessive elastic energy in the two-phase state are the $A'M^P$ phase boundaries between the metastable austenite and the martensite polydomains. The elastic boundary stresses are due to the incompatibility of the crystal lattices of the two phases. The incompatibility is minimized by the structural accommodation, which consists in the formation of a twin substructure with a stacking fault density ν_{sf} within each martensitic polydomain and, in this way, the martensitic lattice deformation γ_M minimizes to a martensitic deformation ε_M so that the boundary stresses $\sigma_M = G \cdot \varepsilon_M < \sigma_y^{A'}$ are staying in the elastic range of the austenite matrix.

The elastic energy of $A'M^P$ phase boundaries increases the free energies of metastable austenite and polydomain martensite equally and consequently of the whole two-phase system without affecting the two-phase equilibrium. Such an energy increase in the two-phase system causes the

necessity of permanent undercooling in order to drive the martensitic transformation forward, which is the reason for the athermal transformation kinetics as the main matter of the thermoelasticity model.

The elastic interaction of the $A'M^P$ phase boundaries as the morphological accommodation mechanism leads to the coalescence of single variants of martensite polydomains to their conglomerates with the pairwise annihilation of the $A'M^P$ phase boundaries and the formation of an internal martensitic $M^P M^P$ polydomain boundary. The elastic energy of the internal martensitic boundaries only increases the free energy of the polydomain martensite and shifts the two-phase equilibrium to lower temperatures. This only happens from a martensite phase fraction about $z \approx 0.4$, in which the dominant effect of $A'M^P$ phase boundaries in the balance of elastic energies changes to dominance of internal martensitic $M^P M^P$ polydomain boundaries through morphological accommodation.

The coalescence of the martensite polydomains causes a complete redistribution of the stress fields in their environment, which leads to a reduction in the stacking fault density in the polydomain substructure, minimizes the free energy of the martensite and shifts the two-phase equilibrium to higher temperatures.

The interaction of the structural and the morphological accommodation results in a complex redistribution of the elastic energy in the two-phase system, which is modeled as a power function $u(z) = (2z - 4z^2 + 3z^3)$ of the martensite phase fraction. Analysis of this function reveals three areas of increase in the martensite phase fraction: The unstable acceleration area $0 < z < 0.16$ of autocatalytic nucleation, the almost linear area

$0.16 < z < 0.74$ of rapid increase between the maximum at $z = 0.16$ and the minimum at $z = 0.74$ of the elastic energy, and the area $0.74 < z < 1$ of slowed increase. In the third area, the last ever smaller austenite gaps are closed by the coalescence of martensite polydomains.

The reverse transformation takes place in the reverse sequence and begins with austenite nucleation as the splitting of an internal martensitic $M^P M^P$ polydomain boundary into two $A' M^P$ phase boundaries. The analysis shows that the main thesis of the thermoelasticity model about the storage of elastic energy, what is probably meant is the energy of $A' M^P$ phase boundaries in austenite, corresponds only very general and very conditional to real redistribution of the elastic energy of the $A' M^P$ phase boundaries, of the internal martensitic $M^P M^P$ polydomain boundaries and of the twin boundaries (*stacking faults*) and their simultaneous intensive dissipation in the entire two-phase range. The driving forces designated as non-chemical f_{nch} and dissipative f_{dis} cannot be separated analytically in the balance of the driving forces $f_{nch} + f_{dis} = K_{el} \cdot (9z^2 - 8z + 2)$ as derivatives of the same elastic energy.

This complex redistribution of the elastic energy results in a complex, hardly predictable course of the equilibrium temperature trajectory $T_0'(z)$ and the transformation trajectory $z(T)$ during the transformation. This is also accompanied by the intense dissipation of the elastic energy released by the coalescence of martensite polydomains.

The quantifying concept of two energetically different martensite forms – with and without substructure, in which the generalized stacking fault energy and the stacking fault density play a decisive role, and each of their

changes not only influences the equilibrium temperature, but also the hysteresis width of the martensitic $A' \leftrightarrow M^P$ -transformations – explains in the simplest possible way the most phenomena known in SMA's. It has also been adequately proven in a lot of illustrious experiments.

Experimental methods and procedures are described, which are particularly suitable for the SMA-investigations and substantiate the postulates of the CODEM. Experimental data for many SMA's are presented. They show the maximal exploitation of both the method possibilities through suitable broad aim setting and experiment planning as well as the measurement results through their analysis and calculation of all derived parameters.

Measurement of acoustic emission (*AE measurement method*) is only one method that is suitable for direct registration of energy dissipation. The *AE* measurement curves show that the annihilation of $A'M^P$ phase boundaries makes the largest contribution to the AE-intensity, i.e. to the dissipation of the elastic energy. The *AE* method is one of the simplest and fastest of the known measurement methods for determining the characteristic transition temperatures. It is therefore suitable for express analysis when producing (*melting*) SMA's and is used to specify the composition during melting.

Resistometry is also a simple and most widely used method for directly recording the transformation hysteresis $R(T, z)$ and determining the characteristic transformation temperatures. The linear temperature dependence of the electrical resistance within the transformation temperature ranges, however, distorts the loop of the thermal hysteresis and must be taken into account at the determination of the transformation temperatures. This

method is also well suited for studies of mechanical hysteresis at the quasiplastic, pseudoelastic and ferroelastic deformation. Here, the geometric factor ensures strong distortion and asymmetry of the mechanical hysteresis loops on the tension and compression sides and must be excluded when analyzing measurement curves $R(\sigma^{t,c})$ and $R(\varepsilon_{q,p,f})$. With the help of resistometry, however, the phase fraction of the stabilized martensite can also be determined, i.e. an indirect phase analysis can be carried out.

Calorimetry provides the direct and calculated thermodynamic transformation parameters that are necessary for calculating the energetic characteristics of the thermal hysteresis. The technically complex measuring method is mostly only used to determine the characteristic transformation temperatures for the certification of SMA's. This certification is also worthless, because the transformation temperature range depends linear on the scanning rate when measuring the latent transformation heat.

The calorimetrically determined thermal hysteresis loops $z(T)$ are free of distortion compared to other methods and apart from the dependence of the hysteresis width on the scanning rate, which makes this method well suited for the investigation of the internal hysteresis in partial thermal cycles. These investigations show the presence of a latent hysteresis between two lines of local equilibrium in SMA's with large transformation hysteresis. The equilibrium temperature trajectory deviate at $z > 0.4$ from vertical lines according to the redistribution of the elastic energy during the transformation. The martensite stabilization through the monodomainization or the texturing and the plastic deformation was investigated with the help of calorimetry. The martensite macromonodomains have the transformation temperatures up to 100°C higher than those of the martensitic polydomains.

The martensite monodomainization in several action cycles leads to the degradation of the memory properties of SMA-actuators, because an ever larger phase fraction of the martensite is switched off as a memory carrier by increasing the reverse transformation temperature above the action temperature range. The complete rehabilitation of the shape memory properties, which have degraded after several action cycles, is achieved by short-time heating above the temperature $T = A_f^{M^p A'} + 100^\circ\text{C} \rightarrow A_f^{M^m A}$ of the reverse $M^m \rightarrow A$ -transformation without damaging the entire device and without impairing other mechanical properties of the SMA-actuator through this heat treatment.

The true plastic deformation of martensite increases the reverse transformation temperatures up to the activation temperature $T_a \approx 0.4T_m$ of the multiplication and movement of dislocations (*e.g. approx. 300°C for Cu-based SMA's with the melting temperature $T_m = 1360\text{K}$*). This allows the two stabilization mechanisms clearly to separate and shows that the true plastic deformation does not play a role in martensite stabilization either in thermal- or in stress-induced transformations and transformation cycles.

It was also calorimetrically determined and confirmed by the isostress-isothermal transformation with a single phase boundary that even the basis of the thermoelasticity model, the thermoelastic behavior, i.e. control of the martensite growth and shrinkage by temperature changes or the proportionality between the martensite phase fraction and the latent transformation heat $z(T) \propto q(T)$ are not true in any case for the SMA's with a small transformation hysteresis. The lattice reverse transformation can detach itself not only from its own latent heat front, but even from its own twin substructure, as the TEM-images also show, and finishes faster on your own.

Spontaneous length changes $\Delta L(T)$ depending on the temperature of non-stressed and non-textured SMA-samples in the two-phase temperature range are recorded directly as hysteresis loops with a help of the dilatometry method. The dilation is caused by the non-accommodated martensitic deformation in the elasticity range of the austenite. This measuring method is the only one that offers the possibility to determine the accommodation degree k_a , but without separately determining the contributions of the structural and morphological accommodation. The accommodation degrees achieved by the two accommodation mechanisms are calculated from the measured dilatations ε_d and vary in the range of $0.997 \geq k_a \geq 0.750$ in all investigated SMA's, so that the spontaneous dilatation remains in the elastic range $\sigma_d < G \cdot \varepsilon_d < \sigma_y$ even with the minimal determined accommodation degree.

The tension-compression deformation method is particularly informative when investigating the mechanical quasiplastic, pseudo- and ferroelastic hysteresis and its interior in partial deformation cycles. Nevertheless, this method is seldom used in experimental investigations. It is apparently because the tensile and compression specimens are subject to different normative requirements for their design. However, the application of these standards to the SMA-specimens is not absolutely necessary because of the much smaller mechanical stresses than at the usual standard tests and can be bypassed with the simplest means.

A number of new knowledges have been ascertained in this process: The independence of the mechanical hysteresis from the temperature at the transition from pseudoelasticity to ferroelasticity, affinity of ferroelastic and ferromagnetic hysteresis, the orientation dependency of mechanical hysteresis, the liquid-like ferroelastic behavior of the single crystal speci-

mens with the orientation axis $\langle 100 \rangle_{B2}$ of the slight deformation, the equilibrium stress line $\sigma_0(\varepsilon_{p,f}) = const$ within the pseudoelastic and ferroelastic hysteresis, which is adequate to the Maxwell line in Van der Waals gas theory.

Formation of a martensite macromonodomain from the thermo-induced polyvariant polydomain martensite only takes place through the complete cycles of the ferroelastic deformation and not through the quasiplastic deformation, as it shows the RPM-effect in partial cycles of the first compression deformation with two yield points and flow lines. The martensite macromonodomain transforms back to the austenite $M^m \rightarrow A$ at elevated temperatures. This provides one of the experimental existence proofs of the $A \leftrightarrow M^m$ -transformations, the thermodynamic parameters of which could even be determined calorimetrically.

The thermo-induced martensitic $B2 \leftrightarrow 9R$ -transformations with a single phase boundary under constant load in $Cu - Al - Zn$ single crystals show the characteristics of the $A \leftrightarrow M^m$ -transformations and can also be regarded as an experimental proof of this concept.

The important role of the stacking fault energy and density for the characteristic transformation temperatures has also been proven experimentally. The martensite stabilization in Cu -based SMA's, which leads to the expansion of the pseudoelastic and ferroelastic hysteresis loops during aging, is caused by diffusion of stoichiometrically excess non-equilibrium vacancies to the stacking faults in the polydomain martensite. The expansion of the thermal hysteresis loop in irradiated $NiTi$ -SMA's can also be explained by the diffusion of radiation defects in the stress gradients caused by irradiation.

The reduction in the stacking fault density in the martensite phase due to the ferroelastic deformation cycles or also in the single martensite polydomains due to changes in the stress field in their immediate vicinity, which is regarded as monodomainization in the quantifying CODEM, causes the actual martensite stabilization in the sense of increasing its reverse transformation temperatures in the temperature range $T_0 \div T_0'$ corresponding to the changing in the stacking fault density $0 \leq \bar{v}_{sf} \leq 1$. This explains **RPM**-effects (**Return Point Memory**) in partial cycles of ferroelastic deformation and in partial cycles of thermo-induced reverse transformations (*also known as the SMART effect or TAME*).

Many of the experimental results obtained so far on the SMA's can no longer be explained by the thermoelasticity model, and some even directly contradict its main postulates. The quantifying concept of **dual-energetic martensite (CODEM)**, on the other hand, has been thoroughly proven experimentally and provides comprehensive and plausible explanations for most of the known shape memory phenomena.

7 References

1. "Shape Memory Effects in Alloys" (Proc. of Int. Symp. on Shape Memory Effect and its Application, Toronto, 1975). Editor Jeff Perkins. Plenum Press, New York and London, 1975.
2. H. Funakubo (*Ed.*). Shape Memory Alloys, Gordon and Breach Science Publishers, 1987.
3. Y. Matsuzaki. Smart structures research in Japan. – Smart Mater. Struct. 6(1997) R1
4. G. V. Kurdjumov, L. G. Khandros, First reports of the thermoelastic behaviour of the martensitic phase of *Au-Cd* alloys. Doklady Akademii Nauk SSSR 66 (1949) 211.
5. V. Prieb. The mechanical behaviour of a *Cu-Al-Zn* shape memory alloy with a single-interface transformation. – Proc. of the 4th Int. Conf. on New Actuators "ACTUATOR '94", Bremen 1994, 365.
6. H.C. Tong, C.M. Wayman. Characteristic temperatures and other properties of thermoelastic martensites. Acta Metallurgica 22 (1974) 887.
7. I. Cornelis, C.M. Wayman. Experiments on hysteresis in a thermoelastic martensitic transformation. Scripta Metallurgica 10 (1976) 359.
8. Yu.I. Paskal' and L. A. Monasevich. Hysteresis features of the martensitic transformation of titanium nickelide. Fiz. Metal. Metalloved. 5 (1981) 1011.
9. V. Prieb, T. Link, M. Feller-Kniepmeier, H. Steckmann, N. Poljakova, V.A. Udovenko. Influence of the structure and orientation of the parent phase on the hysteresis of single-crystal shape memory alloys. Journal de Physique 5 (1995) C8-913.
10. V. Prieb, H. Steckmann. Pseudo-plastic behaviour in single-crystals of Cu-base memory alloys. Journal de Physique 5 (1995) C8-907.
11. V. Prieb, H. Steckmann. Thermoelasticity and hysteresis of martensitic transformation in shape memory alloys. I. Hysteresis of the stress-free thermal transformation. Technical Physics 41 (1996) 1132.
12. V. Prieb, H. Steckmann. Thermoelasticity and hysteresis of martensitic transformation in shape memory alloys. II. Ferroelastic hysteresis in the straining of single crystals of copper-based shape memory alloys in the martensitic state. Technical Physics 41 (1996) 1137.
13. V. Prieb, H. Steckmann, S.L. Prokoshkin, G.G. Zak et al. Thermoelasticity and hysteresis of martensitic transformation in shape memory al-

- loys. III. Features of the hysteresis behaviour. Technical Physics 41 (1996) 1141.
14. H. Steckmann (V. Prieb). Thermoelastisches und Hystereseverhalten von einkristallinen Cu-Basis Formgedächtnislegierungen. Thesis der Doktorarbeit, Institut für Metallphysik, Kiew, Berlin-Kiew 1996, 155 S..
 15. V. Prieb, H. Steckmann, V. Wolff. The hysteresis loop interior of the thermoelastic martensitic transformation. „Kurdyumov Memorial International Conference on Martensite“. Moscow, 1999.
 16. V. Prieb, H. Steckmann, V. Wolff. Thermodynamic parameters of the martensitic transformation of *NiTi-X* shape memory alloys. Materials Sciences Transactions 6 (2000) 12.
 17. C. Quingfu, I. Hurtado, R. Stalmans, J. van Humbeeck. Stabilisation of Martensite During Training of *Cu-Al-Ni* Single Crystals. Journal de Physique 5(1995) C2-181.
 18. C Picornell, J Pons, E Cesari. Stabilisation of martensite by applying compressive stress in *Cu-Al-Ni* single crystals. Acta Materialia 49 (2001) 4221.
 19. Y. Liu, D. Favier, A. Joseph. Stabilisation of martensite due to shear deformation via variant reorientation in polycrystalline *NiTi*. Acta Metallurgica et Materialia 48 (2000) 3489.
 20. Y. Liu, G. Tan, S. Miyazaki. Deformation-Induced Martensite Stabilisation in [100] Single-Crystalline *Ni-Ti*. Materials Science and Engineering A 438-440 (2006) 612.
 21. G. Tan, Y. Liu. Comparative study of deformation-induced martensite stabilisation via martensite reorientation and stress-induced martensitic transformation in *NiTi*. Intermetallics 12 (2004) 373.
 22. M. Chandrasekaran, E. Cesari, J. Wolska, I. Hurtado, R. Stalmans, J. Dutkiewicz. Stabilisation of Martensite in Copper Based Shape Memory Alloys. Journal de Physique 5 (1995) C2-143.
 23. E.M. Mazzera, C.S. Kiminami, C. Bolfarini, R.D. Cava, W.J. Botta, P. Gargarella. Thermodynamic analysis of the effect of annealing on the thermal stability of a *Cu-Al-Ni-Mn* shape memory alloy. Thermochemica Acta 608(2015) 1.
 24. J. García. Stabilization of martensite in *Cu-Zn-Al* shape memory alloys: effects of γ precipitates and thermal cycling. Scripta Materialia 42 (2000) 531.
 25. K. Madangopal, S. Banerjee, S. Lele. Thermal arrest memory effect.

- Acta Metallurgica et Materialia 42 (1994) 1875.
26. G. Airoldi, G. Riva. Step-wise stress-free martensitic transformation in the *NiTi* system. Proc. of the European Conference on Martensitic Transformation in Science and Technology, 1889, Ruhr-Universität Bochum. Editors by E. Hornbogen, N. Jost. Bochum 1989, p. 305.
 27. G. Airoldi, G. Riva. Step-wise martensite to austenite reversible transformation stimulated by temperature or stress: a comparison in *NiTi* alloys. Materials Science and Engineering A 241 (1998) 233.
 28. S. Wang, K. Tsuchiya, L. Wang, M. Umemoto. Martensitic stabilization and defects induced by deformation in *TiNi* shape memory alloys. Int. J. of Minerals, Met. and Mat. 18 (2011) 66.
 29. V. L. Ginzburg, L. D. Landau: To the Theory of Superconductivity. In: Zhurnal Eksperimental'noj i Teoretitscheskoj Fiziki 20 (1950) 1064. Englische Übersetzung in: L. D. Landau: Collected papers. Pergamon Press, Oxford 1965.
 30. T. Suzuki, M. Wuttig. Analogy between spinodal decomposition and martensitic transformation. Acta Metallurgica 23 (1975) 1069.
 31. A. B. Greninger, A. R. Troiano. The mechanism of Martensite formation. Transaction AIME 185 (1949) 590.
 32. N.H.D. Ross, A.G. Crocker. A generalized theory of martensite crystallography and its application to transformations in steels. Acta Metallurgica 18(1970) 405.
 33. C. M. Wayman. The phenomenological theory of martensite crystallography: Interrelationships. Metallurgical and Materials Transactions A 25(1994)1787.
 34. R.S. Elliott, D. S. Karls. Entropic stabilization of austenite in shape memory alloys. Journal of the Mechanics and Physics of Solids 61 (2013) 2522.
 35. O. Benafan, R.D. Noebe, S.A. Padula, A. Garg, B. Clausen, S. Vogel, R. Vaidyanathan. Temperature dependent deformation of the *B2* austenite phase of a *NiTi* shape memory alloy. International Journal of Plasticity 51(2013)103.
 36. F. Iang, Y. Liu, H. Yang, L. Li, Y. Zheng. Effect of ageing treatment on the deformation behaviour of *Ti-50.9 at% Ni*. Acta Materialia 57 (2009) 4773.
 37. V. Sheremetyev, M.F. Ijaz, A. Kudryashova, A. Konopatsky, S. Prokoshkin, V. Brailovski. Characterization of the Superelastic and Struc-

- tural Characteristics of β -Ti Alloys by Strain-Controlled Cycling after Thermomechanical Processing and Subsequent Ageing. *Journal of Metastable and Nanocrystalline Materials* 31 (2019) 43.
38. J.W. Cahn, F. Larche. A simple model for coherent equilibrium. *Acta Metallurgica* 32 (1984) 1915.
 39. A. Roitburd. Domain structure of crystals formed in solid phase. *Soviet Physics - Solid State* 12 (1969) 2870.
 40. E. Bronstein, E. Faran, D. Shilo. Analysis of austenite-martensite phase boundary and twinned microstructure in shape memory alloys: The role of twinning disconnections. *Acta Materialia* 164 (2019) 520.
 41. T. Inamura, H. Hosoda. Crystallography of Martensite in *TiAu* Shape Memory Alloy. *Metallurgical and Materials Transactions A* 42 (2011) 111.
 42. T. Inamura, M. Ii, M. Tahara, H. Hosoda. Formation process of the incompatible martensite microstructure in a beta-titanium shape memory alloy. *Acta Mat.* 124 (2017) 351.
 43. F. Falk. Driven domain walls in shape memory alloys. *Journal of Physics C: Solid State Physics* 20 (1987) 2501.
 44. J. Zhu, K.M. Liew. Describing the morphology of $2H$ martensite using group theory part I: theory. *Mechanics of Advanced Materials and Structures*, 11((2004)197.
 45. M. Krishnan, J.B. Singh. A novel B19' martensite in nickel titanium shape memory alloys. *Acta Materialia* 48 (2000) 1325.
 46. R. Delville, S. Kasinathan, Z. Zhang, J. Van Humbeeck, R. D. James, D. Schryvers. Transmission electron microscopy study of phase compatibility in low hysteresis shape memory alloys. *Phil. Magazine* 90 (2010) 177.
 47. T. M. Simon. Rigidity of branching microstructures in shape memory alloys. Max-Planck-Institut für Mathematik in den Naturwissenschaften, Leipzig 2018. In: <https://arxiv.org/pdf/1705.03664.pdf> (letzter Zugriff: 24.11.2020).
 48. V.E. Prieb, V.P. Ljubiwoj. Acoustic Irradiation at Martensitic Transformation. *Metallophysika* 10 (1988) 94 (Rus.).
 49. V. Prieb, V.A. Udovenko, P.L. Potapov, N. Poliakova. Martensitic Transformation in Antiferromagnetic Alloys of NiMn Intermetallic Compound. *Z. Metallkd.* 86 (1995) 345.

50. M. Ahlers. Martensite and equilibrium phases in *Cu-Zn* and *Cu-Zn-Al* alloys. *Progress in Material Science* 30 (1986) 135.
51. V. Prieb. The limiting of the response time of shape memory alloy actuators by transformation rate. Report to the “Readings on the materials with shape memory and superelasticity effects, 24.-25. May 2000, Kiev”, Kiev 2000.
52. N. Resnina, S. Belyaev. Multi-stage martensitic transformations induced by repeated thermal cycling of equiatomic *TiNi* alloy. *J. of Alloys and Compounds* 48 (2009) 304-308.
53. A. Sibirev, S.P. Belyaev, N. Resnina. Influence of holding between the thermal cycles on recovery in martensitic transformation temperatures in *TiNi* alloy. *Letters on Materials* 9 (2019) 103-106.
54. A. Planes, J.-L. Macgueron, J. Ortin. Energy contributions in the martensitic transformation of shape memory alloys. *Phil. Mag. Lett.* 57 (1988) 298.
55. J. Ortin, A. Planes. Thermodynamic analysis of thermal measurements in thermoelastic martensitic transformations. *Acta Metall.* 36 (1988) 1873.
56. M. Boabdallah and G. Gitzeron. Caractérisation des changements de phase développés dans un alliage AMF du type Cu-Al-Ni, par dilatométrie de trempe et microcalorimétrie différentielle. *The Europ. Phys. J. – Appl. Phys.* 1 (1998) 163.
57. J. Uchil, K.K. Mahesh and K.G. Kumara. Dilatometric study of martensitic transformation in NiTiCu and NiTi shape memory alloys. *J. of Mater. Sci.* 36 (2001) 5823.
58. V. Prieb. Dilatometry of shape memory alloys. Berlin 2009 (38 pages). In: http://www.materialforschungsservice-dr-prieb.de/SMA_Dilatometrie_En.pdf (letzter Zugriff: 14.04.2020).
59. V. Prieb, H. Steckmann. Compression bandages and gradient systems on the basis of *TiNi* shape memory alloys in the field of medicine and medical technique. Proceeding of the 5th European Conference on Advanced Materials and Processes and Applications (EUROMAT '97, Maastricht, 21-23 April 1997. *Materials, Functionality & Design Volume 3: Surface Engineering and Functional Materials*, Maastricht, 1997, pp. 3/585-3/588.
60. V. Prieb, H. Steckmann. Verbundgewebe mit Memory-Metall und deren Anwendung. Deutsches Patent DE 19529500 C1 vom 13.06.2001.

61. V. Prieb, H. Steckmann. Supporting fabric with memory metal and use thereof. European Patent EP 96112965 A2 from 12.03.97.
62. V. Prieb, H. Steckmann. Flat composite fabric with memory metal and its applications. USA-Patent 289265449 US from 1997.
63. V. Prieb, H. Steckmann. Temperaturregelventil mit einer durchflußsteuernden Memory-Metall-Membran. Deutscher Gebrauchsmuster DE 20114702, DPMA 07.01.2002.
64. V. Prieb, H. Steckmann. Zusammengesetzter symmetrischer Biegeaktor mit Memory-Elementen. Deutscher Gebrauchsmuster DE 20201578, Priorität 02.02.2002.
65. V. Prieb. Verbundwerkstoffe und Werkstoffverbunde aus Elastomeren und Memory-Legierungen sowie bewegliche Design-Komponenten hiervon. Deutsche Patentanmeldung DE 10 2010 019 909 A1 - Priorität: 04.05.2010. DPMA 10.11.2011.
66. V. Prieb, H. Steckmann. Elektrische, für die Absicherung des Mehrspannungsbordnetzes besonders geeignete Bruchsicherung mit einem Memory-Einsatz. Vortrag am Seminar bei der "Daimler- Chrysler AG", Worms, 2001.
67. V. Prieb, H. Steckmann, L. Neganow. Elektrische Bruchsicherung mit Memory-Einsatz und dafür geeignete Memory-Legierungen. Deutsche Patentschrift DE 19851311 A1 vom 18.05.2000.
68. V. Prieb, H. Steckmann, L. Neganov. Electrical protective breaking device with memory element and memory alloys therefor. European Patent EP 99121885 from 10.05.2000.
69. V. Prieb, H. Steckmann, L. Neganov. [Electrical rupturing fuse with memory insert and memory alloys suitable therefor. USA-Patent 457359905 US.](#)
70. F. Falk. [Landau theory and martensitic phase transformations. J. de Phys. 43\(1982\)3.](#)
71. M. Achenbach and I. Müller. [A model for shape memory. J. de Physique, 43\(1982\)163.](#)
72. I. Müller. [On the size of the hysteresis in pseudoelasticity. Contin. Mech. Thermodyn. 1 \(1989\) 125.](#)
73. S. Fu, Y. Huo, I. Müller. [Thermodynamics of pseudoelasticity - an analytical approach. Acta Mech. 99 \(1993\) 1.](#)

74. Y. Huo, I. Müller. Nonequilibrium thermodynamics of pseudoelasticity. *Contin. Mech. Thermodyn.* 5 (1993) 163.
75. H. Xu, S. Tan, I. Müller I. Thermodynamics of hysteresis in shape memory alloys. in "Shape Memory Materials`94", Proc. of the Int. Symp., Beijing, China, 1994, p.p. 87 - 91.
76. I. Müller. Thermodynamic of ideal pseudoelasticity. *J. Phys. IV* 5(1995)423.
77. I. Müller, G. Zak. Thermodynamics of twinning. Proc. of "ICOMAT`95", *J. de Phys. IV, suppl. Au J. de Phys. III* 5 (1995) 197.
78. R.M. Bozorth. *Ferromagnetism*. Van Nostrand, 1968, 568 p.
79. J.S. Cory, J.L. McNichols. Nonequilibrium thermostatics. *J. Appl. Phys.* 58(1985)3282.
80. D.C. Jiles, D.L. Atherton. Theory of magnetic hysteresis (invited). *J. Appl. Phys.* 55 (1984) 2115.
81. J.L. McNichols, J.S. Cory. Thermodynamics of Nitinol. *J. Appl, Phys.* 61 (1987) 972.
82. E. N. D. Grassi, G. Chagnon, H. M. R. de Oliveira, D. Favier. Anisotropy and Clausius-Clapeyron relation for forward and reverse stress-induced martensitic transformations in polycrystalline NiTi thin walled tubes. *Mechanics of Materials*, April 2020.
83. G. Rio, D. Favier, H. Desplats. Finite elements simulation of mechanical behaviour of shape memory alloys coupled with a non-stationary thermal field. Proc. of "ICOMAT`95", *J. de Phys. IV, suppl. au J. de Phys. III* 5(1995)215.
84. A. Tourabi, B. Wack, D. Favier. Experimental determination of the hysteretic properties in shape memory alloys. "Proc. of the "ICOMAT`89", Sydney" 1989. *Mater. Sci. Forum* 56-58 (1989) 535.
85. V. Prieb, Yu.I. Paskal', L. A. Monasevich et al. Influence of texture on the shape memory effect in *TiNi*. *Material Science Transaction (Rus.)* 9(1979)62.
86. S. Ichinose, Y. Funatsu, S. Otsuka. Type II deformation twinning in γ' martensite in a *Cu-Al-Ni* alloy. *Acta Metall.* 33 (1985) 1613.
87. Y. Morakami, Y. Nakajima, K. Otsuka. Effect of Existing twin boundaries in martensite on the rubber-like behaviour and ageing effect in *Au-Cd* alloys. Proc. of "ICOMAT`95" *J. de Phys. IV, suppl. au J. de Phys. III* 5(1995)1071.

88. J.M. Ball, C. Chu, R.D. James. Hysteresis during stress-induced variant rearrangement. Proc. of "ICOMAT`95" J. de Phys. IV, suppl. au J. de Phys. III 5 (1995) 245.
89. E. Ising. Beitrag zur Theorie des Ferromagnetismus, Zeitschrift für Physik 31 (1925) 253.
90. A. Abu-Arab and M. Ahlers. The stabilisation of martensite in *Cu-Zn-Al* alloys. Acta Metall. 36 (1988) 2627.
91. Google: Lüders band, Bilder. (letzter Zugriff: 12.03.2020).
92. J. van Humbeeck, J. Janssen, Mwamba-Ngoie, L. Delaey. The stabilisation of step-quenched copper-zinc-aluminium martensite. Part I: The reverse transformation temperatures. Scripta Metallurgica 18 (1984) 893.
93. J. van Humbeeck, D. Segers, L. Delaey. The stabilisation of step-quenched copper-zinc-aluminium martensite. Part III: The annealing-out of vacancies measured by positron annihilation. Scripta Metallurgica 19 (1985) 477.
94. V. Prieb. Structure and properties of *NiTi* alloys after treatment by the powerful electronic impulses with nanosecond length. J. de Phys. 1 (1991) C4-317.
95. V. Prieb. Formation of non-equilibrium structures in metal alloys under high intensity electron beams and metrology of these beams with a help of memory alloy targets. Proc. of 2nd Int. Scient. Conf. „Radiation-thermal effects and processes in inorganic materials“. 14-19 august 2000. Tomsk 2000.
96. A.S. Mahmud, Y. Liu, T. Nam. Gradient anneal of functionally graded *NiTi*. Smart Materials and Structures 17 (2008) 1
97. M.F. Razali, A.S. Mahmud. Gradient deformation behavior of *NiTi* alloy by ageing treatment. J. of Alloys and Compounds 618 (2015) 182.
98. B.S. Shariat, R. Bakhtiari, Y. Liu. Nonuniform transformation behaviour of *NiTi* in a discrete geometrical gradient design. J. of Alloys and Compounds 774 (2019) 1260.
99. M. Piao, S. Miyazaki, K. Otsuka. Characteristics of deformation and transformation in shape memory alloy. Material Transaction JIM 33(1992)346.
100. C. Wei, Z. Liancheng. The reverse transformation of deformation-induced martensite in *Ni-Ti-Nb* shape memory alloy with wide hystere-

- sis. "Shape Memory Materials`94", Proc. of the Int. Symp. on Shape Memory Alloys, China, Beijing 1994, 235.
101. S. Wang, K. Tsuchiya, L. Wang, M. Umemoto. Martensitic stabilization and defects induced by deformation in *TiNi* shape memory alloys. *International Journal of Minerals, Metallurgy and Materials* 18 (2011) 66.
 102. K. Madangopal, J.B. Singh, S. Banerjee. The Nature of Self-Accommodation in *Ni-Ti* Shape Memory Alloys. *Scripta Metallurgica* 29 (1993) 725.
 103. Roshdy George S Barsoum. Active materials and adaptive structures. *Smart Mater. Struct.* 6 (1997) 117.
 104. D. Reynaerts, H. Van Brussel. Development of a SMA high performance robotic actuator. 1991 IEEE, 61-66.
 105. Y. Nakamura, S. Nakamura, S. Miyazaki. Micromachining Process for Thin-Film SMA-Actuators. 1996 IEEE, 493-497.
 106. P.L. Potapov. Thermoelectric triggering of phase transformations in Ni-Ti shape memory alloy. *Mater. Sci. and Eng., B52* (1998) 195.
 107. R.D. James, M. Wüttig. Alternative smart materials. *SPIE*, 2715(1996)420.
 108. K. Ho, P. Jardine, G.P. Carman, and C.J. Kim. Modeling and Measuring the Responce Times of Thin Film TiNi. *SPIE*, 3040 (1997) 10-22.
 109. [A. Planes](#), [L. Mañosa](#), [E. Vives](#). Acoustic emission in martensitic transformations. *J. of Alloys and Compounds*. [577](#) (2013) 699.
 110. [G. B. Olson](#) & [M. Cohen](#). A general mechanism of martensitic nucleation: Part I. General concepts and the FCC → HCP transformation. [Metall. Trans. A](#), 7 (1976) 1897.
 111. S. Jiang, Y. Wang, Y. Zhang, X. Xing. Role of stacking faults in martensite transformation of FeMnSiCrNi shape memory alloy subjected to plastic deformation at high temperatures. *Intermetallics*, 124 (2020) 106841
 112. E. Hornbogen. Fractal dimension of martensitic microstructures. „The martensitic transformation in science and technology“, E. Hornbogen, N. Jost Editors, DGM-Verlag, Oberursel, 1989, p.p. 97-104.
 113. O. A. Likhachev and Yu. M. Koval. Thermoelastic Behaviour, Hysteresis, and Dissipative Forces in Thermodynamics of Martensitic Transformations. *Usp. Fiz. Met.* 16 (2015) 1–22.

114. Acoustic Emission. Ed. by J. Eisenblätter. DGM-Verlag, Oberursel
1988, 321 pages.

115 V SAMPATH1, SAI VENKATA GAYATHRI2 and R SRINITHI1.
Experimental and theoretical analyses of transformation temperatures
of Cu-based shape memory alloys. Bull. Mater. Sci. (2019) 42:229.

8 Appendix: Practical applications of SMA's

8.1 Article to the German and international patent: "Composite fabric with memory metal and its applications"

DE 195 29 500 C2, EP 961 12 965 A2, 289265449 US.

Registration date: 08/10/1995.

Inventor: Dr. V. Prieb and H. Steckmann.

Patent holder: company "1st Memory Alloys GmbH"

Abstract:

Object of the invention: The invention relates to a composite fabric with memory metal (*memory fabric*) as well as applications thereof in medicine, aeronautics and space technology, one of the applications, namely the massage device, being equally suitable for fitness purposes at home.

Applications: Passive press and support bandages, active gradient systems and massage devices as well as pressure suits.

Introduction

The device presented here is based on the properties of metal wires with the memory effect. When heated, a specific deformation process begins, namely the martensitic reverse transformation, which leads to compression. The *TiNi* memory wires are incorporated into an elastic material and are heated by the electrical current. The wires with the starting temperature (M_s) of the martensitic forward transformation below 30°C can be used for pressure bandages. This means that short-term heating above the finish temperature (A_f) of the martensitic reverse transformation ensures permanent compression.

The wires with the finish temperature (M_f) of the martensitic forward transformation above 30°C and a narrow hysteresis are used for the gradi-

ent systems. By connecting memory elements in series, each individual element can be heated separately by means of the electrical current, so that a compression gradient is created that can be used to achieve a massage effect.

Medical problems

The compression treatment of chronic venous diseases and lymphedema in phlebology aims to compensate for venous insufficiency and prevent its progression. In decompensated venous insufficiency with edema, this is achieved with compression bandages and to maintain the compensated state with compression stockings. Apparatus compression is used as an additional measure (*Fundamentals of Phlebology – E. Rabe (Editor) Kagerer Kommunikation, Bonn, 1994*).

The compression bandages and stockings are made of an elastic synthetic material and must ensure the pressure on the edema of $(20 \div 60)mmHg$, depending on the compression class. In the device-based compression therapy, more or one-chamber rubber sleeves are used, which alternately press and relieve the area to be treated due to the air filling. The use of these medical devices is associated with a number of problems:

1. During decongestion stage of the lymphedema treatment by the elastic compression bandage, the force exerted gives way linearly, which makes the use of permanent bandages difficult.

2. The use of compression stockings creates a significant problem in putting on and taking off, namely the greater the working pressure, the more rigid the stocking fabric and the more difficult it is to put on and to take off the stocking.

3. The rubber sleeves are filled with air by a pump. With the multi-

chamber cuff (*so-called gradient system*), each chamber is connected to the pump by a hose in order to generate a continuous pressure wave. The pressure wavelength can accordingly only be reduced to a limited extent. This technique is very massive and therefore requires inpatient treatment.

The compression bandages and gradient systems proposed and patented by us with pressure-exerting working elements made of shape memory alloys allow all these problems to be solved in principle and, moreover, to achieve all three functions in principle in one system.

Production of the memory composite fabric

The compression bandage is made of a composite material consisting of two layers of a light, elastic synthetic material and flat meander-shaped metal springs incorporated between these layers. The springs made of *TiNi* shape memory wires are wound into a meander on a bending form (**Fig. 1**). To keep them in this high temperature shape, they are briefly heated up to 700°C by a current impulse. The length of the current impulse can be set between $(1\div 10)\text{s}$. After the meanders have been removed from the bending form, they are trained to the two-way memory effect through a few thermal cycles under a constant load.

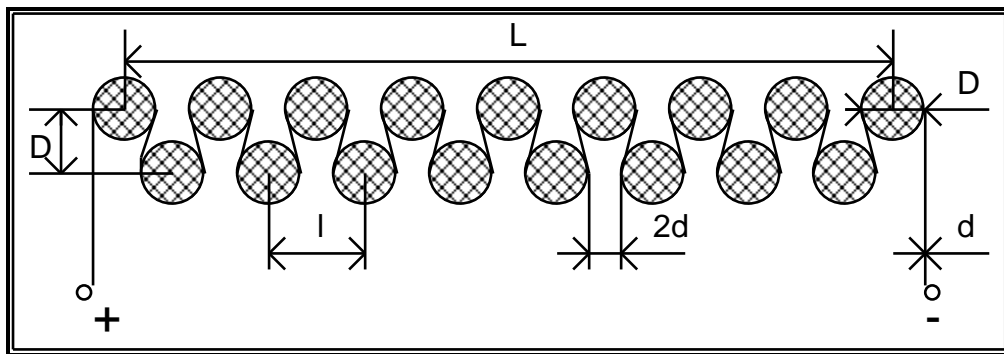


Fig.1. Bending mold with ceramic beads attached to an electrically insulated metal plate for the production of memory meanders

The meanders are embedded between the elastic synthetic material layers with the help of an ultrasonic welding machine so that the meanders are close to one another but separated by the weld seams. The composite fabric produced in this way is then processed either into a bandage with different widths and lengths, or into sleeves of different sizes. Endings of the bandage or sleeve are provided with a zip or Velcro fastener to enable them to be attached to the body.

The finished bandage is stretched at a temperature $T < M_f$. The meanders are in the martensitic state. The deformation takes place at low external stresses because the quasiplastic yield point of the martensite is very small. This allows the bandage loosely putting on and taking off.

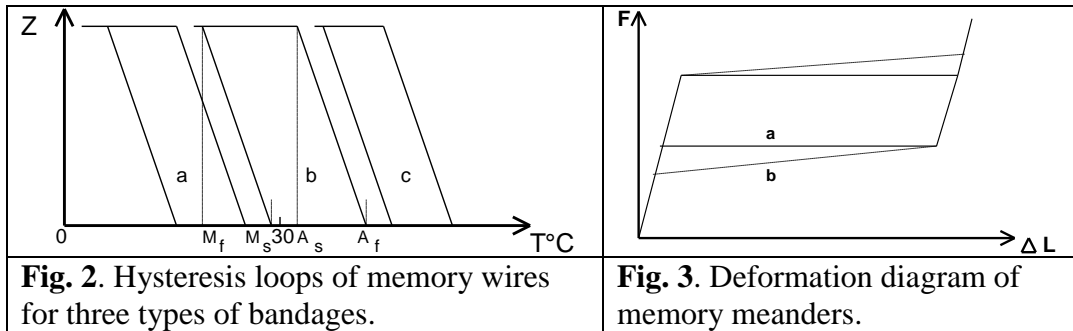
Three variations of bandages differ depending on how they work and on the transformation temperatures of the shape memory wires. They can be viewed as passive and active press systems. The passives are activated by the body temperature $T_b \approx 37^\circ\text{C}$ and the active ones by the heating by means of the electrical current and, in the case of the gradient systems, controlled by an electronic device.

Passive pressure bandages

If the entire transformation hysteresis loop of the memory wire is below the skin temperature $T \approx 30^\circ\text{C} < T_b \approx 37^\circ\text{C}$ (**Fig. 1 a**), the pressure bandage is activated immediately after the application of edema. The compression takes place when the bandage warms up due to the skin temperature. For the removal of the tense bandage must this be cooled down again below the temperature M_f , e.g. by spraying with a coolant.

Since the meanders were trained for the two-way effect during their

production, the bandage loosens when it is transformed into the martensitic state during cooling, and it can then be easily removed. The memory wires with a narrow hysteresis loop are recommended for such bandages. Then the temperature M_f is not so low that the cooling becomes uncomfortable or dangerous for the body.



The transformation temperatures can be selected so that there is between the starting temperatures of the forward M_s and reverse A_s transformations (**Fig. 2 b**). In this case, heating above the temperature A_f takes place by a current impulse after the bandage is applied. After the power is switched off, the bandage remains in a stressed state. They can be removed easily by cooling them down with a coolant below the temperature M_f . The meanders are at this method electrically connected to one another and provided with electrical contacts.

The advantages of this method:

1. The pressing force can be adjusted by means of the amperage by reaching different heating temperatures T_h within the temperature range $A_s < T_h < A_f$.
2. The memory wires made of a *TiNi* two-component alloy with the normal transformation hysteresis width of $(25 \div 30)^\circ\text{C}$ can be used, whereby the take-off-temperature of the bandage is still under 15°C .

Disadvantages, however, include the increase in the bandage cost due to the more complicated production. In terms of functionality, the two bandages do not differ in principle and can be used as permanent bandages (*sleeves*).

A very important advantage of the bandages with memory elements in compression treatment compared to the usual elastic bandages is that the pressure exerted remains constant (**Fig. 3 a**) during the continuous long time treatment and reducing the edema and thus the pseudoelastic martensitic deformation or only sinks slightly (**Fig. 3 b**).

The pressure of a conventional elastic bandage with an initial contact force F_0 and an elasticity coefficient k_{el} on a cylindrical swelling with an initial radius R_0 is calculated using Laplace's law:

$$D_0 = \frac{F_0}{R_0} = \frac{k_{el}(2\pi R_0 - L_0)}{R_0}. \quad (8.1.1)$$

During the reducing the edema, the radius is reduced so that $R_1 < R_0$ is. The contact force decreases linearly. The pressure change is in the result negative:

$$\Delta D = D_1 - D_0 \propto \left(\frac{1}{R_0} - \frac{1}{R_1} \right) < 0. \quad (8.1.2)$$

It is characteristic of the memory meanders made of *TiNi* that the force exerted remains constant (**Fig. 3 a**) while their length (ΔL) is reduced or decreases linearly only slightly with a very small coefficient (**Fig. 3 b**).

The total change in length of a bandage can reach values of (50 ÷ 200)% , depending on the meander shape. The shape is optimized according to the required contact pressure and deformation (*swelling size*).

Active bandages as gradient systems

The third variant of pressure bandages differs fundamentally from the first two in terms of their functionality. All transformation temperatures are above T_b , i.e. $T_b \leq M_f$. The memory meanders are electrically connected to each other in such a way that they can be switched on in a certain order and heated by current impulses. The electronic control system allows to set the duration of the current impulse as well as the pauses between the impulses and the final pause as required. After the final break, the whole process starts all over again.

Such a bandage generates continuous pressure waves and thereby imitates the massage effect. The massage is used very often in the treatment of edema and is still done manually today. Its purpose is to displace the fluid from lymphedema.

On the one hand, the question of the cyclical stability and degradation of the memory properties is very important in this application. On the other hand, it has been shown in experimental investigations that the rehabilitation of these properties is possible by short-time heating the meanders to a certain temperature. This heat treatment, also using a strong current impulse, restores the memory properties without damaging the elastic shell.

8.2 Article to the German and international patent: "Electrical break protection with memory insert"

DE 19851311 A1, EP 99121885, 457359905 US.

Registration date: 06.11.1998.

Inventor: Dr. V. Prieb, Dr. H. Steckmann, Dr. L. Neganov.

Patent holder: company "1st Memory Alloys GmbH"

Abstract

The invention is based on the memory force effect.

Object of the invention: A new electrical fuse with a self-breaking insert made from a memory alloy (*memory self-breaking fuse*). Here, an insert made of a *Cu*-based memory alloy that is particularly suitable for electro-technical purposes is installed in a fuse body of a simplified construction.

Area of application: The fuse properties, above all the high escape speed of the fractions and low triggering temperatures, are particularly suitable for protecting the 42V-DC electrical system in future cars, where the risk of arcing is particularly high if the power is interrupted.

State of the technique and problem definition

With the change at the car manufacturers to the electrical 42V direct current on-board network, a serious security problem arises, because the risk of arcing, which can lead to the total car burning down, increases dramatically with the increase in the network voltage. The fuses currently used cannot withstand the new, higher requirements for electrical on-board network fuses. The most serious disadvantages of fuses are (*1: W. Knies, K. Schierack. Elektrische Anlagentechnik: Kraftwerke, Netze, Schaltanlagen, Schutzrichtungen / München; Wien: Hanser, 1991*):

- Switching off in the event of a critical current only takes place after the melting temperature of the conductor material of the fuse insert

has been reached (1080°C for *Cu*), which leads to a longer total switch-off time.

- When the insert melts, an arc is created which leads to the metallization of fuse components and enables a residual current to pass through.
- The high operating temperature of the fuse, which depends on the cross-section of the fuse insert calibrated to the nominal current, leads to an increase in the temperature of the entire electrical network, to the drying out of insulating materials, to a change in the electrical properties of the fuse insert and to higher temperatures as a result caused or increased aging of the insert alloy.
- The small gap between the melted parts when using a fuse can lead to the creation of an electric arc.

Aims definition

It was therefore made the object of this invention to design an electrical fuse with a reduced overall tripping time, which is easy to manufacture and versatile. This should be an electrical low or high voltage fuse with a breaking insert made of a memory alloy for use in electronics and electrical engineering in electrical systems for their arc-free disconnection in the event of thermal loads, overload and short-circuit currents, which have the following advantages:

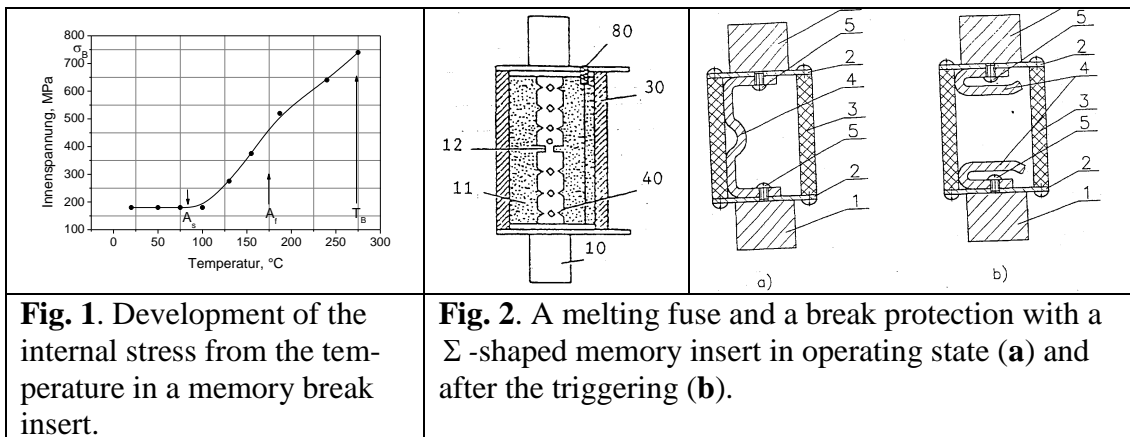
- Reduction of the release temperature to $(60 \div 300)^{\circ}\text{C}$ thanks to a new functional principle.
- Prevention of arcing through the high velocity (*escape velocity*) with which the insert fragments move away from each other after the fuse has been triggered or the insert has broken.

- Reduction of the total release time by a factor of (3 ÷ 5) due to a low release temperature and the high breakage or escape velocity.
- Elimination of the thermal and mechanical stress that leads to the destruction of fuse components if an electric arc occurs.
- Significant simplification and cheaper construction of the fuse by dispensing with a ceramic body, seals and additional or separate contact blades and the indicator.
- Avoidance of the occurrence of an electric arc by a much larger distance of the insert fragments from one another after the fuse has tripped, whereby this maximal distance can be up to 98% of the distance between the contact bases or fastening points of the insert.
- Significant reduction in the operating temperature or the heating temperature of the entire electrical system.
- Reduction of the current density in the insert by increasing the cross section of the insert, which, in contrast to fuses, does not increase the melting time and does not lead to the creation of a stable arc.
- An automatic improvement of the electrical contact of the insert at the fastening points by mechanical self-tensioning of the memory insert when heating due to the current passing through the insert or the formation of sparks when the contact is loosened.
- Possibility of setting time/current-characteristics through a corresponding selection of the composition of the memory alloy for the insert, the cross section of the insert, the martensitic "detent deformation" of the insert, when it is installed in the fuse body and through heat dissipation conditions.

Memory alloys and properties

All these advantages have been achieved through the use of *Cu*-based alloys with memory properties as a material for the production of break inserts in electrical fuses (2: *V. Prieb, H. G. Steckmann, L. Neganov. Elektrische Bruchsicherung mit Memory-Einsatz und dafür geeignete Memory-Legierungen. Offenlegungsschrift DE 198 51 311 A1 vom 18.05.2000 bzw. Europäische Patentanmeldung EP 0 999 570 A1 vom 10.05.2000 Patentblatt 2000/19*)

One of the memory properties is that a specimen made of a memory alloy deformed in the martensitic state at low temperatures remembers its original high-temperature shape when the temperature increases above the temperature range $A_s \div A_f$ of the martensitic reverse transformation, by the martensitic low-temperature deformation is spontaneously reversed [3: *V. Prieb, HG Steckmann. Shape memory alloys and their applications, computer animation, "1st Memory Alloys GmbH", 1998*].



If any force opposes the recovery of the martensitic deformation, an opposing force is developed by the memory sample to continue the recovery. If the recovery of the martensitic deformation is completely prevented by a hard jamming or fastening, the internal stress of the memory sample increases to its own breaking limit when heated beyond the temperature

range of the martensitic reverse transformation, i.e. the specimen breaks itself. Figure 1 shows this behavior by means of a real $(\sigma - T)$ -diagram experimentally measured on a break insert. The temperature in $^{\circ}C$ and the internal stress developed in the memory break insert in Megapascals ($1MPa = 10^6 N \cdot m^{-2} = 0.1kg / mm^2$) are plotted on the x - and y -axes.

The stress increases almost linearly when the temperature increases within the temperature range $A_f < T < T_B$. The martensitic reverse transformation of the unloaded sample ends at this temperature A_f . At the breaking temperature T_B , the internal stresses reach the breaking limit σ_B of the memory material, so that the hard-fastened memory insert breaks at a marked predetermined breaking point.

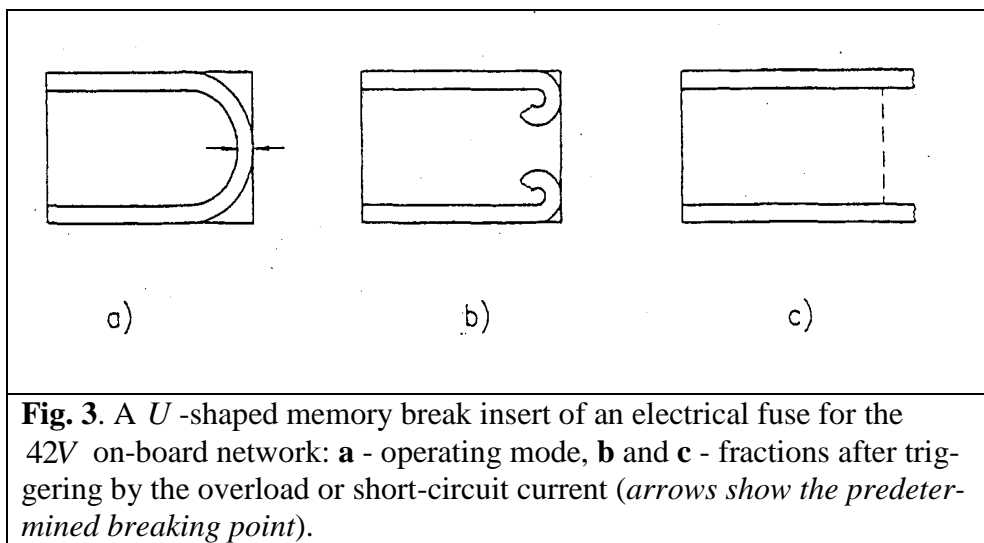
Memory insert of the electrical break protection

Figure 2 (*left*) shows a cross-section of an NH-fuse according to **DIN 43620**, which consists of a ceramic body (30), a fuse insert (12) with a perforation (40), two contact blades (10), an indicator (80) and a sand filling (11). Figures 2 a and b show a break protection device with a memory insert (4) in an embodiment for rated currents $(10 \div 300)A$ and rated voltages $(5 \div 500)V$ [2]. The memory insert is attached to the fuse bases with two screws (5). The fuse also consists of a body (3), which can be made of a heat-resistant plastic and does not need to contain any sand filling or an indicator, as well as two contact blades (1).

Figure 3 shows an electrical break fuse particularly suitable for the 42V on-board network for rated currents of $(5 \div 50)A$ [2]. The insert can be integrated with both ends (**Fig. 3 a, left**) as a contact knife, either as a plug directly into a two-column socket of the electrical system, or it can be in-

stalled in its own fuse body with two contact knives.

An electrical break protection with the memory insert works as follows: When the rated current passes, the memory insert is heated to a temperature below the break temperature (T_B). This heating does not lead to an increase in the mechanical stresses in the memory fracture insert if the operating temperature is below the start temperature of the martensitic reverse transformation (*Fig. 1*).



In the event of a sustained overload current or a short circuit, the memory breaking insert is heated up to the breaking temperature T_B (*Fig. 1*) above the finish temperature of the martensitic reverse transformation A_f in an adjustable time. The internal mechanical stress develops in the memory break insert (*Fig. 2 or 3*) up to its own breaking point σ_B .

This triggers the fuse due to the breaking the memory insert and accordingly switches off the overload or short-circuit current. After the triggering, the insert fractions of the attached to the endings fly apart at such a great velocity and at such a great distance from each other that the creation of an arcing is impossible. Figures 4 a, b and 5 a, b show other embodiments of the memory break insert [2], which are also suitable for protecting the 42V

vehicle electrical system and are based on the same functional principle.

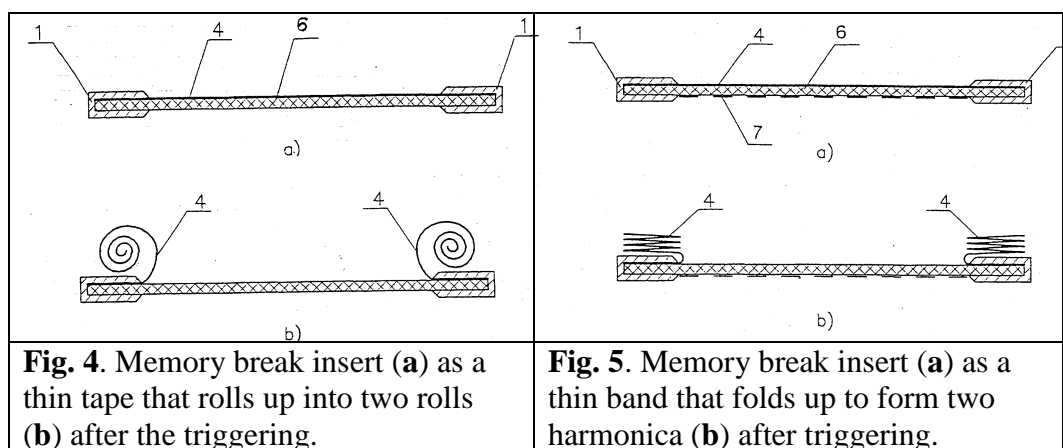


Fig. 4. Memory break insert (a) as a thin tape that rolls up into two rolls (b) after the triggering.

Fig. 5. Memory break insert (a) as a thin band that folds up to form two harmonica (b) after triggering.

Here an amorphous memory tape (4) is attached to an insulating pad (6) under the contact blades (1). After the release, the straps roll into two rolls (Fig. 4 b) or fold into two harmonica (Fig. 5b) at the fastening points. This leads to an even greater distance between the fractions, up to the distance between the fastening points. For additional protection against the occurrence of an electric arc, the opposite side of the insulation plate can be provided with a known electric arc or discharge vessel (Fig. 5, 7).

Automatic protection of the electrical contact

The electrical contact at the fastening points (Fig. 2 a, b, 5) is secured for all types of insert by the fact that the memory insert is operated by the rated current or by the sparks at the released electrical contact up to a temperature within the temperature range $A_s < T < A_f$ is heated. When the rated current passes through the memory insert, a minimal mechanical internal stress, which is necessary for safeguarding or improving the electrical contact, develops, i.e. the insert is in a slightly tensioned state and thus ensures reliable electrical contact.

If the contact loosens in any way, it leads to a spark and thus to rapid additional heating of the insert. The memory insert pulls itself together

through the reversing of its latching deformation (4: V. Prieb, H. G. Steckmann. *Verbundgewebe mit Memory-Metall und Anwendungen hiervon. Offenlegungsschrift DE 195 29 500 A1 vom 13.02.97 bzw. Europäische Patentanmeldung EP 0 761 188 A2 vom 12.03.97 Patentblatt 1997/11*) until the gap at the loosened contact point is closed again. A further reset is then prevented, so that an increase in the internal tension is made possible again. In this way, the lax or loose contact is automatically re-strengthened and secured. This method of automatic protection of electrical contacts can be used not only in electrical fuses, but also at all other contact points in the on-board network.

Calculation of the escape speed and the release time

After the memory insert (*index E*) breaks, the elastic energy stored in it is released in a very short time, just like a released spring. This breaking time t_B of approx. $5\mu s$ is determined by the crack length (*the insert thickness*) and the crack velocity. The escape velocity v_B of the insert fractions can be calculated as follows:

$$F_{el} \cdot t_B = m_E \cdot v_B, F_{el} = \sigma_B \cdot S_E; m_E = \rho_E \cdot S_E \cdot L_E; \quad (8.2.1)$$

$$v_B = \frac{\sigma_B \cdot S_E \cdot t_B}{\rho_E \cdot S_E \cdot L_E} = \frac{900 \cdot 10^6 \text{ kg} \cdot \text{m} \cdot \text{s}^{-2} \cdot \text{m}^2 \cdot 5 \cdot 10^{-6} \text{ s}}{9000 \text{ kg} \cdot \text{m}^{-3} \cdot 0,05 \text{ m}} \approx 10 \text{ m/s}, \quad (8.2.2)$$

where F_{el} is the elastic force, m_E is the mass of the insert, S_E is the cross-sectional area of the insert, ρ_E is the density of the memory alloy and L_E is the length of the insert between the two attachment points. The maximal escape time, during which an arc can occur or be extinguished corresponds to the acceleration of the fractions of approx. $400g$ (g is *the gravity acceleration*) and is:

$$t_L \approx 0,5L_E / v_B \approx 0,0025 s, \quad (8.2.3)$$

The heating time from the temperature $T = A_s < A_f$ to the breaking temperature T_B in the case of a short circuit (*under the adiabatic conditions – without taking heat dissipation into account*) can be calculated as followed:

$$I_s^2 \cdot R \cdot t_h = \rho_E \cdot S_E \cdot L_E \cdot c_p^E (T_B - A_s), \quad (8.2.4)$$

where $R = R_{20^\circ C} [1 + k_T (T_B - 20^\circ C)]$ is the electrical resistance of the insert at the breaking temperature, k_T is the temperature coefficient of the electrical resistance, I_s is the short-circuit current and c_p^E is the specific heat capacity of the insert. For a nominal current of 100A (*a current that does not lead to the fuse breaking under constant load*) and a 200-fold short-circuit current, the following heating time results (*all estimates have been made for memory insert on Figure 2*):

$$t_h = \frac{\rho_E \cdot S_E \cdot L_E \cdot c_p^E \cdot (T_B - A_s)}{I_s^2 \cdot R_{20^\circ C} \cdot (1 - k_T T)} \approx \frac{0,01 \text{ kg} \cdot 400 \text{ J} \cdot \text{kg}^{-1} \cdot \text{K}^{-1} \cdot 100 \text{ K}}{4 \cdot 10^8 \text{ A}^2 \cdot 10^{-4} \Omega} \approx 0,01 \text{ s} \quad (8.2.5)$$

It can be seen that the total switch-off time, even with such a large rated current and in the case of a short circuit, is not limited by the escape time but by the heating time and is approx. 10ms (8.2.5). In the case of an overload current, the total switch-off time is limited by an even greater heating time, which can be calculated from the differential heat balance equation:

$$\begin{aligned} \left(c_p^E \cdot m_E + c_p^M \cdot m_M \right) \frac{\partial T}{\partial t} - \alpha \cdot S_W (T - T_M) = \\ = I_B^2 \cdot R_{20^\circ C} \left[1 + k_T (T - A_f) \right] \end{aligned} \quad (8.2.6)$$

where c_p^E and c_p^M are the specific heat capacities of the memory insert and the medium (*air or fuse body, if it comes into direct contact with the insert*), m_E and m_M are the masses of the memory insert and the medium, α_{EM} is the coefficient of heat transfer between the insert and the medium, S_{WE} is the heat transfer area of the insert, T is the variable temperature of the insert which must reach the breaking temperature T_B in a certain heating time t_h , T_M is the medium temperature.

Control of the nominal current and the total switch-off time

The parameters of the electrical fuse such as the current heat impulse – an important variable for the short-circuit shutdown of electrical protective devices, which is known as the Joule integral [1]:

$$J \equiv I^2 \cdot t = \int_{t_0}^{t_1} i^2 \cdot dt, \quad (8.2.7)$$

the rated current I_N , the rated or breaking temperature T_B and the total switch-off time or the heating time t_h can be determinate, as can be seen from the previous calculations, through the temperature A_f (*the finish temperature of the martensitic reverse transformation*), the cross-sectional S_E area and the length L_E of the memory insert (*i.e. through its shape*), the breaking temperature T_B (*the composition of the memory alloy and the heat treatment*). The breaking temperature depends on the breaking point

σ_B of the memory insert and the slope coefficient $k_T^\sigma = \frac{d\sigma}{dT}$ of the internal stress with the temperature increasing (*Fig. 1*). The heating time should also be long enough, to avoid the triggering or the insert breaking due to the overload current when switching on and off.

The breaking point can be varied by coating the insert at the predetermined breaking line with a chemically active alloy. The coefficient k_T^σ can be influenced by the martensitic "detent deformation": the greater the "detent deformation", the faster the internal stress increases with the temperature increase. The "detent deformation" is indicated by the difference between the low and high temperature shapes of the memory insert. The low-temperature shape corresponds to the installation shape in the martensitic state at room temperature, while the high-temperature shape corresponds to the original production shape in the austenitic state.

The memory insert strives for this shape when heated up to the breaking temperature. This shape results when the two insert fractions are put together after the break protection has been triggered. In addition to the medium parameters, the heat transfer conditions are determined by the insert shape (*heat transfer surface, contact surface with the fuse body*) and the design of the fuse (*heat transfer through the current contacts*), the fuse body and the contact base.

Time/current-diagrams and their influence

Figures 6 a-d show time/current characteristics according to **DIN VDE 0636**. On the logarithmic x - and y -axes, the current strength and the time are plotted correspondingly in amperes and in seconds.

The time/current characteristics characterize the developed and investi-

gated break protectors with break inserts made of *Cu*-based SMA with different compositions or transformation temperatures, cross-sections, "detent deformations" and with different perforation coefficients of the fuse body as the ratio of the area of ventilation holes to the total area of the fuse body.

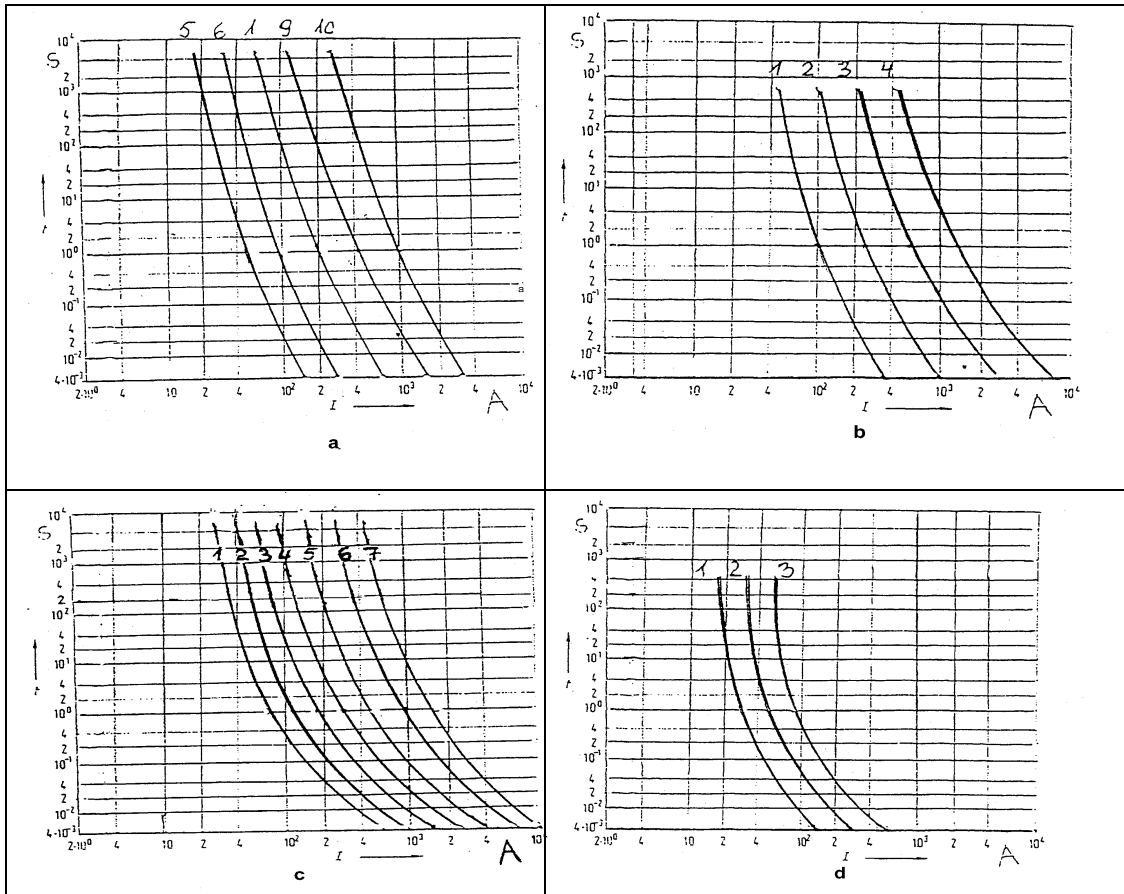


Fig. 6. Experimental time/current characteristics for the Σ -shaped memory inserts in the break protection device (*Fig. 2 b, c*): **a** – with a cross-section 4mm^2 of memory alloys with different transformation temperatures A_f (A_f increases from left to right); **b** – from the same memory alloy, with the same cross-section of 3mm^2 , but with different martensitic "detent deformations": 1 – 8%, 2 – 5%, 3 – 3%, 4 – 1%; **c** – made of the same memory alloy, with the same "detent deformation", but with different cross-sections (mm^2): 1 – 5.0, 2 – 5.5, 3 – 6.0, 4 – 6.5, 5 – 7.0, 6 – 7.5, 7 – 8.0; **d** – from the same memory alloy, with the same cross section of 2mm^2 , but with different perforation coefficients of the fuse body: 1 – 10%, 2 – 20%, 3 – 30%.

The time/current characteristics signpost the developed and investigated break protectors with break inserts made from *Cu*-based SMAs with different compositions or different transformation temperatures, with different cross-sections, with different "detent deformations" and with different per-

foration coefficients of the fuse body.

All of these parameters affect the following:

- Increasing the temperature by changing the composition of the memory alloy and heat treatment of the insert.
- Enlarging the cross section of the insert.
- Reduction of the martensitic "detent deformation".
- Increasing the perforation coefficient of the fuse body (*Fig. 2*) leads to a shift in the time/current characteristics to the right, resulting in higher current values.

These diagrams (*Fig. 6*) show how the safety characteristics are to be set.

New *Cu*-based memory alloys for electrical break protection

The memory alloys for the break inserts must meet strict requirements and have the following properties:

- a high electrical conductivity,
- resistance to temperature and transformation cycles,
- corrosion resistance,
- heat resistance or aging resistance at elevated temperatures with regard to both electrical and memory properties,
- fatigue resistance,
- resistance to the action of an arc plasma and
- a stable breaking temperature related to overload or short-circuit currents, specified by the transformation temperatures.

The known *Cu*-based memory alloys do not meet these requirements (see, for example, 5: "*Proc. Of the Int. Conf. On the Mart. Transformation ICOMAT 95, Lausanne, Switzerland, August 20-25 , 1995* ", Part II, Edit

by R. Gothard and J. Van Humbeeck - in *J. de Physique IV, Vol. 5, Colloque C8, Suppl. Au J. de Physique III, n ° 12, 1995*).

To solve the problem, two new *Cu*-based multicomponent memory alloys with up to 215°C increased transformation temperatures, increased aging and heat resistance up to temperatures of 600°C and increased resistance to temperature and transformation cycles have been developed and manufactured. These alloys have the following physical and technological properties (*austenite* \rightleftharpoons *martensite*):

Density, kg/m ³	8250÷8900
Specific thermal conductivity, W/m·K	80÷120
Specific electrical resistance (20°C), μΩ·m	0.010÷0.030
Temperature coefficient of the specific electrical resistance (20-100°C), K ⁻¹	0.00032÷0.00073
Melting temperature, °C	1050÷1090

Summary

An electrical low or high voltage fuse of a simplified design with automatic protection of the current contacts, a break insert made of a new *Cu*-based memory alloy for use in electronics and electrical engineering in electrical systems, especially in the automotive industry, in 42V DC electrical system for arc-free disconnection at low triggering temperatures and shortened triggering times, in the case of thermal stresses from overload and short-circuit currents, has been developed, examined, checked and provided.

8.3 German patent: "Composite made of elastomers and SMAs and design components thereof"

DE 10 2010 019 909 A1.

Registration date: 04/05/2010, **disclosure date:** 10/11/2011.

Applicant, inventor and patent holder: Dr. V. Prieb

Abstract:

Object of the invention (based on the recurring memory effect without a bias element):

The invention relates to a combination of elastomers (*polymers, silicones, rubber, etc.*) with memory or shape memory alloys either as new composite materials compounds from the elastomer matrix (1) with the memory elements (2) embedded therein or as new materials from the elastomers-parts (1) and the memory elements (2) mechanically combined material composites for the production of industrial products or art objects with movable design components, which make complex and recurring changes in shape when the temperature changes in their surroundings or their memory elements and thus to influence dynamically the appearance of these objects. If such a design component is connected to its own power source, this enables periodic or complex changes in shape controlled according to their size and duration.

Applications:

Art, industrial design, auto industry (*car tires with changeable profile*).

State of the technique.

Various actuators with active memory elements in a mechanical combination with passive elastic bias metal elements are known. Their functional principle is based on a change in shape of a memory element when it is heated by electric current, which is translated into translational or rotational movements, the return to the low-temperature shape of the active memory element being forced by the elastic force of the bias metal element.

In the German patent DE 100 30 025 A1, a device for positioning an actuating element is presented, which contains a reversibly expandable and contractible electromechanical element made of a memory alloy, its forward movement by the electric current with controllable amperage and its return movement by the elastic force a return spring can be initiated when the power is switched off.

In the German utility model DE 201 14 702.5 there is a temperature control valve for heating or cooling systems for regulating the flow temperature of the liquid or gaseous heating or cooling medium by controlling the flow cross-section and thus the flow rate with the help of a thermosensitive membrane made of a memory alloy or memory membrane, which reversibly influences the flow through its temperature-dependent shape changes between two positions: "open" and "closed". The repetitive, reversible shape change of the memory membrane is ensured in various valve designs either by the two-way memory effect or by the counteraction of a metal spring.

In the German utility model DE 202 01 578.5, the restoration of the low temperature or the martensitic detent deformation of a cooled memory element is brought about by the restoring force of another active memory element opposite the first, which symmetrizes the action cycles of such a composite memory actuator in terms of time and allows better control.

On the other hand, applications of elastomers that are easily moldable, elastic at temperatures above their glass temperature, easily moldable through the action of various plasticizers and solidified by polymerization in various processes are known for the manufacture of various products for industrial or medical use: seals, tires, approaches and clothing of various parts, contraceptives, etc. (*1: O. Schwarz, H. Schirber, N. Schlör. Kunst-*

stoffkunde: Aufbau, Eigenschaften, Verarbeitung, Anwendungen der Thermoplaste, Duroplaste und Elastomere. Ebeling (Hrsg.), Vogel Fachbuch, 2007, 304 S.; 2: Rubber parts & rubber-metal-parts. Rubber home of cofermin chemicals. Essen, Germany: <http://www.rubber-products.org>]; Implants including breast silicone implants, dental implants and prostheses, impression materials, etc.; 3: K. Eichner, H.F. Kappert. Zahnärztliche Werkstoffe und ihre Verarbeitung. Stuttgart, 2006).

Elastomers are amorphous materials, for which is characteristic the rubber-elastic behavior at room temperature, i.e. their glass transition temperature range is at very low temperatures (*between* -130°C and -70°C). Rubber-elastic behavior is understood to mean the ability of a material to deform itself strongly (*up to* 400%) – without tearing – under the action of an external force and to completely reverse this deformation after the force removing. Elastomers primarily include natural rubber and synthetic rubber (*polymers including silicones*). The goods made of elastomers are mainly manufactured using casting, injection molding, pressing, centrifugal and foam processes.

Elastomer-metal compounds for vibration damping and noise insulation are also known, in which, however, only conventional, i.e. not memory or shape-memory alloys are embedded in elastomers. Some combinations of polymers and memory or shape memory alloys are known from the prior art, both in immobile and in mobile constructions.

US Pat. No. 5,614,305 describes a polymer shape memory alloy composite, in which several shape memory alloy fibers are embedded in a polymer matrix, which dampen impacts from the stress-induced martensitic transformation and thereby protect the polymer matrix from destruction.

So, in this application, memory elements of the composite material are not used as active movement elements, but as passive damping elements.

The German patent DE 19529500 C2 deals with a composite fabric with memory elements, which consists of two flat layers of a conventional elastic polymer fabric and the meander-shaped memory wires worked between these layers in the manner of a sandwich and for the treatment of swelling and edema in the human body. Reversible periodic changes in the memory meander shape and thus in the entire fabric in the massage devices made from this composite fabric are caused both by the two-way memory effect and by the counterforce of the swelling of the human body created at cooling down of these memory meanders, because of the human body was compressed during the heating phase caused by the electric current. The elastic force of the fabric layers is weak and counteracts the recovery of the low temperature form. The sole purpose of the fabric is to ensure the uniformity of the entire composite fabric and to ensure large changes in length of the fabric due to the changes in length of memory meanders, while the return of the memory meanders to their low-temperature form (*expanded*) takes place through the pressure of the swelling of the human body.

A self-propelled wheel as a robot made of several memory wires built into a ring-shaped elastic polymer belt as wheel spokes is proposed (*4: Will Knight in "New Scientist" of June 30, 2004*), in which the martensitic detent deformation of individual active memory wires occurs at low temperatures is restored by the elastic force of the pipe. Here the elastic force of the polymer belt is used as a construction part with its own function – maturity of the wheel – but the whole construction is too peculiar and the belt shape of the polymer part is far too simple for use as a component or drive in other systems or design products.

Such a combination of elastomers and memory alloys is described by L. Grenacher and the others (5: *L. Grenacher et al. Experimentelle Erprobung eines neuen Spulendesigns zur endoluminalen MRT, Experimentelle Radiologie* 177 (2005) 986), but the silicone cover around the coil made of a nitinol wire with memory properties only serves as a biocompatible protection of the inside of the body from contact with the memory alloy.

In European patent EP 1 278 958 B1, a combination of a shape memory alloy layer applied to *Mo*-substrate and a polymer layer enveloping it is presented as a microsystem actuator, in which the restoration of the martensitic detent deformation, however, is achieved by the elastic force of the *Mo*-substrate takes place, while the polymer layer made of a thermoplastic is intended to fix the high-temperature shape of the construction when it cools below the glass temperature and the restoration of its low-temperature shape by the *Mo*-substrate is only possible when it is subsequently reheated to above the glass temperature in the elastic range of the thermoplastic. So, even in this very specific and incomprehensibly complicated application, the elasticity of polymers is not used, but the same bias principle is applied.

Polymers such as elastomers, which in their softened state can be easily processed into any design shape and have high elasticity in their hardened polymerized state, are used so far as active construction components in combination with shape memory alloy elements or memory elements neither in composites materials nor in materials compounds.

That is the purpose of the present invention to provide new, versatile composite materials or materials compounds with new mechanical properties made of elastomers, such as e.g. silicone or rubber, and shape memory alloys, from which can be produced active, movable industrial or art design

components with large movement amplitudes without additional bias elements, which either change their design form passively by changing the temperature of their environment or can be actively controlled by the electric current and change their profiles in a predetermined way

This purpose is achieved according to the invention by the features of the independent patent main claims 1 and 2. The advantageous embodiments and expedient developments of the invention are described in subclaims 3 to 8.

The advantageous connection of elastomers as an elastomer matrix (1) with shape memory alloys as several memory elements (2) embedded in the elastomer matrix (1) results in new composite materials for the production of industrial and art design products or design components, which change their shape or their profile repeatedly and recurring when the temperature changes in their environment or in their memory elements (2) by switching on and off the electrical current in the circuit connected to them under the opposite effect of the pseudoelastic force of memory elements (2) embedded in the elastomers matrix (1) and the elastic force of the elastomer matrix (1).

The advantageous mechanical assembly according to claim 2 of this invention of the elastomer parts (1) and the shape memory elements (2) results in new material compounds for the production of industrial and art design products, which change their shape or their profile as in claim 1 repeatedly and recurring with the temperature change in their environment or in their memory elements (2) by switching on and off the electrical current in the circuit connected to them under the opposite effect of the pseudoelastic force of the memory elements (2) mechanically assembled with the elastomer parts (1) and the elastic force of the elastomer parts (1).

The advantageous embedding according to claim 3 of the memory elements (2) in the elastomer matrix (1) in a conventional injection molding process facilitates the production of the composite material according to this invention and ensures its functionality as a unit during the changes between the target low-temperature and target high-temperature forms by temperature changes in the environment or in their memory elements (2) and results in new versatile composite materials with new mechanical properties. Due to the martensitic deformation of the memory elements (2) in their “soft” martensitic state at room temperature to their target low-temperature shape, the shape of the memory elements (2) is adapted to the design shape of the elastomer matrix (1). The memory elements (2) return to this design form or to this target low temperature under the elastic force of the elastomer matrix (1) during their cooling.

The advantageous inventive polymerizing according to claim 4 of the elastomer matrix (1) with the shape memory elements (2) embedded therein in their design form in a self-curing or cold curing process or in a vulcanization process at temperatures lower than the start temperature of the martensitic reverse transformation (A_s) the memory elements (2) prevents the pseudoelastic force of the memory elements (2) from developing during the polymerization process and thereby ensures that the low-temperature design form and the uniformity of the elastomer matrix (1) with the memory parts (2) as a composite material.

Due to the advantageous molding and polymerizing according to claim 5 of this invention in a conventional injection molding process, the elastomer parts (1) are produced in their design form, for which these should strive due to their elasticity, when the memory elements (2) cool down be-

low the starting temperature of the martensitic forward transformation (M_s).

The advantageous mechanical assembly according to claim 6 of this invention of the elastomer parts (1) formed according to claim 5 with the memory elements (2) in their target low-temperature shape adapted to the design shape of the elastomer parts (1) by the martensitic deformation to an uniform design construction results in new versatile material composites with new mechanical properties, which change their design shape between two specified target shapes when the temperature of the environment or the memory elements (2) changes,. The target high-temperature shape of the memory elements (2) is impressed by its heat treatment in a framework that holds the target high-temperature shape specified at room temperature and prevents this shape from being restored. The martensitic deformation given at room temperature is transformed into plastic deformation during this heat treatment. When the memory elements (2) are heated, they strive for this desired high-temperature shape by developing the pseudoelastic restoring force acting against the elastic force of the elastomer parts (1).

Due to the advantageous installation or attachment according to the claim 7 of the design components made of the composite materials or material compounds according to the invention in various lighting or heating systems, reversible movements are generated by the their heating through the system heat after it is switched on, because the pseudoelastic force of the memory elements (2) exceeds the elastic force of the elastomer matrix (1) or the elastomer parts (1), as well as the force of the elastomer matrix (1) or the elastomer parts (1) exceeds the pseudoelastic force of the memory elements (2) that decreases when the system cools down after the system is switched off, which can let use these design components as indi-

cators or actuators.

Due to the advantageous connection according to the claim 7 of the memory elements (2) through electrical contacts at their ends to a power source, periodic changes in shape of the design components made of the composite materials according to the invention are enables, which are controlled by switching the electrical current on and off.

The annular embedding according to the claim 9 of several memory elements (2) deformed by their martensitic expansion at room temperature in the tire rubber as a rubber matrix (1) between the steel belt and the tread, which has the summer tire profile in the middle, a winter tire profile on both sides and several steel pins as thorns also on both sides, on the outermost edges around the tire, results in a new type of adaptive high-tech car tire, which in a normal case the summer profile creates the connection with dry ground, while the winter profile and the thorns are laterally out of contact with the road.

By heating according to claim 10 of the memory elements (2) embedded ring-shaped in the rubber matrix (1) of the adaptive car tires through the electric current controlled on the control board in the car, the even pressure is created due to the pseudoelastic force of the memory elements (2) on the steel belt of the car tires in their full extent and the summer profile is pressed in with a weather-related worsening in its grip with the road, so that first the winter profile and then steel pins are transported as thorns from their lateral position in contact with the road when the memory elements (2) are further heated and their pseudoelastic force increases and thus considerably increase the grip of the tires to the road when it is iced over. The electrical connection between the car generator and the memory elements (2) in the rubber matrix (1) of the car tires, controlled by the car's

control board, the can be made through electrical lines in the axles and the sliding contacts, which are described e.g. in German patent DE102008001361 A1 of 05.11.2009 and connected to the contacts to the steel wires in metal rim horns or the lead wires of the two bulges.

Further details, embodiments, features and advantages of the present invention can be found in the drawings and in the following description.

It will be shown:

Fig. 1 schematic representation of the martensitic forward and reverse transformations under a constant load and their hysteresis, indicated by the characteristic transformation temperatures, whereby ε is the martensitic deformation developed and reversibly returned during cooling and heating over the temperature range of the martensitic forward and reverse transformations under a constant load, M_s and M_f are the start and finish temperatures of the martensitic forward transformation, A_s and A_f are the start and finish temperatures of the martensitic reverse transformation.

Fig. 2 schematic representation of the relative change in the pseudoelastic stress of a clamped memory element and the elastic stress of an elastomer part when their temperature changes, where $\sigma_{El}(T_c)$, $\sigma_{El}(T_h)$, $\sigma_{ME}(T_c)$ and $\sigma_{ME}(T_h)$ are corresponding stress values for elastomers (El) and memory elements (ME) when they are heated (h) and cooling down (c).

Fig. 3 Development of the pseudoelastic stress of a with 180MPa preloaded real memory element made of a Cu-based memory alloy when its temperature changes over the temperature range of the martensitic forward and reverse transformations, where T_B and σ_B are the temperature (*break-*

ing temperature) and stress (*breaking stress*) at which a memory element breaks itself when it is clamped.

Fig. 4 a, b a design lamp or a design component made of the composite material according to the invention: (a) – of a transparent or colored silicone matrix (1) and several memory elements (2), which when heated by a heat source (*light bulb* (3) or heated metal base (3)) change the original design shape of the lamp in a complicated way (b) that is dependent on the placement of the memory elements (2) in the elastomer matrix (1).

Fig. 5 a, b a design component or a design heat indicator made of the material compound according to the invention – of a silicone matrix (1) and a memory element (2), which when heated by a heat source (*radiator in contact with the metal base* (3) of the design indicator) the original design shape (a) – a ball e.g. – changed to a different design shape (b) – "candle" e.g. – through the effect of its pseudoelastic force.

Fig. 6 a, b, c a designer car tire made of the composite material according to the invention (a) – of a rubber matrix (1) and several memory elements (2), which when heated by the electrical current supplied at the contact point between the two bulges 7 and the rim horns 8, flatten the original round design shape of the rubber tire so that the tread of the car tire in contact with the roadway changes from summer profile 4 (a) to summer-winter profile 5 (b) and finally, in an extreme case, to summer-winter thorn profile 6 (c) complicates and can thereby significantly increase the grip of the car tire with the road surface.

Fig. 7 a, b a memory element (2) cut out of a roll plate (a) for the material compound according to the invention shown in figure 5, different its conical spiral shape is imprinted by the heat treatment in a framework that holds this target high-temperature shape (b).

Workpieces made of shape memory alloys have the property their geometry between an original, e.g. by their production (*wire drawing, rolling, etc.*) predetermined high-temperature shape and a low-temperature shape introduced by the martensitic deformation at low temperatures to change with temperature changes, i.e. to remember their original high-temperature shape or their low-temperature shape and to restore them reversibly due to cyclical temperature changes.

This property is based on the martensitic transformations, i.e. changes in the crystal lattice that occur through cooperative displacement of several atomic planes. The forward transformation (**Fig. 1**) from the high-temperature phase “austenite” to the low-temperature phase “martensite” takes place during cooling in a temperature range $M_s \div M_f$, start (*s*) and finish (*f*) temperatures of the forward transformation. The reverse transformation of the martensite into the austenite takes place accordingly during heating in a characteristic temperature range $A_s \div A_f$. The total transformation or deformation temperature interval $M_f \div A_f$ can be from ten to hundreds of degrees between -200°C and $+400^\circ\text{C}$, depending on the alloy composition.

The spontaneous reversible change in shape of a memory element between its low and high temperature shape without the influence of external forces and only through temperature changes is possible through appropriate thermomechanical training for the two-way memory effect. The value of the two-way memory effect is limited to approx. 2%, whereby a memory element is not able to do the work against an external force.

The one-way memory effect, on the other hand, consists in the fact that a memory element its martensitic low-temperature deformation, e.g.

through tension $\varepsilon_M = \frac{\Delta L}{L_0}$ up to 8% , completely resets when it is heated

above the temperature A_f and returns to its target high-temperature shape.

If this resetting is prevented by an external force F^{ext} , the memory element (ME) with a cross-section S_{ME} and an initial length L_0 does the corresponding work $A_{ME} = F^{ext} \cdot \Delta L = \sigma_{ME} \cdot \varepsilon_M \cdot S_{ME} \cdot L_0$.

For the complete return to its low-temperature shape during cooling, an external force acting in the opposite direction must then act on the memory element, which is fulfilled in technical applications of memory alloys as so-called memory actuators due to the elastic bias element acting on memory elements, such as e.g. steel spring.

The solution suitable for the composite materials according to claim 1 or materials compounds according to claim 2 uses the shape memory effect (**Fig. 1**) and the associated force memory effect (**Fig. 2**) of the memory elements and the elastic counteracting force (*stress*) of the elastomer matrix (**Figs. 4 and 6**) or of the elastomer part (**Fig. 5**). Reversible movements with certain frequencies and amplitudes can on this way be realized only by alternating heating and cooling of the memory elements without special bias elements.

The advantageous connection of the pseudoelastic force of the mechanical or electro-mechanical memory elements (2) in a counter-relationship with the elastic force of the elastomer matrix (1) or the elastomer parts (1) ensures the restoration of the martensitic deformation of the memory elements (*the return to their target high-temperature form*) when their pseudoelastic force (*stress*) when heated exceeds the elastic force (*stress*) of the elastomer matrix (1) or the elastomer parts (1) (**Fig. 2, heating**) and

the restoration of the martensitic deformation (*the return to its desired low-temperature shape*) when the elastic restoring force of the elastomer matrix (1) or the elastomer parts (1) exceeds the pseudoelastic force (*stress*) of the memory elements during their cooling (**Fig. 2**, *cooling*). Further information on the memory effects and their background can be found in the publications (6: V. Prieb, H. Steckmann. *Thermoelasticity and hysteresis of martensitic transformation in shape memory alloys. Parts I - III. Tech. Phys. 41 (1996) 1132-1144*; 7: D. Stöckel. *Shape Memory Actuators for Automotive Applications. In "Engineering Aspects of Shape Memory Alloys" (eds.) T.W. Duerig, K.N. Melton et al., 11 (1990) 302-307*).

Since the memory elements (2) are in the cooling stage or in a cooled, completely martensitic state with the small quasiplastic yield point σ_{qy}^{ME} of martensite, they are deformed martensitically by the elastic force of the elastomer matrix (1, **fig. 4 and fig. 6**) or the elastomer parts (1, **fig. 5**). This design simplifies the construction by eliminating a passive elastic bias element, which restores the original martensitic deformation during the cooling of the active memory element (2).

The pseudoelastic force $F_{ME}(T)$ or pseudoelastic stress $\sigma_{ME}(T) = \frac{F_{ME}}{S_{ME}}$ (**Fig. 2**) of the memory elements (2) determined by the thickness or the cross-section S_{ME} can far exceed during their heating the elastic restoring force $F_{El}(T)$ or elastic restoring stress $\sigma_{El}(T) = \frac{F_{El}(T)}{S_{El}}$ (**Fig. 2**) of the elastomer matrix (1, **Figs. 4 b and 6 b, c**) or the elastomer parts (1, **Fig. 5**), which decreases with the increase in temperature, the pseudoelastic stress of the memory elements should be set always below

the breaking limit value $\sigma_{ME}(T) < \sigma_B$ (**Fig. 3**) through the current intensity and the temperature increase less than the breaking temperature $T < T_B$. The pseudoelastic stress of the real memory element made of a *Cu*-based memory alloy (**Fig. 3**) increases with the increase in temperature to more than 700MPa or $70\text{kg} \cdot \text{mm}^{-2}$, so that a pseudoelastic force necessary for the specific application can be achieved due to the cross-section and the number of memory elements.

In this way, the stress difference $\sigma_{ME}(T) - \sigma_{El}(T) = \Delta\sigma(T)$ can be increased up to its maximal value $\Delta\sigma(T) = \sigma_{\max}$ and used for the useful mechanical work $W = F_{\max} \cdot A_{ME} = \sigma_{\max} \cdot \varepsilon_M \cdot S_{ME} \cdot L_a$ at the movement amplitude $\Delta L = L_b - L_a$ (**Fig. 4 a, b**) of an actuator made from the composite materials according to claim 1 (**Figs. 4 and 6**) or from the materials compounds according to claim 2 (**Fig. 5**).

As memory elements (2) for the composite materials according to claim 1, straight memory wires or memory strips stretched in a martensitic state can be embedded in the elastomer matrix (1), while memory elements (2) for the materials compounds according to claim 2 in their various geometries and shapes can be mechanically connected to elastomer parts (1), as it shows figure. 7 for the materials compounds in figure 5. The memory element (2) is made as a conical spring (b) from a memory roll plate (a), using e.g. a laser cut out, pulled apart in a martensitic state, annealed in this spring form (b) at 800°C in a framework holding this shape, after cooling to its original shape (**Fig. 5 a**) deformed martensitically and inserted in the elastomer part (1, **Fig. 5**).

All of the features described above and each of their conceivable combinations with one another fall under the scope of this invention, insofar as

it is technically or logically sensible. Furthermore, all changes and modifications which are obvious to those skilled in the art from the invention just described also fall within the scope of the invention as defined in the appended claims.

For this:

10 claims and

7 drawings

Claims (10)

1. Composites of elastomers and memory alloys **characterized in** that it consists of resilient elastomeric matrix (1) In any of its forms and the desired design made of an alloy having memory properties or shape memory alloy and in their low temperature shape in this elastomer matrix (1) Embedded memory elements (2) Exist which are suitable for the production of movable industrial and art design products that can be used in various structures as a portable design components in various ways, wherein the mobility of these design components or as their recurring shape changes with changes in temperature of its surroundings (. their memory elements 2) By switching the electric current in these memory elements (2) Connected circuit by the opposite action of the elastic force of the elastomer matrix (1) And the pseudo-elastic force in these elastomeric matrix (1) Embedded memory elements (2) Is ensured.
2. Composite materials made of elastomers and memory alloys characterized in that it consists of resilient elastomeric parts (1) In one of their desired design shapes and made of an alloy with memory properties or shape memory alloy and its low-temperature form with these elastomeric parts (1) Mechanically assembled memory elements (2), And can be applied as a portable design components in various ways in various constructions, the mobility of these design components than their recurring shape changes with changes in temperature of their environment or of their memory elements (2) By switching the electric current in these memory elements (2) Connected circuit by the opposite action of the elastic force of the elastomer parts (1) And the pseudo-elastic force of these elastomeric

- parts (1) Mechanically assembled memory elements (2) Is ensured.
3. Composite of elastomer and memory alloys according to claim 1, characterized in that the memory elements (2) As amended by the martensitic deformation of the design shape of the elastomer matrix (1) Adapted low-temperature form in the elastomer matrix (1) Are embedded in a conventional injection moulding process, in which the elastomer matrix (1) Is formed into their design form at room temperature which these by their elasticity on cooling of the memory elements (2) Under the starting temperature of martensitic Hinumwandlung (M_s) seeking, and in conjunction with the memory elements (2) Forms a new composite material with new mechanical properties.
 4. Composite of elastomer and memory alloys according to claims 1 and 3 characterized in that the elastomer matrix (1) With the embedded into these memory elements (2) In their design form in a self- or cold cure or in a vulcanization at temperatures lower than the starting temperature of martensitic transformation back (A_s) of memory elements (2) Is polymerized.
 5. Composite materials made of elastomers and memory alloys according to claim 2, characterized in that the elastomer part (1) Is shaped into its design shape at room temperature in a conventional injection moulding process and polymerized in this design form, which of these by its elasticity during the cooling of the memory element (2) Under the starting temperature of martensitic Hinumwandlung (M_s) aspires.
 6. Composite materials made of elastomers and memory alloys according to claims 2 and 5, characterized in that the memory element (2),

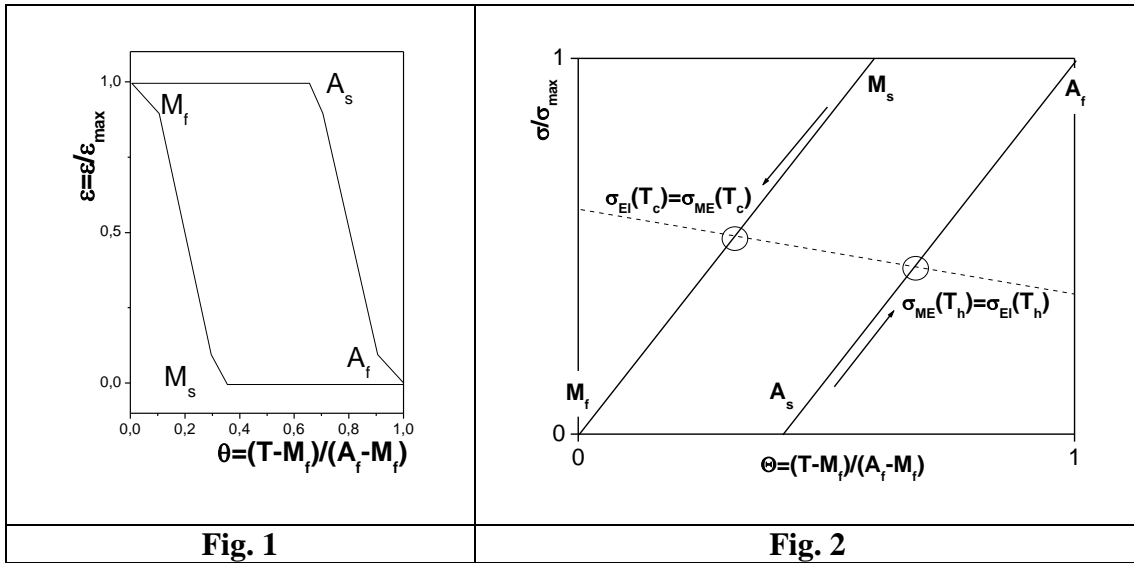
As amended by the martensitic deformation of the design shape of the elastomer part (1) Adapted low-temperature form with the formed according to claim 5 elastomer part (1) Is mechanically assembled to form a unitary construction design and thus together with the elastomer part (1) Forms a new composite material with new mechanical properties.

7. Composites and composite materials made of elastomers and memory alloys according to claims 1 to 6, characterized in that this or made from these design components can be activated in different light- or heating and heat plants and are grown and their reversible movements by the immediately after switching on the heating by the heat generated during the installation and the elastic force of the elastomer matrix or the elastomer part (1) In excess of pseudo elastic force of the memory elements (2) And by the cooling after turning off the system (the waning power of the pseudo-elastic memory elements 2) Exceeding elastic force of the elastomer matrix (1) And the elastomer part (1) Are generated.
8. Composites and composite materials made of elastomers and memory alloys according to claims 1 to 7, characterized in that the memory elements (2) Can be connected through the electrical contacts on its endings to a power source and heated by the electric current.
9. Car tires in a composite material according to claims 1, 3, 4 and 8, characterized in that the rubber elastomer as matrix (1) And more in its deformed by the martensitic strain state in this rubber matrix (1) Via the steel belt at room temperature ring-shaped embedded under the tread memory elements (2), And the car tires made of this composite material in the middle of a summer tire profile, at either end a

winter tire profile and also on both sides, have at extreme edges around the tire several steel pins as thorns, so that in a normal case, the summer profile that connects to a dry surface, while the winter tread and the thorns are laterally without contact with the road.

10. Car tire according to claims 1, 3, 4, 8, and 9, characterized in that the summer heat profile in weather-related deterioration of its adhesion to the road by turning on the electric current to the control board of the car and through which the memory elements (2) Is pressed by the pseudo elastic force, so that only the winter profile, and then upon further heating of the memory elements (2) And enlarge their pseudo-elastic force the steel pins are carried as thorns in their lateral position in contact with the road and thus greatly increase the grip of the tires and the road.

Drawings:



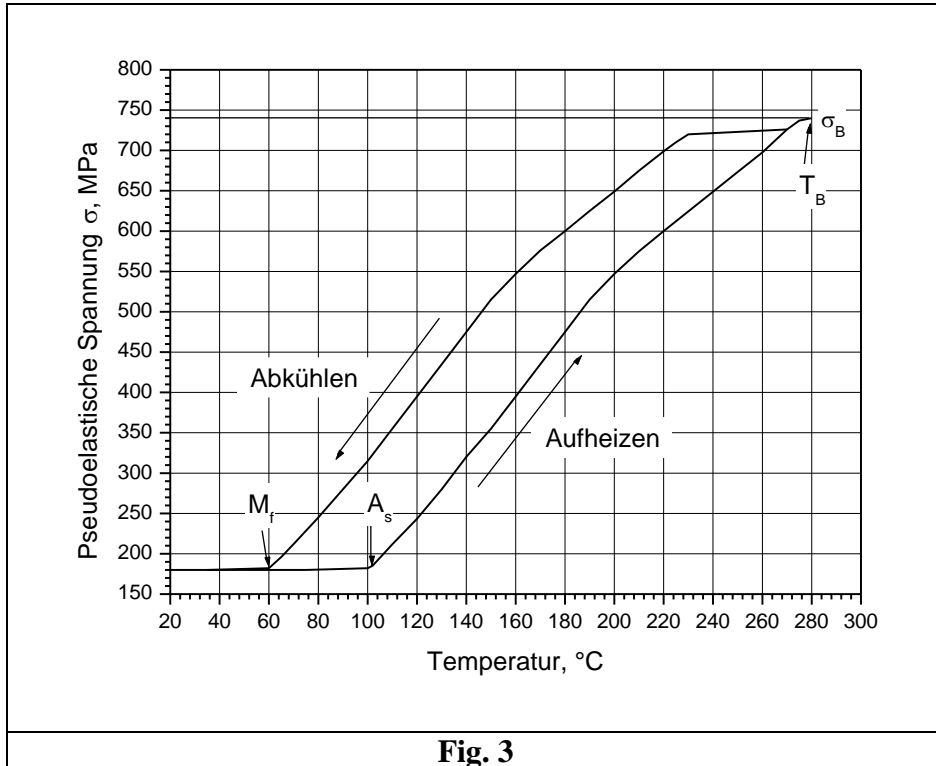


Fig. 3

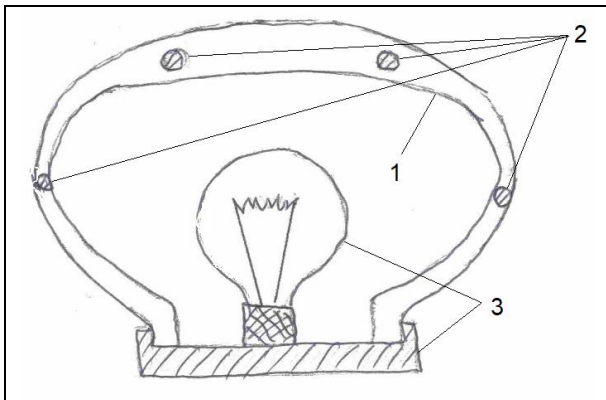


Fig. 4 a

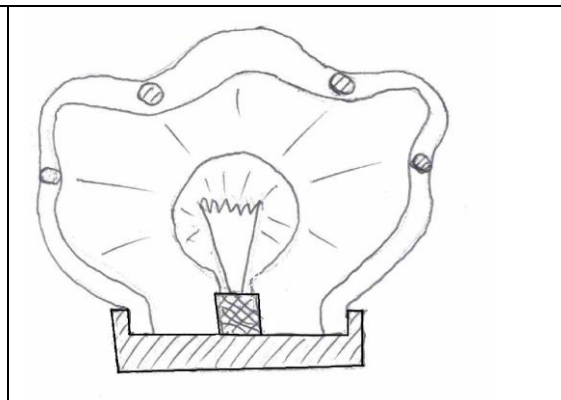


Fig. 4 b

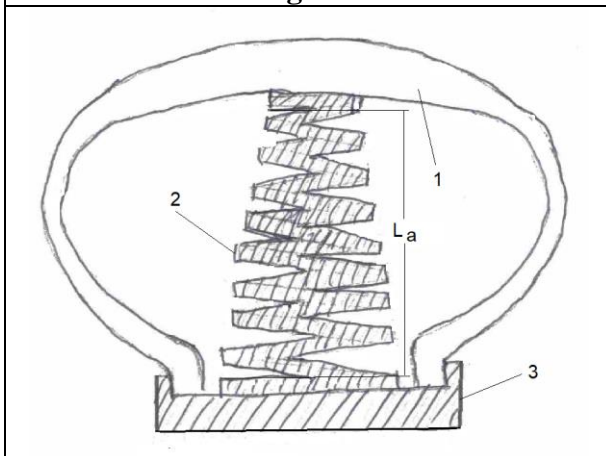


Fig. 5 a

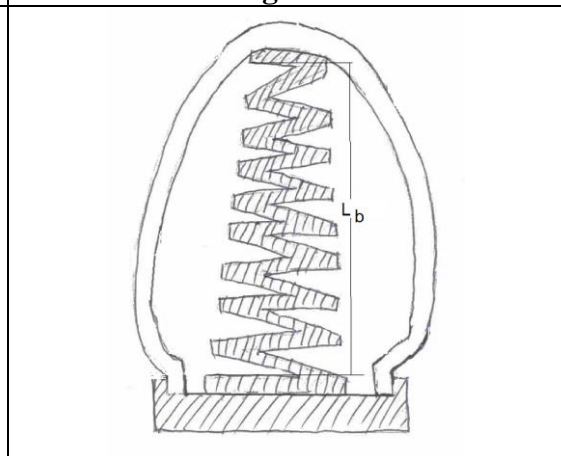


Fig. 5 b

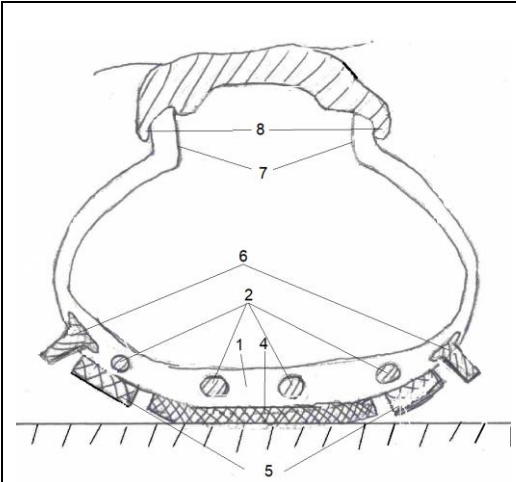


Fig. 6 a

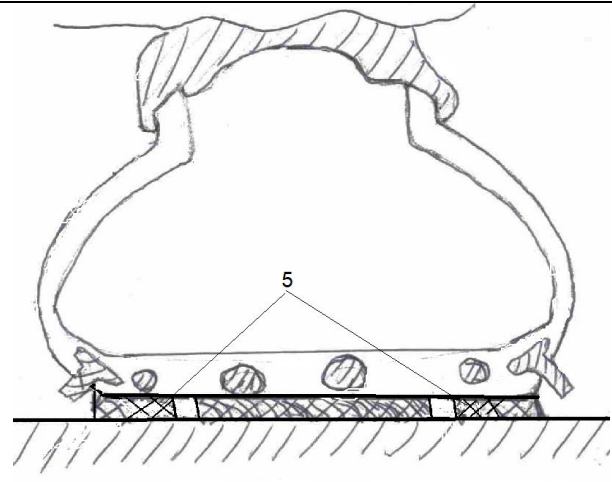


Fig. 6 b

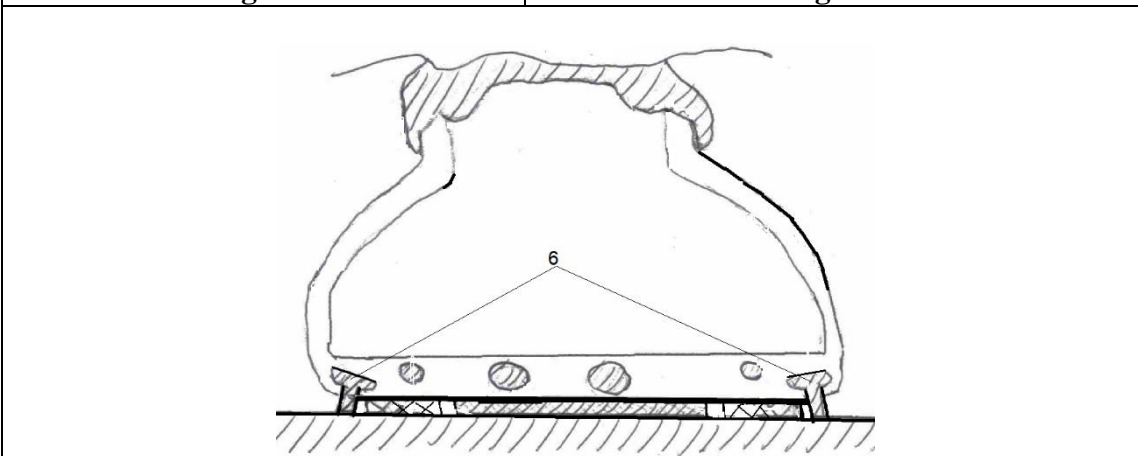
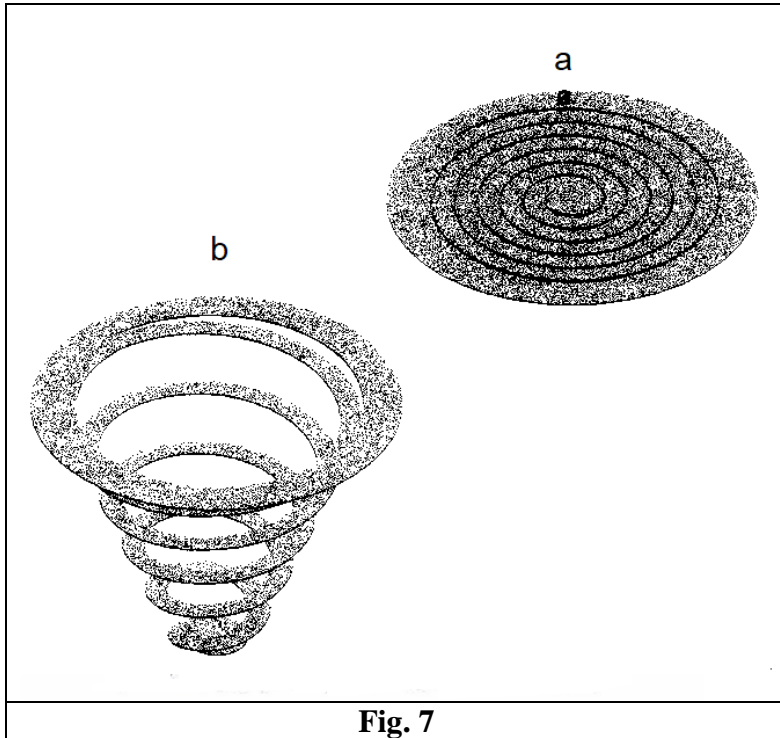


Fig. 6 c



8.4 German utility model: "Temperature control valve with a memory membrane"

DE 20114702 U1 dated January 17, 2002.

Inventor: Dr. V. Prieb, Dr. H. Steckmann, Dr. L. Neganov

Utility model holder: Company "1st Memory Alloys GmbH"

Abstract:

Object of the invention (based on recurring memory effect through bias springs):

A temperature control valve of a simple construction without thermal sensors, without signal processing and without drive mechanisms, in which all these functions are taken over by a single component, so that every temperature change of the heating or cooling medium leads to an immediate change in the flow cross section or the Flow rate and thus to compensate for the temperature deviation.

Applications:

The temperature control valve according to the invention can be used in a very wide temperature range both in cooling (*e.g. when cooling down plastic injection molded parts*) and in heating systems of all kinds.

Description:

The invention relates to a temperature control valve for heating or cooling systems for regulating the flow temperature of the liquid or gaseous heating or cooling medium by controlling the flow cross section and thus the flow rate with the aid of a thermosensitive membrane made of a memory alloy or memory membrane, which reversibly effects the flow through its temperature dependent changes in shape between two positions "open" and "closed".

The state of the technology includes the generally known temperature

control valves, which are used in various technical areas such as heating, medical, vehicle, plant engineering, etc. as thermostatic valves or temperature control devices.

The function of such temperature control valves is to keep the temperature of the heating or coolant constant at a target value by changing the flow cross-section and accordingly the flow rate. This task has so far been achieved by fulfilling three functions: the target/actual temperature difference measurement, the conversion of the measured value into a signal and the transmission of this signal to a drive and the setting in motion of a valve element causing the flow through a drive.

These functions are taken over by various valve components, such as temperature sensors, signal converters or amplifiers, drive mechanisms and thus determine in advance the design and construction of various known temperature control valves.

DE 44 31 463 describes a compact controller for a control valve controlled by a pneumatic diaphragm drive, in which a signal converter converts a temperature deviation detected by a thermal sensor into a pneumatic pressure signal for the diaphragm drive. The diaphragm drive actuates a valve tappet, which then changes the flow rate accordingly.

DE 43 36 914 describes a temperature control device, in which the variable flow cross-sectional size of an expansion valve is controlled as a function of the temperature of a coolant measured by temperature sensors and thereby the temperature in the coolant circuit.

The both controls described above are complex, costly and have a large number of components. In order to avoid the temperature sensors and complex signal processing, DE 198 55 926 proposes a control valve in which

two thermostats take over the functions of the temperature sensor and drives, so that a valve tappet is actuated through a transition piece by the length change of the thermostats caused by the thermal expansion of the thermostat filling, and thus the flow rate of the heat transfer medium is effected.

This control valve also has a no less complicated structure and an expensive construction. In addition, the changes in length caused by thermal expansion and thus the movements of the valve tappet are too small to effect the flow within broad limits.

The purpose of the present invention is to develop a temperature control valve of a simple design without a temperature sensor, without signal processing and without drive mechanisms, in which all three functions are taken over by a single component of the control valve, so that every temperature change of the heating or cooling medium is used leads to an immediate change in the flow cross-section or the flow rate and thus to compensate for the temperature deviation.

This purpose is achieved according to the invention by the features of claims 1 to 6.

A new temperature control valve results based on a new functional principle of a simplified design, in which a membrane made of a memory alloy or memory membrane (2) is incorporated in the valve body (1) according to claim 1, which membrane has the two-way memory effect according to claim 4 and thus its shape and accordingly the flow cross-section changes reversibly as a function of the temperature (*Fig. 1 a, b, c*), or the memory membrane (2) according to claim 5 has the one-way memory effect, where the resetting of the shape change of the memory membrane (2) caused by the temperature change and the associated reversible change in the flow

cross-section take place through the opposite bias force of an elastic counter-spring (5) (**Fig. 2 a, b, c**), that is easy to manufacture and versatile to use.

The advantageous production of the memory membrane (2), according to claim 2, from a memory alloy with a narrow hysteresis allows more precise regulation of the heating or cooling medium temperature within a narrow temperature range.

The advantageous use, according to claim 3 of a multi-component memory alloy on the (*Cu – Al*)- or *NiTi*-based allows the transformation temperatures and the hysteresis range and thereby the control temperature and the temperature range of the control valve by varying the composition with an accuracy of up to 1°C in a temperature range of –200°C up to +400°C and thus cover all possible application areas of the control valve according to the invention.

The advantageous use of the two-way memory effect leads according to claims 4 and 9 to a further simplification of the control valve construction.

The advantageous installation of an elastic counter spring increases the flow rate difference between the “open” and “closed” states and reduces the temperature range of the control valve according to the invention.

The advantageous cutting of different opening profiles into the memory membrane (2) expands the possibilities of varying the flow characteristics of the temperature control valve according to the invention depending on the application.

The advantageous embossing of the memory membrane (2) or its opening flaps according to claim 7 their high temperature shape due to the plastic deformation at high temperatures and according to claim 8 their low

temperature shape due to the martensitic deformation lets vary the initial opening of the temperature control valve according to the invention as well as the flow rate difference between the end opening and the initial opening depending on the application requirements and leads to an additional expansion of its application field.

The advantageous installation of the memory membrane (2) in the valve body (1) according to claim 12 against the flow direction of the heating or cooling medium (*Figs. 1 c, 2 c*) leads to a reduction in the flow rate and accordingly the flow mass as well as to the fact that the pressure of the heating or cooling medium flowing through is used as an additional restoring force that serves to close the membrane when the temperature is lowered.

The advantageous installation of the memory membrane (2) in the valve body (1) according to claim 13 in the flow direction of the heating or cooling medium (*Figs. 1 c, 2 c*) leads to an additional increase in the flow rate and according to the flow mass.

Further details, features and advantages of the invention are revealed in the following drawings and their description.

It shows:

Fig. 1a, b, c a temperature control valve for cooling systems with a memory membrane trained to a two-way memory effect in the “closed” initial state (a) and in the “open” final state when installing the memory membrane in the flow direction (b) and in the opposite direction (c).

Fig. 2a, b, c a temperature control valve for cooling systems with an elastic counter-spring and a memory membrane having the one-way memory effect in the “closed” initial state (a) and in the “open” end state when installing the memory membrane in the flow direction (b) and in the opposite direction (c).

Fig. 3a, b the simplest low (a) and high temperature shapes (b) of the

memory membrane without opening flaps.

Fig. 4 a, b the low (**a**) and high temperature shapes (**b**) of the memory membrane with a round cut opening flap.

Fig. 5 a, b the low (**a**) and high temperature shapes (**b**) of the memory membrane with two rectangular opening flaps.

Fig. 6 a, b the low (**a**) and high temperature shapes (**b**) of the memory membrane with four triangular opening flaps.

Fig. 7 a, b the low (**a**) and high temperature shapes (**b**) of the memory membrane with a spiral cut opening flap.

Fig. 8 Flow-temperature deviation diagram for the five memory membranes shown in Figs. 3 to 7 (*curve number corresponds to said figure number*) in cooling systems (*temperature deviation* $(T - T_R)/(A_f - T_R)$) and in heating systems (*temperature deviation* $(T - T_R)/(M_f - T_R)$).

Fig. 9 Schematic deformation-temperature diagram of a memory membrane that characterizes the characteristic transformation temperatures (M_s, M_f, A_s, A_f) of the memory membrane and the resulting control temperature (T_R), control accuracy ($\delta = A_s - M_s$), and temperature range ($\Delta T = A_f - M_f$) of the control valve.

A distinction is made between the one-way memory effect and the two-way memory effect. In the case of the one-way memory effect, the shape (*high temperature shape*) of a memory metal piece impressed by the plastic deformation at high temperatures is changed at temperatures below the finish temperature M_f of the martensitic forward transformation (**Fig. 9**) by the martensitic deformation under the action of an external mechanical force (*low temperature shape*). When the memory metal piece is heated beyond the temperature interval $(A_s - A_f)$ of the martensitic reverse transformation (**Fig. 9**), the martensitic deformation is reversed and the memory metal piece assumes its original high-temperature shape again. A further cooling down beyond the temperature range $(M_s - M_f)$ does not lead to any further shape change of the memory metal piece. The maximal marten-

sitic deformation that can be restored with the one-way memory effect reaches up to (7 ÷ 8)% in the known memory alloys.

With repeated one-way memory effect cycles described above, in which the memory metal piece is martensitically deformed again and again to the same low-temperature shape after each cooling by an external mechanical force, or when the thermal cycles are carried out on a memory metal piece loaded by a constant external force, the memory metal piece is trained to the two-way memory effect. In the two-way memory effect, the memory metal piece changes its shape spontaneously and reversibly between the low and high temperature shapes during heating up over the temperature interval $A_s \div A_f$ and cooling down over the temperature interval $M_s \div M_f$. The reversible martensitic deformation in the two-way memory effect is then only (2 ÷ 3)% .

If the reset of the martensitic deformation is prevented by an external force F^{ext} , the memory metal piece (*memory element ME*) develops a restoring force F_{ME} , which does the work against the hindering external force and enforces the restoration of the martensitic deformation under the condition $F^{ext} < F_{ME}$. The restoring force $\frac{dF_{ME}}{dT} = S_{ME} \cdot \frac{d\sigma_{ME}}{dT} > 0$ depends linearly on the temperature. For these reasons, the relationship between a constant external force $F^{ext} = const$ or external stress $\sigma^{ext} = const$ and the restoring force or the martensitic stress $\sigma_{ME}(T)$ can change with the temperature.

Further details on this are known, for example, from the reprint of the “Zeitschrift für Wirtschaftlichen Verwaltung”, 81, volume 1986, issue 12, p. 203 and are shown in my computer animation “Shape memory effects

and their applications”.

Figures 1a, 1b, 1c show the first, simplest embodiment of the temperature control valve according to the invention. The control valve consists of a valve body (1), which have an inlet and an outlet opening, and a memory membrane (2) trained for the two-way memory effect, which is fastened on the one side with a screw (3) on the body ground (4). As the valve body (1) can be used a customary, commercially available transition piece for different pipe diameters, so that the temperature control valve according to the invention can be easily installed in any heating cooling medium line.

The high-temperature shape of the memory membrane (2) trained for the two-way memory effect is selected so that the control valve is maximal opened at higher temperatures (**Figs. 1 b, 1 c**). The low-temperature shape of the memory membrane, on the other hand, corresponds to the minimal opening of the control valve or its complete closing (**Fig. 1 a**). This construction is suitable for the cooling systems. As long as the coolant remains at a control or cooling temperature T_R , which is determined by the memory alloy composition, the flow cross-section or the flow rate of the coolant is minimal.

If this flow rate is no longer sufficient for cooling and the temperature increases $\delta/2 = A_s - T_R$, the change in shape of the memory membrane (2) begins to its high temperature shape, which leads to the valve opening and an increase in the flow rate of the coolant. When the temperature increase reaches the value $\Delta T/2 = A_f - T_R$ and the increased flow rate of the coolant leads to the temperature decrease above the value $\delta/2 = T_R - M_s$, the change in shape of the memory membrane starts back to its low temperature shape, which is complete at $\Delta T/2 = M_f - T_R$.

In this way, the control temperature T_R is kept in the range $\delta = A_s - M_s$ determined by the control accuracy. An additional flow rate regulation of the coolant is achieved by installing the memory membrane (2) in the flow direction (*Fig. 1 b*) or in the opposite direction (*Fig. 1 c*). When installed in the opposite direction, the opening memory membrane (2) offers greater resistance to the coolant flow and thus reduces the amount of coolant flowing through. In addition, the liquid pressure on the memory membrane (2) installed in the opposite direction promotes its return to the low-temperature shape when temperature decreases below the temperature M_s .

Figures 2a, 2b and 2c show the second embodiment of the temperature control valve according to the invention, which also consists of a valve body (1), a memory membrane (2) having the one-way memory effect, which is either sits free on the body ground (4) or can also be fastened with one or more screws (3), and consists of an elastic counter spring (5). The counter spring (5) acts on the memory membrane (2) with a force F^{ext} that will be exceeded $F_{ME} > F^{ext}$ by the restoring force F_{ME} when the temperature increases and does not prevent the memory membrane (2) from returning to its high-temperature form.

When the temperature decreases below the temperature M_s , the memory membrane (2) changes into the martensitic state without returning to its low-temperature shape. Because the yield point σ_{qy}^{ME} of quasiplastic deformation becomes low in the martensitic state at lower temperatures, the elastic spring force exceeds this yield point, so that the martensitic deformation takes place, and the memory membrane (2) is pressed back to its low-temperature shape by the counter spring (*cooling systems*) or back pulled (*heating systems*). The installation of the memory membrane (2) in

the flow direction (**Fig. 2 b**) or in the opposite direction (**Fig. 2 c**) contributes to the balance of the forces and can be used accordingly.

For the heating systems, for example for an outlet temperature control valve of a radiator, the memory membrane (2) is impressed with its low-temperature shape at temperatures below the temperature M_s through the martensitic deformation so that the control valve opens when the temperature decreases, and its high-temperature shape impressed with the plastic deformation at high temperatures in such a way that the control valve closes when the temperature rises.

The installation of the memory membrane (2) in the valve body (1) of the control valve according to the invention then takes place in the manner as shown in fig. 2, the counter spring (5) is installed in such a way that it is firmly connected with the memory membrane (2) and does not press back the memory membrane (2) as in cooling systems, but pulls back upwards. The memory membrane (2) is martensitically deformed by the elastic force of the counter spring (5), which leads to the opening of the control valve when the temperature decreases, while the restoring force F_{ME} of the memory membrane (2) exceeds $F_{ME} > F^{exz}$ the elastic force F^{exz} of the counter spring (5) when the temperature rises, the memory membrane (2) or its opening flap assumes its high-temperature shape and the control valve thus closes.

Figs. 3 to 7 show different embodiments of the memory membrane (2) in the closed (**a**) and open (**b**) states. The memory membrane (2) has openings cut in different ways, through which the flow cross-section or the flow rate is effectively caused, as it shows the flow-temperature deviation diagrams in fig. 8.

Fig. 3 shows the simplest embodiment of the memory membrane (2) already described with reference to figs. 1 and 2 without opening flaps, in which the entire memory membrane (2) is deformed by bending and ensures for the opening-closing of the control valve in the event of temperature changes (**Fig. 8, line 3**).

Fig. 4 shows an analogous embodiment, in which a round opening flap is cut into the memory membrane (2), which is bent in exactly the same way and functions just like the entire memory membrane (2) in fig. 3. The opening of this opening flap (**Fig. 4 b**) or its closing (**Fig. 4 a**) changes at the temperature changes the flow cross-section or the flow rate parabolically from the temperature (**Fig. 8, line 4**). This embodiment is advantageous in that the maximum flow rate is determined by the diameter of the incision and not by the diameter of the outflow. The remaining ring of the memory membrane (2) is used for better fastening, for example with several screws (5) of the memory membrane (2) on the body base (4) of the valve body (1), especially when installing the memory membrane (2) without a counter spring in the opposite direction of flow (**Fig. 1 c**).

Fig. 5 a, b shows the memory membrane (2) with two incised rectangular opening flaps, which opening (**Fig. 5 b**) or closing (**Fig. 5 a**) changes the flow cross-section or the flow rate linearly (**Fig. 8, line 5**) of the temperature changes. The dimensions of the incision can also determine the outlet amount of the outlet pipe.

Fig. 6 a, b shows the memory membrane (2) with four incised triangular opening flaps, which opening (**Fig. 6 b**) or closing (**Fig. 6 a**) changes the flow cross-section or the flow rate parabolically (**Fig. 8, line 6**) of the temperature changes.

Fig. 7 a, b shows an embodiment of the memory membrane (2) which is

particularly suitable for low pressures and large flow rates, into which a spiral-shaped opening flap is cut, which opening (**Fig. 7 b**) or closing (**Fig. 7 a**) changes the flow cross-section or the flow rate exponentially (**Fig. 8, line 7**) of the temperature.

All of the memory membranes with the opening flaps shown in figs. 4 to 7 are installed in the body (1) of the control valve according to the invention in the manner shown in figs. 1 and 2 for the memory membrane (2) in fig. 3 and they also work in the same way as described above.

Fig. 8 shows four lines of the flow-temperature deviation diagram, which characterize the opening flaps of the memory membrane (2) shown in figs. 4 to 7. An embodiment of the memory membrane (2) suitable for a specific application can be selected on the basis of these flow-temperature deviation characteristics. This flow-temperature deviation diagram is the same for cooling systems, in which the temperature increase over the temperature interval $A_f - T_R$ leads to the complete opening of the control valve, as well as for heating systems, in which the temperature decrease over the temperature interval $T_R - M_f$ down leads to the complete opening of the regel valve.

Fig. 9 shows schematically the deformation or the reversible shape change of the memory membrane (2) as function of the temperature in the temperature range $M_f - A_f$. The deformation lines during cooling and heating form a hysteresis, the extent $M_f - A_f$ of which determines the temperature range ΔT , which determines the control temperature T_R set to the middle of the temperature interval $M_s - A_s$ and the width of the temperature interval $\delta = A_s - M_s$, which determines the control accuracy of the temperature control valve according to the invention. Temperatures

M_s , A_s are the characteristic start temperatures and the characteristic finish temperatures of the forward and reverse martensitic transformation, correspondingly. These characteristic temperatures can be set by varying of the memory alloy composition.

For this 9 drawings:

Fig.1

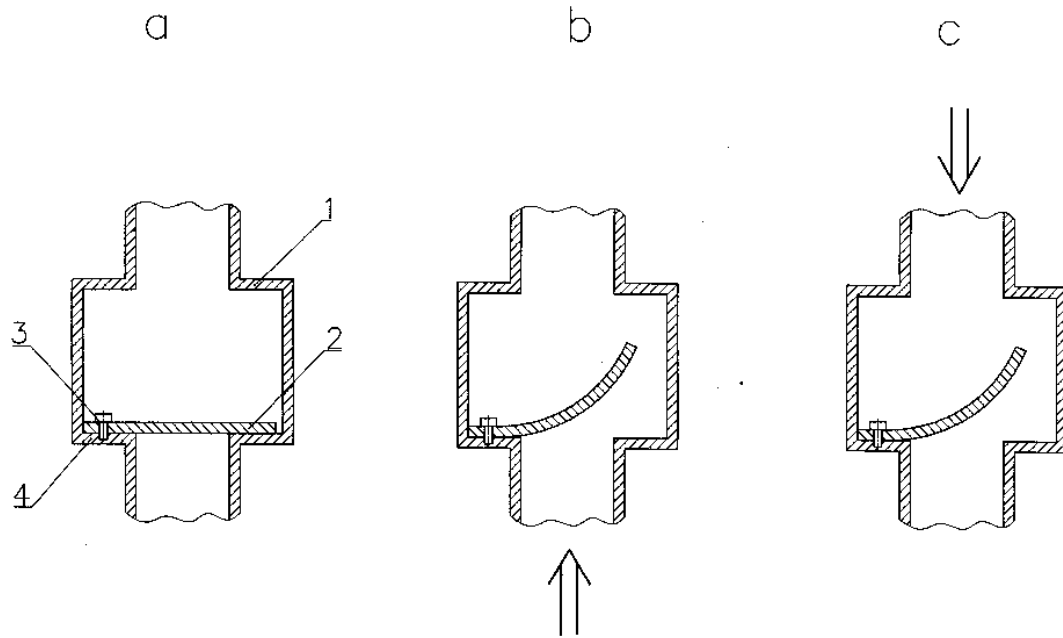
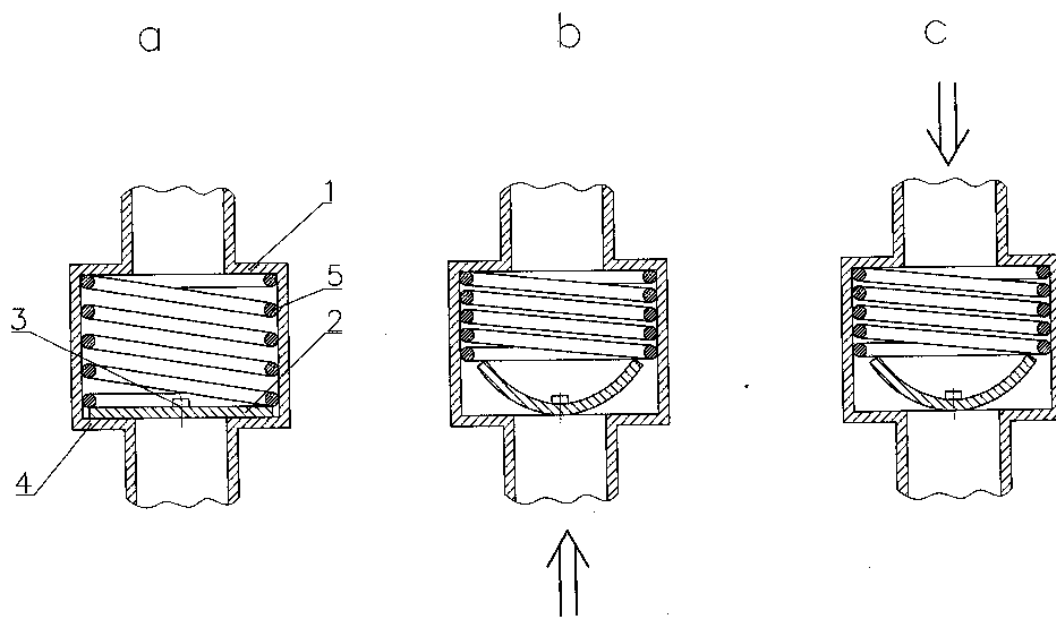
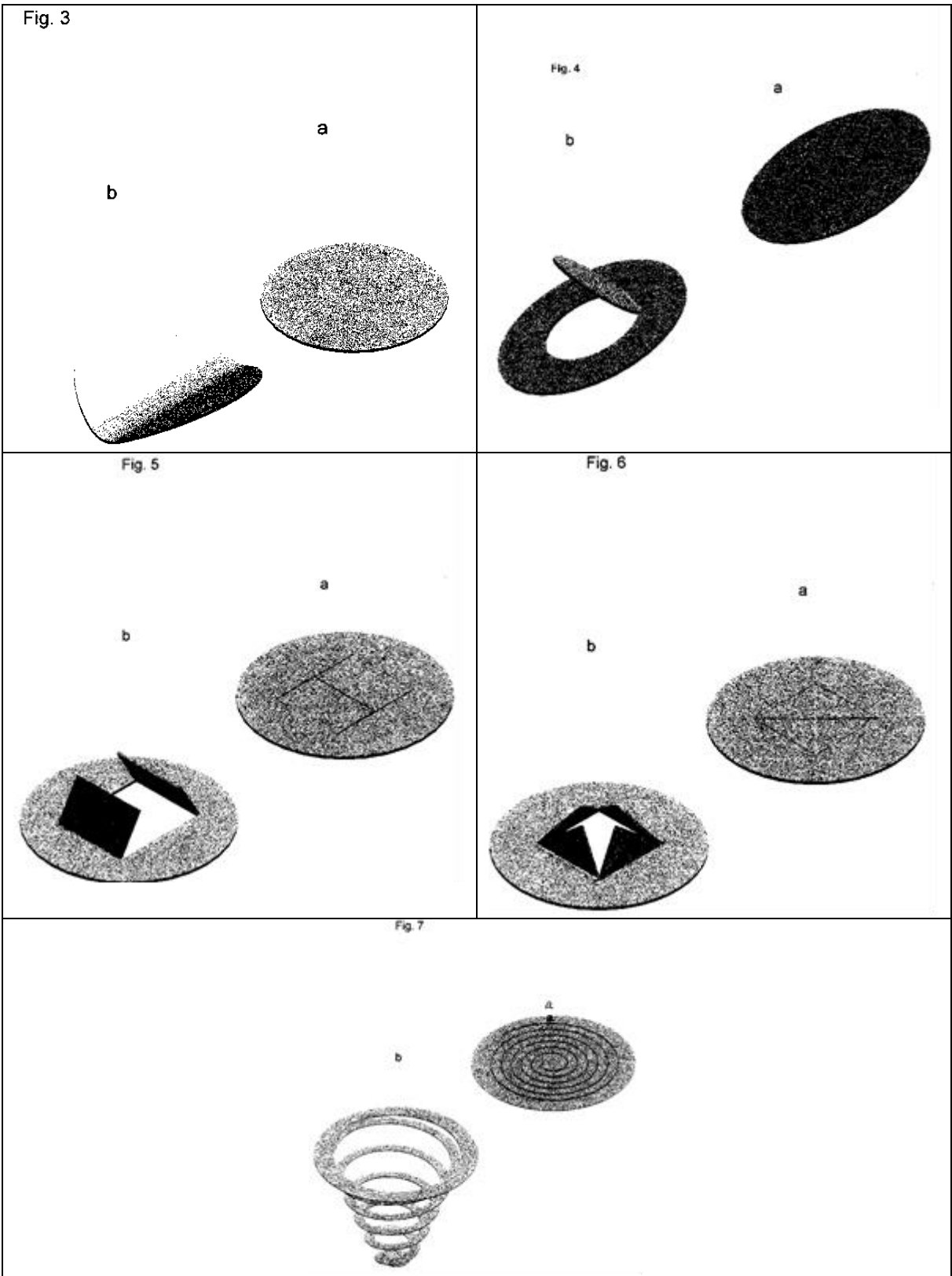
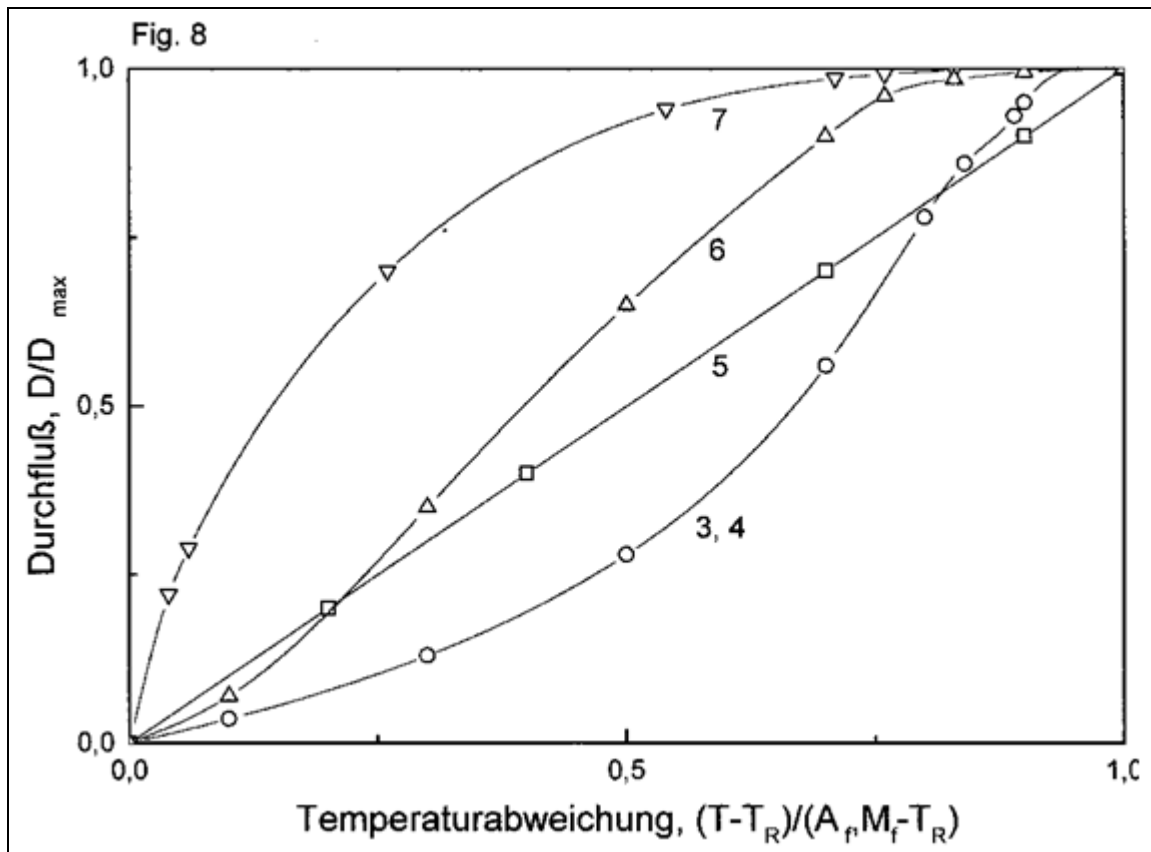
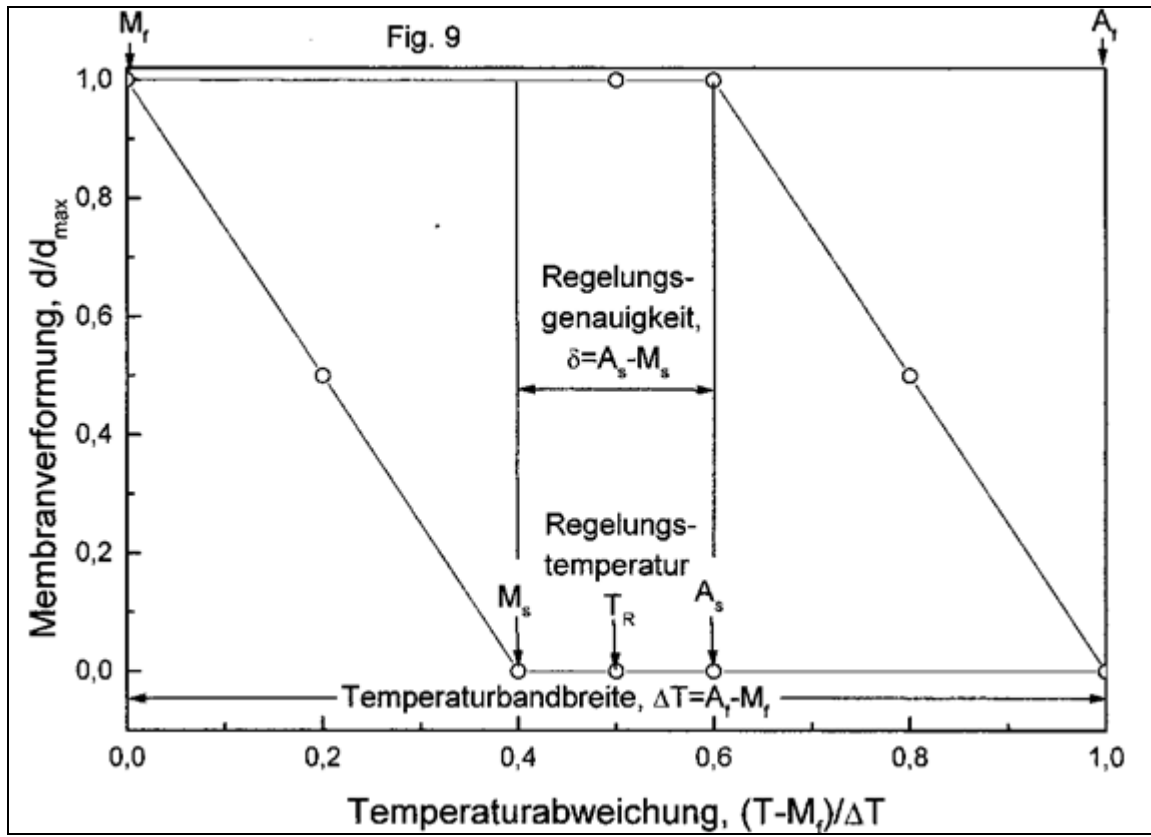


Fig.2









Protection claims:

1. Temperature control valve with a flow-controlling membrane made of a memory alloy or memory membrane (2) built into the body (1) of the temperature control valve, which, through its temperature-dependent shape changes, changes the flow cross-section of the temperature control valve and influences thus the flow rate of the Heating or cooling medium (*Figs. 1 a, b, c; 2 a, b, c*).
2. Temperature control valve according to claim 1, characterized in that the memory membrane (2) is made of a memory alloy with a narrow hysteresis, so that the control accuracy δ determined temperature difference $A_s - M_s$ between the starting temperatures A_s of the martensitic reverse transformation, in which the increase in flow cross-section begins during a temperature increase, and M_s of the martensitic forward transformation, in which the reduction in the flow cross-section begins during a temperature decrease, is less than 5°C (*Fig. 9*).
3. Temperature control valve according to claims 1 and 2, characterized in that the memory alloy is a multi-component alloy on the (Cu - Al) - or NiTi - base and the control temperature T_R , the temperature range $M_f - A_f$ (*Fig. 9*) and the control accuracy $\delta = A_s - M_s$ of the control valve can be adjusted through the memory alloy composition.
4. Temperature control valve according to claim 1, characterized in that the memory membrane (2) has the two-way memory effect and, through the temperature-dependent reversible movements between two low and high temperature shapes impressed on it influences the flow cross-section and thus the flow rate of the heating or cooling medium (*Figs. 1 a, b, c*).

5. Temperature control valve according to claim 1, characterized in that the memory membrane (2) has the one-way memory effect, is deformed when the temperature of the heating or cooling medium increases to its impressed high temperature shape and when the temperature decreases by the elastic force of a counter spring (5) is deformed back to its original low-temperature shape, so that these shape changes influence the flow cross-section and thus the flow rate of the heating or cooling medium (*Figs. 2 a, b, c*).
6. Temperature control valve according to claims 1 and 4, 5 characterized in that different opening profiles or opening flaps are cut into the memory membrane (2) (*Figs. 4 – 7*), which cause different flow-temperature deviation characteristics of the control valve (*Fig 8*).
7. Temperature control valve according to claims 1 to 6, characterized in that the memory membrane (2) or its opening flaps is their high-temperature shape impressed by the plastic deformation at temperatures of 700°C to 800°C , that comes about during heating and leads either in cooling systems to increase the flow cross-section (*Figs. 1 b, 2 b*), thus to open the valve, or in heating systems to reduce the flow cross-section, thus to close the valve (*Fig. 2a*).
8. Temperature control valve according to claims 1 to 7, characterized in that the memory membrane (2) is installed in the valve body in its shape or shape of its opening flaps that is changed at lower temperatures by martensitic deformation, which results either has in cooling systems a minimum flow cross-section (*Figs. 1 a, 2 a*) or in heating systems a maximum flow cross-section (*Fig. 2 b*).
9. Temperature control valve according to claims 1 to 4 and 6, characterized in that the memory membrane (2) or its opening flaps is trained to the two-way memory effect by repeated thermal transfor-

mation cycles with repeated shape changes by an external force at lower temperatures according to claim 7 and it is then installed in the valve body (1) according to claim 8 (*Fig. 1 a, b, c*).

10. Temperature control valve according to claims 1 to 3 and 5 to 8, characterized in that in the valve body (1) an elastic counter spring (5) is used (*Fig. 2 a, b, c*), the elastic force of which counteracts when heated the restoring force of shape-changing memory membrane (2) without being able to prevent this shape change, and, on the other hand, promotes the martensitic deformation of the memory membrane (2) or the opening flaps cut into the memory membrane (2) to their low-temperature shape at the temperature decreasing (*Fig. 2 a, b, c*).
11. Temperature control valve according to claims 1 and 4 to 10, characterized in that the memory membrane (2) is attached to the bottom (4) of the valve body (1) with one or more screws (3) (*Figs. 1, 2*).
12. Temperature control valve according to claims 1 and 4 to 11, characterized in that the memory membrane (2) is installed in the valve body (1) so that its shape change or the shape change of its opening flaps when the temperature rises takes place in the flow direction of the heating or cooling medium (*Figs. 1 b and 2 b*).
13. Temperature control valve according to claims 1 and 4 to 11, characterized in that the memory membrane (2) is installed in the valve body (1) in such a way that its shape change or the shape change of its opening flaps when the temperature rises takes place against the flow direction of the heating or cooling medium (*Fig. 1 c and 2 c*).

8.5 German utility model: „Assembled, symmetrical bending actuator with memory elements“

DE 202 01 578.5 dated 02/02/2002

Inventor: Dr. V. Prieb, Dr. H. Steckmann

Utility model holder: Company "1st Memory Alloys GmbH"

Abstract:

Object of the invention (based on the recurring memory effect due to the bias counterforce of two memory elements): The invention relates to a memory bending actuator for generating periodic, symmetrically reciprocal bending movements by means of time-controlled current impulses.

Areas of application: robotics, automation, positioning.

Description.

The invention relates to a composite symmetrical memory bending actuator for generating periodic reciprocal bending movements, which consists of two strips made of a memory alloy or two memory elements (1) and one elastically flexible, the two memory elements from each other electrically and thermally well insulating intermediate layer (2) and symmetrical bending movements in two opposite directions with the alternating heating of one of the memory elements after the other by electrical current impulses.

The memory actuator assembled in this way is connected to a power source through a change-over switch, so that each memory element is alternately connected to a circuit with the power source by a change-over switch and is heated by periodic current impulses. The current impulses are controlled by an electronic timer. In order to increase the cooling rate of the memory elements and thereby the action frequency of the memory actuator according to the invention, the memory actuator can be connected with its

passive, immovable end to a cooling thermostat.

Various actuators with electromechanical memory elements are known from the state of technology. Their functional principle is based on a shape change of a memory element when it is heated by electrical current, which is translated into translational or rotational movements.

DE 198 43 739 A1 describes an elastic joint element which consists of a tube-like polymer base body and some memory wires built into its wall. Different types of movement can be achieved by heating the pre-deformed memory wires in different sequences. The restoration of the martensitic detent deformation of memory elements, which is necessary for reversible and recurring movements, takes place during the cooling stages when the electrical current is switched off by the effect of the elastic force of the polymer tube filled with a liquid and by the pressure of this liquid.

DE 100 30 025 A1 presents a device for positioning a control element, which contains a reversibly expandable and contractible electromechanical element made of a memory alloy, whose forward movement be initiated by the electric current with controllable amperage and whose back movement be initiated by the elastic force of a return spring when the power is switched off.

A bending actuator with large deflections from a memory wire embedded in an elastic tube is proposed by Wang and Shahinpoor in “A new design for a bending muscle with an embedded SMA wire actuator” (*SPIE, Vol. 2715, 1996, 51-61*), in which the martensitic detent deformation of an active memory wire in the low temperature state is also restored by the elastic force of the tube.

In all of these solution variants, an elastic counterforce from a passive

bias element is needed to restore the low-temperature shape or the martensitic detent deformation of memory elements while they are cooling, which counteracts during the heating, increases linearly with its elastic deformation and thereby greatly reduces the active force of the actuator.

The same authors describe in “Design for shape memory alloy rotatory joint actuators using shape memory effect and pseudoelastic effect” (*SPIE, Vol.3040, 1997, 23-30*) a rotary actuator, in which a passive memory wire in its pseudoelastic state – instead of a normal elastic counter-spring – another active memory wire is opposed in its quasiplastic state, that is heated by the electric current,. Although this avoids the linear increase in the elastic counterforce, but the tension level in the passive memory wire, which is necessary for its pseudoelastic deformation, remains high, which also reduces the efficiency of the memory actuator.

In addition to the disadvantages identified above, such memory actuators also have a significant disadvantage. An action cycle of these actuators consists of an active heating stage and a subsequent passive cooling stage, which lasts much longer than the first due to heat exchange conditions. This means for all previously known actuators with active memory elements that they not only have the disadvantage of the force-related asymmetry caused by the use of a passive elastic element, but also the time-related asymmetry of their action cycle.

The invention presented here aims development of a memory bending actuator, which exerts a great force or makes great deflections, can be actively controlled in both bending directions and has an action cycle that is symmetrical relative both force and time.

This problem is solved according to the invention by the features of the independent protection claim 1. The solution suitable for a mutually active-

ly controlled symmetrical actuator uses the memory and the associated force effect of two quasiplastic pre-deformed memory bending elements combined in a twin relationship of the detent deformation, which act against each other when they are alternately heated by the electric current.

The advantageous combination of two active memory elements according to the invention excludes the use of a passive bias element and thus simplifies the construction of the actuator.

Advantageous embodiments and expedient developments of the invention are described in subordinate claims 2-12.

The advantageous use according to the invention of the same memory alloy with the same transformation temperatures and memory properties according to protection claim 2, the same bending deformation to the same high-temperature shape according to protection claim 3, the same martensitic quasiplastic deformation at room temperature to its straight low-temperature shape according to protection claim 4 and the composition of the two memory elements in a twin relationship with their concave sides (*compression side*) facing each other ensures the force- and time-related symmetry of the actuator according to the invention.

The advantageous use of the electrical current to control the memory actuator according to the invention is possible due to an insulating intermediate layer according to protection claims 6, 7, three electrical contacts according to protection claims 8, 9 and the connection to a power source via a change-over switch and an electronic timer according to protection claim 10. Actuator as well as the inventive advantageous connection of its passive end to a cooling thermostat according to protection claim 11 ensure the force- and time-symmetrical movements of the memory actuator according to the invention with a certain frequency and produce a great amount of

useful work, which can be used as a drive for various mechanisms according to protection claim 12.

Further details, construction details and special features are explained using the drawings. It shows:

Fig. 1. One of the embodiments of the memory actuator according to the invention in its neutral position (**a**) and two mutual deflection positions (**b**, **c**).

Fig. 2. High-temperature bending shape of the two memory elements (I) with thickness $2t$ and with a deflection d , with a deflection radius R_d (**a**, **b**), and the assembly of the two memory elements (**c**) in a twin relationship to the memory bending actuator according to the invention with a connected cooling thermostat (4).

Fig. 3. General stress-deformation (*quasiplastic deformation of martensite*) for the convex tensile and for the concave compression side (**a**), deformation-temperature (*deformation under constant load*) (**b**) and the stress-temperature (*restoring force*) (**c**) diagrams of memory bending elements.

Fig. 4. Action cycle diagrams: time dependencies of the electric current $I(\tau)$ and the relative temperatures $\theta_{E1}(\tau)$, $\theta_{E2}(\tau)$ in memory elements

($E1$, $E2$) (**a**), the deflection $d(\tau)$ (**b**) and the relative force $\Phi = \frac{F}{F_{\max}}$ in

individual memory elements ($E1$, $E2$) and in the composite memory bending actuator (**c**).

Fig. 1 shows schematically the embodiment of the electric current operated memory actuator (**a**) according to the invention and its mode of operation (**b**, **c**). The memory actuator (**a**) consists of two memory elements (I), an elastically flexible, electrically and thermally insulating intermediate layer (2) and a fastening bolt (3), which is used simultaneously as an electrical contact that is permanently connected to a power source for the two memory elements (I).

Two further electrical contacts at the movable ends of the memory elements (I) are alternately connected to the same power source through a

change-over switch and an electronic timer, which are not defined in detail here, as well as the wiring of the change-over switches and the power source itself,. Applying the electrical current to the upper memory element (*E1*) leads to a deflection of the memory bending actuator according to the invention with a certain downward deflection *d* (**b**), while the electrical current is switched to the lower memory element (*E2*) causes the deflection of the memory bending actuator according to the invention with the same deflection *d* upwards (**c**). In the further description, the work phases in the positive (**b**) and in the negative area (**c**) are drawn.

More construction details of the memory bending actuator according to the invention are shown in Fig. 2 a, b, c. The two memory elements (*I*) with the thickness $2t$ and the active length L_A to be heated (*the distance between the two electrical contacts of one of the memory elements*) are plastically deformed into an arc with the same radius (**Fig. 2 a, b**). This plastic deformation can be impressed in two ways: either the two are bent at room temperature by the lighter martensitic quasiplastic deformation and annealed in a device that fixes this shape at approx. 800°C , or directly deformed at this temperature plastically.

The two sides of the memory elements should be marked as convex (*tension side*) and concave (*compression side*) before further treatments. The high-temperature shape impressed by the plastic deformation is then changed to the straight low-temperature shape by the martensitic quasiplastic deformation at room temperature. The two memory elements (*I*) are assembled in this modified low-temperature shape with the sides marked as concave (*compression side*) to one another, i.e. are placed in a twin relationship (**Fig. 2c**) and fastened with a bolt (3), with an elastically flexible, electrically and thermally well insulating intermediate layer (2) between the

two memory elements (1), which is in a freely sliding contact with both memory elements (1). The passive, with the bolt (3) fastened edge of the memory bending actuator can be brought according to the invention into good thermal contact with a cooling thermostat (4), for example at 0°C (**Fig. 2c**), so that a greater and constant cooling rate of the memory elements (1) is achieved.

Memory alloys have a limited resource of martensitic quasiplastic or pseudoelastic deformation ε_{\max}^M , which can be $0.05 \div 0.06$ in polycrystalline *NiTi*-SMA and in (*Cu – Al*)-based $\langle 100 \rangle$ single crystals. After this resource is exhausted when a memory element is exposed to external loads, the yield point σ_y of true plastic irreversible deformation is reached. For these reasons, the quasiplastic detent deformation must not exceed this limit at action cycles with total deflection. This means for the original quasiplastic deformation $\varepsilon_q = \frac{t}{R_d} \leq 0.5\varepsilon_{\max}$ or for the high-temperature shape

$$R_d \geq \frac{2t}{\varepsilon_{\max}}.$$

Fig. 3 shows the diagrams which are specific to the memory alloys and which help to understand the functional principle of the memory bending actuator according to the invention. The stress-deformation diagram (**Fig. 3 a**) shows the quasiplastic deformation of the martensite at temperatures $T \leq M_s$ (**Fig. 3 b**). The quasiplastic tensile deformation (*the 1-st quadrant of the diagram, top right: $0 - \sigma_{qy} - A - A'$*) arises on the concave side of the high-temperature shape when it changes to the straight, low-temperature installation shape, while the compression deformation (*the 3-d quadrant of the diagram, bottom left: $0 - \sigma_{qy} - B - B'$*) occurs the other

convex side takes place. Relative tension and deformation units are plotted on the axes.

In the following action cycles, the diagram (**Fig. 3 a**) only applies to the memory element E2 to be cooled in connection with the stress development in the memory element E1 to be heated (**Fig. 3 c**) during the resetting of its detent deformation $\varepsilon_q = 0.5\varepsilon_{\max}$ when heated about the temperature $T \geq A_s$ (**Fig. 3 b**). As soon as the stress of the memory element E1 (**Fig. 3 c**) reaches the yield point of the memory element E2 at point A (**Fig. 3 a**), the memory element E2 is further deformed quasiplastically above its original detent deformation $\varepsilon_q = 0.5\varepsilon_{\max}$ along the line $A-C-C'$ or the line $B-D-D'$ (**Fig. 3 a**) up to the maximum detent deformation $\varepsilon_q = \varepsilon_{\max}$ due to the stress $\sigma(T = T_{\max}) = \sigma_{\max}$ (**Fig. 3 c**).

During the subsequent heating of the memory element E2 with the detent deformation $\varepsilon_q = \varepsilon_{\max}$ and cooling of the memory element E1, the latter is further deformed quasiplastically according to the same scheme until its new detent deformation $\varepsilon_q = \varepsilon_{\max}$. In further action cycles the interaction of the two elements is repeated symmetrically between $-\varepsilon_{\max} \leq \varepsilon_q = +\varepsilon_{\max}$.

Fig. 4 a, b and c represent schematically the timing diagrams of the above-described action cycles of the memory bending actuator according to

the invention in relative units for the current impulses $I(\tau) = \frac{I(\tau)}{I_{\max}}$, for the

cooling-heating stages $\Theta(\tau) = \frac{T(\tau) - T_{\min}}{T_{\max} - T_{\min}}$ of the two memory elements,

for the deflection $d(\tau) = \frac{d(\tau)}{d_{\max}}$ of the assembled memory bending actuator

and for the force development $\Phi(\tau) = \frac{F(\tau)}{F_{\max}}$ both in individual memory

elements and in the assembled memory bending actuator.

If one of the two memory elements E1 is subjected to a current impulse lasting for example 2 seconds (**Fig. 4 a**, *solid line I*), the temperature of this memory element rises along the dashed line θ_{E1} to its maximum value $T_{E1} = T_{\max}$ ($\theta_{E1} = 1$). Meanwhile, the other memory element E2 is in the cooling stage along the dotted line θ_{E2} up to its minimum value $T_{E2} = T_{\min}$ ($\theta_{E2} = 0$). The memory bending actuator turns out with a deflection in the range $0 \leq d(\tau) \leq 1$ to one side (**Fig. 1 b**).

If the electrical current is switched to the other memory element E2 (**Fig. 4 a**, *solid line I in the lower negative area*), the temperature change in the two memory elements takes place in reverse order, and the memory bending actuator turns out with a time delay with the deflection in the range $-1 \leq d(\tau) \leq 1$.

The new action cycles begin after that with the same deflection $-1 \leq d(\tau) \leq 1$. The cycle period of $\tau_c = 4s$ with current impulse duration of $\tau_I = 2s$ arbitrarily selected in this example corresponds to an operating frequency of $f_{MA} = 1/\tau_c = 0.25Hz$. This frequency is about an order of magnitude higher than the limit frequency value of $0.01Hz$ (*V. Prieb. The limiting of the response time of shape memory alloy actuators by transformation rate. Report to the "Readings on the materials with shape memory and superelasticity effects, May 24-25, 2000, Kiev", Kiev 2000*).

The action frequency of the memory bending actuator according to the

invention can be increased in that the complete forward transformation of the passive memory element due to its slow cooling is not necessary. The restoration of the martensitic detent deformation of the memory element to be cooled can already take place in the pseudoelastic temperature range $T > A_f$ through the restoring force of the other twin memory element, as soon as the restoring force $S_{ME} \cdot \sigma_{E1}(T \uparrow)$ of the active memory element E1, which increases with the temperature increase, overcomes the yield point $\sigma_{py}^{E2}(T \downarrow)$ of the pseudoelastic deformation of the passive memory twin element E2 is reached as the temperature decreases:

$$S_{ME} \cdot \sigma_{E1}(T \uparrow) \geq S_{ME} \cdot \sigma_{py}^{E2}(T \downarrow). \quad (8.5.1)$$

If the amperage is set so that the heating time is sufficient to cool a memory twin element down to temperature M_s , the action cycle of the memory actuator according to the invention consists of the same heating times of the two twin elements and is therefore symmetrical in time.

The time delay $\Delta\tau$ between the return points on the deflection and force-time diagrams of the memory bending actuator according to the invention (**Fig. 4 b, c**) is determined by the time required to achieve equal stress (8.5.1). The total time τ_{ME} required for a heating-cooling cycle of one of the memory elements (**Fig. 4 a**) depends on the cooling (\dot{T}_c) and heating (\dot{T}_h) rates, on the maximal temperature T_{\max} (**Fig. 3 c**), on the hysteresis width ΔT of the martensitic transformation (**Fig. 3 b, c**) and on the minimal temperature (T_{\min}):

$$\tau_{ME} = \tau_h + \tau_c = \frac{T_{\max} - (T_{\min} + \Delta T)}{\dot{T}_h} + \frac{T_{\max} - (T_{\min} + \Delta T)}{\dot{T}_c}. \quad (8.5.2)$$

On the other hand, an action cycle (*action period* τ_{MA}) of the memory actuator according to the invention consists of the deflection time from the negative to the positive area and back as well as two delay times $\Delta\tau$ between the both (**Fig. 4 b**);

$$\tau_{MA} = 2(\tau_{d\pm} + \Delta\tau) = \tau_{ME} \quad (8.5.3)$$

It follows from equations (8.5.2) and (8.5.3): the closer the temperatures T_{\min} and T_{\max} are to each other, the smaller the thermal transformation hysteresis and the greater the cooling \dot{T}_c and heating \dot{T}_h rates, the smaller the time delay $\Delta\tau$ between the return points an action cycle and thus the shorter the action period of the composite memory bending actuator according to the invention.

The useful work done by the memory bending actuator according to the invention is performed by the active memory element through the excess force $F_{MA} = S_{ME} \cdot \Delta\sigma$ on the way $2d$ after the quasiplastic detent deformation of its twin element:

$$A_{MA} = S_{ME} \cdot [\sigma_{\max} - (\sigma_{qy} + k_q \cdot \varepsilon_q)] \cdot 2d = 2t \cdot b_{ME} \cdot \Delta\sigma \cdot 2d, \quad (8.5.4)$$

where b_{ME} is the width of the memory elements. This work depends linearly on the maximal restoring stress and on the geometry of the memory elements (*their thickness and width*). It is therefore advantageous that the quasiplastic flow line $\varepsilon_q(\sigma)$ in memory alloys normally has a very small

quasiplasticity coefficient $k_q = \frac{d\sigma}{d\varepsilon_q}$, so that the stress difference

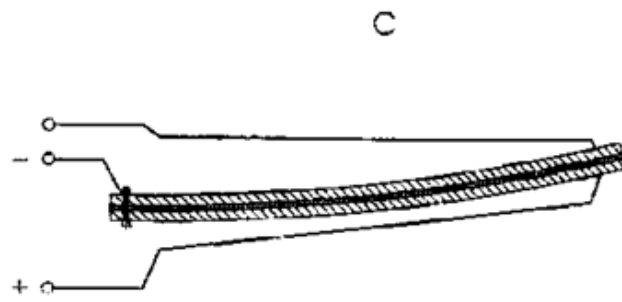
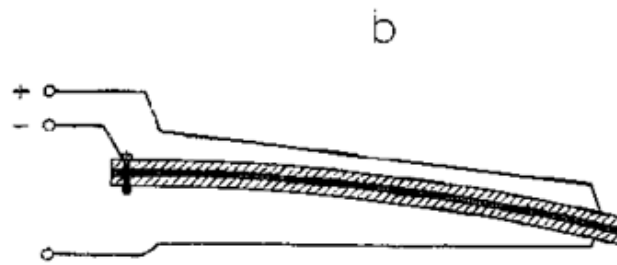
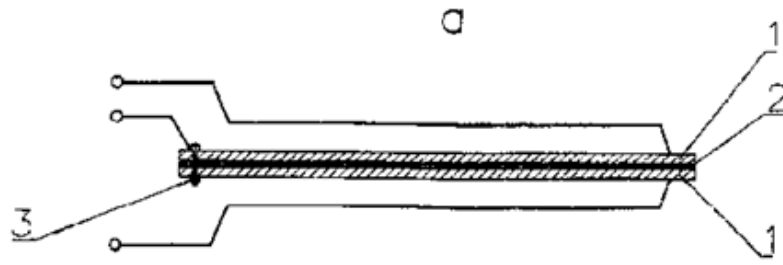
$\Delta\sigma = k_q \cdot \varepsilon_q$ is very small.

Increasing the power $P_{MA} = A_{ME} / \tau_{MA} = A_{ME} \cdot f_{MA}$ through these pa-

rameters is due to several boundary conditions such as the one for maximal stress $\sigma_{\max}(T) < \sigma_y$, which must not exceed the yield point of the real plastic deformation when the temperature increases. An increase in power by enlarging the cross section is limited by the fact that it leads to an increase in the mass $m_{MA} = 2t \cdot b_{ME} \cdot L_A \cdot \rho$ of the memory actuator made of a memory alloy with the density ρ and thus its inertia (*lowering of the action frequency f_{ME}*), especially through a prolonged cooling stage. Depending on the aim of the composite memory bending actuator according to the invention – maximum force or maximum deflection – careful optimization of these related parameters is therefore required.

For that 4 drawings:

Fig.1



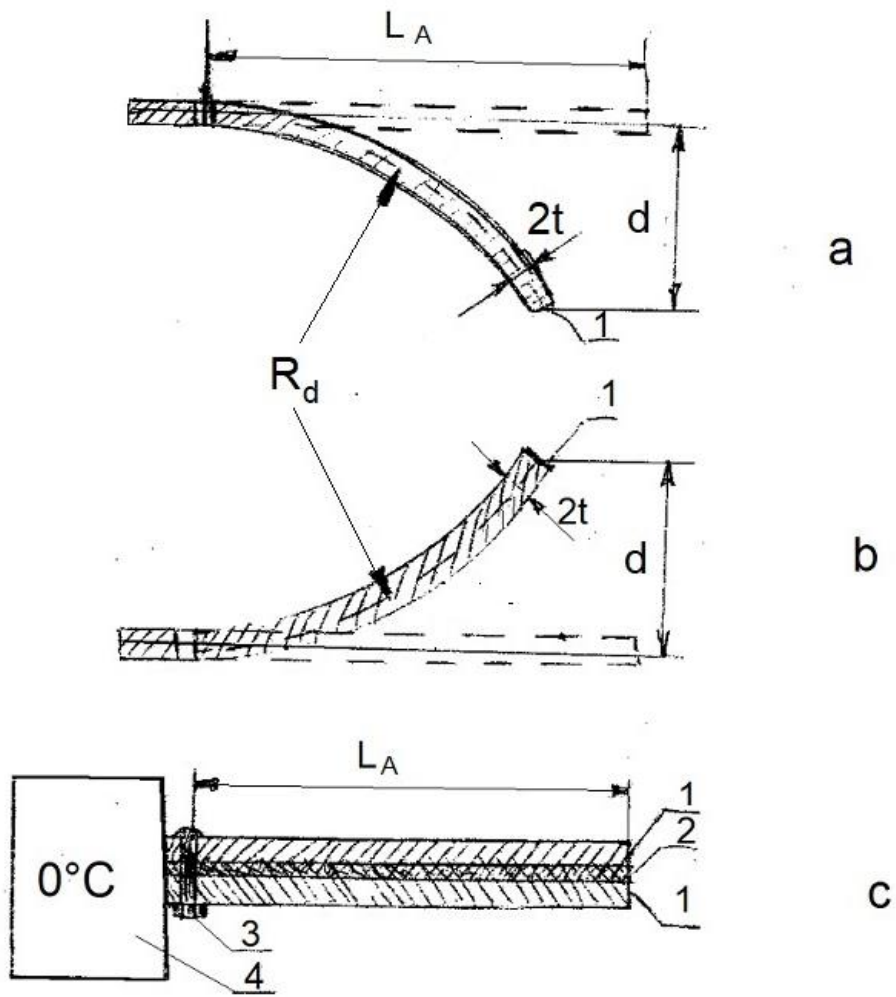
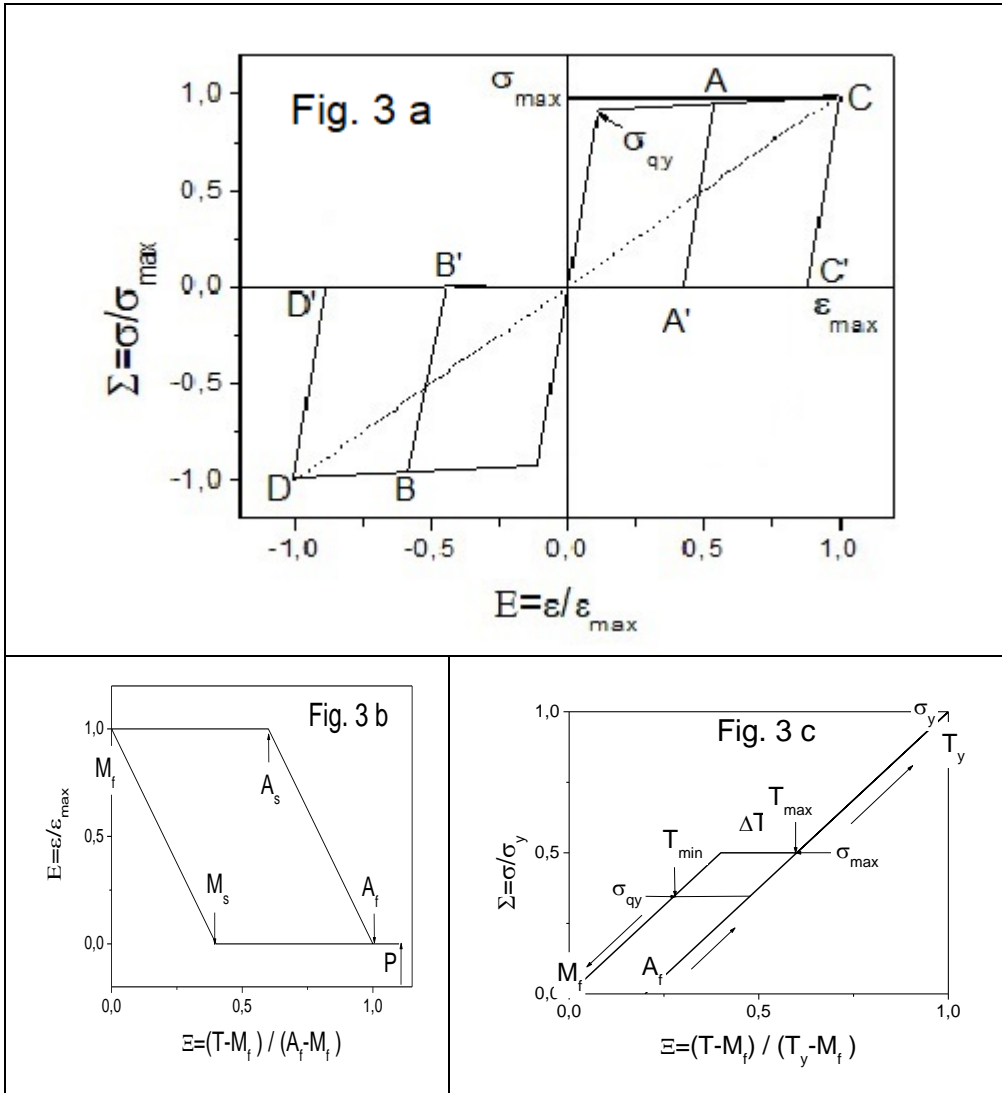
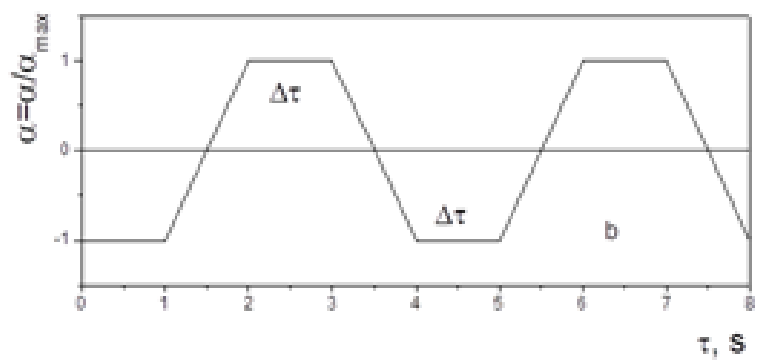
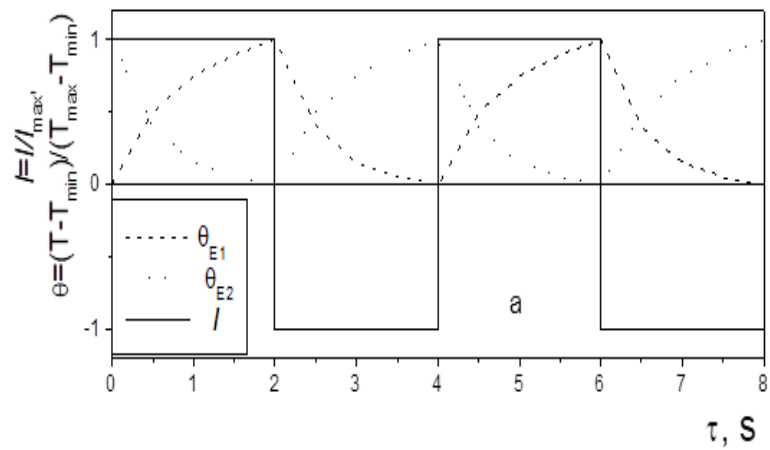


Fig. 2





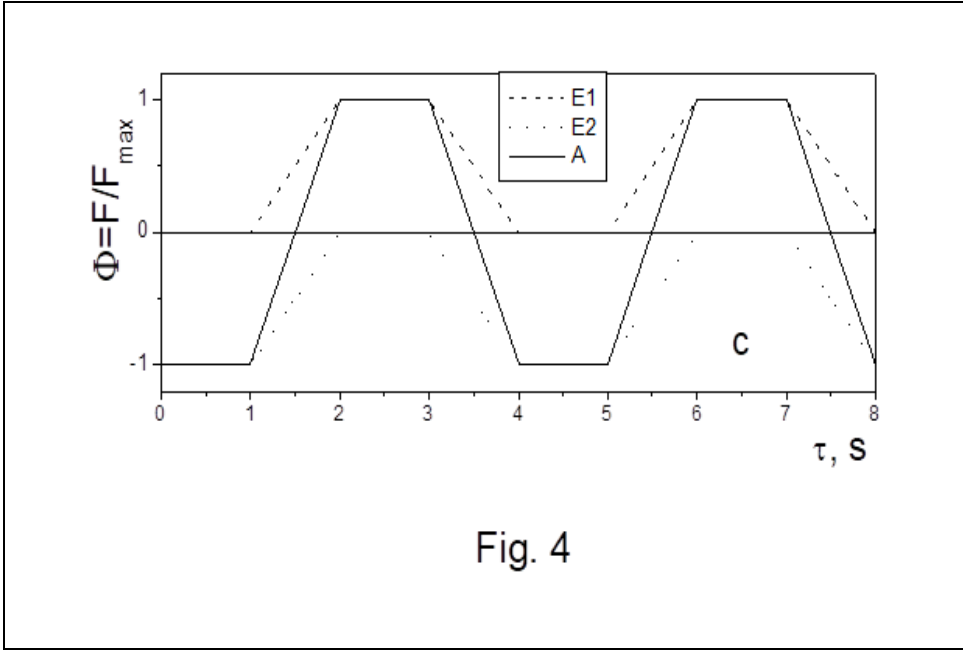


Fig. 4

Protection claims:

1. Actuator for generating periodic bending movements, characterized in that the actuator consists of two elements made of a memory alloy or memory elements (*1*), which are heated alternately and separately by the electronically controlled current impulses (***Fig. 1 a, b, c***).
2. Actuator according to claim 1, characterized in that the memory elements (*1*) consists of the same memory alloy with the same transformation temperatures and memory properties.
3. Actuator according to claims 1 and 2, characterized in that the memory elements (*1*) are impressed with the same high-temperature shape (***Fig. 2 a, b***) by the same plastic bending deformation.
4. Actuator according to claims 1 to 3, characterized in that the plastically impressed high-temperature shape of the two memory elements (*1*) is changed to its straight low-temperature shape (***Fig. 2 c***) by the quasiplastic martensitic deformation at room temperature.
5. Actuator according to claims 1 to 4, characterized in that the two memory elements (*1*) are assembled in their straight low-temperature shape in a twin relationship, so that the radii determined the curvature by their high-temperature shape or their concave sides are directed opposite one another (***Fig. 2 c***).
6. Actuator according to claims 1 and 5, characterized in that a thin, elastically flexible intermediate layer (*2*) is set between the two memory elements (*1*) (***Figs. 1 a, b, c and 2 c***).
7. Actuator according to claims 1, 5 and 6, characterized in that the elastically flexible intermediate layer (*2*) consists of an electrically and thermally good insulating material.
8. Actuator according to claims 1, 5 and 6, characterized in that the two

memory elements (1) separated by an intermediate layer (2) are fastened together at their passive edge, for example with a bolt (3), which is designed at the same time as an electrical contact for the two memory elements (1) (**Fig. 1**).

9. Actuator according to claims 1 to 8, characterized in that each of the two memory elements (1) is provided with an electrical contact at its other, active edge.
10. Actuator according to claims 1 and 5 to 9, characterized in that a power source is connected to the two memory elements (1) by a timer and a change-over switch, so that each of the two memory elements (1) is heated alternately through the current impulses, where the pulse duration is controlled by an electronic timer.
11. Actuator according to claims 1 and 10, characterized in that the two memory elements (1) are connected to a cooling thermostat by good thermal contact at their passive, fastened edge (**Fig. 2 c**).
12. Actuator according to claims 1 to 11, characterized in that it is used as a drive for various mechanisms by repeatedly exerting a maximal force $F_{\max} = (\sigma_y - \sigma_{py}) \cdot S_{ME}$ over a maximal way $2d_{\max}$ and thereby doing a useful work $A_{MA} = (\sigma_y - \sigma_{py}) \cdot S_{ME} \cdot 2d_{\max}$.

9 Nomenclature

Abbreviations:

AE acoustic emission

DSC differential Scanning Calorimetry

DIL dilatometry

SMA shape memory alloy

HT heat treatment

REM scanning electron microscopy

TEM transmission electron microscopy

RPM **R**eturn **P**oint **M**emory

SMART **S**tep-wise **M**artensite to **A**ustenite **R**eversible **T**ransformation

TAME **T**hermal **A**rrest **M**emory **E**ffect

(*i*) invariant shear plane

fcc cubic face-centered

fcc face-centered tetragonal

p.c.c. partial cooling cycles

p.c.h. partial heating cycles

Subscript or superscript indices:

a actuator

ad adiabatic

A austenite

A' metastable austenite

A'M^P austenite-martensite phase boundaries

A'+M^P austenite-martensite two-phase state

A'→M^P austenite-martensite transformation

B energetic barrier

B breaking point

B2 as *CsCl* ordered, body-centered cubic austenite structure

$B19$ orthorhombic martensite
 $B19'$ orthorhombic martensite with monoclinic distortion
 c completely
 c, h cooling, heating
 cr critical
 δ the smallest deviation
 d deflection of a SMA bending actuator
 DO_3 as Fe_3Al ordered face-centered cubic austenite structure
 el elastic or electrons
 E memory insert
 fy ferroelastic yield
 $[hkl]$ Miller indices
 i cycle number
 l latent hysteresis
 M martensite
 M^m martensite macromonodomain
 M_m^m martensite micromonodomain
 M^+ tension monodomain
 M^- compression monodomain
 M^\pm monodomain mix
 M^p martensite polydomain
 ME memory element
 MA memory actuator
 p pseudoelastic
 py pseudoelastic yield
 q quasiplastic
 qy quasiplastic yield

R electrical resistivity
 R rhombohedral martensite of *NiTi*-SMA
 $9R$ rhombic martensite of SMA *Cu*-based SMA
 s softened or stabilized
 sf stacking fault
 t, c tension, compression
 T thermal, thermal induced
 y true plastic yield

Symbols and units of measurement

Latin symbols:

$a [J \cdot kg^{-1}]$ specific mechanical work
 $A [J]$ mechanical work
 $A [m^2]$ attack surface
 $A_H [-]$ asymmetry measure of dilatometrically determined hysteresis loops
 $A_s, A_s' [^{\circ}C]$ to $z = 1$ extrapolated and measured start-temperatures of the martensitic forwards transformation
 $A_f, A_f' [^{\circ}C]$ to $z = 0$ extrapolated and measured finish-temperatures of the martensitic reverse transformation
 $A_{sf} [m^2]$ stacking fault area
 $b [m]$ Burgers vector
 $b_{tr} [m]$ width of the transition zone
 $\bar{B} [T]$ magnetic induction
 $B_R [T]$ residual magnetization (*remanence*)
 $B [m]$ width of a martensite band
 $C [MPa]$ elasticity constant
 $d [m]$ diameter of the memory wire

$D[m]$ diameter of the round contact surface or of the ceramic beads when manufacturing memory meanders $D_0[MPa]$ Laplasian pressure

$c_p \left[\frac{J}{kg \cdot K} \right]$ isobaric specific heat capacity

$\vec{e}[m]$ shear vector

$E_0[eV]$ acceleration energy of electron pulses

$E_{el}[J]$ elastic energy

$E_{pl}[J]$ plastic energy

$E_{total}[J]$ total energy

$E_{int}[J]$ Interaction energy

$f_a[Hz]$ action frequency of SMA actuators

$f[J]$ specific free energy

$f_{ch}[J]$ chemical driving force

$f_{nch}[J]$ non chemical driving force

$f_{dis}[J]$ dissipative driving force

$\vec{F}[N]$ force

$F^X[J]$ free energy of the X - state

$\Delta F^{XY}[J] = F^X - F^Y$ difference in free energies between X - and Y -states

$G[MPa]$ shear modulus

$G_{eff}^{A+M^P}[MPa]$ effective shear modulus

$h[W]$ heat flow measured in DSC

$h[MPa]$ dissipation parameter for systems with friction

$\vec{H} [A \cdot m^{-1}]$ magnetic field strength

$H_c [A \cdot m^{-1}]$ coercive force, coercive field force

$I[A]$ electrical current

$I_s[A]$ short circuit current

$I_N [A]$	rated current
$I_{AE} [imp \cdot s^{-1}]$	acoustic emission intensity
$I_{[hkl]} [imp \cdot s^{-1}]$	Intensity of an $[hkl]$ X-ray reflex
$j_{el} [A/m^2]$	current density of an electron pulse
$J [A^2 \cdot s]$	Joule-Integral
$k_a^I [-]$	accommodation degree due to structural mechanism
$k_a^{II} [-]$	accommodation degree due to morphological mechanism
$k_c [-]$	transformation incompleteness parameter
$k_T [\Omega \cdot m \cdot K^{-1}]$	temperature coefficient of electrical resistivity
$k_{sf}^{M^P} [MPa]$	specific (per volume unit) stacking fault energy
$k_f [J \cdot kg^{-1}]$	energetically ferroelasticity coefficient
$k_p [J \cdot kg^{-1}]$	energetically pseudoelasticity coefficient
$k_q [J \cdot kg^{-1}]$	energetically quasiplasticity coefficient
$k_R [\Omega]$	linearity coefficient of the function of electrical resistance from deformation
$k_T^{XY} [J \cdot kg^{-1}]$	energetically thermoelasticity coefficient
$k_T [J \cdot kg^{-1}]$	energetic thermos-elasticity coefficient of a symmetrical hysteresis loop
$k_T^l [J \cdot kg^{-1}]$	dissipated energy of the latent thermal hysteresis
$k_{sf}^{M^P} [MPa]$	specific stacking fault energy
$k_{A_f}, k_{M_f} [s]$	coefficients of the hysteresis expansion by increasing the scanning rate
$K_{el} [J]$	specific elastic energy of the phase boundaries
$K_{12} [-]$	x-ray intensity redistribution factor
$L [m]$	length

$L_0[m]$ initial length

$\Delta L[m]$ length change

$m[kg]$ mass of a SMA sample

\bar{m}^{M^P} average mass of a martensite poly domain

$M_s, M_s' [^\circ C]$ to $z = 0$ extrapolated and measured start-temperatures of the martensitic forwards transformation

$M_f, M_f' [^\circ C]$ to $z = 1$ extrapolated and measured finish-temperatures of the martensitic revers transformation

$n_l[-]$ number of lamellae in the premartensitic temperature range

$N^{M^P} [-]$ number of martensite polydomains

$N_{AE}[-]$ number of acoustic pulses

$p[N \cdot m^{-2}]$ mechanical pressure

$P[N]$ mechanical external load

$Q(X)[J \cdot m^{-1}]$ electron energy losses

$Q_J[J]$ Joule heat

$q^{XY}[J \cdot kg^{-1}]$ specific XY -transformation heat

$Q^{XY}[J]$ latent heat of transformation between X – and Y -phases

$r_{tw}[-]$ reorientation factor

$R^X[\Omega]$ electrical resistivity

$\Delta R^{XY}[\Omega]$ resistivity difference between X – and Y -phases

$R_{eff}[m]$ effective penetration depth of the electrons

$S[m^2]$ cross-section

$S_{sf}[m^2]$ total area of a stacking fault

$S^X\left[\frac{J}{K}\right]$ entropy of X -phase per mass unit

$S_{config} \left[\frac{J}{K} \right]$ configuration entropy

$S_{vib} \left[\frac{J}{K} \right]$ vibration entropy

$\Delta s^{XY} \left[\frac{J}{kg \cdot K} \right]$ entropy difference between X – and Y -phases per mass unit

$\Delta s \left[\frac{J}{kg \cdot K} \right]$ average value of the entropy difference between X – and Y -phases per mass unit

$t[s]$ time

$t_{imp}[s]$ impulse duration

T temperature

$T_b[^\circ C]$ body temperature

$T_N[^\circ C]$ Neel temperature

$T_t[^\circ C]$ temperature of $fcc \leftrightarrow fct$ -transformation or test temperature

$T_0[K]$ global equilibrium temperature between austenite and a martensite monodomain

$T_0'[K]$ local equilibrium temperature between A' and martensite polydomains

$T_a[^\circ C]$ activation, tempering temperature

$T_m[^\circ C]$ measuring temperature

$T_m[^\circ C]$ melting temperature

$T_s[^\circ C]$ softening temperature

$T_R[^\circ C]$ control temperature

$\dot{T} [K \cdot s^{-1}]$ scanning rate

$\Delta T_{0.5}[^\circ C]$ width thermal hysteresis at $z = 0.5$

$U_{ep}[J]$ interaction energy between beam electrons and SMA electron-phonon system

$U_e[V]$ acceleration voltage of electrons

$\Delta U[V]$ Voltage drop across an electrical resistor
 $U[J] \equiv F(T = 0)$ internal energy
 $U(r)[J]$ Lenard-Jones interaction potential
 $U_a(T)[J]$ activation energy
 $\bar{u}_{el}^{M^P} [J]$ average elastic energy of a martensite polydomain
 $u_{i,i+1}[J]$ energy of a martensite micromonodomain as an energy quantum
 $U_{el}^{A'M^P} [J]$ elastic energy of the $A'M^P$ -phase boundaries
 $U_{M_s}^{A'M^P} [J]$ elastic energy of the $A'M^P$ -phase boundaries at the M_s -temperature
 $U_{sf}[J]$ stacking fault energy
 $v[m \cdot s^{-1}]$ velocity of a martensite boundary
 $v_B[m \cdot s^{-1}]$ escape velocity of the fractions
 $V[m^3]$ volume
 $w_D[J \cdot kg^{-1}]$ dissipated energy
 X alloy elements or phase states ($A, M, A + M$)
 z martensite phase fraction
 z_s phase fraction of stabilized martensite
 Z^A phase fraction of a one of the austenite phases
Greek symbols:
 $\alpha[-]$ angle between the normal to the habitus plane and the single crystal longitudinal axis
 $\alpha^{X,Y,XY}[K^{-1}]$ coefficients of the linear thermal expansion of the X -, Y - and $X + Y$ -phases
 $\alpha_V[K^{-1}]$ coefficient of thermal volume expansion
 $\beta[-]$ shear angle of a martensite monodomain
 \bar{b}_l average width of lamellae in premartensitic temperature range

$\delta_{ij}[-]$ Kronecker delta

$\delta^l[-]$ lamellae density in premartensitic temperature range

$\delta[^\circ C]$ control accuracy of a temperature control valve

$\varepsilon[-]$ deformation

$\varepsilon_{el}^{M^P}[-]$ non-accommodated elastic deformation

$\Delta\varepsilon_f[-]$ deformation amplitude of ferroelastic hysteresis loop

$\varepsilon_d[-]$ linear dilatation

$\varepsilon_M[-]$ martensitic deformation generally

$\varepsilon_r[-]$ recoverable martensitic deformation

$\dot{\varepsilon}[s^{-1}]$ deformation rate

$\phi_c[-]$ coalescence probability factor

$\gamma[J \cdot m^{-2}]$ generalized stacking fault energy

$\gamma_M[-]$ martensitic lattice shear deformation

$\eta[-]$ order parameter or lattice deformation parameter

$\kappa_{ij}[MPa^{-1}]$ compressibility coefficient

$\lambda\left[\frac{J}{K \cdot m^2}\right]$ convection coefficient

$\lambda_m[-]$ morphology factor

$\lambda_R[-]$ geometrical factor for resistance measurements at tension-compression deformation

$\mu[-]$ Schmid orientation factor

$\mu\left[\frac{V \cdot s}{A \cdot m}\right]$ magnetic permeability

$\nu_{sf}[m^{-3}]$ stacking fault density

$\vartheta[-]$ displacement angle of a martensite polydomain

ρ	$[kg \cdot m^{-3}]$	density
ρ	$[\Omega \cdot m]$	specific electrical resistance
σ	$[MPa]$	mechanical stress
σ^{int}	$[MPa]$	internal mechanical stress
σ^{ext}	$[MPa]$	external mechanical stress
$\sigma_{c,t}$	$[MPa]$	compression, tension stress
$\Delta\sigma_f$	$[MPa]$	stress amplitude of ferroelastic hysteresis loop
σ_0	$[MPa]$	equilibrium stress
$\ \sigma_{ij}\ $	$[MPa]$	stress tensor
τ	$[MPa]$	shear stress
$\ \tau_{ij}\ $	$[MPa]$	shear stress tensor
ξ	$[-]$	angle between the single crystal longitudinal axis and the normal to the shear plane
ζ	$[-]$	angle between the single crystal longitudinal axis and shear direction